université PARIS-SACLAY

Approche multi-modèle adaptative pour la propagation d'endommagement dans de grandes structures composites stratifiées

An adaptive multi-model approach for damage propagation simulations in large composite structures

Thèse de doctorat de l'Université Paris-Saclay

École doctorale n° 579, Sciences mécaniques et énergétiques, matériaux, géosciences, SMEMAG
Spécialité de doctorat : Mécanique des solides
Unité de recherche : Université Paris-Saclay, ONERA, Matériaux et Structures, 92322, Châtillon, France
Référent : ENS Paris-Saclay

Thèse présentée et soutenue à Paris-Saclay, le 31 Mars 2021, par

Eva BORAKIEWICZ

Composition du jury

Alain RASSINEUX Professeur, UTC	Président
Joël CUGNONI Professeur associé, HEIG-VD	Rapporteur
Pierre KERFRIDEN HDR, Mines ParisTech	Rapporteur
Federica DAGHIA HDR, LMT - ENS Université Paris-Saclay	Examinatrice
Carlos DÁVILA Professeur, NASA, Langley Research Center	Examinateur

Direction de la thèse

Frédéric LAURIN HDR, Onera Université Paris-Saclay	Directeur de thèse
Vincent CHIARUTTINI PhD, Onera Université Paris-Saclay	Co-encadrant
Philippe PETERS Ingénieur de recherche, Airbus Operations	Co-encadrant

Thèse de doctorat

NNT: 2021UPAST029

Acknowledgements

Ces travaux de thèse ont été réalisés dans le cadre d'un partenariat entre l'Onera et Airbus, sous une convention CIFRE. Ainsi, j'ai pu découvrir les mondes de la recherche académique et industrielle, et j'en suis très reconnaissante.

Je remercie d'abord Frédéric Laurin, mon directeur de thèse, pour avoir partagé son goût de la recherche et son engagement dans le transfert des connaissances et des outils pour des applications industrielles. Je remercie ensuite Vincent Chiaruttini, mon encadrant à l'Onera, pour son suivi sur les aspects numériques de la thèse, et pour ses idées toujours riches et créatives. Je le remercie également pour m'avoir accueillie dans son unité MS2. Je remercie Antoine Hurmane, m'ayant également encadré à l'Onera, pour sa disponibilité et sa patience.

Je remercie sincèrement Philippe Peters, mon encadrant d'Airbus, qui, malgré la distance, a su être très présent, tant du point de vue technique qu'humain. C'était un plaisir de travailler avec une personne ayant une grande expertise technique et en même temps beaucoup d'humilité. Je le remercie également de la confiance qu'il m'a accordée pour mener ces travaux de thèse.

J'adresse mes remerciements aux membres du Jury pour avoir accepté d'évaluer ce travail de thèse : en particulier à Joël Cugnoni et Pierre Kerfriden pour avoir accepté de rapporter ce manuscrit, à Alain Rassineux pour avoir accepté de présider le Jury, et à Federica Daghia et Carlos Dávila pour avoir participé au Jury.

Je tiens également à remercier les équipes d'Airbus pour leur accueil chaleureux et pour les réunions toujours enrichissantes sur le plan technique. Je tiens en particulier à remercier Jean-Michel Laborie et Mélanie Herman pour m'avoir intégrée dans leurs équipes, et Michel Fouinneteau et Maxime Hamadi qui ont dirigé le projet dont fait partie cette thèse.

Je remercie chaleureusement tous les stagiaires, doctorants, post-doctorants, techniciens, ingénieurs et chercheurs des unités MS2 et MC2 du Département Matériaux et Structures (DMAS) de l'Onera. J'ai passé de très bons moments au sein de ces équipes, généralement autour de l'aquarium à la pause café. Je remercie également le groupe de yoga pour les moments de dépaysement et de détente, et en particulier Sylvia, qui guide bénévolement les séances.

Enfin, je suis très reconnaissante du soutien bienveillant et constant de mes amis, de mes amis qui sont comme la famille, et de ma grande famille, mes oncles, mes tantes, et mon grand-père. Merci à Toto Louise pour son implication dans mon parcours. Et bien sûr, merci à mon père et à ma mère, toujours plein de projets, généreux et tournés vers les autres, et qui sont pour moi un parfait exemple du "live and let live". Merci à ma sœur, ma complice ;), avec qui j'ai partagé tant de moments importants, et dont la réflexion singulière m'inspire toujours. Je suis profondément reconnaissante de l'éducation de ma grand-mère, qui a toujours cru en moi, et pour les valeurs qu'elle m'a transmises. J'espère être à la hauteur de son héritage.

Enfin, mon entière gratitude va à Dimitri, "l'autre doctorant", avec qui je partage ma vie. Je le remercie pour son soutien, pour ses relectures du manuscrit, mais surtout pour les beaux moments de vie. Il est pour moi un exemple d'ouverture d'esprit, de curiosité, de persévérance, et de culot !

Contents

Acknowledgements **iii**

1 Introduction **1**

2 Numerical strategies for the simulation of local complex behaviour for large composite structure applications **7**

2.1 Computation of large slender multilayered structures 8
2.1.1 Numerical strategies for large problem resolution 8
2.1.2 Simplified modeling of slender multilayered structures 11
2.1.3 Conclusion 15
2.2 Predictive material models for composite laminates 16
2.2.1 Introduction on unidirectional composite laminates 17
2.2.2 Modelling of composite laminate's behaviour 18
2.2.3 Finite element resolution using the composite damage laws 24
2.2.4 Conclusion 26
2.3 Elements of bibliography on multiscale finite element strategies for problems with two levels of modelling 27
2.3.1 Engineering methods 27
2.3.2 Model coupling strategies 28
2.3.3 Model improvement/enrichment 35
2.3.4 Conclusion 38

3 Multidimensional finite element coupling for large composite laminate structures **41**

3.1 Introduction 42
3.1.1 Reference multi-model problem 42
3.1.2 From continuous to discrete formulation 43
3.2 Multidimensional coupling 44
3.2.1 Bridge between 2D and 3D formulations - 3D stress recovery 44
3.2.2 Review of multidimensional coupling strategies 46
3.2.3 Conclusion 53
3.3 Discrete multi-model problem 54
3.3.1 Multidimensional coupling condition 54
3.3.2 "Smart" local remeshing strategy 56
3.3.3 Conclusion 59

3.4 Application cases . . . 60
3.4.1 Influence of the coupling on the buckling behaviour . . . 60
3.4.2 Influence of the coupling on the out-of-plane stress state . . . 64
3.4.3 Influence of the coupling in presence of an anelastic behaviour . . . 66
3.4.4 Conclusion . . . 69

4 Progressive model adaptation through remeshing 71
4.1 Progressive model adaptation strategy . . . 72
4.1.1 Brief overview of adaptive remeshing techniques . . . 72
4.1.2 Multi-model adaptation scheme . . . 74
4.2 Model adaptation indicator and criterion . . . 76
4.3 Smart remeshing strategy . . . 78
4.3.1 Identification of areas to be remeshed . . . 78
4.3.2 Remeshing steps . . . 79
4.3.3 Mesh refinement with quadrangular elements . . . 79
4.3.4 Preservation of mesh in degraded areas . . . 81
4.3.5 Conclusion . . . 82
4.4 State update . . . 83
4.4.1 Field transfer operators . . . 83
4.4.2 Field transfer strategy . . . 85
4.4.3 Equilibrium . . . 87
4.4.4 Conclusion . . . 88
4.5 Numerical application case . . . 89
4.5.1 Description of the academic test case . . . 89
4.5.2 Numerical results . . . 89
4.5.3 Sensitivity to user parameters . . . 90
4.5.4 Accuracy assessment . . . 93

5 Experimental and virtual testing of a large composite structure 95
5.1 Introduction . . . 96
5.2 Designing for failure of a complex structural test case . . . 97
5.2.1 A typical aeronautical component: the laminated stiffened panel . . . 97
5.2.2 Preliminary computations . . . 98
5.2.3 Conclusion: Design of the stiffened panels . . . 101
5.3 Initial damage introduced by low velocity/low energy impact . . . 102
5.3.1 Experiments . . . 102
5.3.2 Numerical comparisons . . . 111
5.3.3 Numerical results . . . 114
5.4 Residual strength of impacted stiffened panels using the adaptive meshing strategy 118
5.4.1 Experiments . . . 118
5.4.2 Numerical comparisons for the compression of an impacted stiffened panel 128
5.4.3 Conclusion . . . 136

6 Conclusion **139**

A Numerical implementation **143**

B Résumé de synthèse **145**

List of Figures

1.1 Full scale static bending test of the wings of an Aircraft Dewoitine 520 1
1.2 Full scale static bending test of the wings of an Aircraft A350 XWB 2
1.3 Virtual testing of a wing 2

2.1 Typical large problem in the aeronautical industry: Wing FEM 8
2.2 Non-overlapping and Overlapping Domain Decomposition methods 9
2.3 Illustration of the different shell theories 13
2.4 Composite mass proportion in the Airbus fleet 16
2.5 Illustration of a CFRP laminate 16
2.6 Main failure mechanisms in a composite laminate 18
2.7 Evolution of failure mechanisms in a composite laminate with the loading level . 19
2.8 Gaussian distribution of the viscous mechanisms 20
2.9 Principle of formation of permanent indentation 21
2.10 Examples of longitudinal behaviours of a ply after fibre failure 21
2.11 Strain-softening effects in compression observed at the British Columbia University 22
2.12 Different cohesive zone models 22
2.13 Finite element model of a stiffened panel 25
2.14 Coupling of Newmark numeric schemes with different time stepping 29
2.15 Flip-flop mechanism between two resolution schemes 29
2.16 Illustration of a global-local approach 32
2.17 Application case of the Arlequin method on a composite laminate plate 34
2.18 Incompatible geometrical decomposition of a domain 34
2.19 Example of patch insertion using mortar methods 34
2.20 Illustration of an adaptive mesh refinement approach 38

3.1 Multi-model mechanical problem with a decomposition of the domain Ω into two domains $\Omega^{(E)}$ and $\Omega^{(AE)}$ 42
3.2 Illustration of a transition solid-shell element 50
3.3 Illustration of a transition solid-multilayered shell element 51
3.4 Interface coupling G between the $T^{(E)}$ and the $T^{(AE)}$ domains 54
3.5 Remeshing strategy to create a 3D stacked volume mesh from a 2D initial geometry 57
3.6 Models for interface regularity assessment 58
3.7 σ_{11} stress fields of an anisotropic plate in tension 58
3.8 Remeshing strategy to create a 3D stacked volume mesh from a 2D initial geometry 59

3.9 Finite element model of a simply supported buckling composite plate subjected to an uni-axial loading . . . 61
3.10 First two buckling modes of a composite simply supported plate . . . 62
3.11 First buckling mode of a composite simply supported plate . . . 62
3.12 Free edge laminate problem . . . 64
3.13 Normal and shearing out-of-plane stress fields of a laminate in tension . . . 65
3.14 Experimental mounting and principle of the compressive-bending test . . . 67
3.15 Finite element model on a holed plate loaded in compressive-bending . . . 67
3.16 Load deflection curve of a compressive-bending holed plate . . . 68
3.17 Damage pattern of a compressive-bending holed plate . . . 69

4.1 Illustration of an adaptive remeshing procedure on a composite laminate bending holed plate . . . 72
4.2 Shape of failure envelopes, with $\alpha = 0.8$. . . . 76
4.3 Localisation criterion implementation . . . 77
4.4 Identification steps of the local area to be remeshed . . . 78
4.5 Remeshing strategy to create a 3D stacked volume mesh from a 2D initial geometry 79
4.6 Remeshing of a non-plane geometry . . . 80
4.7 Mesh refinement using quadrangles . . . 80
4.8 Remeshing strategy to create a 3D stacked volume mesh from a 2D initial geometry with quadrangles . . . 81
4.9 Underlying 2D mesh driving the remeshing process . . . 82
4.10 Field transfer principle . . . 83
4.11 Models involved in the field transfer. . . . 86
4.12 Local equilibrium step . . . 87
4.13 Local equilibrium step . . . 88
4.14 Initial and reference FE model of a bending holed plate made of 16-plies unidirectional laminate . . . 89
4.15 Failure indexes f_2 for the case of a bending holed plate laminate plot over the undeformed shape at the center of the probe. . . . 90
4.16 Computational time evaluation respective to the reference case for different sets of localisation criterion α and remeshing distance D. . . . 91
4.17 Relative error between the global displacement response between the adaptive result and its reference result for different meshes. . . . 93

5.1 Image of a compression test of a stiffened panel . . . 96
5.2 Stiffened panels geometry . . . 97
5.3 Finite element model of a stiffened panel . . . 98
5.4 Load vs Displacement for different panel stringer heights . . . 100
5.5 Strain vs Load results . . . 100
5.5 Strain vs Load results . . . 101
5.6 Final geometry of the designed panel . . . 101
5.7 Low velocity impact machine - C-scan pool . . . 102

5.8 Position and mounting of impact testings . . . 103
5.9 Experimental impact load vs time results . . . 104
5.10 Experimental energy vs time results . . . 105
5.11 C-scan images of the top stringer impacted area . . . 105
5.11 C-scan images of the top stringer impacted area . . . 106
5.12 C-scan images of the skin impacted area . . . 106
5.12 C-scan images of the skin impacted area . . . 107
5.13 Assembly of two half panel tomographies . . . 108
5.14 Tomography of Panel 1 . . . 108
5.15 Tomography of Panel 2 . . . 108
5.16 Thickness evolution measured by tomography of Panel 1 . . . 109
5.17 Thickness evolution measured by tomography of Panel 2 . . . 109
5.18 Tomography of the delaminated area of Panel 1 . . . 109
5.19 Finite element model of the impact on the top stringer of the Panel 1 . . . 111
5.20 Finite element model of the impact on the skin of the Panel 2 . . . 111
5.21 Finite element mesh of the different entities for the simulation of impacts on stiffened panels . . . 112
5.22 Boundary conditions for the impact simulation . . . 113
5.23 Impact load of the impact I_1 on Panel 1 . . . 114
5.24 Impact load of the impact I_2 on Panel 2 . . . 115
5.25 Damage fields for impact on Panel 1 . . . 116
5.26 Damage fields for impact on Panel 2 . . . 117
5.27 Stiffened panel mounting on a compression machine . . . 119
5.28 First loading phase of the compression of Panel 2 . . . 120
5.29 Digital image correlation of the Panel 2 at the maximal load of the first loading phase . . . 121
5.30 Second loading phase of the compression of Panel 2 . . . 121
5.31 Digital image correlation of the Panel 2 at the acoustic threshold load during the second loading phase . . . 122
5.32 Digital image correlation of the Panel 2 at the buckling threshold load during the second loading phase . . . 123
5.33 Digital image correlation of the Panel 2 at the maximal load of the second loading phase . . . 124
5.34 Third and ultimate loading phase of the compression of Panel 2 . . . 124
5.35 Digital image correlation of the Panel 2 just before the failure load during the third loading phase . . . 125
5.36 Infrared images of the failure scenario of the Panel 2 in compression . . . 126
5.37 DIC of the Panel 2 after the global failure in compression . . . 126
5.38 Initial finite element model for the compression of the Panel 2 . . . 129
5.39 Initial mesh of for the compression of the Panel 2 . . . 129
5.40 Load vs time numerical result of Panel 2 with two remeshing steps . . . 130
5.41 U_z displacement for three different meshes . . . 131

5.42 U_z displacement during the first loading phase 132
5.43 U_z displacement during the second loading phase 132
5.43 U_z displacement during the second loading phase 133
5.44 U_z displacement during the third and ultimate loading phase 133
5.45 Failure indicator f_2 during the third and ultimate loading phase 134

A.1 Numerical implementation 144

List of Tables

2.1 Computational time of a stiffened panel in compression for an elastic model and a damage model 25

3.1 Material and geometrical data of a composite laminated plate. 61
3.2 Critical loads results 63
3.3 Material T7006C/M21 and geometrical data of the studied composite plate . . . 66

4.1 Field transfer methods available in Z-set 85
4.2 Sets of parameters of the adaptive multi-model approach for the compressive-bending holed plate 91

5.1 Impact results on stiffened panels 110
5.2 Computational time for three meshes during the progressive adaptive simulation 135

List of Abbreviations

2D	two **D**imensional
3D	three **D**imensional
BVID	**B**arely **V**isible **I**mpact **D**amage
CFRP	**C**arbon **F**iber **R**einforced **P**olymer
CLT	**C**lassical **L**amination **T**heory
CWB	**C**enter **W**ing **B**ox
DDM	**D**omain **D**ecomposition **M**ethod
DIC	**D**igital **I**mage **C**orrelation
ESL	**E**quivalent **S**ingle **L**ayer
FE	**F**inite **E**lement
FEM	**F**inite **E**lement **M**ethod
FSDT	**F**irst **S**hear **D**eformation **T**heory
GP	**G**auss **P**oint
HOT	**H**igher **O**rder **T**heories
NDT	**N**on **D**estructive **T**esting
OPFM	**O**nera **P**rogressive **F**ailure **M**odel
PGD	**P**roper **G**eneralized **D**ecomposition
TOF	**T**ime **O**f **F**light
ZZ	**Z**ig- **Z**ag

Ho any bebe Ra-Madeleine,

1 Introduction

Context

For several decades, the aircraft materials and structures have progressively increased in complexity in order to achieve a better ratio between performances and weight. Jointly to this evolution, the experimental facilities for aircraft structural testing have significantly been developed over time.

As an illustration, Figures 1.1 and 1.2 show two configurations, at different periods of time, of full scale structures subjected to a static bending test dedicated to estimate the robustness of an aircraft wing. Figure 1.1 is a photography of the wing of an Airbus aircraft Dewoitine 520. At that time, a large amount of sandbags with a predefined mass were progressively stacked over the wing to estimate its bending strength. Such a test is complex with a long duration and the boundary conditions are not mastered.

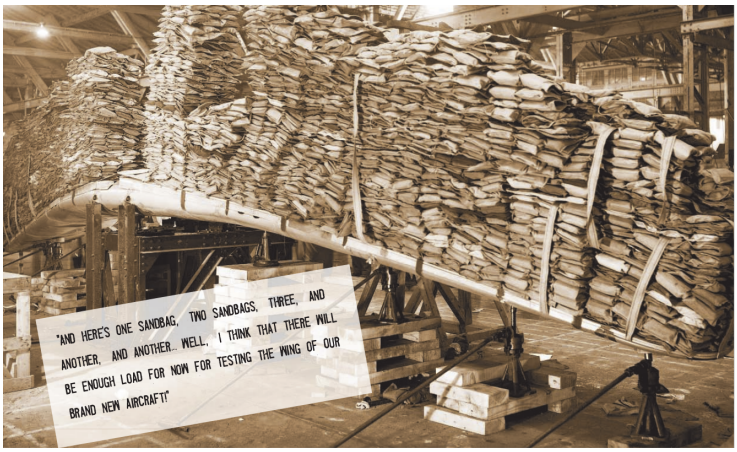

FIGURE 1.1: Full scale static bending test of the wings of an Aircraft Dewoitine 520 [Blumenfeld and Piquet, 2011] in 1939.

Several decades after, the experimental testing facilities have substantially been improved. The final tests are performed on the whole aircraft structures. In particular the Figure 1.2 is a photography of the full scale wing bending static test of the Airbus aircraft A350 XWB led in 2013. The A350 XWB wings, tested at ultimate load, showed a five-metre deflection at the wing tips. This achievement depicts the amount of progress made in terms of material, structures and testing capabilities through the aircraft production history.

Generally, the amount and complexity of experimental campaigns led for the development of a new aircraft remain quite costly and imposes a long duration for the development of innovative



FIGURE 1.2: Full scale static bending test of the wings of an Aircraft A350 XWB [https://www.airbus.com/,].

structures. This reason motivates developments in the virtual testing domain especially targeting the early development phases of an aircraft. Being able to simulate, with a detailed stress analysis, some experimental tests would enable firstly to reduce the volume of experimental test campaigns and secondly to optimize the experimental configurations. While the virtual simulation, especially using finite element methods, of elementary structures is now well understood, leading detailed stress analysis on large components is still an on-going research topic, as reported in Figure 1.3.

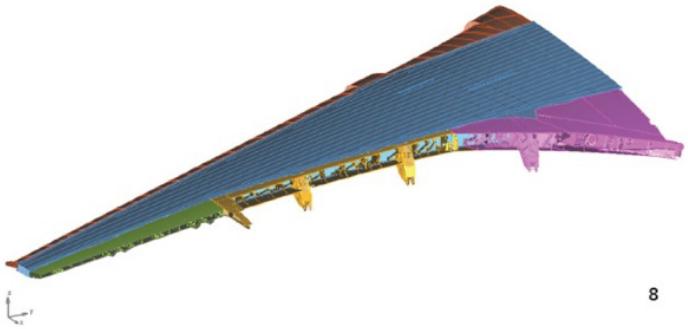

FIGURE 1.3: Virtual testing of a wing [https://www.digitalengineering247.com/, 2016].

In this manuscript, we focus on slender structures made of composite laminate materials constituted with unidirectional plies. Composite laminate materials have undergone a raise in popularity through the past twenty years in the aeronautical industry due to their flexible material properties and lightness compared to other metallic structures.

Nevertheless, due to their structural complexity composite laminates present a particular behaviour which differs from the usual behaviour of metallic materials. As an example, composite laminates may contain internal damages that are not visible externally. The visibility threshold is by convention designated as the 'Barely Visible Impact Damage" (BVID) in the aeronautical

industry. The structures must withstand the different on-service loadings even in presence of such an internal damage.

Consequently, industrials are interested in the development of numerical methods to be able to model the evolution of damage in composite laminates and its effects on the global strength of a structure which has been previously impacted. It is referred as residual strength estimation in the aeronautical jargon. The primary objective of this doctoral PhD is to focus on the residual strength problematic for composite laminate including an initial damage.

The scope of the PhD is extended to the investigation of numerical methods allowing to monitor damage propagation requiring a detailed stress level analysis for large composite laminate structures.

Objective

As introduced beforehand, the objective of this doctoral study is to provide a numerical strategy efficient to monitor damage propagation, notably requiring a detailed stress level analysis, even for large composite laminated structures. This doctoral study is funded under the CIFRE convention with the Airbus company. Consequently, one of the main goals is to provide a numerical method usable within the Airbus company, and in particular with the commercial Finite Element code Abaqus.

Positioning of the numerical strategy

The underlying problematic of the numerical strategy developed in this manuscript is the resolution of problems involving two levels of modelling. Some classical engineering methods such as submodelling and local refinement can be considered. The engineering methods are simple to implement but lack of accuracy and flexibility. More elaborate numerical methods will be presented and differentiated in two parts, the model coupling and the enrichment methods.

Model coupling methods are based on the consideration that two different types of models are involved in the system, a coarser one and a refined one. Numerous numerical techniques have been developed to solve such a system such as exact zooming, iterative global-local and superposition techniques. The implementation of those methods is generally delicate due to the limited flexibility of commercial solvers used in the industrial context.

Alternatively to model coupling methods, enrichment strategies will be described. The possible extension of the non-linear phenomena localisation during the simulation backs the use of such adaptive techniques that may be more efficient. For instance, methods based on the partition of unity such as X-FEM, the floating node method, and the phantom node method will be presented. They are mostly relevant for modelling strong discontinuities. However, the intended application scope is the continuum damage mechanics. Consequently, the methods based on the partition of unity are not retained. Another possibility for enrichment strategies, is the adaptive remeshing methods. The adaptive remeshing methods allow to maintain a monolithic resolution

of the Finite Element problem by a commercial Finite Element solver reducing the intrusiveness of the numerical strategy.

The choice for the developed method is to perform an adaptive multi-model strategy based on adaptive remeshing depending on the damage propagation occuring in the composite laminated structure. The principle is to adapt the Finite Element and the material modelling to the need through the structure and the simulation time. This choice results from a compromise between among others intrusiveness, robustness, flexibility, and user-friendliness.

Approach of the doctoral thesis

The present manuscript is decomposed into five chapters including the introduction being the first chapter.

In the second chapter, the general problematic of computing, with a fine level of details, a large composite structure is discussed. The relevant hypotheses and models for computing large slender multilayered structures are presented. Then, the specific material constitutive equations to predict damage and failure of composite laminates which describe complex phenomena, such as transverse cracking, fibre failure, or delamination, are presented. Such complex material behaviour requires a fine level of Finite Element model. It highlights the need of using a numerical strategy to address such problems involving two levels of modelling. Several numerical strategies in that aim are described. This chapter ends by introducing a new numerical approach for the simulation of local complex phenomena on large composite structures based on a multi-model adaptation approach.

The third chapter presents the setting-up of the studied multi-model reference problem at a fixed decomposition (i.e. the solid and shell parts are fixed before the simulation). It consists of an elastic domain with some anelastic inclusions where the model is more refined to capture complex phenomena occurring in composite laminates. The elastic domain is modelled with multilayered shell elements while the anelastic domain is modelled with solid elements with, at least, one element per ply through the thickness. This technique requires to couple two mesh domains with different kinematics. After the introduction of the reference multi-model, a brief overview of multidimensional coupling conditions is presented. The choice of the selected coupling, the "shell-to-solid" coupling from Abaqus, is documented.

The fourth chapter tackles the progressive adaptation of the multi-model problem through remeshing. After an introduction on the general adaptive strategy, the specificities of the strategy are detailed. In particular, the model adaptation triggering strategy, the remeshing strategy, and the state update problematic is detailed. The remeshing strategy is one of the main contributions of this work as it allows simplifying the other operations such as the state update. The fourth chapter ends with an application of our method to an academic test case of a compressive-bending holed plate showing the flexibility provided by our method.

The fifth chapter aims at applying the developed numerical strategy to a complex industrial test case, the estimation of the residual strength of an impacted stiffened panel. First, the design of

the selected test case is presented. Then, the damage introduced by impact is addressed with an experimental and numerical comparison. Finally, the residual strength in compression of the impacted stiffened panel is detailed.

Numerical tools

Several numerical tools were used in the development of the numerical adaptive multi-model strategy. Appendix A presents a detailed schematic diagram of the numerical implementation of the numerical adaptive multi-model strategy.

The numerical adaptive multi-model strategy is piloted by the Z-set software, a Finite Element software co-developed by Onera and Ecole des Mines. Z-set includes several modules, among others, Zebulon, a Finite Element solver, Zmat, a material library, and Zcracks, a tool for advanced remeshing. In particular, Zcracks includes advanced meshing capabilities and advanced field transfer strategies. Zcracks was mostly developed for adaptive meshing applied to metallic structures. The adaptation of Zcracks to composite laminate problematic, was another one of the main contributions of this doctoral study.

One of the objective of this work is to provide a method compatible with a commercial FE software. Hence, Airbus Operations' teams should be able to use the method with the Finite Element solver included in their calculation processes. Here, the used Finite Element solver is Abaqus standard with an implicit solver. The material damage law, called Onera Progressive Failure Model (OPFM), developed at Onera and used in this PhD, is integrated in the UMAT form.

2 Numerical strategies for the simulation of local complex behaviour for large composite structure applications

This chapter presents the problematic of computing, with a fine level of details, a large composite structure. First, the computation of the behaviour of large structures is detailed. Then, the specific material constitutive equations used for composite laminates which describe complex phenomena such as damage are presented. At last, several numerical strategies to address the problems involving two levels of modelling are examined. This chapter ends by introducing a new numerical approach for simulations of local complex phenomena on large composite structures.

2.1 Computation of large slender multilayered structures

The current constraints of lightness, resistance and aerodynamic performances in the design process of structures affect their complexity. The materials and topologies are increasingly intricate. Moreover, the escalation of the size of the considered problems makes their simulation unaffordable if no numerical strategy or simplification hypotheses are implemented. For instance, a classic order of magnitude for the size of an aeronautical system of equations is about one to ten million degrees of freedom in a finite element model. This is typically the case of a full model of wing as presented in Figure 2.1. The treatment of such a problem requires so much memory and such a large number of linear system resolutions that they are currently unaffordable even on a high end super-computer. The computational requirements are even higher when considering non-linear problems which requires an incremental resolution.

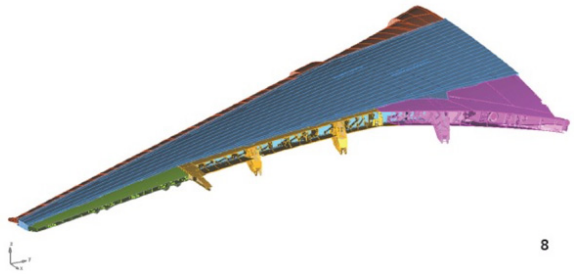

FIGURE 2.1: Typical large problem in the aeronautical industry: Wing FEM [*https://www.digitalengineering247.com/*]

When solving such large problems, several numerical strategies, that can be jointly used, can be explored. A first family of strategy consists in computing the full order model while using numerical strategies for large problem resolutions. Such approaches are detailed in section 2.1.1.

Another way to deal with large problems consists in making the relevant hypotheses to set-up a simplified model. This requires to acknowledge the representativeness and the limitations of the simple model. This is detailed in section 2.1.2 with a focus on the case of slender multilayered structures made of composite materials.

2.1.1 Numerical strategies for large problem resolution

To address large structural problems, increasingly effective parallelisation strategies are developed. Those methods allow treating both large problems such as those involving more complex physical phenomena, and numerous small problems such as for optimization. They present the advantage of being well suited to the architecture of current scientific computers. Most parallel resolutions rely on the Domain Decomposition Methods (DDMs) initially introduced by Schwarz in [Schwarz, 1870]. Even long before the very first numerical method, Schwarz originally proposed a resolution strategy of a partial differential equation (PDE) over a domain composed of an overlapping square and circle. Based on his idea, a large amount of methods have been developed by the scientific community.

The basic principle of DDMs is to divide the domain into several sub-domains and to solve the problem in each sub-domain independently with a regular synchronization of the data between the sub-domains. The spatial decomposition should be performed such that there is none or small overlap of the domains with respect to its size. This allows to limit the size of the data exchange operations at the interfaces.

DDMs can first be divided in two categories, the non-overlapping and the overlapping techniques as presented in Figure 2.2.



FIGURE 2.2: Non-overlapping (A) and Overlapping (B) Domain Decomposition methods

The principle of the non-overlapping strategies is to divide the whole domain into several sub-domains, bounded by faces and edges so that no sub-domain overlaps on one another and solve the problem in each domain separately with iterative information exchange at interface. Reflections where led on the interface problem which should enforce conservation principles arising the following questions.

- what data to exchange and over what domain ?
- what frequency to use for the synchronization ?

A state-of-the-art of those methods is available in [Gosselet and Rey, 2006]. The main trends are the Balanced Domain Decomposition (BDD) approaches also called primal approaches based on displacement conditions and the Finite Element Tearing and Interconnecting (FETI) approaches also called dual approaches based on effort conditions. Those methods are developed in this section with first the presentation of the mechanical problem and then its resolution by DDMs.

Reference problem Let's consider a static mechanical problem over a domain Ω. This domain is subjected to a volumetric effort density $\boldsymbol{f}_d$. External forces are applied at the boundary $\partial\Omega$ of Ω by the mean of imposed displacements $\boldsymbol{u}_d$ on $\partial_u\Omega$ and imposed loads such that $\boldsymbol{\sigma}\cdot\boldsymbol{n} = \boldsymbol{F}_d$ on the complementary boundary $\partial_F\Omega = \partial\Omega \setminus \partial_u\Omega$. Ω is divided into two non-overlapped sub-domains $\Omega^{(1)}$ and $\Omega^{(2)}$ sharing a common interface $\Gamma = \partial\Omega^{(1)} \cap \partial\Omega^{(2)}$. The reference problem over each sub-domain (s) can hence be written as:

$$\begin{cases} \boldsymbol{\nabla}\cdot\boldsymbol{\sigma}^{(s)} + \boldsymbol{f}_d^{(s)} = 0 & \text{in } \Omega^{(s)} \\ \boldsymbol{\varepsilon}^{(s)} = \frac{1}{2}\left(\boldsymbol{\nabla}\boldsymbol{u}^{(s)} + \boldsymbol{\nabla}^T\boldsymbol{u}^{(s)}\right) & \text{in } \Omega^{(s)} \\ \boldsymbol{\sigma}^{(s)} = \Lambda^{(s)} : \boldsymbol{\varepsilon}^{(s)} & \text{in } \Omega^{(s)} \\ \boldsymbol{\sigma}^{(s)}\cdot\boldsymbol{n}^{(s)} = \boldsymbol{F}_d^{(s)} & \text{on } \partial_F\Omega \cap \partial\Omega^{(s)} \\ \boldsymbol{u}^{(s)} = \boldsymbol{u}_d^{(s)} & \text{on } \partial_u\Omega \cap \partial\Omega^{(s)} \end{cases} \quad \vee\, s \in \{1,2\} \tag{2.1}$$

with additional constraints at the interface:

- displacement continuity: $\boldsymbol{u}^{(1)} = \boldsymbol{u}^{(2)}$ on Γ,
- equilibrium: $\boldsymbol{\sigma}^{(1)} \cdot \boldsymbol{n}^{(1)} + \boldsymbol{\sigma}^{(2)} \cdot \boldsymbol{n}^{(2)} = \boldsymbol{0}$ on Γ.

In the case of small strain linear elasticity, the resulting global finite element discrete problem, consisting of a linear system of equations, can be formulated as such:

$$\boldsymbol{K}\boldsymbol{u} = \boldsymbol{f} \tag{2.2}$$

where $\boldsymbol{K}$ is the stiffness matrix, $\boldsymbol{u}$ is the displacement vector and $\boldsymbol{f}$ is the vector of generalized force.

The problem solved on each sub-domain $\Omega^{(s)}$ is thus:

$$\boldsymbol{K}^{(s)}\boldsymbol{u}^{(s)} = \boldsymbol{f}^{(s)} + \boldsymbol{\lambda}^{(s)} \tag{2.3}$$

where $\boldsymbol{\lambda}^{(s)}$ is the reaction that the other sub-domains apply on the domain $\Omega^{(s)}$ and is non-zero only at interface. When considering only the effect of neighbors, the previous linear system can be re-arranged as follow:

$$\begin{bmatrix} \boldsymbol{K}_{ii}^{(s)} & \boldsymbol{K}_{ib}^{(s)} \\ \boldsymbol{K}_{bi}^{(s)} & \boldsymbol{K}_{bb}^{(s)} \end{bmatrix} \begin{bmatrix} \boldsymbol{u}_i^{(s)} \\ \boldsymbol{u}_b^{(s)} \end{bmatrix} = \begin{bmatrix} \boldsymbol{0} \\ \boldsymbol{\lambda}_b^{(s)} \end{bmatrix} \tag{2.4}$$

where b refers to interface data and $\boldsymbol{\lambda}_b^{(s)}$ is defined such that $\boldsymbol{\lambda}^{(s)} = \boldsymbol{t}^{(s)^T}\boldsymbol{\lambda}_b^{(s)}$, $\boldsymbol{t}^{(s)}$ being the operator of projection of $\Omega^{(s)}$ over Γ. This allows to retrieve the following relation:

$$\left(\boldsymbol{K}_{bb}^{(s)} - \boldsymbol{K}_{bi}^{(s)}\boldsymbol{K}_{ii}^{(s)^{-1}}\boldsymbol{K}_{ib}^{(s)}\right)\boldsymbol{u}_b^{(s)} = \boldsymbol{S}_p^{(s)}u_b^{(s)} = \boldsymbol{\lambda}_b^{(s)} \tag{2.5}$$

where $\boldsymbol{S}_p^{(s)}$ is called the Schur primal complement. Based on the previous formulations, several approaches of resolutions are available in the literature. The main families of approaches are detailed below.

Primal approaches [Tallec et al., 1991], [Mandel, 1993] The primal approaches consist in an iterative resolution of Equation 2.5 where the displacement $\boldsymbol{u}_b^{(s)}$ is the unknown.

Dual approaches [Farhat and Roux, 1994] In the dual approaches, the Equation 2.3 is written as:

$$\boldsymbol{S}_p^{(s)^+}\boldsymbol{\lambda}_b^{(s)} = \boldsymbol{S}_d^{(s)}\boldsymbol{\lambda}_b^{(s)} = \boldsymbol{u}_b^{(s)} \tag{2.6}$$

where $\boldsymbol{S}_d^{(s)}$ is the Schur dual complement. The problem is solved iteratively with the efforts at the interface $\boldsymbol{\lambda}_b^{(s)}$ as unknown whilst satisfying the continuity of displacements.

Mixt approaches [Ladevèze, 2012], [Series et al., 2003] The mixt approaches consist in solving iteratively an unknown which is a linear combination of the displacements, $\boldsymbol{u}_b^{(s)}$, and efforts, $\boldsymbol{\lambda}_b^{(s)}$, at the interface.

Conclusion A strong advantage of DDMs methods in addition to their parallelisation capabilities is allowing the implementation of different models through the structure. Different levels of modeling details can be added. For instance, structural details such as holes, micro-structural patterns or a complex material law can be added in the critical parts of the structure. This capability is of particular interest for industrials which want to minimize the computational resources and is emphasized in several research works.

Nevertheless, due to the use of iterative solvers, the efficient implementation of DDMs highly depends on the number of generated system of equations and the ability to build robust preconditionners. It is complex to implement them in a robust and non-intrusive manner compatible with a commercial finite element software. Moreover, their sole use can be insufficient when treating very large problems.

For those reasons, those strategies are not retained for the developed method in this manuscript. But the principle of using several models through the structure is kept.

2.1.2 Simplified modeling of slender multilayered structures

For problems with a small dimension in one direction compared to the two others, which is often the case for aeronautical structures, plate and shell theories are relevant. Those theories have been largely studied in the literature. The use of such structural models allows a gain in computational cost compared to full 3D formulations. For this reason, they are still used in industry and more particularly for aeronautical structures.

The objective of this section is to present the relevant theories for composite laminates structures which are an important input for our further developments. Composite laminates are multilayered structures. The following section presents some basics on the problematic of such structures. Then multilayered shell theories are developed. Finally, their FE implementation is presented.

2.1.2.1 Principal issues

When dealing with multilayered slender structures, several physical phenomena arise such as the effects of anisotropy on the stress distribution, structural instabilities and edge effects. These are important to be accounted in the development of structural models to reduce potential errors. They are presented hereunder.

In-plane anisotropy The composite laminate structures are made of unidirectional layers stacked together. In the case of Carbon Fibers Reinforced Polymer (CFRP), each layer is highly anisotropic ($E_L/E_T = 10 - 20$ where E_L is the longitudinal stiffness modulus and E_T is the transverse stiffness modulus). This anisotropy induces shear transverse and normal effects that impacts the global behavior of a structure [Reddy, 1997].

Heterogeneity through thickness The multilayered anisotropic structures generally presents a Zig-Zag (ZZ) pattern of the displacement field through thickness. At layer interfaces, there can be a discontinuity of in-plane stresses but the out-of-plane stresses are continuous. This

level of details in the stress distribution is required when local complex phenomena are studied. Moreover, there might be a coupling between in-plane and out-of-plane strain for the cases of asymmetrical laminates. Using non-linear geometrical analysis is required in such cases.

Structural instability (buckling) Slender structures are known to be subjected to buckling, a structural instability. The buckling corresponds to the loss of solution uniqueness in the equilibrium problem. It is very important to model precisely this effect as it may be at origin of the failure of the structure, especially for thin components. An important aspect when studying such structures is taking into account geometrical non-linearity. Another important aspect of buckling is its sensitivity to imperfections (geometry, material,...).

Edge effect The edge effects are important in the case of composite laminated structures as it may induce a three dimensional stress state at the edges that can initiate damage, such as for instance, delamination. It is thus important to be able to render this effect.

Those four points are basic issues encountered when modeling slender multilayered structures. The following section addresses the available theories and their ability to reproduce those physical phenomena.

2.1.2.2 Multilayered plate and shell theories

The previous section treated the main behavioural phenomena observed in multilayered structures. The objective of this section consists in informing on the modelling of those behaviours and the validity domain of the models. When modelling slender structures that may undergo a bending behaviour, the use of shell types of theories are interesting. Those are explored in this section which addresses in particular the case of multilayered types of structures such as composite laminates.

Considering the amount of proposed advanced theories for multilayered, anisotropic plates and shells, several authors published reviews such as [Reddy and D. H. Robbins, 1994] [Carrera, 2002] [Zhang and Yang, 2009]. The multilayered theories can be divided in three main categories as follow:

- Equivalent Single Layer (ESL): The variables are at the laminate scale.
  - Classical Lamination Theory (CLT)
  - First-order Shear Deformation Theory (FSDT)
  - Higher-order Shear Deformation Theories (HSDT)
- Layer Wise (LW): Each layer is stated as an independent plate or shell.
- 3D.

Those categories are illustrated in Figure 2.3. The ESL theories are relevant to study the macroscopic behavior of a structure and are the most common theories used for industrial problems. The LW and 3D theories allow a finer description of the stress state.

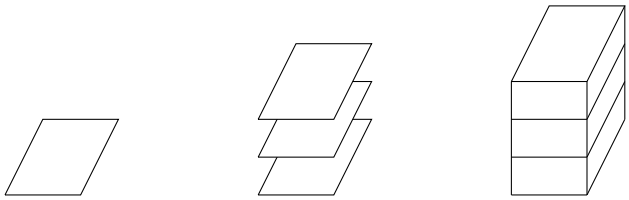

FIGURE 2.3: Illustration of the different shell theories: (A) ESL; (B) LW; (C) 3D.

CLT The most common theory for multilayered structures is the CLT [Reddy, 1997]. It relies on the Kirchhoff-Love kinematic hypotheses which state that the normals to the mid-plane in the undeformed configuration remain normal to the mid-plane through deformation. The displacement field is described as follow for the plate case.

$$\begin{cases} u_x(x,y,z) = u_x^0(x,y) - z u_{z,z}^0(x,y) \\ u_y(x,y,z) = u_y^0(x,y) - z u_{z,z}^0(x,y) \\ u_z(x,y,z) = u_z^0(x,y) \end{cases} \tag{2.7}$$

where u is the displacement field, x and y are the in-plane directions, z is the normal direction, the superscript ^{0} refers to the mid-plane and the lower-script $_{,z}$ is the partial derivative with respect to z.

Additional curvature parameters are required for the curved shell case but the equations will not be detailed here. The basic principle of the curved shell is to define a curved referential with curvature parameters and to apply the kinematic equations in the defined curved referential. The CLT is effective for thin plates in general. Nevertheless, when dealing with composite laminates, even if they are thin, their in-plane anisotropy can be at the origin of transverse shear effects and normal deformation that are not represented by the CLT. Those effects are detailed in [Reddy and D. H. Robbins, 1994] and [Pagano, 1970]. Moreover, when treating large deflections, this theory may no longer be accurate enough. For those reasons, finer models have been developed.

FSDT To overcome the non-representation of transverse shear strain in the CLT, the FSDT has been developed. It reproduces the Reissner-Mindlin [Reissner, 1945] [Mindlin, 1951] [Whitney and Pagano, 1970] kinematics with a uniform transverse shear strain distribution through thickness. This theory is generally available in commercial FE softwares. The displacement field is described as follow for the plate case.

$$\begin{cases} u_x(x,y,z) = u_x^0(x,y) + z\theta_y(x,y) \\ u_y(x,y,z) = u_y^0(x,y) - z\theta_x(x,y) \\ u_z(x,y,z) = u_z^0(x,y) \end{cases} \tag{2.8}$$

where θ_x and θ_y are the rotations which the normal to the mid-surface makes with the z direction in respectively the plane normal to the y direction and the plane normal to the x direction.

The FSDT is a good trade-off in terms of computational efficiency and representation of transverse shear effects at the global scale of the structure. Nevertheless, when looking at local effects, such a kinematic is not able to capture accurately the description of the out-of-plane stresses and thus to describe interlaminar phenomena such as delamination.

HSDT HSDT have been developed to provide an even more accurate transverse shear state description through thickness. The principle is to increase the polynomial order in the through thickness description of the displacement field. Higher-order theories are nevertheless costly and are not available in commercial FE softwares.

LW When a more detailed interlaminar stress state is needed and the ESL theories achieve their limitations, LW theories can be used. The principle is to solve the governing equations for each layer independently with interface conditions. The ESL theories (CLT, FSDT, HSDT), described previously can be implemented for each layer. Then an interface condition is enforced to ensure the interlaminar continuity at interface. LW theories are not practical yet for large structure applications or structures with a great number of layers as the number of unknowns is directly related to the number of layers.

3D The 3D continuum-based theory is yet the one that gives the best interlaminar stress state representation [Pagano, 1978] when implemented LW. The computational cost of its FE implementation is prohibitive on a large structural case. In fact, to avoid numerical locking of solid elements, a fair aspect ratio of the elements is required to avoid distorted elements. The thickness of the composite laminate layers limits thus the other dimensions of the elements. Consequently, a large amount of solid elements are required for the FE analysis compared to the use of shell elements. For those reasons, the use of LW theories is still limited to elementary structures or a confined local area.

2.1.2.3 Finite Elements for multilayered structures

The theories developed in the previous section allow to solve analytically simple problems. When moving to more complex engineering problems, the analytic resolution is no longer possible and the FE method is still the preferred resolution method. A survey of problematic regarding the finite element implementation of the different shell theories is available in [Yang et al., 2000]. In the continuity of the theories developed in section 2.1.2.2, the development of the corresponding structural elements allowed treating bigger problems.

FEs based on shell theories Elements have been developed based on CLT and are still used for thin structures when transverse effects are negligible. The first developed elements based on FSDT presented numerical shear locking mechanisms. This phenomenon appears when using linear elements in bending solicitations. An additional shear stress appears in the elements which decreases the obtained displacement at equilibrium. The elements are stiffer in bending. The use of selected/reduced integration schemes allowed limiting that effect but induced at the same occasion the apparition of zero energy modes, also called hourglass effects. Consequently,

numerical techniques have been developed to prevent elements from hourglassing. Those types of plate/shell elements have now reached a high level of maturity. They are widely used for large structural FE resolutions when local stress details are not necessary.

FEs based on 3D formulation The 3D elements are still the most precise in describing the full 3D stress state. For multilayered shell, it is important to have at least one element through each layer thickness to be able to capture the ZZ effect. Moreover, the use of 3D solid elements requires more elements compared to shell elements to have elements with a fair aspect ratio. This is not ideal as it substantially increases the size of the FE problem to be solved.

2.1.3 Conclusion

To address large size problems, parallel strategies are a powerful tool. Nevertheless, their efficient implementation within a commercial framework is limited yet and not sufficient to deal with all kind of problems.

For those reasons, industrials still widely use simplified structural models such as plates and shells for slender structures. For large problems, those are still the preferred solution given that the studied influential physical phenomena can be represented. For instance, in presence of geometrical singularities such as holes and bolted joints the use of shell elements does not allow describing accurately the local 3D stress state which is essential to predict possible damage initiation. In a more general manner, simple plate and shell models are usually insufficient to model transient local phenomena such as damage initiation and propagation.

2.2 Predictive material models for composite laminates

Currently, there is a tendency of using composite laminated materials in modern aircraft fuselages or wings. They represent more than 50% of the structural mass of the Airbus A350 for instance as illustrated in Figure 2.4.

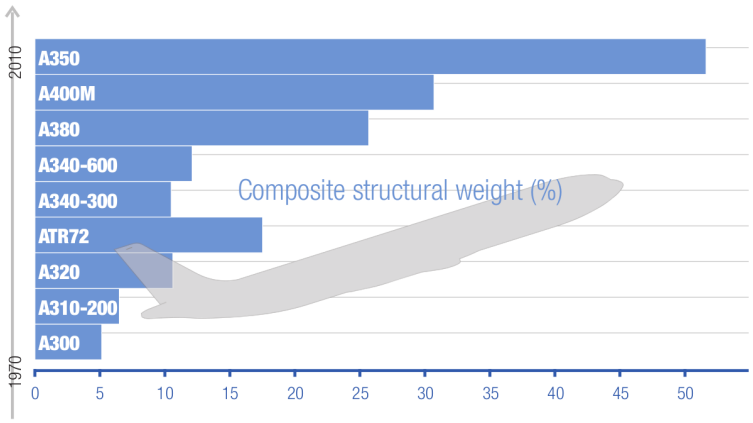

FIGURE 2.4: Composite mass proportion in the Airbus fleet [Blumenfeld and Piquet, 2011]

Composite materials are chosen for their material properties' flexibility and lightness. Their flexibility originates from the multilayered configuration of a composite laminate. A laminate is constituted of stacked layers with different orientations. For the case of CFRP (Carbon Fibres Reinforced Polymer) laminates with unidirectional layers, each layer, also called ply or laminae, is composed of continuous carbon fibres embedded in a polymer matrix as described in the Figure 2.5.

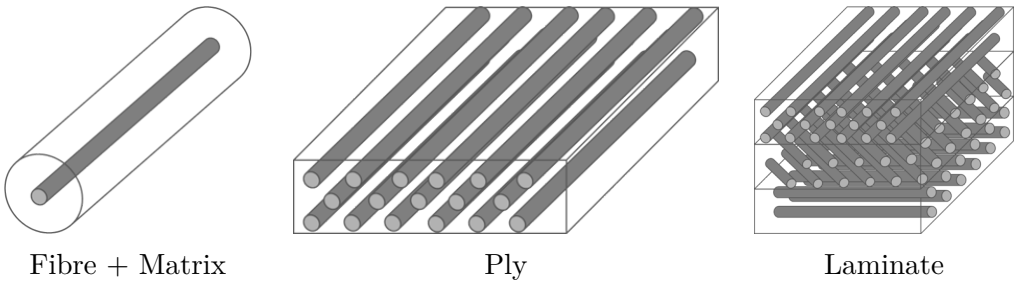

FIGURE 2.5: Illustration of a CFRP laminate

For the last decades, a huge effort has been made in the material modeling community to build efficient and predictive mechanical models of laminates. Most of those are formulated at the ply scale, so-called mesoscale to qualify structural integrity. The laws essentially present a quasi-linear elastic behaviour at low levels of deformation and then a non-linear behaviour due to complex damage mechanisms. Due to the highly non-linear equations, those models are usually implemented within explicit finite element solvers because of possible convergence issues when using an implicit finite element solver. However, some research groups develop laws than can be used with both implicit and explicit resolution schemes.

In the first section, the elastic behaviour of such a material is presented. Then, the following section aims at describing more complex anelastic phenomena occurring in composite laminates that are not represented in the frame of elasticity. Finally, an example of a medium size structural case is presented to highlight the difficulties of using more complex constitutive equations on a large structure.

2.2.1 Introduction on unidirectional composite laminates

This sections aims at providing a brief overview of the non-linear behaviour of a unidirectional composite laminate. The behaviour of any composite laminate can be studied at three different scales as represented in Figure 2.5. The most refined scale is the fibre-matrix scale, so-called "microscale", where the fibres and the matrix are modelled separately and usually linked by an interface condition. The intermediary scale is the ply scale, so-called "mesoscale". And finally, the largest scale is the laminate scale, so called "macroscale" and which is usually used when treating large structures. Nevertheless, the macroscale model is too coarse to represent the more complex physical phenomena occurring in a composite laminate. Moreover, the microscale model would require too much modelling effort for large structure applications. For those reasons, most of the material models are formulated at the mesoscale which presents a fair trade-off between the accuracy of the prediction and the computational time.

In the following sections, the ply transverse isotropic elastic first behaviour is first developed. Then, the anelastic mechanisms occurring in the plies under intense loading are briefly explained.

2.2.1.1 Elastic behaviour of a laminae

When addressing large problems, the constitutive equations are often chosen as quasi-linear elastic. However, such simple linear properties cannot account for the numerous nonlinear phenomena that a laminae can exhibit such as for instance hardening in traction and softening in compression [Hahn and Tsai, 1973]. Due to the polymer matrix, a viscoelastic behaviour [B.F.Oliveira and G.J.Creus, 2000] [Maire, 1992] [Remy-Petipas, 2000] is also observed, especially for shear loadings. This shows that even the quasi-linear part of a laminae behaviour is already complex. When leading more refined analyses, ie to study structural instabilities like buckling, those aspects can be significant and must be modelled.

2.2.1.2 Degradation mechanisms in a laminate

The complexity of the material architecture of a laminate induces specific anelastic degradation mechanisms. Some major mechanisms occurring in CFRP composites, under severe loading, are listed in [Allix, 2001] and hereunder:

- Plasticity of the matrix,
- Transverse matrix cracking,
- Brittle failure of the fibres followed by fibre bridging,
- Debonding between the layers which is also called delamination.

Some of them are represented in Figure 2.6 as follow.

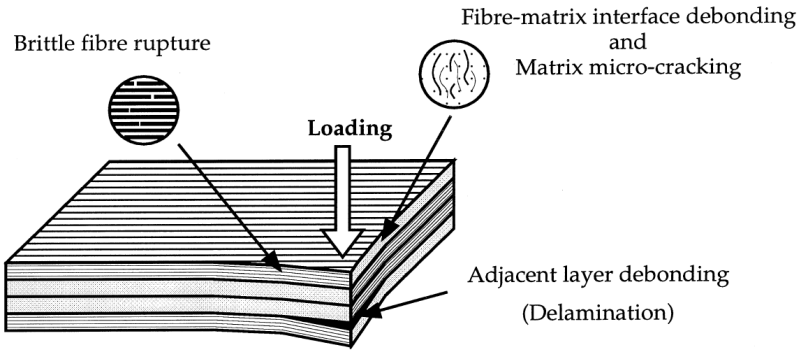

FIGURE 2.6: Main failure mechanisms in a composite laminate [Ladevèze et al., 2000].

Such complex anelastic behaviour, involving different physical phenomena that interact with one another, is tricky to introduce in a material model. As an example, an impact over a composite laminate structure may induce a substantial delamination damage which is mostly an internal damage. It is thus important to model accurately the effect of delamination for the impact loadings. A consequent amount of research and efforts have been done in the modelling of composite laminate's behaviour and will be further detailed in the following section.

2.2.2 Modelling of composite laminate's behaviour

The elastic behaviour of a unidirectional ply is transverse isotropic. The governing equations are detailed as follow using the Voigt notations.

$$\begin{bmatrix} \varepsilon_1 \\ \varepsilon_2 \\ \varepsilon_3 \\ \varepsilon_4 \\ \varepsilon_5 \\ \varepsilon_6 \end{bmatrix} = \begin{bmatrix} \frac{1}{E_1} & -\frac{\nu_{12}}{E_1} & -\frac{\nu_{13}}{E_1} & 0 & 0 & 0 \\ -\frac{\nu_{12}}{E_1} & \frac{1}{E_2} & -\frac{\nu_{23}}{E_2} & 0 & 0 & 0 \\ -\frac{\nu_{13}}{E_1} & -\frac{\nu_{23}}{E_2} & \frac{1}{E_3} & 0 & 0 & 0 \\ 0 & 0 & 0 & \frac{1}{G_{23}} & 0 & 0 \\ 0 & 0 & 0 & 0 & \frac{1}{G_{13}} & 0 \\ 0 & 0 & 0 & 0 & 0 & \frac{1}{G_{12}} \end{bmatrix} \begin{bmatrix} \sigma_1 \\ \sigma_2 \\ \sigma_3 \\ \sigma_4 \\ \sigma_5 \\ \sigma_6 \end{bmatrix} \tag{2.9}$$

where $\varepsilon_i \quad i \in \{1,2,3,4,5,6\}$ and $\sigma_i \quad i \in \{1,2,3,4,5,6\}$ are respectively, the strain and the stress variables, $E_i \quad i \in \{1,2,3\}$ are the Young modulus, $\nu_{12}, \nu_{13}, \nu_{23}$ are the Poisson ratios and G_{12}, G_{13}, G_{23} are the shear modulus, with $E_2 = E_3$ and $G_{12} = G_{13}$.

Usually, when considering simpler elastic behaviours, the previous equations are integrated through thickness to obtain a macroscopic elastic behaviour using the CLT method which was presented in section 2.1.2. Such a macroscopic law allows modelling the global behaviour of a structure for numerous applications. Some behaviour are nevertheless neglected in this approach, such as for instance the influence of the stacking sequence of the composite laminate. This later point is not detailed in this manuscript.

At the ply level, the laws essentially present a linear elastic orthotropic behaviour at low levels of loading for different types of solicitations (longitudinal tension/compression, transverse tension/compression). Nevertheless, for in-plane shear loading, a non-linear behaviour at the ply scale is observed experimentally [Remy-Petipas, 2000] due to the viscosity of the polymer matrix. Moreover, a loading rate effect is also observed especially for shear loading. For those reasons, it is important to model the effect of viscosity.

Furthermore, at high levels of loading, the effect of damage on the composite laminate behaviour is substantial. The different damage mechanisms occurring in a composite laminate can be modelled using discrete or continuum damage mechanics. A review of some methods used when addressing failure in composite laminate is available in [Orifici et al., 2008]. Some authors [Hongkarnjanakul, 2013], [Bouvet et al., 2009], [Hallett et al., 2009], [Hallett et al., 2008] implement a discrete damage model for all failure mechanisms of the laminate. Most research laboratories prefer to reduce the implementation of discrete interfaces due to the resulting computational issues. Mainly, continuum damage mechanics are used for in-plane, also called intra-ply damages. For out-of-plane damages either continuum or discrete representations are used. The main out-of-plane damage being the delamination, which is a macroscopic crack, the discrete modelling is physically representative.

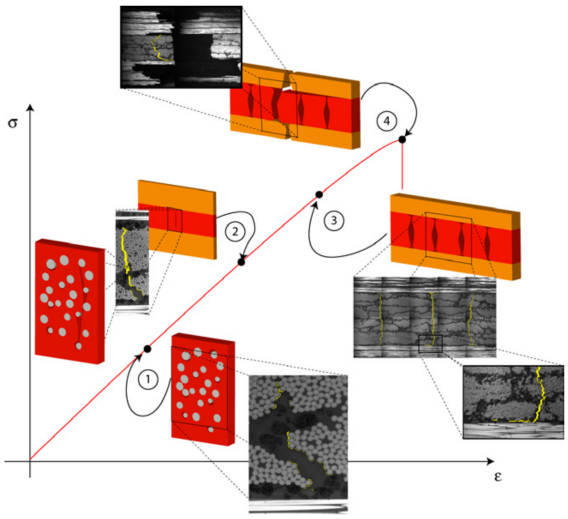

FIGURE 2.7: Evolution of failure mechanisms in a composite laminate with the loading level [Huchette, 2005].

In the following sections, the modelling of the different parts of the behaviour will be presented as there are determining factors for the further developed numerical strategy.

2.2.2.1 Viscosity modelling

When studying a large problem, the viscous behaviour can play an important role in failure involving buckling [B.F.Oliveira and G.J.Creus, 2000]. Such a behaviour can be modelled using a spectral viscoelastic nonlinear approach [Remy-Petipas, 2000]. The principle is to assume that the viscous behaviour results from a pondered sum over a finite number, N, of elementary viscous mechanims ξ_i which are each described by a ponderation coefficient μ_i and a relaxation time τ_i.

The viscous mechanisms are supposed to follow a Gaussian spectral distribution (Figure 2.8, Equation 2.10) where n_0 is the mean and n_c is the standard deviation.

$$\begin{cases} \mu_i &= \frac{1}{n_0\sqrt{\pi}} \exp\left(-\left(\frac{i-n_c}{n_0}\right)^2\right) \\ \tau_i &= \exp(i) \end{cases} \qquad i \in [1,..,N] \tag{2.10}$$

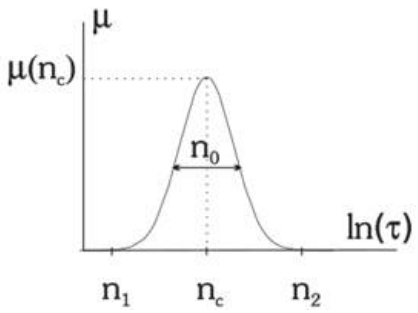

FIGURE 2.8: Gaussian distribution of the viscous mechanisms [Remy-Petipas, 2000]

The strain is then computed using the Equation (2.11) [Remy-Petipas, 2000].

$$\dot{\varepsilon}^{ve} = g(\sigma) \sum_{i=1}^{i=N} \dot{\xi}_i \quad \begin{cases} g(\sigma) &= 1 + \gamma \left(\sqrt{{}^t\sigma : S^R : \sigma}\right)^n & \text{Nonlinear part} \\ \dot{\xi}_i &= \frac{1}{\tau_i}\left(\mu_i g(\sigma) S^R : \sigma - \xi_i\right) & \text{Viscoelastic part} \end{cases} \tag{2.11}$$

where ε^{ve} is the viscoelastic strain, σ is the stress, S^R is the viscous compliance, g is a function describing the non-linear evolution of the viscous strain as a function of the stress, and γ and n are material parameters of this non-linear function. The advantage of using such an approach is the ability to reproduce the non-linear viscoelastic behaviour of a laminate. Moreover the identification protocol is simple.

2.2.2.2 Permanent indention modelling

The non-linear behaviour observed for shear loading can also be modelled using a plastic behaviour. After unloading, residual strain can be observed, especially during tensile tests on [±45] laminates.

Moreover, a "plastic-like" model can be used as in [Bouvet et al., 2012] to address the simulation of residual permanent indentation (Figure 2.9) observed on a composite laminate after an impact on its surface. It is interesting to be able to reproduce well this phenomenon to assess if it has an impact on the damage tolerance estimations of the laminates and also as it is used for Barely Visible Impact Damage (BVID) measurements. In this respect, a model described in the article [Bouvet et al., 2012] computes permanent indentation using a "plastic-like" model at the matrix cracking interfaces.

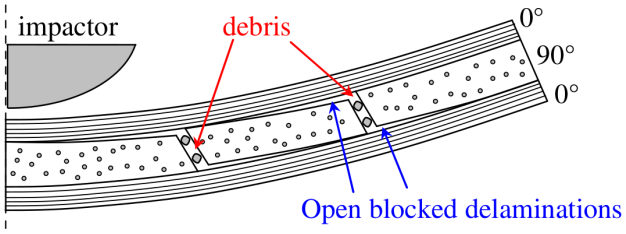

FIGURE 2.9: Principle of formation of permanent indentation [Bouvet et al., 2012]

2.2.2.3 Fibre rupture modelling

In the longitudinal direction, the fibres are the main contributors to the stiffness of the ply of a well designed structure. For tension loadings, the fibre rupture is the main failure mechanism. It is usually modelled using variables that produce linear, bilinear or smooth degradation behaviour as reported in Figure 2.10 (A). Such failure laws are for instance used at the Universities of Porto and Girona [Turon et al., 2006], [Maimí et al., 2007a], [Maimí et al., 2007b], the LMT Cachan [Ladevèze et al., 2000], [Allix, 2001], and at ONERA-Université Paris-Saclay [Laurin et al., 2007], [Laurin et al., 2013], [Laurin, 2009].

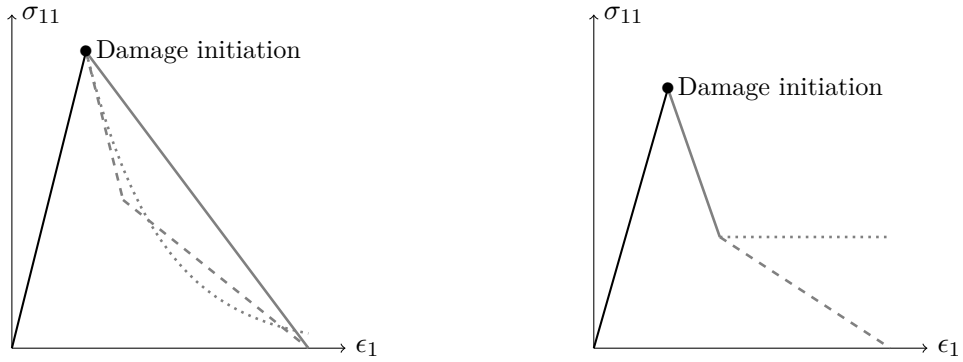

FIGURE 2.10: Examples of longitudinal behaviours of a ply after fibre failure.

For compression loadings, another mechanism takes place which is called fibre kinking. The fibres locally begin to buckle in the plane until their shear strength is reached. Reaching a certain level, a batch of several fibres breaks rapidly which leads to the matrix rupture as well. This induces a substantial decrease of the ply stiffness. This behaviour can be observed as presented in Figures 2.10 (B) and 2.11.

2.2.2.4 Transverse matrix cracking modelling

The damage in the transverse direction is mainly due to matrix cracking induced by transverse tension or in-plane shear loading. The transverse cracks correspond to the coalescence of local fibre/matrix debonding.

2.2.2.5 Out-of-plane damage modelling - Delamination

The delamination is a debonding phenomenon between plies. There are several methods to account for it. It can be represented as a loss of stiffness in the out-of-plane direction in the

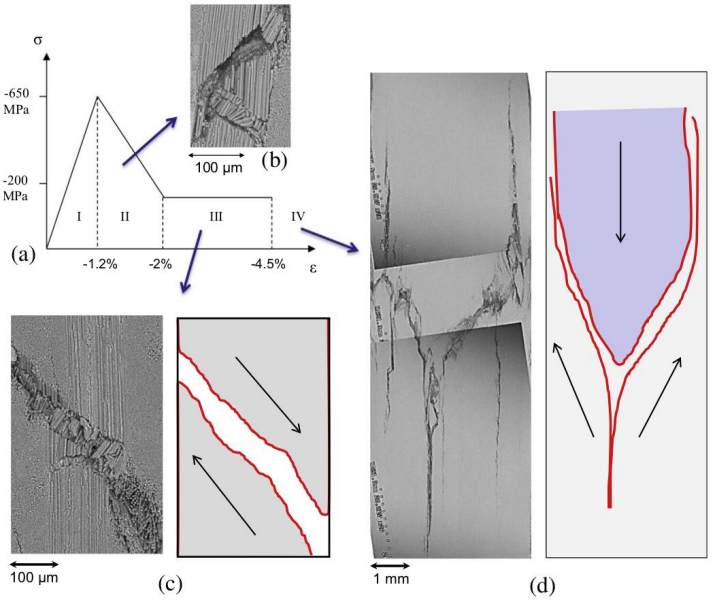

FIGURE 2.11: Strain-softening effects in compression observed at the British Columbia University [Zobeiry et al., 2015].

frame of continuum damage mechanics. This induces a smoother propagation of the damage. The damage can also be modelled with fracture mechanics' techniques. For instance one can use a cohesive interface between plies (Figure 2.12). The onset criterion is usually based on a stress criterion. The degradation law is based on energetic considerations which takes into account the propagation mode.

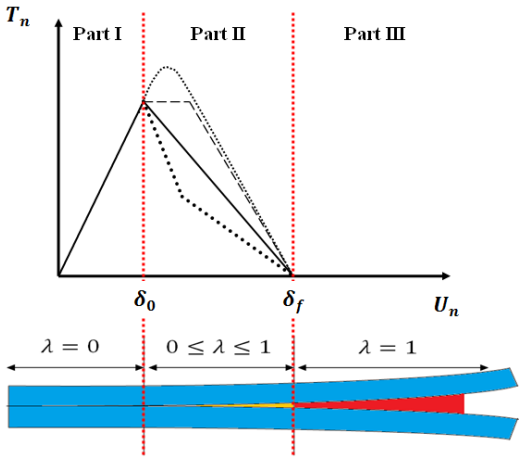

FIGURE 2.12: Different cohesive zone models [Todeschini, 2014]

2.2.2.6 Chosen continuum damage model - Onera Progressive Failure Model

The chosen material law to predict the anelastic behaviour of a unidirectional composite ply in this work has been developed at Onera and is named Onera Progressive Failure Model. This damage and failure model is predictive with respect to experiments on elementary structures and on diverse test cases and is formulated in full 3D. Thus all damage mechanisms are accounted in

the frame of continuum mechanics avoiding the handling of discrete interfaces and the resulting numerical issues.

The hereunder section describes the different aspects that are accounted for in the OPFM model and the set of equations involved in its formulation. The global behaviour can be described by the Equation (2.12) where $\tilde{C}$ is the effective elastic ply compliance, ϵ the total strain, ϵ^{th} the thermal strain, ϵ^{ve} the viscoelastic strain (2.2.2.1), and ϵ^{nl} the non-linear elastic strain.

$$\sigma = \tilde{C} : (\epsilon - \epsilon^{th} - \epsilon^{ve} - \epsilon^{nl}) \tag{2.12}$$

Continuum damage behaviour in all directions. The damage in the out-of-plane direction is represented by a diffuse damage variable. The damage is modelled in three steps: onset of damage, damage evolution law and effect on the behaviour.

1. Computation of failure indexes ($f_i^+, f_i^- \quad for \quad i \in \{1,2,3\}$ - Equation (2.13)) based on stress, (σ_{ii}, τ_{ij}) and strength parameters, $X_c, X_t, Y_t, Y_c, Z_t, Z_c, S_{23}^R, S_{12}^R, S_{13}^R$ (which are respectively the longitudinal compression and tension strength, the transversal compression and tension strengths and the shearing strengths), coupling parameters, p_{ij} and shape parameters $f_{i\to j}$. The shape and coupling parameters allow accounting for coupling occurring during multiaxial combined loading.

$$\begin{cases} f_1^+ = \left(\frac{\sigma_{11}}{X_t}\right)^2 \\ f_1^- = \left(\frac{\sigma_{11}}{X_c}\right)^2 + \left(\frac{\sqrt{1-f_{6\to1}^2}}{S_{12}^R}\frac{\tau_{12}}{1-p_{12}\sigma_{22}}\right)^2 + \left(\frac{\sqrt{1-f_{5\to1}^2}}{S_{13}^R}\frac{\tau_{13}}{1-p_{13}\sigma_{33}}\right)^2 \end{cases}$$

$$\begin{cases} f_2^+ = \frac{1}{\left(1-d_{1f}\right)^2}\left(\left(\frac{\sigma_{22}}{Y_t}\right)^2 + \left(\frac{\tau_{12}}{S_{12}^R(1-p_{12}\sigma_{22})}\right)^2 + \left(\frac{\tau_{23}}{S_{23}^R(1-p_{23}\sigma_{22})}\right)^2\right) \\ f_2^- = \frac{1}{\left(1-d_{1f}\right)^2}\left(\left(\frac{\sigma_{22}}{Y_c}\right)^2 + \left(\frac{\tau_{12}}{S_{12}^R(1-p_{12}\sigma_{22})}\right)^2 + \left(\frac{\tau_{23}}{S_{23}^R(1-p_{23}\sigma_{22})}\right)^2\right) \end{cases} \tag{2.13}$$

$$\begin{cases} f_3^+ = \frac{1}{\left(1-d_{1f}\right)^2}\left(\left(\frac{\sigma_{33}}{Z_t}\right)^2 + \left(\frac{\tau_{13}}{S_{13}^R(1-p_{13}\sigma_{33})}\right)^2 + \left(\frac{\tau_{23}}{S_{23}^R(1-p_{23}\sigma_{33})}\right)^2\right) \\ f_3^- = \frac{1}{\left(1-d_{1f}\right)^2}\left(\left(\frac{\sigma_{33}}{Z_c}\right)^2 + \left(\frac{\tau_{13}}{S_{13}^R(1-p_{13}\sigma_{33})}\right)^2 + \left(\frac{\tau_{23}}{S_{23}^R(1-p_{23}\sigma_{33})}\right)^2\right) \end{cases}$$

Where $d_{1f} = \frac{1-f_{2\to1}}{1-f_{1\to2}^2}\left\langle sup\left(f_1^+\right) - f_{1\to2}^2\right\rangle$, $\langle\rangle$ being the Macauley brackets

The onset of failure correspond to $f_i = 1$. The failure indexes f_1, f_2, and f_3 correspond respectively to the fibre failure, to the matrix failure, and to the delamination.

2. Computation of damage variables based on failure indexes f_i and damage kinetic parameters α_i: The damage kinetic parameters allow to give a weight to each damage type to

control their respective influence on the load tensor.

$$d_i = \alpha_i \left\langle \sqrt{\eta_i f_i^+ + (1-\eta_i) f_i^-} - 1 \right\rangle^+, where \quad \eta_i = \begin{cases} 1 & if \quad \sigma_{ii} \geq 0, \\ 0 & if \quad \sigma_{ii} < 0, \end{cases} \quad , \quad i \in \{1,2,3\} \tag{2.14}$$

3. Computation of the effective compliance (Equation 2.15) based on the damage variables and effect tensors (Equation 2.16): The effect tensors describe the effect of the damage on the global mesoscopic behaviour of the ply in the different directions assuming that the crack orientation are piloted by the microstructure of the material. For instance a damage in the transverse direction not only affects the behaviour in that direction but also decreases the in-plane and out-of-plane shear rigidity of the ply.

$$\tilde{S} = S_0 + \sum_{i=1}^{3} d_i H_i \tag{2.15}$$

$$H_1 = \begin{pmatrix} \left(\eta_1 h_{11}^+ + (1-\eta_1) h_{11}^-\right) S_{11}^0 & 0 & 0 & 0 & 0 & 0 \\ 0 & 0 & 0 & 0 & 0 & 0 \\ 0 & 0 & 0 & 0 & 0 & 0 \\ 0 & 0 & 0 & 0 & 0 & 0 \\ 0 & 0 & 0 & 0 & h_{55}^{FF} S_{55}^0 & 0 \\ 0 & 0 & 0 & 0 & 0 & h_{66}^{FF} S_{66}^0 \end{pmatrix} \tag{2.16}$$

The other effect tensors H_2 and H_3 can be obtained by permutations of the index.

The OPFM law is thus retained for the representation of complex behaviour in composite laminate at the ply scale. The interested reader can find a more detailed presentation of the OPFM law in [Laurin et al., 2007].

2.2.3 Finite element resolution using the composite damage laws

2.2.3.1 Finite element model

The classical single layer formulation of multilayered structures provides an accurate description of the global behaviour but a coarse description of the stress state. When a more refined stress state is wanted, a local analysis is necessary. For instance, close to the geometrical singularities more refined meshes are preferred for a better stress description. To have a representative stress state, a ply-per-ply mesh is required, either made of shell elements or 3D elements. The use of shell elements provides a rough estimation of the transverse shear and normal out-of-plane stress. If the failure mechanisms are driven by those components, 3D elements are preferred. However the use of 3D elements for thin structures is restrictive in order to limit mesh distortion.

2.2.3.2 Resolution scheme

Usually the composite damage laws are implemented within explicit finite element solvers for numerical issues, especially in presence of fibre failure. However, some laboratories develop laws than can be used with both implicit and explicit resolution schemes such as the Universities

of Porto and Girona [Turon et al., 2006], [Maimí et al., 2007a], [Maimí et al., 2007b], [Pinho et al., 2005], the ONERA [Laurin et al., 2013], [Laurin, 2009],[Laurin et al., 2007] and the LMT [Ladevèze et al., 2000], [Allix, 2001]. The implicit scheme is preferred here for two reasons: firstly to reduce computational time given that the material law is efficiently implemented with such a scheme, and secondly because any obtained result is much more self consistent and does not require an expert critical analysis to be validated.

2.2.3.3 Example of a stiffened panel in compression

The objective of the following example is to assess the difference in computational effort of a medium sized structural problem with, on one hand, an elastic law, and on the other hand, a damage law. The considered model is a stiffened panel in compression along the stiffeners' direction. The finite element model is a full shell model, with 136 950 dofs, and is illustrated in Figure 2.13.

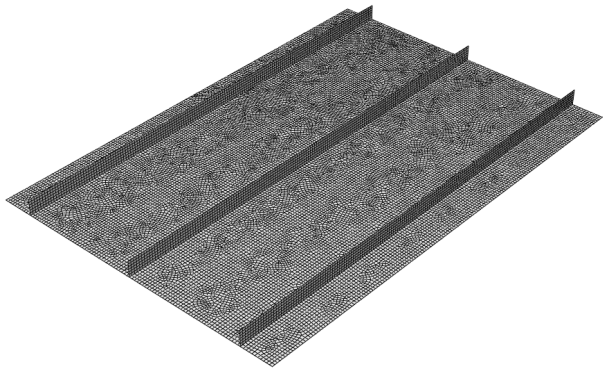

FIGURE 2.13: Finite element model of a stiffened panel

The computational time results are presented in Table 2.1.

Model	**Computational time**
Elastic model	10min 40s
OPFM model	6h 53min 43s

TABLE 2.1: Computational time of a stiffened panel in compression for an elastic model and a damage model.

The use of the more complex law (here OPFM) increases by a 32 factor the computational time of this structural case. When aiming to even bigger structures, the cost becomes unreasonable. When treating a large composite structure, in the context of wide aircraft components, for instance, the material law usually considered is a linear elastic behaviour.

Moreover, the represented damages are limited in this case due to the shell kinematics. In order to model out-of-plane phenomena, 3D elements would have to be employed. This would give an even bigger computational effort with the risk of non-convergence of the simulation.

2.2.4 Conclusion

To reproduce accurately the failure of composite laminates, several features detailed in this section 2.2 are modelled. The material model is enforced at the ply scale which is a fair trade-off between the desired level of details and the computational cost. It enables to obtain a detailed enough stress state to simulate damage and failure in the different plies.

Different material laws can be found in the literature and remain as it is too costly to be used directly on a large composite structure where a simplified model mostly linear elastic, seems mandatory. The following section 2.3 aims at providing elements of bibliography for treating such large problems where two levels of modelling are considered at the same time.

2.3 Elements of bibliography on multiscale finite element strategies for problems with two levels of modelling

When different levels of modelling are required in a finite element simulation (typically a damage occurs at a characteristic size of 0.1-1mm in a composite structure while the structure's size can reach 1-10m), several levers of action are possible. When the scales are clearly distinct with a macroscopic and a microscopic ones, multi-level methods based on material homogenisation can be used. Those methods will not detailed in this manuscript since there is no clear separation of scales in our studied cases. In fact, the damages involved in composite laminates are mainly macroscopic.

When treating large problems, several works are available in the literature. For the sake of clarity, those methods will be clustered into two main groups of approaches: one based on model coupling and one based on progressive model enrichment. On one hand, the principle of model coupling methods is to couple an initial finite element model with another model to incorporate the wanted level of details without altering the initial model. On the other hand, the enrichment methods rely on the update of the initial model to translate the wanted level details.

Moreover, industrials want the method to work with their choice of finite element solver which can be certified for their use. Consequently, the method developed in this manuscript is designed to fit the current models and to provide flexibility over the choice of solver used by the industrial.

In this section, first the general engineering methodologies are explained. Then the model coupling approaches are detailed. The model coupling encompasses both a coupling in time (section 2.3.2) and in space (section 2.3.2). Then the enrichment methods are exposed.

2.3.1 Engineering methods

The so-qualified as engineering methods are the procedures usually performed by industrial engineers. To fit the computational time constraints, there is a need of modelling simplification. Generally, two levels of modelling are required, a simpler one such as detailed in section 2.1.2 and a more detailed one. To perform the numerical analysis, two types of methods are usually used, sub-modelling and local refinement which are detailed hereunder.

2.3.1.1 Sub-modelling

The sub-modelling consists in performing a global analysis on a coarse model and in using its results to apply boundary conditions on a local, more detailed, model. When repeating several times this operation, the method is also referred as the approximate zooming technique. This type of analyses usually involves the following steps:

- Global analysis of a coarse model,
- Localisation of potential problematic areas,
- Building of a more refined local model in the target zone of interest,
- Extraction of the boundary conditions to be applied to the local model,

- Local analysis with the corresponding global boundary conditions.

Several types of boundary conditions may be applied to the local model. The conditions can be either displacement based, load based or mixed. The local model usually contains more elements than the global one at the boundary. The meshes are called not conforming, meaning that some nodes are not shared between the global and the local models. Consequently, the boundary conditions to be applied are refined before being applied to the local boundary. This is usually performed by interpolation using the shape functions of the global model to retrieve the boundary condition values at the nodes of the local mesh.

Dirichlet boundary conditions The displacement based conditions [Kelley, 1982] are the simplest to implement. In the case of mesh non-conformity at interface with a leaner mesh on the more detailed model, the displacement are interpolated. The main disadvantage of the Dirichlet boundary condition is its stiffness description.

Load based conditions The method which transmits load based conditions is named Specified Boundary Stiffness Method (SBSM) [Jara-Almonte and Knight, 1988]. The advantage of using load based condition is the ability to account for the global structure which gives more accurate results. Nevertheless, it is more difficult to implement in the frame of a closed finite element solver as one has to retrieve the internal forces.

The sub-modelling methods present the disadvantage of skipping the possible stress redistribution and the influence the local model could have on the response of the global model. This cannot be neglected for the case of buckling analyses for instance which are sensitive to local changes.

2.3.1.2 Local refinement

An alternative to sub-modelling is the model refinement over a defined area where more details are required. This method presents the advantage of being more precise on the global response. Nevertheless, it requires an initial identification step of the critical areas, efforts on model creation and to re-run the analysis from scratch. The resulting lack of flexibility of this method restricts its use in an industrial context.

2.3.2 Model coupling strategies

When considering problems requiring several levels of modelling, model coupling approaches are a good alternative to the use of a refined model over the whole domain. There is an extensive literature on model coupling strategies, especially focused on which quantity to couple and how to implement the coupling. In this section, first the methods of coupling in time are presented. They are relevant for problems where a differentiated time-stepping and resolution scheme through the domain can be advantageous. Then the methods of coupling in space are detailed where the finite element model and material behaviour is differentiated through the spatial domain.

Coupling in time approaches Several methods explore the possibility of using different time discretizations through the domain. For example, the works of [Gravouil and A.Combescure,

2001], [Combescure and Gravouil, 2001], [Chantrait, 2014] and [Chantrait et al., 2013] present methods for the coupling of domains with different Newmark resolution schemes and different time-stepping (Figure 2.14). This arises the opportunity of coupling for instance two implicit domains or one implicit to one explicit domain with different time-stepping.

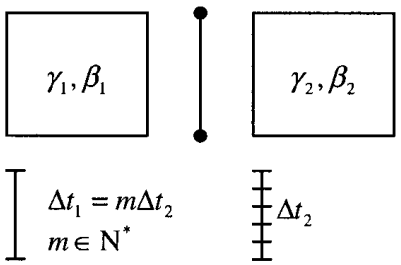

FIGURE 2.14: Coupling of Newmark numeric schemes with different time stepping [Gravouil and A.Combescure, 2001]

In [Chantrait, 2014], a method for an adaptive evolution of the resolution scheme through the spatial domain along with damage propagation is developed. The Figure 2.15 presents this mechanism with in dark grey the explicit domain, in light grey the implicit domain and in red the interface. A flip-flop mechanism was introduced only for one direction from the implicit scheme with a coarser time stepping to an explicit scheme with a thinner time stepping.

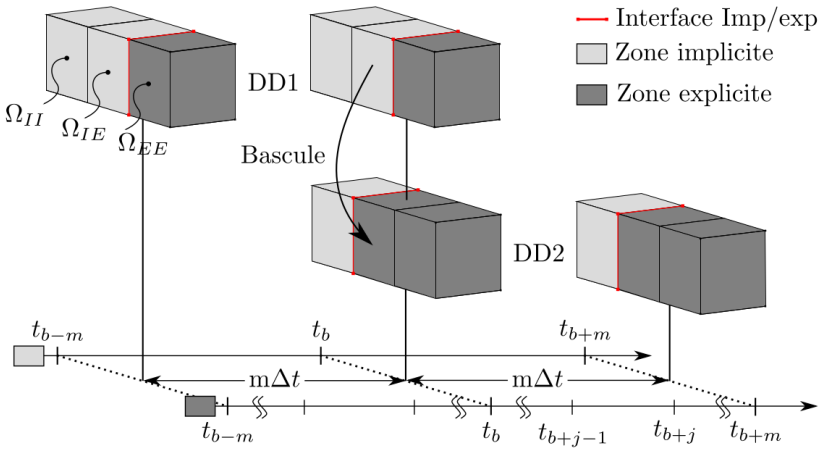

FIGURE 2.15: Flip-flop mechanism between two resolution schemes [Chantrait, 2014].

The multiscale in time strategies are especially relevant for the case of dynamic phenomena occurring in the local region. Thus a differentiated resolution scheme per region can be beneficial. In this manuscript, the target application are quasi-static problems that can mainly be solved using implicit schemes, while the case of non-linear strain on the global model makes the computation of Schur complements unaffordable.

Coupling in space approaches The coupling in space involves the use of different levels of modelling through the spatial domain. Generally, two levels of modelling are required, a coarse one and a refined one which is localized and with a lower level of details. Usually the coarse model

is called global and the refined model is called local. Here two types of approaches are detailed, one based on an iterative scheme between the two models and one based on superposition of the models through some coupling conditions.

2.3.2.1 Exact zooming approaches

The previous presented engineering methods present the strong advantage of being easily implemented in an industrial context. The sub-modelling is a cost-effective approach but it does not account for the local effects on the global behaviour. On the contrary, the local model refinement is exact but requires to recompute the whole model each time which makes it time consuming.

As a trade-off, other approaches have been developed, called "exact zooming". Two of those methods are described here, one based on re-analysis techniques and one on static condensation.

Re-analysis techniques The re-analysis techniques are used for small modification (geometry, behaviour...) cases when one does not want to recompute the full system. The response of the original system is used to retrieve the solution of the modified system. A review of those methods is available in [Kassim and Topping, 1987]. They are usually qualified as either exact or approximative. The exact or direct methods are more efficient for the cases of small changes and are detailed in this section.

The general principle of static reanalysis is here detailed for a linear problem. Let's define the following equilibrium equation of the original problem identified by the subscript 0 with K_0 the initial stiffness matrix, $\boldsymbol{u}_0$ the displacement vector and $\boldsymbol{F}_0$ the vector of the generalized forces.

$$\boldsymbol{K}_0 \boldsymbol{u}_0 = \boldsymbol{F}_0 \tag{2.17}$$

When applying a small change in the structure, both the stiffness and the load are modified. This modification is expressed as follow:

$$\begin{cases} \boldsymbol{K} = \boldsymbol{K}_0 + \Delta \boldsymbol{K} \\ \boldsymbol{F} = \boldsymbol{F}_0 + \Delta \boldsymbol{F} \end{cases} \tag{2.18}$$

Often, the vector of generalized forces is assumed being independent from the change, resulting in $\Delta \boldsymbol{F} = \boldsymbol{0}$. The system to be solved is thus the following.

$$\left(\boldsymbol{K}_0 + \Delta \boldsymbol{K}\right) \boldsymbol{u} = \left(\boldsymbol{K}_0 + \Delta \boldsymbol{K}\right) \left(\boldsymbol{u}_0 + \Delta \boldsymbol{u}\right) = \boldsymbol{F}_0 \tag{2.19}$$

There has been an extensive amount of work on the resolution of Equation 2.19. Some methods explore the fact that the matrix $\Delta \boldsymbol{K}$, being mostly sparse, can be compressed by the elimination of the zero columns and rows. Then, successive steps of inexpensive mathematical operations allow retrieving the change in displacement $\Delta \boldsymbol{u}$. More details on the explored methods and procedures are developed in [Kirsch, 2008] [Wang and Pilkey, 1980].

The exact reanalysis techniques are efficient for the cases of small changes given that the mathematical operations and data storage are performed optimally. Those methods may present a high computational cost when there are larger modifications, for instance for finite strain problems.

Exact zooming techniques based on static condensation Another type of zooming techniques relies on static condensation. It allows to solve a global-local system with a reduced number of dof given the hypothesis of a linear behaviour. This is performed by condensing the dofs located inside a specified zone and account for it through a global stiffness. The size of the system to be solved is thus limited. This method is appreciated by industrials as they can exchange condensed models with lesser details for confidentiality purposes.

In [Hirai et al., 1984], the authors propose to perform an exact zooming step followed by a reanalysis. Let i refer to the initial system, f to the final system after zooming, a to the dof outside the local region, b to the original dof inside the local region and c to the additional dof inside the local region. Then the reference problem can be written as:

$$\begin{bmatrix} \boldsymbol{K}^i_{aa} & \boldsymbol{K}^i_{ab} & \boldsymbol{0} \\ \boldsymbol{K}^i_{ba} & \boldsymbol{K}^i_{bb} + \boldsymbol{K}^f_{bb} & \boldsymbol{K}^f_{bc} \\ \boldsymbol{0} & \boldsymbol{K}^f_{cb} & \boldsymbol{K}^f_{cc} \end{bmatrix} \begin{bmatrix} \boldsymbol{u}^f_a \\ \boldsymbol{u}^f_b \\ \boldsymbol{u}^f_c \end{bmatrix} = \begin{bmatrix} \boldsymbol{F}^i_a \\ \boldsymbol{F}^i_b \\ \boldsymbol{0} \end{bmatrix} \tag{2.20}$$

The Equation 2.20 can be rewritten under the following form which makes it suitable for reanalysis operations.

$$(\boldsymbol{K}_0 + \Delta\boldsymbol{K})\,\boldsymbol{u} = \boldsymbol{F}_0 \tag{2.21}$$

The methods based on static condensation present the advantage of being exact and robust for linear applications. Nevertheless, the condensation step can become computationally unaffordable when tackling problem of great size. Moreover, it requires the extraction of operators which is complex in the context of a commercial FE software.

2.3.2.2 Iterative global-local methods

The global-local iterative methods [Mao and Sun, 1991], [Whitcomb, 1991], [Gendre, 2009] were introduced to provide a better alternative to the engineering methods detailed in section 2.3.1. The principle is to perform alternatively the finite element resolutions of the global and local models through an iterative procedure to exchange information at the interface as illustrated in Figure 2.16. This is usually performed by the following general steps. The last two steps, 3 and 4, can be reiterated until convergence but generally one iteration is sufficient. Generally, the difference between the several approaches lies on the handling of the step 4.

1. Global analysis of a coarse model,
2. Extraction of the boundary conditions to be applied to the local model,
3. Local analysis with the corresponding global boundary conditions,
4. Correction of the global analysis by the local response.

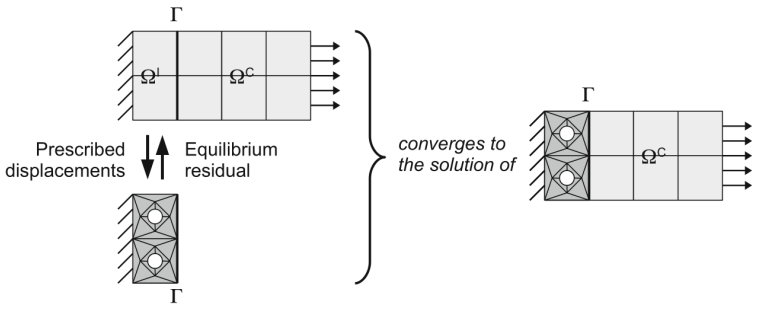

FIGURE 2.16: Illustration of a global-local approach [Gendre, 2009]

The simplest method is to extract the global displacements of the analysis 1. Then those displacements are applied as boundary conditions for the local analysis 3. Finally, the global correction analysis is launched. Several methods for the global correction analysis are detailed hereunder.

The method introduced by [Mao and Sun, 1991] called RGL (Refined Global-Local) treats the correction of the global model by displacements fields. The global correction is launched with the following form of displacement of an element.

$$\boldsymbol{u} = \boldsymbol{u}^{local} + \sum_i N_i \left(\boldsymbol{u}_i - \boldsymbol{u}_i^{local} \right) \tag{2.22}$$

where $\boldsymbol{u}$ is the displacement field over an element, $\boldsymbol{u}^{local}$ is the resulting displacement from the local analysis, N is the shape function of the element, and the subscript i refers to the nodes of the considered element. With this form of displacement field, the equilibrium is expressed as follow.

$$\boldsymbol{K}_i \boldsymbol{u}_i = \boldsymbol{F}_i + \boldsymbol{F}_i^{local} \tag{2.23}$$

where $\boldsymbol{K}_i$ is the stiffness matrix of the element, $\boldsymbol{u}_i$ is the displacement vector, $\boldsymbol{F}_i$ is the nodal forces vector and $\boldsymbol{F}_i^{local}$ is a supplementary vector which depends on the solution of the local analysis. This allows to improve the accuracy of the method.

This method is particularly suitable for elastic linear problems requiring only a mesh refinement operation. Several of such application cases are developed in [Mao and Sun, 1991] with the results in terms of computational efficiency and accuracy. The formulation of the method does not allow to separate directly the global linear equilibrium from the local phenomena. It is thus more delicate to treat accurately non-linear local behaviour with such a method. This method is consequently quite intrusive which is a substantial limitation.

An improvement of this method is proposed by [Whitcomb, 1991] with the IGL (Iterative Global-Local) method. The principle is to perform an iterative modified Newton-Raphson procedure. After the local analysis, the following residual is computed:

$$\boldsymbol{r} = \left(\boldsymbol{K}^{global \backslash local} + \boldsymbol{K}^{local} \right) \boldsymbol{u} - \boldsymbol{F} \tag{2.24}$$

where $\boldsymbol{r}$ is a residual, $\boldsymbol{u}$ is the displacement, $\boldsymbol{K}^{global \backslash local}$ and $\boldsymbol{K}^{local}$ are respectively the ... and the ... stiffness matrices, and $\boldsymbol{F}$ is the force. The correction to global displacement is then

computed as:

$$\Delta \boldsymbol{u} = -\left(\boldsymbol{K}^{global\backslash local} + \boldsymbol{K}^{local}\right)^{-1} \boldsymbol{r} \tag{2.25}$$

Those operations are repeated until $\boldsymbol{r}$ is small enough. This allows to monitor the convergence of the method. Its performance has been assessed on academic linear cases [Whitcomb and WOO, 1993] and cases with geometrical non-linearity [Whitcomb, 1993]. This method is thus more accurate than the RGL but requires more iterations to converge. As for RGL, this method only applies in the case of conform local meshes which is highly restrictive.

Based on those strategies, several global-local iterative procedures are available in the literature. For instance, a "non-intrusive" global-local approach is presented in [Gendre et al., 2009] based on the principle of IGL. The difference lies in a different formulation of the computed residual which imposes the continuity of the displacement across the interface and ensures the equilibrium of the forces at a defined precision. Additional acceleration techniques can be used to improve the convergence rate of the modified Newton-Raphson scheme.

2.3.2.3 Superposition methods

The principle of those methods is to superpose the local model to the global one and solve the resulting coupled system. Thus the stress redistribution between the global and the local models is satisfied.

A variety of strategies are proposed in the literature to address the coupling between different models. There are different aspects involved in the coupling that are:

- On what domain to perform the coupling ?
- How to enforce the coupling ?

To answer the first question, the coupling can be performed over a boundary surface or within a volume. The first set is called non-overlapping and the second one overlapping methods.

The Arlequin method [BenDhia, 1999], [Touzeau, 2012] proposes to couple the models in a subset of an overlapping zone. Energy conservation constraints are implemented. There is a transition zone around the interface where the energies from both subdomains are pondered such that the sum of the ponderation coefficients remains equal to unity. At last, a coupling condition is needed. Several coupling conditions are possible. For instance an energetical coupling through Lagrange multipliers can be used as in [Touzeau, 2012]. The Arlequin method can be used for instance to introduce a patch with a thinner level of details. For instance, the Figure 2.17 represents a possible case of application of the method. A hole with a more detailed modelling is superposed to an initial composite laminate plate without geometrical singularities. The main drawback of those methods is that they are intrusive when implemented with a commercial FE software and they may induce a loss of robustness.

Furthermore, there are several methods to enforce the coupling. The mortar method [Bernardi et al., 1993], [Anagnostou et al., 1990], [Belgacem, 1999] is popular and enforces weakly the conditions through Lagrange multipliers or by the Nitsche method [Fritz hueber,2004], [Hansbo

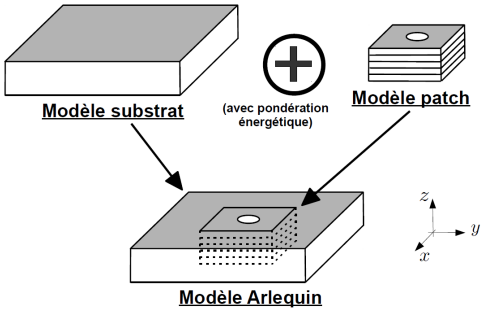

FIGURE 2.17: Application case of the Arlequin method on a composite laminate plate [Touzeau, 2012]

and Hansbo, 2004] [Nguyen et al., 2013]. In many problems, it can be binding to maintain a mesh compatibility condition at the domain interfaces. Mesh compatibility means that all edges share two extremities (Figure 2.18). The mortar methods allows dealing such incompatible meshes.

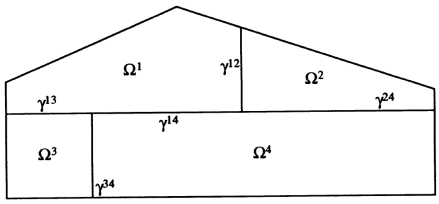

FIGURE 2.18: Incompatible geometrical decomposition of a domain [Bernardi et al., 1993]

Mortar methods can be used with a huge variety of problems. For instance in solid mechanics, they can be used to tackle contact problems or patch insertion (Figure 2.19). For patch insertion problematic, prior to using mortar methods, a cutting mesh algorithm has to be used to redefine the boundary of the host mesh. Nevertheless, in such methods involving incompatible meshes, there are integration difficulties at the interface that have to be dealt with.

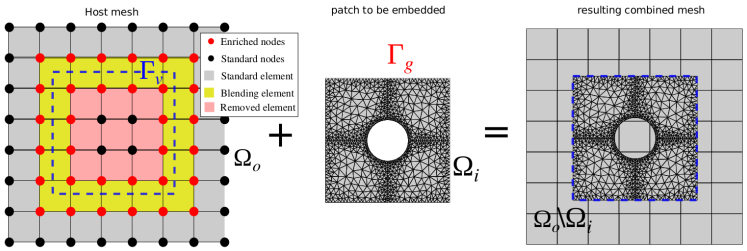

FIGURE 2.19: Example of patch insertion using mortar methods [Yastrebov et al., 2017]

Conclusion

Global-local methods are widely developed in the literature to compute problems where two levels of modelling are required. They provide good accuracy for a wide range of problems. Nevertheless, they are still complex to implement with closed commercial FE solvers. To tackle

this problem, a branch of global/local methods [Gendre, 2009], called non-intrusive in the sense that numerical operator of the global model is not modified, is developed. Such operations ease the implementation of the strategy in the framework of a commercial finite element solver.

2.3.3 Model improvement/enrichment

An alternative to model coupling methods are the model enrichment methods. Model enrichment methods are based on a monolithic formulation and allow a progressive updating of the model through the resolution when it is needed. In fact, in many structural problems the target complex local behaviour may not be known a priori and can evolve on the fly. For this reason enrichment methods can be advantageous given that the model update is performed in a strategic way.

In this section, first some methods based on the partition of unity [Melenk and Babuška, 1996] with a progressive enrichment of the approximation spaces are presented. Then adaptive meshing methods are introduced.

2.3.3.1 Methods based on partition of unity

Partition of Unity Methods (PUM) The PUMs rely on the enrichment of the approximation spaces by analytical fields. It was first introduced in [Melenk and Babuška, 1996] as the partition of unity finite element method (PUFEM).

The principle of the method is to construct for a domain Ω a global subspace V of $H^k(\Omega)$. In order to do that, first a partitioning that can be overlapping, $\{\Omega_i\}$ of Ω, is defined. Let $\{\phi_i\}$ be a set of functions covering $\{\Omega_i\}$ such that $\sum_i \phi_i \equiv 1$. They form a partition of unity. Let V_i be the local approximation spaces. Then the global V subspace is defined as $V = \sum_i \phi_i V_i$. When the PU is based on FE shape functions, the global displacement field is of the following form for the case of only one additional enrichment term.

$$\boldsymbol{u} = \underbrace{\sum_{i\in I} N_i \boldsymbol{u}_i}_{\text{FE approximation}} + \underbrace{\sum_{i\in I} N_i^+ \psi \boldsymbol{a}_i}_{\text{enrichment term}} \tag{2.26}$$

where $\boldsymbol{u}$ is the displacement, N_i, N_i^+ are respectively a FE shape function of the element and a function related to the enrichment term, usually equal (they both form a partition of unity), ψ is the enrichment function, $\boldsymbol{a}_i$ are additional nodal unknowns, the i subscript refers to the nodes and I is the set of all nodes.

The main advantage of the PUMs is the ability to construct a global conforming space out-of local approximation spaces that may not satisfy inter-element continuity (ex non-polynomial local approximation spaces). The performance of PUM relies partly on the ability to prepare "good" local approximation spaces. Thus they are great candidates for modelling discontinuities.

Several methods were developed from the PUMs such as the G-FEM (Generalized Finite Element Method) introduced in [Strouboulis et al., 2000] and the X-FEM (Extended Finite Element Method) introduced in [Belytschko and Black, 1999], [Moës et al., 1999]. An extensive overview

of those methods is available in [Fries and Belytschko, 2010]. Those methods are particularly suitable for the modelling of strong discontinuities (rapid change of field quantities or gradient over a small distance respective to the global domain).

Extended Finite Element Method (X-FEM) The X-FEM relies on the PU principle. In X-FEM, the partition of unity is based on the FE shape functions and the enrichment is performed at a local level on a subset of nodes.

$$\boldsymbol{u} = \underbrace{\sum_{i \in I} N_i \boldsymbol{u}_i}_{\text{FE approximation}} + \underbrace{\sum_{i \in I^{local}} N_i^+ \psi \boldsymbol{a}_i}_{\text{enrichment term}} \tag{2.27}$$

The choice of enriching only a subset of nodes produces three types of elements, ones with standard FE nodes, ones with all enriched nodes and ones with mixed nodes. This latter type of elements produces some inconvenience as the functions N_i^+ are not a partition of unity. This may affect both the convergence rate and the error. Different integration strategies have been developed to limit those issues and are described in [Fries and Belytschko, 2010].

Phantom node method (PNM) When looking at the failure of composite structures, the fracture paths are complex as detailed in section 2.2.1.2. Those failure mechanisms can generally be qualified as "weak" discontinuities. To reproduce them, specific numerical methods based on PU have been developed such as [Song et al., 2006], [Meer and Sluys, 2009], [Remmers et al., 2003] and are presented hereunder. First the concept of level-set function is introduced.

The level-set function is a signed distance function used for partitioning a domain. It is defined over the whole domain Ω, negative over $\Omega_1 \subset \Omega$, positive over the complementary domain $\Omega_2 = \Omega \setminus \Omega_1$ and zero at the interface $\Gamma = \Omega_1 \cap \Omega_2$. The level set function is in general stored at nodes and interpolated using the shape functions at every location of the model. Let χ be the level-set function.

The work presented in [Hansbo and Hansbo, 2004] proposes to introduce additional dofs at each node. From this two sets of shape functions are defined, one over each domain separated by the discontinuity. Based on this work, the Phantom Node Method was introduced in [Song et al., 2006]. The paper [Areias and Belytschko, 2006] proves that PNM is similar to X-FEM but with Heaviside enrichment. The Heaviside function is defined as follow.

$$H(\chi) = \begin{cases} 0 & \text{if } \chi \leq 0, \\ 1 & \text{if } \chi > 0. \end{cases} \tag{2.28}$$

The displacement is then expressed as:

$$\boldsymbol{u} = H(\chi)\,\boldsymbol{u}_1 + H(-\chi)\,\boldsymbol{u}_2 \tag{2.29}$$

where $\boldsymbol{u}_1$ and $\boldsymbol{u}_2$ are respectively the displacements fields from the two superposed elements.

Several works explored the capability of PNM to reproduce failure in composite materials as [Meer and Sluys, 2009]. The PNM as well as X-FEM present the drawbacks of having a different discontinuity geometrical representation in the physical space than in the natural space and also having to perform the integration over partial domains as detailed in [Fries and Belytschko, 2010]. Errors are thus introduced compared to methods involving crack propagation through remeshing. In remeshing methods, the crack is propagated along the mesh edges allowing to maintain the standard FE formulation in the elements and thus full integration. To counter those effects, the Floating Node Method (FNM) was developed in [Chen et al., 2014], [Kocaman et al., 2019]. The main advantage of this method is the ability to use the frame of X-FEM and PNM whilst formulating the discontinuity as if there was a remeshing operation. This method was meant to be implemented in the context of commercial FE codes through a user element. The authors stress the performance of this method in modelling weak and cohesive discontinuities. This is well suited when modelling explicitly matrix cracking and delamination.

Conclusion

The previous methods are effective for the modelling of discontinuities but require some degree of intrusiveness into the finite element software as the approximations spaces have to be defined. They are of particular interest when modelling "rough" phenomena such as discrete damage. For instance, for the case of composite laminates, they are relevant for modelling delamination. Discrete modelling involve a loss a robustness that is not wishable. In this manuscript, the choice is to develop a method that explores the limits of continuum mechanics to model damage in composite laminate structures.

2.3.3.2 Methods based on adaptive remeshing

When modelling diffuse damage in composite, SMCs are most adequate as detailed in section 2.2. This is the case when the crack is mostly driven by fibre failure for instance. To use those models, the stress state of the elements should be rich enough. In order to achieve it, a main lever of action is modifiying the mesh by refining it and/or by switching elements when necessary. In the litterature, adaptive remeshing methods are mostly driven by local error indicators [Zienkiewicz and Zhu, 1987] [Babuška and Rheinboldt, 1978] [Johnson and Hansbo, 1992]. The basics of mesh adaptation are first recalled in this section before the particular case of composite structures is elaborated.

A general formulation of an adaptive meshing technique is developed in this paragraph. Given a discrete formulation of a FE problem with a given mesh. Let the mesh be depending on two functions $h(\boldsymbol{x}, t)$, the local mesh size, and $p(\boldsymbol{x}, t)$, the order of the polynomial approximation, where $\boldsymbol{x}$ is the spatial localisation and t the time. Then a meshing algorithm is used to find the best mesh candidate to ensure for a given norm $||.||$ and a given tolerance ϵ_{tol} that the finite element solution $\boldsymbol{u}_{h,p}$ verifies the following equation.

$$||\boldsymbol{u} - \boldsymbol{u}_{h,p}|| \leq \epsilon_{tol} \tag{2.30}$$

As the exact solution $\boldsymbol{u}$ is unknown, an *a posteriori* error $E(h, p, \boldsymbol{u}_{h,p}, f)$, f being an additional data from the problem, is constructed such that:

$$||\boldsymbol{u} - \boldsymbol{u}_{h,p}|| \leq E(h, p, \boldsymbol{u}_{h,p}, f) \leq \epsilon_{tol} \tag{2.31}$$

The optimal mesh is thus obtained by the minimization of the number of dof whilst complying with Equation 2.31. When both the mesh size and the polynomial approximation are revised, the methods are called h-p methods [Oden et al., 1989] [Johnson and Hansbo, 1992]. It may be difficult to adjust the polynomial approximation in a closed FE software. Furthermore, the irregularities of damage laws does not give many interest to higher order interpolations in our context. The adaptation of the mesh size is in this case more manageable.

The h-method [Demkowicz et al., 1985] consists in adapting only the elements' size. This is illustrated in Figure 2.20 from the work of J.C Zhu and O.C Zienkiewicz [Zhu and Zienkiewicz, 1988] [Zienkiewicz and Zhu, 1987], on adaptive techniques for FEM.

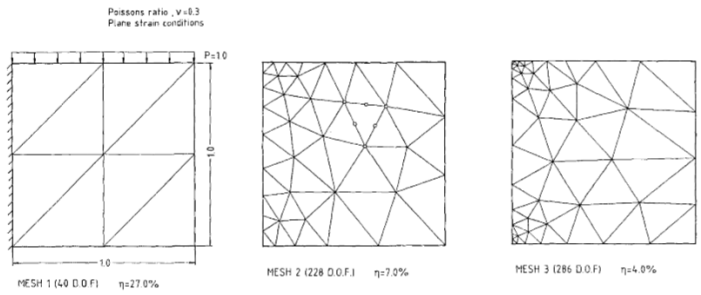

FIGURE 2.20: Illustration of an adaptive mesh refinement approach [Zhu and Zienkiewicz, 1988]

The main problematics involved in adaptive remeshing is the construction of the error estimator, the adaptive algorithm and finally the transfer of the fields between two different meshes for state upate. Several transfer operators [Dureisseix and Bavestrello, 2006], [Perić et al., 1996], [Villon et al., 2002] have been developed. Some of them are presented in a further section 4.4.

2.3.4 Conclusion

To summarize this section, when dealing with problems involving different modelling levels, several numerical strategies are possible. At first, engineering methods such as submodelling and local refinement were presented. The engineering methods are simple to be implemented but lack of accuracy and flexibility. The main drawback consist in not considering the influence of the modification of local stiffness due to a material or a geometrical non-linearity on the global behaviour. More elaborate numerical methods were presented and differentiated in two parts, the model coupling and the enrichment methods.

Model coupling methods are based on the consideration that two different types of models are involved in the system, a coarser one and a refined one. Then numerical techniques have been developed to solve such a system. The main arisen problematics are the realisation of the

coupling and the resolution of the system. Some approaches are disclosed in section 2.3.2 such as exact zooming, iterative global-local and superposition techniques. The implementation of those methods is generally delicate due to the limited flexibility of commercial solvers used in the industrial context.

In section 2.3.3, enrichment strategies are described. The possible extension of the non-linear phenomena localisation during the simulation backs the use of such adaptive techniques that may be more efficient. First methods based on the PU are developed. They are mostly relevant for strong discontinuities modelling. As the intended application scope is the continuum damage mechanics, those solutions are not retained.

Finally, the choice for the developed method is to perform an adaptive meshing strategy adapted to damage propagation in composite laminates structures. This would comply to the commercial FE solver constraints by preserving the monolithic resolution of the FE problem which is potentially efficient from a numerical point of view. Some generalities on adaptive meshing are presented in 2.3.3.2. Those cannot be directly applied to the case of composite structures which has specific issues due to its architecture and material behaviour. Consequently, an adaptive multi-model approach suited for damage propagation simulations in large composite structures is developed and detailed in the following chapters.

Conclusion

This first chapter draws the global positioning of this doctorate thesis. It responds to the following problematic:

How to simulate local complex behaviour such as damage for large composite structure applications ?

First, a review of techniques used for the treatment of large problems was presented. Two approaches that can be combined were detailed. The first one relies on parallel resolution strategies. Those are increasingly effective but not yet fully deployed within commercial FE softwares. The second one is the model simplifications that can be made for the structural cases of composite structures. The simplified model are sufficient to describe the elastic part of the global behaviour of a composite structure. When addressing the failure of structures, this level of details becomes insufficient.

When studying in detail the damage phenomena occurring in composite structures, advanced material laws are required. Several research teams have been developing material models to predict the non-linear behaviour of a composite laminate until final failure. Those laws are mature enough to reproduce the behaviour of elementary structures such as open-holes and bolted joints. Nevertheless, the modelling effort in term of dof remains considerable for those laws to be used anywhere on a large structural application. There is thus a strong need to develop a numerical strategy to simulate the effect of a local non-linear phenomena on the global behaviour of a large composite structure.

Several numerical strategies have been presented. The choice of the numerical strategy results in a compromise between among others intrusiveness, robustness, flexibility, and user-friendliness. The chosen method, developed in this manuscript, is an adaptive multi-model strategy which consists in adapting the modelling (FE model, material law) to the need through the structure and the simulation time. This is performed by exploiting adaptive meshing techniques during a numerical resolution.

3 Multidimensional finite element coupling for large composite laminate structures

This chapter presents the setting-up of the studied multi-model reference problem. It consists of an elastic domain with some anelastic inclusions where the model is more refined to capture complex phenomena occurring in composite laminates. In the discretization, the elastic domain is modelled with multilayered shell elements while the anelastic domain is modelled with solid elements with, at least, one element per ply through the thickness. This technique requires to couple two domains with different kinematics.
First, the reference multi-model is introduced. Then, a brief overview of multidimensional coupling conditions is presented. It is decided to select the "shell-to-solid" coupling from Abaqus because of its availability. The validation of this coupling is performed on some relevant test cases, with an increasing complexity.

Contents

2.1 Computation of large slender multilayered structures 8
2.1.1 Numerical strategies for large problem resolution 8
2.1.2 Simplified modeling of slender multilayered structures 11
2.1.3 Conclusion 15
2.2 Predictive material models for composite laminates 16
2.2.1 Introduction on unidirectional composite laminates 17
2.2.2 Modelling of composite laminate's behaviour 18
2.2.3 Finite element resolution using the composite damage laws 24
2.2.4 Conclusion 26
2.3 Elements of bibliography on multiscale finite element strategies for problems with two levels of modelling 27
2.3.1 Engineering methods 27
2.3.2 Model coupling strategies 28
2.3.3 Model improvement/enrichment 35
2.3.4 Conclusion 38

3.1 Introduction

3.1.1 Reference multi-model problem

In this chapter, the resolution of a mechanical multi-model problem, evolving in the time interval $t \in [0, T]$ over a continuous domain Ω, is addressed. This domain is subjected to a volumetric effort density $\boldsymbol{f}_d$. External forces are applied at the boundary $\partial\Omega$ of Ω, by the mean of imposed displacements $\boldsymbol{u}_d$ on $\partial_u\Omega$ and imposed loads such that $\boldsymbol{\sigma}\cdot\boldsymbol{n} = \boldsymbol{F}_d$ on the complementary boundary $\partial_F\Omega = \partial\Omega \setminus \partial_u\Omega$.

The domain is divided in two types of non-overlapping regions $\Omega^{(E)}$ and $\Omega^{(AE)}$ such that $\Omega = \Omega^{(E)} \cup \Omega^{(AE)}$ and $\Omega^{(E)} \cap \Omega^{(AE)} = \{\}$, where $\Omega^{(E)}$ and $\Omega^{(AE)}$ are respectively the regions where an elastic model is sufficient and the regions where the stress levels are such that a more complex anelastic model is required. The interface between $\Omega^{(E)}$ and $\Omega^{(AE)}$ is called Γ. Such mechanical multi-model reference problem is illustrated in Figure 3.1.

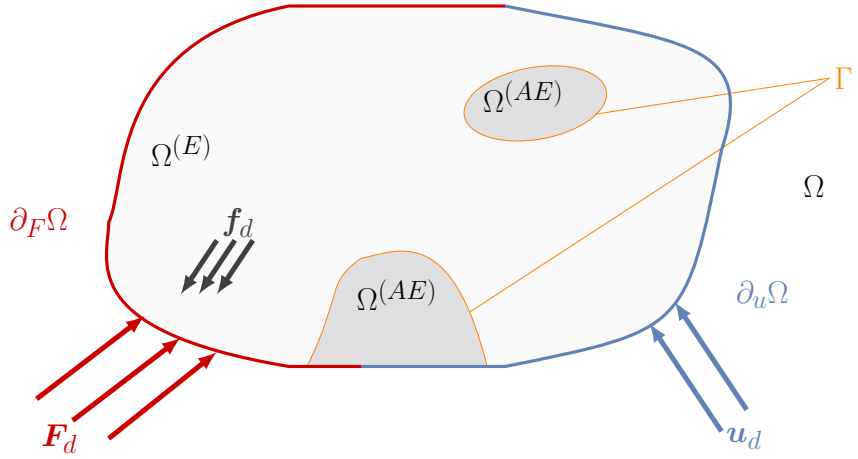

FIGURE 3.1: Multi-model mechanical problem with a decomposition of the domain Ω into two complementary domains $\Omega^{(E)}$ and $\Omega^{(AE)}$.

For the sake of simplicity, the approach is developed under the small deformation hypothesis. The global mechanical state of the system is described by the displacement field $\boldsymbol{u}(M,t)$, the stress field $\boldsymbol{\sigma}(M,t)$, and a set of internal variables $\boldsymbol{\xi}(M,t)$ at each point $M \in \Omega$ for each value t in the studied time interval. The internal variables $\boldsymbol{\xi}(M,t)$ depends on the considered material model. Thus, the mechanical system to be solved is described by:

$$\begin{cases} \boldsymbol{\varepsilon} &= \frac{1}{2}\left(\boldsymbol{\nabla u} + \boldsymbol{\nabla}^T\boldsymbol{u}\right) & \\ \boldsymbol{\sigma} &= \Lambda^{(E)}(\xi^{(E)}, t) : \boldsymbol{\varepsilon} & \text{in } \Omega^{(E)} \\ \boldsymbol{\sigma} &= \tilde{\Lambda}^{(AE)}(\boldsymbol{\sigma}, \boldsymbol{\xi}^{(AE)}, t) : (\boldsymbol{\varepsilon} - \boldsymbol{\varepsilon}^a) & \text{in } \Omega^{(AE)} \end{cases} \tag{3.1}$$

where $\boldsymbol{\varepsilon}$ is the tensor of linearized strain, $\boldsymbol{\varepsilon}^a$ corresponds to a non-linear strain, $\Lambda^{(E)}$ is the elasticity tensor of the elastic material (E), $\tilde{\Lambda}^{(AE)}(\boldsymbol{\sigma}, \boldsymbol{\xi}, t)$ is the effective compliance of the complex behaviour (AE). The law used for the description the (AE) behaviour is OPFM,

detailed in section 2.2.2.6. It is a damage law that renders non-linear aspects of the composite ply behaviour such as longitudinal non-linear elasticity, non-linear visco-elasticity and damage.

A the interface $\Gamma = \partial\Omega^{(E)} \cap \partial\Omega^{(AE)}$, it is necessary to fulfil the equilibrium and compatibility conditions of the problem. Let $\boldsymbol{n}$ denotes a normal to the interface Γ. Using all the prescribed conditions, behaviour relations and balance equations, the global resolution of such a multi-model problem leads to the resolution of the following system of equations:

$$\begin{cases} \boldsymbol{\nabla} \cdot \boldsymbol{\sigma} + \boldsymbol{f}_d = 0 & \text{in } \Omega \\ \boldsymbol{\varepsilon} = \frac{1}{2}\left(\boldsymbol{\nabla}\boldsymbol{u} + \boldsymbol{\nabla}^T\boldsymbol{u}\right) & \text{in } \Omega \\ \boldsymbol{\sigma} = \Lambda^{(E)}(\xi^{(E)}, t) : \boldsymbol{\varepsilon} & \text{in } \Omega^{(E)} \\ \boldsymbol{\sigma} = \tilde{\Lambda}^{(AE)}(\boldsymbol{\sigma}, \boldsymbol{\xi}^{(AE)}, t) : (\boldsymbol{\varepsilon} - \boldsymbol{\varepsilon}^a) & \text{in } \Omega^{(AE)} \\ \boldsymbol{\sigma}^{(AE)} \cdot \boldsymbol{n} = \boldsymbol{\sigma}^{(E)} \cdot \boldsymbol{n} & \text{on } \Gamma \\ [[\boldsymbol{u}]] = \boldsymbol{0} & \text{on } \Gamma \\ \boldsymbol{\sigma} \cdot \boldsymbol{n} = \boldsymbol{F}_d & \text{on } \partial_F\Omega \\ \boldsymbol{u} = \boldsymbol{u}_d & \text{on } \partial_u\Omega \end{cases} \tag{3.2}$$

where $\sigma^{(E)}$ and $\sigma^{(AE)}$ define respectively the stress computed from the behavioural models (E) and (AE) and $[[\boldsymbol{u}]]$ is the displacement jump on Γ defined by $[[\boldsymbol{u}]] = \boldsymbol{u}^{(E)}|_\Gamma - \boldsymbol{u}^{(AE)}|_\Gamma$.

On the $\Omega^{(E)}$ domain an ESLM (see section 2.1.2) is sufficient to describe the elastic behaviour. On the $\Omega^{(AE)}$ domain, as more complex phenomena are rendered, a layer-wise theory is considered.

3.1.2 From continuous to discrete formulation

The continuous mechanical multi-model problem has been exposed in a previous section. This chapter focuses now on the transposition of the continuous problem onto a discrete formulation in order to solve the problem using a numerical FE method. Two main issues of the discretized problem are identified and tackled in the following sections:

- The coupling between two different material models,
- The coupling between elements with two different kinematics.

By placing Γ at a sufficient distance from the anelastic phenomena, it is assumed that the material behaviour is elastic at the boundary of $\Omega^{(AE)}$. By respecting this hypothesis the issue on the material behaviour discrepancy is overcome leaving the problematic on how to couple two discretized spaces with different kinematics. The kinematic discrepancy is treated in the next sections. It should be kept in mind that a coupling has generally to be put away from stress concentration areas.

3.2 Multidimensional coupling

This section aims at providing general strategies when dealing with multidimensional coupling. First, the link between a 2D formulation to a 3D formulation is presented. Then, a brief overview of some coupling possibilities is exposed and our final choice of coupling is justified.

3.2.1 Bridge between 2D and 3D formulations - 3D stress recovery

Several works available in the literature tackle the subject of the ability of a plate/shell model to represent the behaviour of a structure compared to a fully 3D model. This behavioural discrepancy was first computed for the Kirchhoff-Love model in [Koiter, 1970], [Simmonds, 1972] and gave a bound depending on the thickness and a characteristic length of the element. This bound was nevertheless not satisfied in cases involving edge effects. Some approaches to counter those effects have been developed in [Ladevèze and Pécastaings, 1988] for the Reissner-Mindlin theory in order to satisfy this bound. Consequently, the discrepancy in the representation of transverse state by current plate and shell theories is bounded by a threshold depending on the thickness and a characteristic length of the element.

Now, it is interesting to compare 2D and 3D solutions. Some authors studied the error between 2D and 3D solutions and on the 3D stress recovery from a 2D solution. This operation can be performed either *a-priori* with assumptions on the stress model or *a-posteriori* by an integration step of the 3D equilibrium equations in the thickness direction. An assessment of the performances of those estimations is available in [Carrera, 2000].

For instance let's describe the *a-posteriori* stress recovery techniques as detailed in [Kant and Manjunatha, 1994], [Guguin, 2015], [Guguin et al., 2014], [Främby et al., 2016]. The principle is to derive the transverse shear and normal stresses from the equilibrium equations in two steps as follow.

1. Computation of the 2D stresses with a plate/shell theory,

1. Recovering the 3D stresses from the 2D stresses.

Let k be the kth ply of a composite laminate. Then, the elasticity equilibrium equations for this ply are as follow:

$$\frac{\partial \sigma_x}{\partial x} + \frac{\partial \tau_{xy}}{\partial y} + \frac{\partial \tau_{xz}}{\partial z} = 0 \tag{3.3}$$

$$\frac{\partial \tau_{xy}}{\partial x} + \frac{\partial \sigma_y}{\partial y} + \frac{\partial \tau_{yz}}{\partial z} = 0 \tag{3.4}$$

$$\frac{\partial \tau_{xz}}{\partial x} + \frac{\partial \tau_{yz}}{\partial y} + \frac{\partial \sigma_z}{\partial z} = 0 \tag{3.5}$$

The out-of-plane stresses are obtained by integrating the Equations (3.3), (3.4) and (3.5). The integration can be performed by several methods as direct integration or finite difference techniques which are developed in [Kant and Manjunatha, 1994] and detailed hereunder.

Direct integration For the direction integration, first the in-plane stresses are computed based on the constitutive law. Then, the Equations (3.3) and (3.4) allow to retrieve the transverse shear stresses by isolating those terms and integrating along the z coordinate. By deriving the Equation (3.5) and substituting the z derivatives from Equations (3.3) and (3.4), the following second order Equation is obtained.

$$\frac{\partial^2 \sigma_z}{\partial z^2} = \frac{\partial^2 \sigma_x}{\partial x^2} + \frac{\partial^2 \sigma_y}{\partial y^2} + 2\frac{\partial^2 \tau_{xy}}{\partial x \partial y} \tag{3.6}$$

The transverse normal stress σ_z is computed by a double integration of the Equation (3.6). Then, the stress distribution is deduced by a through thickness integration over the laminate with adequate boundary conditions.

The direct integration involves the second order derivative of stresses and thus the third order of displacement derivatives. It implies the use of elements with at least a cubic integration. High order polynomial approximations introduce numerical errors in the computation of out-of-plane stresses. For this reason, direct integration is not usually used. Thus, Finite Difference Methods (FDM) are preferred.

Finite Difference Methods As for the direct integration, the first step of FDM is to compute the in-plane stresses. Then Equations 3.3 and 3.4 are written as follow:

$$\frac{\partial \tau_{xz}\left(GP_i\right)}{\partial z} = -\left[\frac{\sigma_x\left(GP_{i+j}\right) - \sigma_x\left(GP_i\right)}{\Delta X}\right] - \left[\frac{\tau_{xy}\left(GP_{i+l}\right) - \tau_{xy}\left(GP_i\right)}{\Delta Y}\right] \tag{3.7}$$

$$\frac{\partial \tau_{yz}\left(GP_i\right)}{\partial z} = -\left[\frac{\sigma_y\left(GP_{i+j}\right) - \sigma_y\left(GP_i\right)}{\Delta Y}\right] - \left[\frac{\tau_{xy}\left(GP_{i+l}\right) - \tau_{xy}\left(GP_i\right)}{\Delta X}\right] \tag{3.8}$$

where GP_i refers to the current Gauss Point i, GP_{i+j} is the next Gauss point along the x direction and GP_{i+l} is the next Gauss point along the y direction. Then, the Equations (3.7) and (3.8) are integrated according to the z coordinate. The finite difference methods allow to overcome the polynomial order constraints on the displacement approximation.

Conclusion

It is not trivial to recover the accurate 3D stress field from a 2D formulation. Additional stress recovery steps can be performed either *a-posteriori* or *a-priori*. However, the stress recovery can be performed as a preliminary step in a coupling strategy between a 3D domain to a 2D domain as presented in [Guguin, 2015]. Another important application of the 3D stress recovery technique is to be able to check the validity of the shell theory. It can be used for detecting if a threshold value based on the transverse stresses from a material law is exceeded. For instance, a damage can be initiated in the transverse direction in composite laminates and this method would capture it.

3.2.2 Review of multidimensional coupling strategies

In this section, a brief review of multidimensional couplings between shell and solid elements is proposed for composite laminated applications. Several methods exist such as multipoint constraints, Lagrange multiplier methods, penalty methods or transition elements. Some fundamental ideas on coupling constraints are explained in [Felippa, 2004]. Those methods are detailed in this section with the following general notation: the subscript $\cdot_v$ refers to volume domain and $\cdot_s$ to shell or plate domains.

3.2.2.1 Multipoint constraint (MPC)

The principle of multipoint constraints is to build relations between dofs on each side of the coupling interface. Such dofs will be respectively divided into two groups, the master ones and the slave ones. These are linked by the following relation:

$$\boldsymbol{A}_m \boldsymbol{u}_m + \boldsymbol{A}_a \boldsymbol{u}_a = \boldsymbol{g} \tag{3.9}$$

where $\boldsymbol{u}_m$ and $\boldsymbol{u}_a$ are respectively the dofs of the master and the slave surface, $\boldsymbol{A}_m$ and $\boldsymbol{A}_a$ are matrices of transformation, with Ker $(\boldsymbol{A}_a) = \{0\}$, $\boldsymbol{g}$ is a second member vector, the subscripts m and a respectively refer to the master and the slave dofs. The notations of the equations are taken from [Felippa, 2004].

The discrete problem to be solved can be rearranged as:

$$\underbrace{\begin{bmatrix} \boldsymbol{K}_{uu} & \boldsymbol{K}_{um} & \boldsymbol{K}_{ua} \\ \boldsymbol{K}_{um}^T & \boldsymbol{K}_{mm} & \boldsymbol{K}_{ma} \\ \boldsymbol{K}_{ua}^T & \boldsymbol{K}_{ma}^T & \boldsymbol{K}_{aa} \end{bmatrix}}_{\boldsymbol{K}} \begin{bmatrix} \boldsymbol{u}_u \\ \boldsymbol{u}_m \\ \boldsymbol{u}_a \end{bmatrix} = \begin{bmatrix} \boldsymbol{f}_u \\ \boldsymbol{f}_m \\ \boldsymbol{f}_a \end{bmatrix} \tag{3.10}$$

where $\boldsymbol{K}$ is the stiffness matrix, $\boldsymbol{f}$ is the force vector where MPCs are introduced, and the subscripts m, a and u refer respectively to the master, the slave and the remaining unconstrained dof.

The slave dofs are eliminated explicitly leaving modified equations with only the master and the unconstrained dofs. The system becomes:

$$\begin{bmatrix} \boldsymbol{K}_{uu} & \boldsymbol{K}_{um} + \boldsymbol{K}_{ua}\boldsymbol{T} \\ \boldsymbol{K}_{um} + \boldsymbol{K}_{ua}\boldsymbol{T} & \boldsymbol{K}_{mm} + \boldsymbol{T}^T\boldsymbol{K}_{ma}^T + \boldsymbol{K}_{ma}\boldsymbol{T} + \boldsymbol{T}^T\boldsymbol{K}_{aa}\boldsymbol{T} \end{bmatrix} \begin{bmatrix} \boldsymbol{u}_u \\ \boldsymbol{u}_m \end{bmatrix} = \begin{bmatrix} \boldsymbol{f}_u - \boldsymbol{K}_{ua}\boldsymbol{A}_a^{-1}\boldsymbol{g} \\ \boldsymbol{f}_m - \boldsymbol{K}_{ma}\boldsymbol{A}_a^{-1}\boldsymbol{g} \end{bmatrix} \tag{3.11}$$

where $\boldsymbol{T} = -\boldsymbol{A}_a^{-1}\boldsymbol{A}_m$.

It is important to note that the matrix $\boldsymbol{A}_a$'s regularity is mandatory when using an MPC method.

Based on this principle, in [McCune et al., 2000], the authors propose a specific formulation of Equation (3.9) for 3D-2D couplings. The 2D dofs are eliminated and computed based on the 3D dofs. This relation is deduced from an equivalence between the work done by the surface stresses

on both sides of the interface. This method allows to retrieve continuity and accuracy of the stresses at interface even for transverse shear stresses.

The MPC are already available in commercial softwares such as Abaqus where it is referred as MPC "SS" for 3D-2D couplings. The MPC "SS" ensures kinematic constraints based on the following equivalences:

- between the displacement of a shell node and the displacement of a corresponding solid node within a line of through thickness solid nodes,
- between the rotation of a shell node and the rotation of the corresponding line of through thickness nodes.

The displacement constraint is expressed in Equation (3.12).

$$\boldsymbol{u}_j^{(E)} = \sum_{i=1}^{n} w_i \boldsymbol{u}_i^{(AE)} \tag{3.12}$$

where $\boldsymbol{u}_j^{(E)}$ and $\boldsymbol{u}_i^{(AE)}$ are respectively the displacements of the multilayered shell nodes and of the solid nodes, the subscripts i, j refer to the node number, n is the total number of solid nodes that are coupled with the shell node j and w_i are weighting coefficients related both to the polynomial approximation and to the distance between the solid node i and the shell node j. The rotation constraint is formulated such that the shell node undergoes the same rotation as the corresponding line of solid nodes through thickness.

This MPC condition allows to link kinematically a shell node to a corresponding line of solid nodes. This formulation requires a nodal correspondence between the shell and the solid discretization. Hence it requires mesh conformity. Nevertheless, the MPC is a strong coupling and may produce an over-stiff junction.

3.2.2.2 Penalty method

In the penalty method, spurious elastic elements are introduced between some dofs of the system to enforce the coupling. The contribution of those elements is weighted by penalty parameters γ. They are called penalty elements. γ acts as a "rigidity" between the linked dofs. The total potential energy of the system is augmented as expressed in the following equation.

$$\Pi = \Pi_{\Omega_s} + \Pi_{\Omega_v} + \frac{1}{2}\gamma_s \int_{\Gamma} (\boldsymbol{v} - \boldsymbol{u}_s)^2 \, \mathrm{d}\Gamma + \frac{1}{2}\gamma_v \int_{\Gamma} (\boldsymbol{v} - \boldsymbol{u}_v)^2 \, \mathrm{d}\Gamma \tag{3.13}$$

where Π, Π_s and Π_v are respectively the total potential energy, the potential energies of Ω_s and of Ω_v. $\boldsymbol{u}_s$, $\boldsymbol{u}_v$ and $\boldsymbol{v}$ are respectively the displacements on the Γ_s, Γ_v and Γ interfaces. γ_s and γ_v are constants called penalty parameters.

The higher γ, the more enforced is the coupling. But taking a too large value of γ causes numerical issues since the stiffness matrix becomes more and more ill-conditioned. When using penalty methods, careful attention should be paid to the choice of the penalty parameters.

The advantage of this formulation is that the dofs are the same with or without the constraints so that the resolution of the system can be performed all at once. The drawbacks of the method lie on the augmented system of equation which is no longer positive definite and on the choice of the weighting parameters which requires user experience.

3.2.2.3 Lagrange multipliers

The Lagrange multipliers method is mostly used for the application of Dirichlet boundary conditions. But it can also be used for interface coupling as in the mortar method presented in [Belgacem, 1999]. Two surfaces are defined, a master one and a slave one, and the displacement continuity is enforced weakly using Lagrange multipliers. To overcome this hierarchic formulation, hybrid three field approaches were developed as presented hereunder.

The general principle is to enforce a coupling through the application of constraint forces. A vector, noted $\boldsymbol{\lambda} = [\lambda_1, \lambda_2, ...]$ is introduced. Each λ_i is called a Lagrange multiplier and is an additional unknown of the system. The number of these additional unknowns is relative to the number of unknowns on the interface. To compensate the introduction of force unknowns, constraint conditions on dof are applied. In the three field approach, the equilibrium is satisfied when following conditions are met.

$$\begin{cases} \boldsymbol{\lambda}_s & = & \boldsymbol{\sigma} \cdot \boldsymbol{n}_s \\ \boldsymbol{\lambda}_v & = & \boldsymbol{\sigma} \cdot \boldsymbol{n}_v \\ \boldsymbol{\lambda}_s + \boldsymbol{\lambda}_v & = & \boldsymbol{0} \\ \boldsymbol{u}_s & = & \boldsymbol{v} \\ \boldsymbol{u}_v & = & \boldsymbol{v} \end{cases} \tag{3.14}$$

where $\boldsymbol{\lambda}_s$ and $\boldsymbol{\lambda}_v$ are respectively the Lagrange multiplier vectors associated to the s and to the v domains, σ is the stress, $\boldsymbol{n}_s$ and $\boldsymbol{n}_v$ are respectively normal vectors from the surfaces Γ_s and Γ_v, $\boldsymbol{u}_s$, $\boldsymbol{u}_v$ and $\boldsymbol{v}$ are respectively the displacements on the Γ_s, Γ_v and Γ interfaces.

The total potential energy of the system is expressed by the following equation.

$$\Pi = \Pi_{\Omega_s} + \Pi_{\Omega_v} + \int_\Gamma \boldsymbol{\lambda}_s \cdot (\boldsymbol{v} - \boldsymbol{u}_s)\, \mathrm{d}\Gamma + \int_\Gamma \boldsymbol{\lambda}_v \cdot (\boldsymbol{v} - \boldsymbol{u}_v)\, \mathrm{d}\Gamma \tag{3.15}$$

In the discrete resolution, the constraint conditions on dofs are introduced under the form $\boldsymbol{Au} = \boldsymbol{b}$. Then, the augmented system of equations to be solved expressed as follows:

$$\begin{bmatrix} \boldsymbol{K} & \boldsymbol{A}^T \\ \boldsymbol{A} & \boldsymbol{0} \end{bmatrix} \begin{bmatrix} \boldsymbol{u} \\ \boldsymbol{\lambda} \end{bmatrix} = \begin{bmatrix} \boldsymbol{f} \\ \boldsymbol{b} \end{bmatrix} \tag{3.16}$$

The Lagrange multiplier method is a more accessible method for users as it does not require much intervention. This method can also be used in a large variety of cases.

3.2.2.4 The Nitsche method

The Nitsche method was first introduced in the paper [Nitsche, 1971]. It provides a tool to apply Dirichlet conditions without having to use Lagrange multipliers. It has been widely used for imposing of discontinuous displacement conditions in the frame of elliptic and parabolic problems. The Nitsche method is also known as a Discontinuous Galerkin method. Its application to interface problems is more recent. In [Hansbo, 2005], the author compares the application of the Nitsche method to different interface methods such as mesh, polynomial approximation and behaviour discrepancies.

The interface problem is formulated as a variant of the Poisson's equation as in Equation (3.17).

$$\begin{cases} -\triangle \boldsymbol{u} & = \boldsymbol{f} \quad \text{in} \quad \Omega_s \cup \Omega_v, \\ \boldsymbol{u} & = \boldsymbol{0} \quad \text{on} \quad \partial\Omega, \\ [[\boldsymbol{u}]] & = \boldsymbol{0} \quad \text{on} \quad \Gamma, \\ [[\partial_n \boldsymbol{u}]] & = \boldsymbol{0} \quad \text{on} \quad \Gamma. \end{cases} \tag{3.17}$$

where $\triangle$ is the Laplace operator, $[[\cdot]] = \cdot_s - \cdot_v$ is the jump operator, $\partial_n \cdot = \langle \boldsymbol{n}, \bigtriangledown \cdot \rangle$, where $\boldsymbol{n}$ is an outward pointing normal. The Nitsche problem is then formulated weakly as the search of $\boldsymbol{u} = (\boldsymbol{u}_s, \boldsymbol{u}_v) \in V^h = V_s^h \times V_v^h$, with $V_s^h = \{\boldsymbol{v}_s \in H^1(\Omega_s) | \boldsymbol{v}_s$ is a polynom of degree $p | \partial \boldsymbol{v}_s / \partial \boldsymbol{n}_s \in L_2(\Gamma) | \boldsymbol{v}_s |_{\partial\Omega \cap \partial\Omega_s} = 0\}$, and $V_v^h = \{\boldsymbol{v}_v \in H^1(\Omega_v) | \boldsymbol{v}_v$ is a polynom of degree $p | \partial \boldsymbol{v}_v / \partial \boldsymbol{n}_v \in L_2(\Gamma) | \boldsymbol{v}_v |_{\partial\Omega \cap \partial\Omega_v} = 0\}$ such that:

$$\int_\Omega \bigtriangledown \boldsymbol{u} \cdot \bigtriangledown \boldsymbol{v} \mathrm{d}\Omega + \int_\Gamma \alpha \, [[\boldsymbol{u}]] \cdot [[\boldsymbol{v}]] \mathrm{d}\Gamma - \int_\Gamma \partial_n \boldsymbol{u} \cdot [[\boldsymbol{v}]] \mathrm{d}\Gamma - \int_\Gamma \partial_n \boldsymbol{v} \cdot [[\boldsymbol{u}]] \mathrm{d}\Gamma = \int_\Omega \boldsymbol{f} \cdot \boldsymbol{v} \mathrm{d}\Omega \qquad \forall v \in V_h \tag{3.18}$$

where α is a penalty-like stabilization coefficient that can be taken dependent on the mesh size.

The resulting discrete problem is then formulated and solved. The assets of this method are its consistency, stability and convergence capabilities. Furthermore, this method allows to approximate discontinuous fields inside the elements which are crossing the interface Γ. The Nitsche method has also been applied to the case of multidimensional coupling in the frame of isogeometric analyses in [Nguyen et al., 2013]. The authors show the good performances of this method for the linear static case. Those results exhibit that the Nitsche method is a promising technique for interface problem resolutions.

3.2.2.5 Transition element

Another strategy for multidimensional coupling is the development of transition elements. The coupling is not straightforward as there is an incompatibility of the dof between solid and shell/plate elements. On one hand the 3D elements present three dofs of translation at each node and the 2D elements present six dofs (three of translation and three of rotation at each node). In [Surana, 1980], the author develops a formulation such that on one face, the dofs are the same as in a 3D element and on the opposite face, the dofs are the same as in a 2D element. An illustration of this principle of transition element is presented in Figure 3.2.

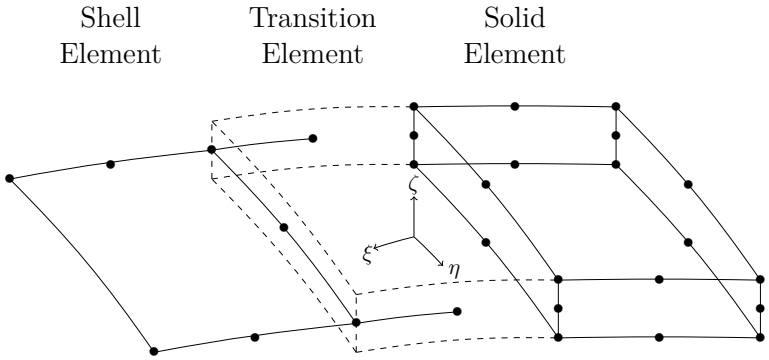

FIGURE 3.2: Illustration of a transition solid-shell element (with 13 nodes in this case).

The displacement field results from the adjunction of the solid-type and shell-type nodal contributions as follow:

$$\begin{Bmatrix} u_x \\ u_y \\ u_z \end{Bmatrix} = \underbrace{\sum_{i=1}^{i=m} N_v^i(\xi,\eta,\zeta) \begin{Bmatrix} u_x^i \\ u_y^i \\ u_z^i \end{Bmatrix}}_{\text{contribution of "volume" nodes}} + \underbrace{\sum_{i=m+1}^{i=n} N_s^i(\xi,\eta) \left(\begin{Bmatrix} u_x^i \\ u_y^i \\ u_z^i \end{Bmatrix} + \frac{\zeta}{2} t_i \left[-\theta_x^i \boldsymbol{v}_2 + \theta_y^i \boldsymbol{v}_1 \right] \right)}_{\text{contribution of "shell" nodes}} \tag{3.19}$$

where u_x, u_y, u_z correspond to the nodal components of the displacement field, $i \in [1, m]$ refers to the nodes of the transition element on the face $\xi = -1$, $i \in [m+1, n]$ to all the remaining nodes of the transition element, N_v and N_s are respectively the shape functions of the solid and the shell formulations, (ξ, η, ζ) are the local coordinates of the iso-parametric element, t is the nodal thickness, θ_x and θ_y are the rotation angles of the normal vector at the considered node along respectively the directions $\boldsymbol{v}_2$ and $\boldsymbol{v}_1$.

For the computation of the stresses and strains, several strategies are possible. The stress-strain relation can be of solid-type, shell-type, or a mixed approach. The choice stress-strain relation relies on the most relevant hypothesis for the considered test case. For the mixed approach case, a simple technique is to divide the integration points into two categories: those closer to the 3D formulation and those closer to the 2D formulation. Then, the strategy for the integration of the stiffness matrix is differentiated per region. The stiffness of the transition element is obtained by the following equation.

$$\boldsymbol{K} = \int_V \boldsymbol{B}^T \boldsymbol{D} \boldsymbol{B} \mathrm{d}V \tag{3.20}$$

where $\boldsymbol{K}$ is the element stiffness matrix, $\boldsymbol{B}$ is the strain-displacement matrix which contains both the components related either to solid type or shell type nodes and $\boldsymbol{D}$ is the elasticity matrix.

This formulation of transition element has been extended to non-linear geometric analysis in [Surana, 1982]. In [Liao et al., 1988], the authors expand the method to anisotropic laminate shell elements in the frame of non-linear geometrical analysis. The principle for the construction of the transition element remains the same. The nodes on the face connected to laminated solid elements have 3D interpolation functions. The other nodes have a laminated shell elements alike

interpolation functions. The displacement field in the transition element results of the addition of those contributions. Then, the integration of the stiffness matrix, corresponds to the sum of the contributions of each layer and is calculated as follow.

$$\boldsymbol{K} = \sum_{k=1}^{k=p} \int_{V_k} \boldsymbol{B}^T \boldsymbol{D}_k \boldsymbol{B} \mathrm{d}V_k \tag{3.21}$$

where the subscript k refers to the kth layer of the laminate and p to the total number of plies in the laminate. The case of laminates is treated here as if there were several layers of shell elements superposed. Currently, the use of homogenized multilayered shell elements is more popular and this method is not relevant in that case. Multilayered shell theories are detailed in section 2.1.2.2.

In [Dávila, 1994], the author tackles the case of laminated structures with homogenized shell elements coupled to several layers of solid elements as illustrated in Figure 3.3. The principle is to derive the transition elements from the solid formulation with a kinematic constraint on one face. Imposing this constraint on one face implies that all the nodes of the face except the shell ones are slave to the displacements of the shell nodes. The author proposes to apply two different kinematics, one based on Reissner-Mindlin's theory because of its simplicity of use and its good representation of the interlaminar stresses and one based on higher-order theories to allow out-of-plane elongation.

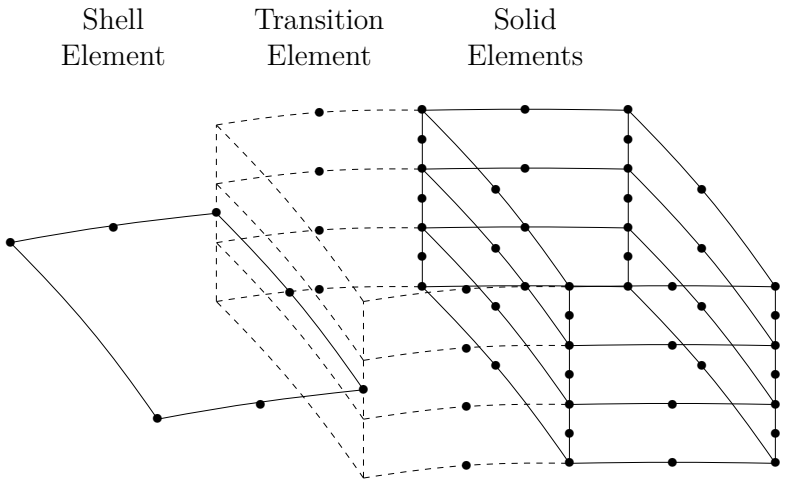

FIGURE 3.3: Illustration of a transition solid-multilayered shell element.

The assumption of the Reissner-Mindlin kinematic formulation is that the through thickness material lines remain rigid but can undergo rotation. This can be translated by the following constraint on the displacement field based on the shell mid-plane displacement vector.

$$\begin{cases} u_x(x,y,z) = u_x^0(x,y) + z\theta_y(x,y) \\ u_y(x,y,z) = u_y^0(x,y) - z\theta_x(x,y) \\ u_z(x,y,z) = u_z^0(x,y) \end{cases} \tag{3.22}$$

In higher order theories the out-of-plane displacement is not constant through thickness. The theory used in [Dávila, 1994] provides a displacement of the following form.

$$\begin{cases} u_x(x,y,z) = u_x^0(x,y) + z\theta_y(x,y) \\ u_y(x,y,z) = u_y^0(x,y) - z\theta_x(x,y) \\ u_z(x,y,z) = u_z^0(x,y) + zw_1 + z^2 w_2 \end{cases} \tag{3.23}$$

Those formulations are extended to geometrical non-linear analysis in the same paper [Dávila, 1994] with an incremental formulation of the displacement field. For the cases involving a corner, the kinematics can be applied on several faces of the transition element.

Transition elements show good accuracy and efficiency. The application of Reissner-Mindlin kinematic yields to a larger error for out-of-plane stresses estimation near the face of application of the constraint whereas the higher order theory is more accurate even in the transition region. The author highlights that the higher-order theory is more complex to enforce even if it provides more precise results. The Reissner-Mindlin kinematic gives also accurate stress state results sufficiently far from the coupling (beyond the transition elements).

A drawback of the transition elements is that it requires nodal correspondence between the solid and the shell parts of the structure which is not always practical. Each node of the constrained face of the transition element should have its corresponding master shell node that is usually at the mid-plane location. The displacement of the transition element node (on the constrained face) is then deduced from the shell one. Hence, transition elements does not handle mesh non-conformity, whereas other methods such as the Nitsche method presented before are able to handle such non-conform meshes.

3.2.3 Conclusion

Several strategies can be explored when addressing the multidimensional coupling between solid and shell/plate elements.

First, the multipoint constraints present the advantage of being already available in commercial FE softwares. Nevertheless, the resulting coupling can be too stiff and precautions have to be taken to minimize errors.

Other methods have been developed allowing to enforce the multidimensional coupling weakly such as the penalty method, Lagrange multipliers and the Nitsche method. Those methods present good accuracy with different levels of user experience requirement.

Another possible weak approach for multidimensional coupling is the use of transition elements which guarantees a kinematic consistency at interface. This method imposes a nodal conformity of the meshes at the interface. Consequently, its direct use has limited flexibility on element size discrepancy between the different domains. Finally, this technique requires the development of a user element that should be as general as possible. The development of a user element presents difficulties regarding its implementation within commercial finite element softwares, such as Abaqus and Z-set, and in presence of an user material.

In this work, the objective is to use the available coupling conditions in the commercial software Abaqus and build a relevant mesh especially at the interface to reduce errors. Two coupling conditions are available. The first one is based on the multipoint constraint formulation. The second one is based on the use of Lagrange multipliers to enforce weakly a load equivalence in a mean sense. To limit stress concentrations, a supplementary kinematic constraint, such as for transition elements, is applied at the interface.

The building of the mesh is performed with the Z-set software which contains a powerful mesher. The following section 3.3 focuses on the discrete implementation of the reference multi-model problem and the practical building of the discrete model.

3.3 Discrete multi-model problem

The continuous reference multi-model problem was introduced in section 3.1.1. Then a trade-off of possible multidimensional couplings between solid and laminated shell elements is presented in the section 3.2.2. The retained strategy is to use the couplings available in the commercial software Abaqus. Two different types of couplings are available, one based on MPC and one on Lagrange multipliers. They are presented in more details in section 3.3.1. This section focuses on the development of the discrete multi-model problem.

The semi-discretization in time is performed through a temporal integration scheme than can be solved by either an implicit or an explicit solver. The method being independent from this aspect, the time-line decomposition is supposed to be in a sequence $0 \leq t_n \leq t_{tot}$ linked to the specificities of the chosen resolution method, whilst complying with the chosen behaviour laws and with the convergence criteria of a non-linear implicit solver. Here the used material law (see section 2.2.2.6) complies with both an implicit or an explicit scheme.

For the semi-discretisation in space, the multi-model approach includes the discrete spaces $T^{(E)}$ and $T^{(AE)}$ corresponding respectively to the domains $\Omega^{(E)}$ and $\Omega^{(AE)}$ in the reference problem presented in section 3.1.1. For the domain $T^{(E)}$, multilayered shell finite elements [Chapelle and Bathe, 2011] are used to model an elastic evolution with bending and eventually buckling under complex loadings. For the domain $T^{(AE)}$, solid elements are used to provide a more accurate formulation in the representation of interlaminar stresses that are at the origin of delamination for instance. A coupling condition is implemented at the interface G corresponding to Γ in the reference problem as illustrated in Figure 3.4.

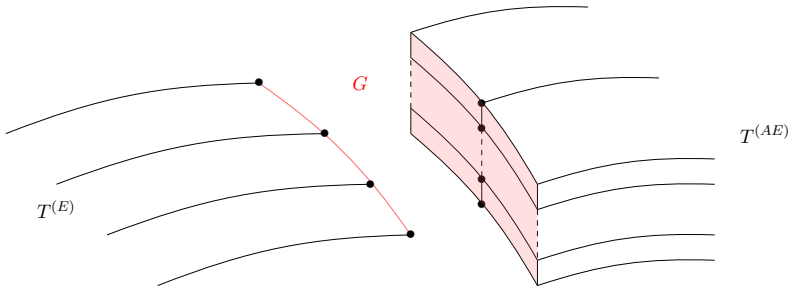

FIGURE 3.4: Interface coupling G between the $T^{(E)}$ and the $T^{(AE)}$ domains.

3.3.1 Multidimensional coupling condition

The pragmatic choice made in this work is to impose a coupling condition already available in the commercial software Abaqus. The practical implementation uncouples the kinematic or load "equivalence" between the shell and the solid interfaces from the constraint of a shell kinematic at the solid interface, $G \cap T^{(AE)}$. Two different types of coupling conditions are available for multidimensional coupling in the commercial software Abaqus. The first one is an MPC referred as "MPC SS" detailed in a previous section. The second one, called "shell-to-solid coupling", is based on the enforcement of a load equivalence between the shell and the solid interfaces through Lagrange multipliers which are both are hereafter. The "shell-to-solid coupling" are

chosen because they make it possible to manage incompatible meshes. Then, the enforcement of a shell kinematic on the solid interface is presented.

"Shell-to-solid coupling" Contrary to the MPC, this constraint is surface-based. The principle is to couple a reference shell node to a set of solid nodes called "coupling nodes" in an average sense by the following approach.

The resultant of forces at the reference node is taken equal to the resultant of forces of all the weighted contributions of the coupling nodes. The load and moment distribution hence satisfies the following equation.

$$\left\{ \begin{array}{lcl} \sum\limits_i \boldsymbol{F}_i^{(AE)} & = & \boldsymbol{F}^{(E)}, \\ \sum\limits_i \boldsymbol{x}_i^{(AE)} \boldsymbol{F}_i^{(AE)} & = & \boldsymbol{M}^{(E)} + \boldsymbol{x}^{(E)} \boldsymbol{F}^{(E)}. \end{array} \right. \tag{3.24}$$

where $\boldsymbol{x}^{(E)}$ and $\boldsymbol{x}_i^{(AE)}$ are respectively the positions of the reference node and the coupling node i, $\boldsymbol{F}^{(E)}$ and $\boldsymbol{M}^{(E)}$ are respectively, the load and the moment applied to the reference node and $\boldsymbol{F}_i^{(AE)}$ is the load applied to the coupling node i. The choice of the $\boldsymbol{F}_i^{(AE)}$ distribution among the coupling nodes is not unique. Consequently a formulation of $\boldsymbol{F}_i^{(AE)}$ is chosen in Abaqus that results in the following constraint on nodal displacement and rotation.

$$\left\{ \begin{array}{lcl} \delta\boldsymbol{x}^{(E)} & = & \sum\limits_i w_i \delta\boldsymbol{x}_i^{(AE)} + \left(T^{-1} \cdot \sum\limits_i w_i \left(\boldsymbol{r}_i^{(AE)} \times \delta\boldsymbol{x}_i^{(AE)} \right) \right) \times \boldsymbol{r}^{(E)}, \\ \delta\boldsymbol{w}^{(E)} & = & T^{-1} \cdot \sum\limits_i w_i \left(\boldsymbol{r}_i^{(AE)} \times \delta\boldsymbol{x}_i^{(AE)} \right). \end{array} \right. \tag{3.25}$$

where T is an "inertia" tensor, $\boldsymbol{r}^{(E)} = \boldsymbol{x}^{(E)} - \sum\limits_i w_i \boldsymbol{x}_i^{(AE)}$, $\boldsymbol{r}_i^{(AE)} = \boldsymbol{x}_i^{(AE)} - \sum\limits_i w_i \boldsymbol{x}_i^{(AE)}$ and w_i are weighting coefficients. Several weighting methods can be used to determine the w_i coefficients. The weighting distribution can be chosen to follow a linear, quadratic or monotonically decreasing law according to the radius between the solid node and the shell reference node.

Then, the weak formulation of the problem is augmented with this constraint (Equation (3.25)) contribution by the mean of Lagrange multipliers. More details can be found in section 3.2.2.3.

Additional kinematic constraint The above mentioned condition does not ensure kinematic compatibility at interface (the shell and the solid kinematics are different). Furthermore, it is advised in Abaqus's manual to place the coupling in an area where the shell kinematic is a valid assumption and to add a kinematic constraint at the solid interface, $G \cap T^{(AE)}$. The Reissner-Mindlin kinematic is applied due to its representation capability of transverse shear stresses. Hence, the nodes of this face respect thus the Equation (3.22). It means that the solid nodes on the interface evolve only on the same material line through the thickness. This is performed by a MPC called SLIDER in Abaqus. Then the displacement of all the solid nodes on a material line are determined by the displacement of only one solid node.

Conclusion The retained condition is the "shell-to-solid coupling" used in conjunction with a shell kinematic constraint on the solid interface the using MPC "SLIDER". This choice of

coupling condition is a pragmatic decision. It presents the advantage of being easily used in conjunction with the industrial models and being already implemented in the commercial FE software Abaqus. Moreover, it presents the advantage, as it is surface-based, of loosening the constraint on mesh conformity.

Nevertheless, it shows some limitations and loss of accuracy when mesh conformity is not satisfied at the junction and when the interface is not sufficiently "smooth". Edgy corners tend to over-constrain the $G \cap T^{(AE)}$ interface. For this reason, the retained coupling condition is used jointly with a remeshing strategy to build a "smooth" interface when defining the spatial distribution of the domains $T^{(E)}$ and $T^{(AE)}$. This remeshing strategy is developed in the following section.

3.3.2 "Smart" local remeshing strategy

The building of a multidimensional coupling may induce stress concentrations and inaccuracy at the vicinity of the coupling. In the considered problem the area modelled with solid elements $T^{(AE)}$ presents also an anelastic law. To prevent the apparition of parasite anelastic behaviour near the coupling due to stress concentrations, an elastic behaviour is imposed to a layer of solid elements near the coupling.

As presented in the introductory part of this manuscript, the remeshing of the multi-model problem is performed with the commercial software Z-set. This software has rich and flexible remeshing capabilities using the mesher yams distributed by Distene. The details of the remeshing strategy are disclosed in section 3.3.2.1. Then, the building of a regular interface G from a geometric point of view, is discussed in section 3.3.2.2.

3.3.2.1 Remeshing strategy

The remeshing strategy focuses on the local construction of a 3D refined mesh consistent with the laminate architecture from an initial full shell model. Several aspects are accounted for to provide the best mesh such as nodal conformity at interface when it is possible and through thickness of the volume part. Those aspects are detailed hereunder.

When it is possible, the remeshing stages allow to maintain the nodal conformity at interface. The objective is to match each shell node at interface with a line of solid nodes. This allows to limit the inaccuracy induced in the displacement field by the weighting factors presented in section 3.3.1 by avoiding the interpolation of the displacement field in the reference plane. This conformity imposes the mesh size of shell elements to the solid elements at the interface. Nevertheless, a smaller mesh size is required in the solid $T^{(AE)}$ domain. Consequently, an element size decay law is implemented through the domain $T^{(AE)}$ to obtain the wanted element size in the area of interest.

The remeshing strategy also produces a conform mesh in the volume area through thickness. This allows to avoid the use of additional coupling conditions between the solid layers of the composite laminate. This also simplifies the future introduction of cohesive zone models between the different layers of the laminate if needed.

To comply with the two previous developed points, the remeshing is performed in three steps which are illustrated in Figure 3.5:

1. Determination of the areas to mesh, coloured in red in Figure 3.5, based on a 2D initial model as a subset of elements. The determination of the areas to be meshed is developed in the next chapter.
2. Remeshing in 2D respecting the frontier of the elements determined in step [1.] to have a nodal conformity over G.
3. Extrusion of the 2D mesh to a 3D stacked mesh complying with the number of layers of the composite laminate in this area.

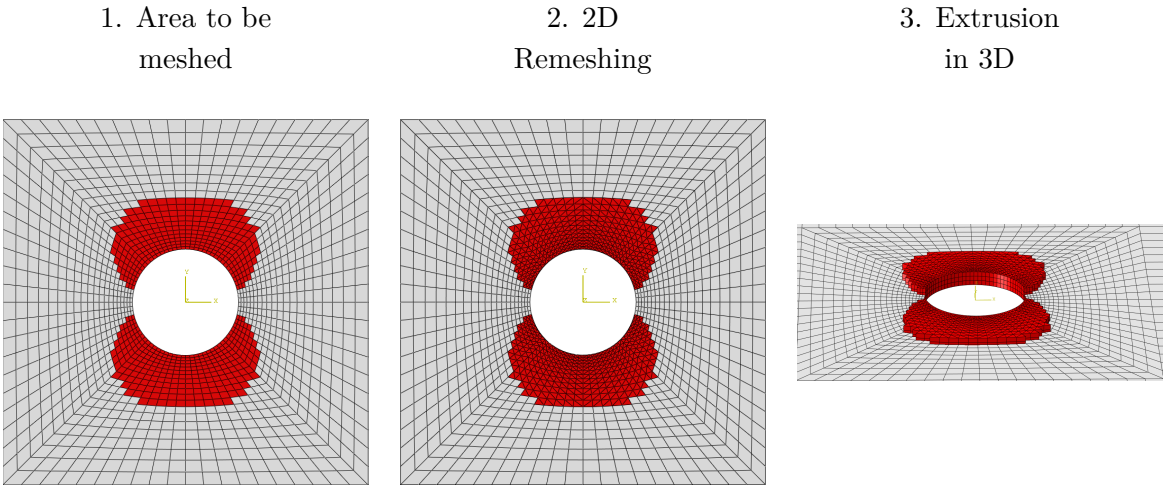

FIGURE 3.5: Remeshing strategy to create a 3D stacked volume mesh from a 2D initial geometry.

It is also important to note that the remeshing strategy gives the possibility of imposing an adequate mesh size in the remeshed area.

This section focused on the generic remeshing strategy. It is here illustrated for the case of remeshing with extruded triangles (called wedge elements in Abaqus). It has been extended to extruded quadrangles. In this latter case, the used mesher does not guarantee nodal conformity at interface. In this manuscript, extruded triangles are used in most of the tested cases.

An issue of this method is the construction of the frontier between the two domains. It results from the edges of the selected initial elements which provides an irregular frontier. The consequence of this choice and an answer to this issue is proposed in the following section.

3.3.2.2 Building a smoother frontier

The chosen constraint tends to produce stress concentrations in presence on edgy corners. This is illustrated here by the following example. Let's consider a laminate with ta stacking sequence [0°,45 °,90 °], with the dimensions $l = L = 2$mm, $h = 0.05$mm $\times 3$ and with the following material properties: $E_1 = 160$GPa, $E_2 = E_3 = 9$GPa, $G_{12} = G_{13} = 5$GPa, $G_{23} = 2$GPa, $\nu_{12} = \nu_{13} = 0.32$ and $\nu_{23} = 0.4$. This composite coupon is subjected to an imposed displacement at one side and

is clamped at the other side. Three different models are compared, one with a full volume model (Figure 3.6(A)), one with a flat junction between the shell and solid zones (Figure 3.6(B)) and one with an edgy junction of 90°angle between the shell and solid zones (Figure 3.6(C)).

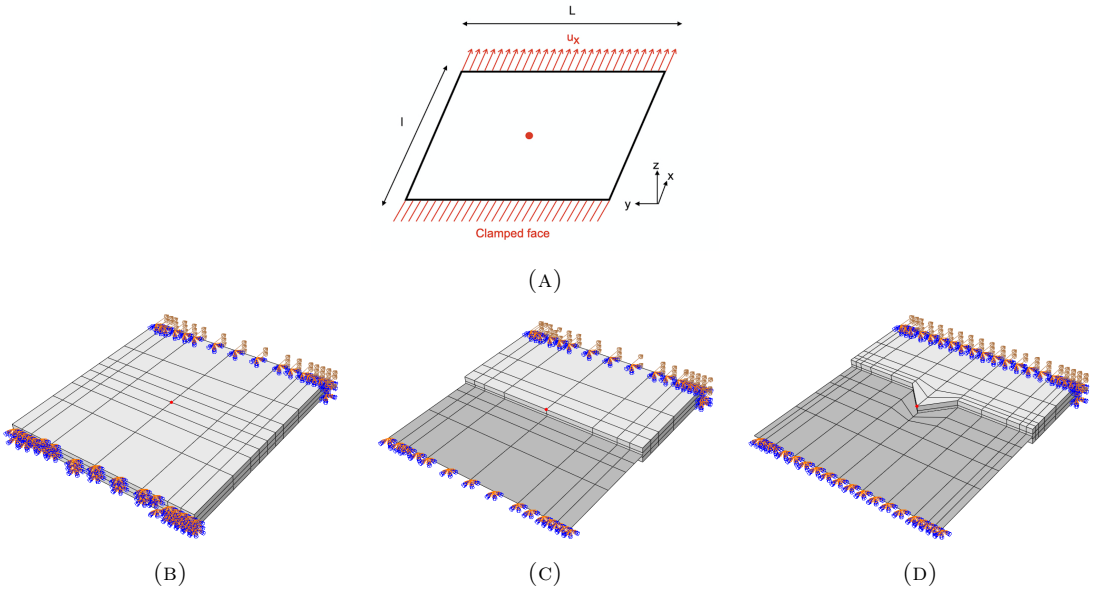

(A) (B) (C) (D)

FIGURE 3.6: (A) Reference test case; FE model: (B) Volume reference mesh; (C) Flat coupling; (D) Edgy coupling.

The values of stress components were evaluated at the central point of the coupon, represented in red in Figure 3.6. The results are reported in Figure 3.7 where u_x is the imposed displacement, in the x direction, on one end of the plate, more precisely on the volume part.

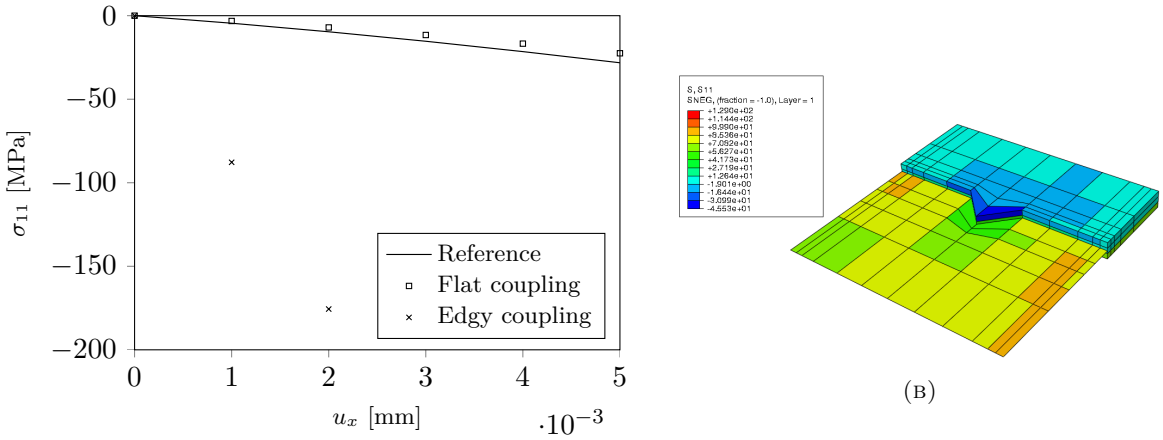

(A) (B)

FIGURE 3.7: (A) σ_{11} stress field at the center point on the top surface of the composite laminate coupon; (B)σ_{11} stress field plot over the plate.

The Figure 3.7 shows that edgy corners produce stress concentration compared to a flat coupling. This tendency is illustrated here with the σ_{11} component, although the same trend is observed for all stress components in this developed case. This phenomenon is particularly visible in this

case because of its severity due to the high anisotropy and the non-symmetrical stacking sequence of the considered laminate.

Being non-physical, such stress concentrations must be avoided especially when using non-linear material laws with stress based criteria as OPFM (see section 2.2.2.6). To address this issue, a smoothing strategy of the 2D/3D frontier was developed to obtain a sufficiently regular interface. Additional steps are added into the remeshing strategy as illustrated in Figure 3.8.

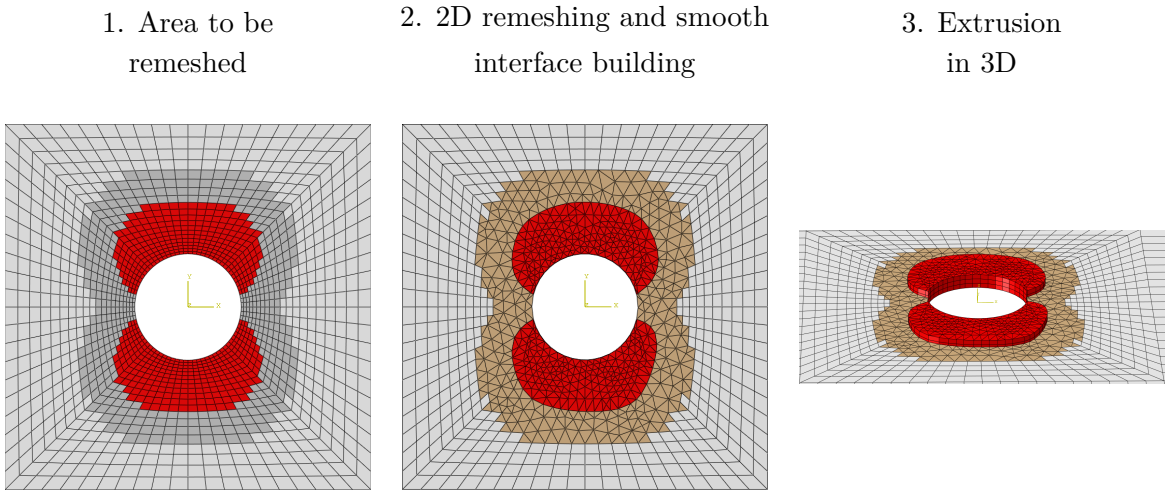

FIGURE 3.8: Remeshing strategy to create a 3D stacked volume mesh from a 2D initial geometry.

From the initial area to be remeshed in red, a larger area (in dark grey) is extracted. Within this area a regular spline is constructed near the frontier of the elements in red. Then, a 2D remeshing is performed respecting this spline. This technique is easier to perform with triangular elements. Then the mesh is extruded in 3D respecting the architecture of the composite laminate. It can be noted that there might be remaining edgy frontiers, especially at the model boundaries. Nonetheless, those edgy frontiers are fewer compared to the original strategy.

3.3.3 Conclusion

This section addressed the setting-up of the discrete multi-model problem. First, the multidimensional coupling choice is presented which is the "shell-to-solid" coupling from the Abaqus software. Then, a limitation of this coupling has been pointed up. It produces stress-concentration at edgy corners. Therefore, the use of this coupling requires thus a smooth frontier.

The main lever of action in this work is the generation of the mesh. This is performed with available remeshing modules of the Z-set software which is an in-house code. A remeshing strategy in three steps is chosen. First, the area to be meshed is defined. The strategy for determining the area to be meshed is developed in a further chapter. Then, a 2D remeshing is performed respecting a mesh size evolution law. Finally, the 2D area is extruded in 3D respecting the number of laminate layers and their thicknesses. An additional smoothing strategy is developed to enhance the regularity of the frontier between the shell and the solid areas.

3.4 Application cases

Three application cases are selected in this section to assess the performance of the chosen shell/solid coupling condition for different phenomena of interest as detailed hereunder.

- The first test case, developed in section 3.4.1 corresponds to the analysis of the buckling response of a simple elastic composite laminate plate. This test case is chosen because buckling is a typical phenomenon that contributes to the ruin of composite laminated structures, hence it is important to predict it accurately.
- The influence of the coupling on the out-of-plane stress state is evaluated in the second test case in section 3.4.2. This is achieved by the comparison of the transverse stress state to analytic solutions for the case of an elastic plate in tension. The transverse stress state is important as it can initiate and propagate out-of-plane damage in composite laminated structures.
- The last test case, developed in section 3.4.3, aims at evaluating the influence of the coupling in presence of an anelastic behaviour. This chosen test case is more complex. The global response and the damage propagation in a holed plate subjected to a compressive-bending loading is simulated with a comparison to experimental results. The main objective of the coupling is to manage the cases of anelastic inclusions into a global elastic domain as explained in section 3.1.1 for composite laminates. This point is assessed in this last test case.

3.4.1 Influence of the coupling on the buckling behaviour

3.4.1.1 Buckling analysis of a simply supported composite laminate plate

First, let's investigate the ability of the solid/shell coupling to represent the buckling behaviour of a composite structure. This loading was chosen because buckling is one of the most critical case for slender structures. A simple case is chosen to be able to compare the numerical FE results with analytic ones. The first two buckling modes of a simply supported composite laminated plate [90°/0°/0°/90°] subjected to an uni-axial compressive loading are estimated. The plate is square shaped with a length and width of dimension a and with a thickness $h \times 4$ plies. The analysis is performed under the elasticity hypothesis.

The analytical buckling analysis of the plate is performed in several steps. First, the unidirectional ply stiffness matrix is estimated. Then, the classical laminate theory is used to determine the extensional stiffness A, the tension/torsion coupling stiffness B, and the bending stiffness D of the laminate which depend on the stacking sequence. The different material coefficients and structural parameters of the considered laminate are provided in Table 3.1.

Finally, the buckling equation of a simply supported plate under uni-axial compression is used to determine the buckling loads and modes. The analytical resolution is presented in more details in the Chapter 23 of [Berthelot, 2010]. The critical loads for the considered case is given by the

Stacking	[90°/0°/0°/90°]
h [mm]	0.25
a [mm]	200
E_1 [MPa]	115000
E_2 [MPa]	8300
G_{12} [MPa]	4500
ν_{12} [-]	0.31
ν_{21} [-]	0.02
D_{11} [MPa mm^3]	1816
D_{12} [MPa mm^3]	215.9
D_{22} [MPa mm^3]	8531
D_{66} [MPa mm^3]	375

TABLE 3.1: Material and geometrical data of a composite laminated plate.

following equation:

$$N(m) = \frac{\pi^2}{m^2 a^2}\left[m^4 D_{11} + 2m^2\left(D_{12} + 2D_{66}\right) + D_{22}\right] \tag{3.26}$$

where N, the buckling load, is a function of the coefficient m which is an integer depending on the buckling mode. The mode shape is then given by the following equation.

$$w\left(x, y\right) = A_{m1} \sin\left(m\pi\frac{x}{a}\right) \sin\left(\pi\frac{y}{a}\right) \tag{3.27}$$

where w is the deflection of the plate and A_{m1} is its magnitude.

The analytic results are compared with numerical analyses involving the chosen coupling, detailed in section 3.3.1. Several finite element models were built on the same principle than that represented in Figure 3.9. A solid ply per-ply inclusion delimited by a black line is coupled to a multilayered shell area. In Figure 3.9, the dark grey zone represents the solid ply-per-ply part and the light gray zone represents the shell part. A linear perturbation step was performed with the Abaqus software to retrieve the first two buckling modes.

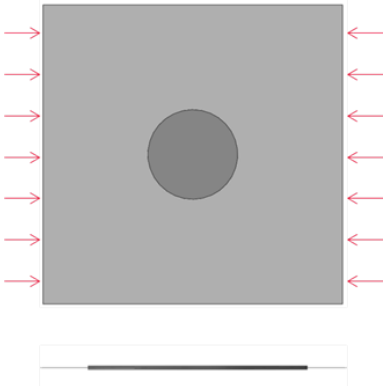

FIGURE 3.9: Finite element model of a simply supported buckling composite plate subjected to an uni-axial loading.

3.4.1.2 Analytical and numerical results

Mode shapes The analytical and FE mode shapes for the model noted FEM1 (Figure3.9) are presented in Table 3.10 for the first two buckling modes.

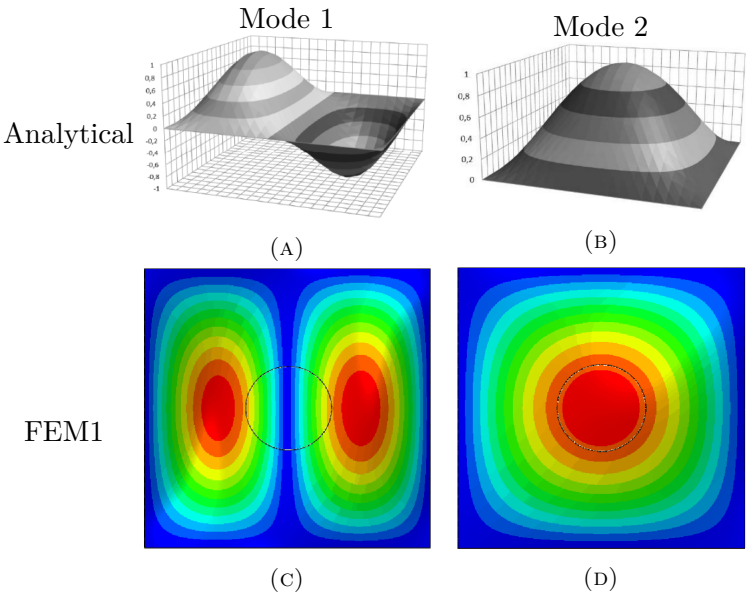

FIGURE 3.10: First two buckling modes of a composite simply supported plate.

Several FE models were tested to evaluate if the result is sensitive to the change in position, shape and proportion of the solid ply-per-ply inclusion. Those different FE models are listed as FEMi for i$\in$ [1; 8]. The results of the first mode shape for those different FE models are plotted in Figure 3.11. In each case, the black line represents the frontier between the solid ply-per-ply mesh and the multilayered shell mesh.

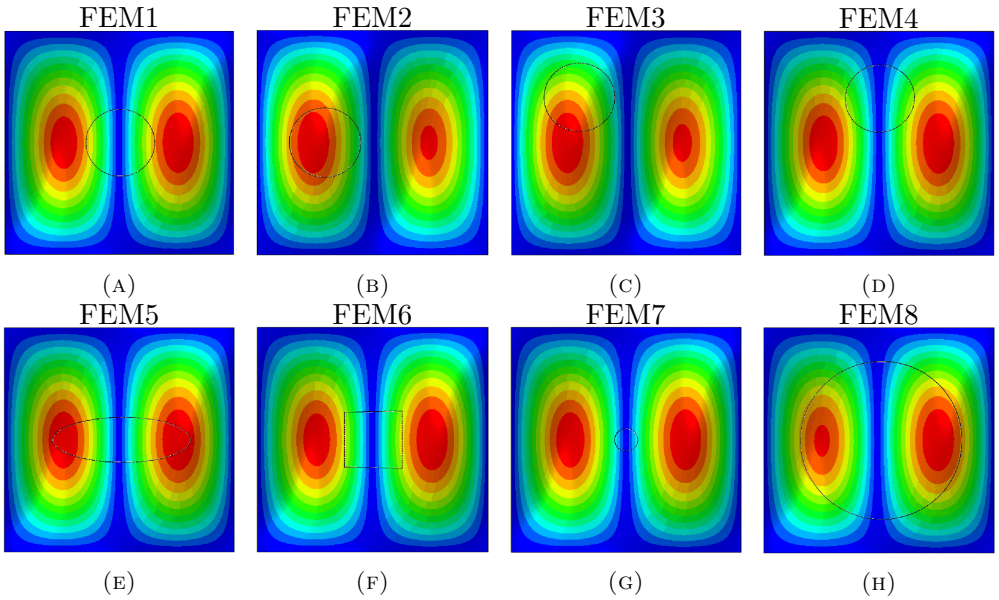

FIGURE 3.11: First buckling mode of a composite simply supported plate.

Critical loads The critical loads and the errors of the numerical simulations relative to the analytical loads ($Error = (N_{FEMi} - N_{Analytic})\backslash N_{Analytic}$) are presented in Table 3.2.

Model	N^1[N]	Error^1 [%]	N^2[N]	Error^2 [%]
Analytical	559.04	-	605.93	-
FEM1	556.99	0.37	599.08	1.13
FEM2	557.27	0.32	601.04	0.81
FEM3	556.99	0.37	601.69	0.70
FEM4	556.92	0.38	600.36	0.92
FEM5	558.90	0.03	594.82	1.83
FEM6	556.90	0.38	600.94	0.82
FEM7	557.57	0.26	600.62	0.88
FEM8	542.91	2.88	576.58	4.84

TABLE 3.2: Critical loads results where the superscript 1 and 2 refer respectively to the 1st and 2nd modes.

3.4.1.3 Discussion

The mode shape results give a quantitative overview of the capabilities of the FEM model to render the buckling behaviour. Figures 3.10 and 3.11 point out that the modal FE shapes are roughly the same than the analytical ones. Nevertheless, in some results such as Figures 3.11 (B), 3.11 (C) and 3.11 (H), there is a loss of the anti-symmetrical pattern of the first buckling mode shape. For the Figures 3.11 (B) and 3.11 (C), it may be explained by the loss of geometrical symmetry and by the closeness of the inclusion to the boundary of the model. Also, when the volume part becomes very significant compared to the global model, the interface draws nearer to the edge and it affects the mode shape. Only the first buckling modes are illustrated in Figure 3.11 but the shape of the second buckling mode is also roughly the same as the analytical ones for all FE models. To conclude, the mode shape FE results are not very sensitive to the position, shape and size of the volume part.

Regarding the critical loads, the errors of the FE results compared to the analytic ones are below 5 % for the first two modes. When removing the model FEM8 which presents the largest volume area, the errors are below 2%. Some trends are nevertheless observed. The changes of the position and shape of the volume part do not really affect the error on the computation of the buckling loads which remain generally small. Regarding the change in size, a clear trend is observed. The smaller the volume part, the smaller is the error. This can be explained by the fact that the analytical results are based on a shell theory. Hence, the smaller the volume regions, the more fitted the FE model is to the analytical one.

To conclude, the results of the different cases are close to the analytic results in terms of buckling shape and load given that the volume inclusion is in a restricted area. If the need for a volume part spreads all over the structure, the use of a coupling would lose interest in any case. This allows us to validate the retained coupling for buckling in linear elasticity.

3.4.2 Influence of the coupling on the out-of-plane stress state

3.4.2.1 Analysis of a composite laminated plate in tension

The objective of this test case is to estimate the influence of the coupling on the out-of-plane stress state in the volume part. Let's consider a four ply symmetrical laminated $[0/90]_s$ plate in tension. This well-known problem presents the particularity of producing an out-of-plane stress state at the boundary edge due to the mismatch in material properties between layers. This problem was solved analytically in [Pagano, 1978] and used as a the reference for validating a transition element formulation developed in [Dávila, 1994] and presented in section 3.2.2.5.

The problem is illustrated in Figure 3.12 (A), h being the ply thickness, $2d$ the width of the plate, L the length of the plate and ε_x the uniform in plane deformation applied to the extremities of the plate. The ply material properties are defined as such: $E_{11} = 20.00 \times 10^6$ psi, $E_{22} = E_{33} = 2.10 \times 10^6$ psi, $G_{12} = G_{13} = G_{23} = 0.85 \times 10^6$ psi, $\nu_{12} = \nu_{13} = \nu_{23} = 0.21$.

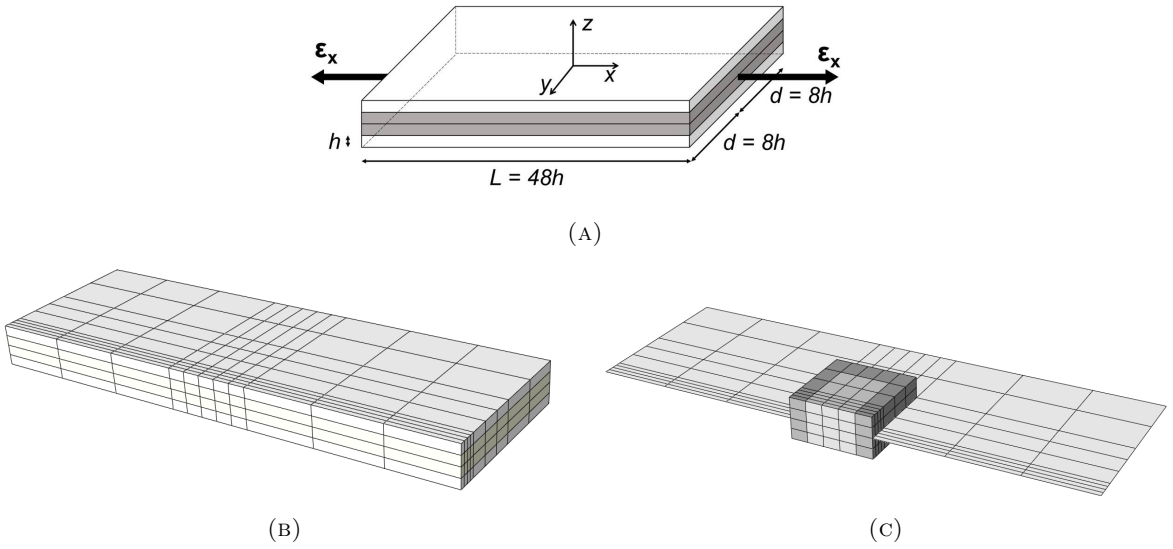

(A)

(B) (C)

FIGURE 3.12: Free edge laminate problem $[0/90]_s$: (A) Schematic outline; (B) FE reference problem; (C) FE multidimensional problem.

Three FE models are considered and listed hereunder.

- A full volume FEM is taken as a reference and illustrated in Figure 3.12 (B).
- A model with shell and volume elements illustrated in Figure 3.12 (C) with a MPC SS coupling from Abaqus at the interface.
- A model with shell and volume elements illustrated in Figure 3.12 (C) with the shell-to-solid coupling condition from Abaqus. This conditions allows to manage non-conformity of the meshes at interface.

All the meshes are made of quadratic elements, S8R for shell elements and C3D20 for solid elements. The mesh basis is taken similar to the mesh used in [Dávila, 1994].

3.4.2.2 Analytic and FE results

Only the transverse stress fields are compared here. The stress state near the coupling and near the free edge is of particular interest. The results of the out-of-plane stress fields at $(x = 0, z = h)$, meaning at the [0/90] interface, and for $y \in [0, b]$ is presented in Figure 3.13.

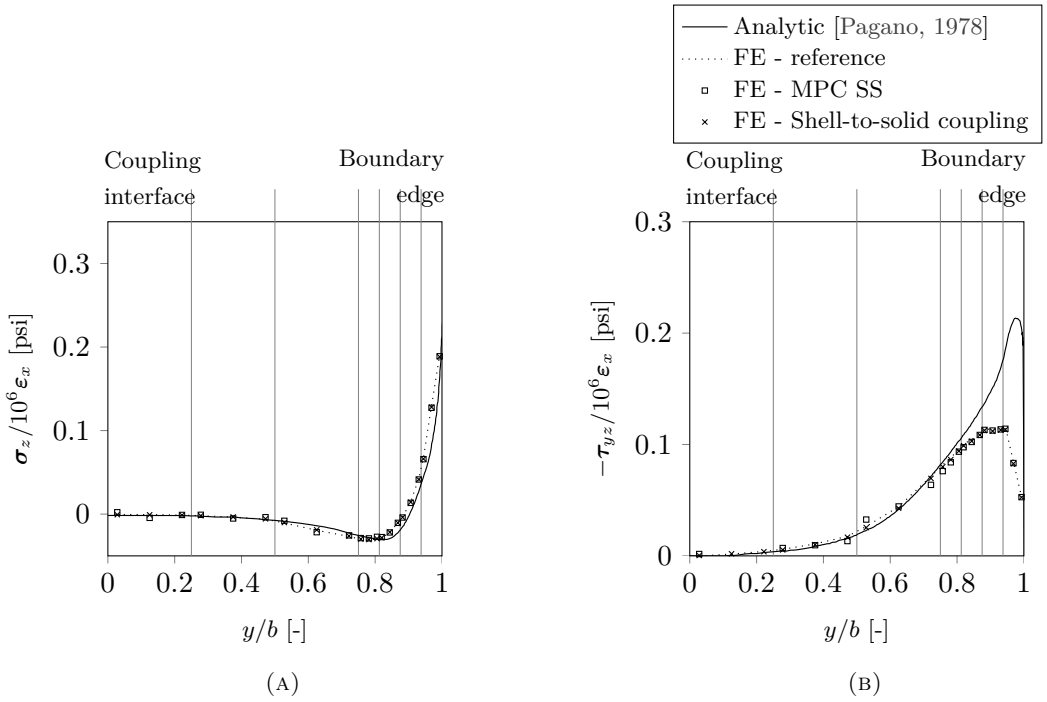

FIGURE 3.13: Stress fields at the [0/90] interface of a laminate in tension: (A) Normal out-of-plane stress; (B) Shearing out-of-plane stress.

3.4.2.3 Discussion

Both conditions, MPC SS and shell-to-solid coupling, provide a good accuracy compared to the reference finite element results both for the normal and shear out-of-plane stress as displayed on Figure 3.13. Compared to the analytic fields, all finite element solutions present an accurate description of the normal stress profile near the coupling interface and the boundary edge both quantitatively and qualitatively. For the inter-laminar shear, there is an underestimation of the field at the boundary edge (when y/b approaches 1) but the couplings do not induce errors at the interface between the shell and the volume zone.

There is a small difference between the results of both conditions since there is a nodal conformity at interface in the mesh. The surface based condition is more relevant when dealing with a mesh size discrepancy between the volume zone and the shell zone. Should the volume zone be more refined, the anelastic phenomena occurring in this region would be better captured. Hence the surface based condition (shell-to-solid coupling), of the proposed method is more adequate. This coupling is thus able to produce an accurate out-of-plane stress field within the volume domain.

3.4.3 Influence of the coupling in presence of an anelastic behaviour

This section aims at illustrating the coupling capabilities in damage simulations of composite laminates. The coupling is implemented at the interface between an elastic and an anelastic non-linear law. As presented in section 3.1, the occurring anelastic phenomena are supposed to be sufficiently far from the coupling. The selected use-case is a compressive-bending holed plate.

3.4.3.1 Failure analysis of a holed composite laminate plate subjected to a compressive-bending load

The test case is a holed laminated plate made of 16 unidirectional T7006C/M21 plies oriented at 0 deg. The material properties of this material and the geometric specifications of the holed plate are detailed in Table 3.3. The holed plate is subjected to a compressive-bending loading until final failure. The numerical FE results are compared with experimental results from an experimental campaign performed at Onera.

Length [mm]	130
Width [mm]	60
Thickness [mm]	4.19 (16 plies)
Hole diameter [mm]	12.7
E_1 [MPa]	115000
E_2 [MPa]	8500
G_{12} [MPa]	4500
ν_{12} [-]	0.32
ν_{23} [-]	0.4
X_t [MPa]	2000
X_c [MPa]	-1300
Y_t [MPa]	76
Y_c [MPa]	-260
Z_t [MPa]	46
Z_c [MPa]	-260

TABLE 3.3: Material T7006C/M21 and geometrical data of the studied composite plate.

Experimental testing The compressive-bending test is performed by applying a non-centred compression loading on the edges of the specimen which is mounted on two pivots. It allows to subject the specimen to both compression and bending. The eccentricity of the load application, illustrated in Figure 3.14, is performed by the insertion of the specimen into two jaws, in light gray, with a wedge, in red, on one side. A constant displacement rate of 0.01mm.s^{-1} is applied to the crossbar.

To monitor the global and local response of the specimen, several instrumentation techniques were used as illustrated in Figure 3.14 (A) and listed hereunder:

- Digital image correlation to measure the displacement and the strain field,
- Acoustic emission to monitor the damage evolution.

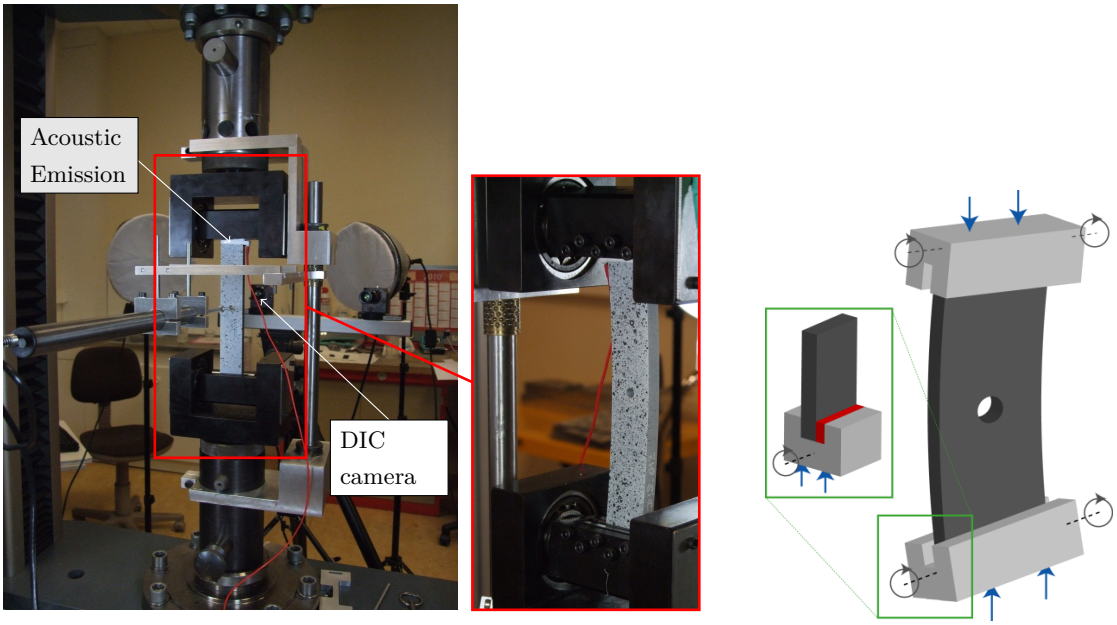

(A) (B)

FIGURE 3.14: Compressive-bending test: (A): Experimental mounting; (B) Schematic outline.

FE model The FE model, depicted in Figure 3.15, allows to simulate damage propagation initiated from the surroundings of the hole. The model is divided into three parts. The dark grey color represents the steel jaws and is modeled using shell elements. The light grey color represents the composite laminate modeled with elastic multilayered shell elements. Finally the blue area represents the composite laminate modeled with solid elements and a damage law. The material damage law is OPFM (see section 2.2.2.6) and is implemented through a UMAT file. The volume part is coupled to the shell area using the retained coupling condition detailed in section 3.3.1. The solver used is Abaqus/Standard. A constant longitudinal displacement rate is applied on one side of the structure while on the other side, the longitudinal displacement is blocked. The rotations are let free. Moreover, geometrical non linearity is taken into account, due to the non negligible deflection.

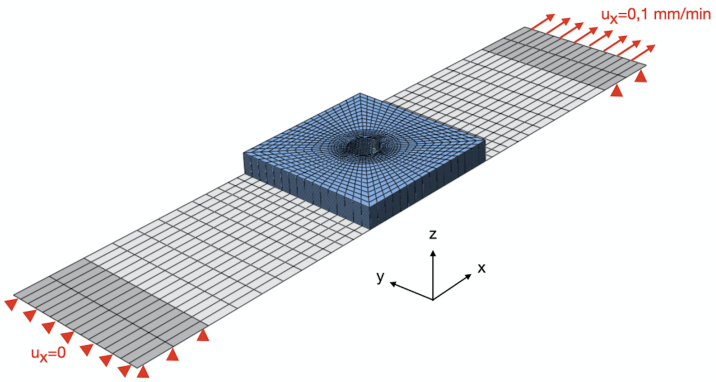

FIGURE 3.15: Finite element model on a holed plate loaded in compressive-bending.

3.4.3.2 Experimental and FE results

Two different mechanisms are investigated to compare the numerical results to the experimental ones. Firstly, the global response of the structure is examined quantitatively. Secondly, the damage patterns are confronted qualitatively.

Global response The error on the global response is assessed by comparing the numerical and the experimental load versus maximal deflection curves. This is plotted Figure 3.16. Four specimens have been tested experimentally to estimate the scattering of experimental results. The experimental results are represented by dots in Figure 3.16 while the numerical results are plotted with a full line.

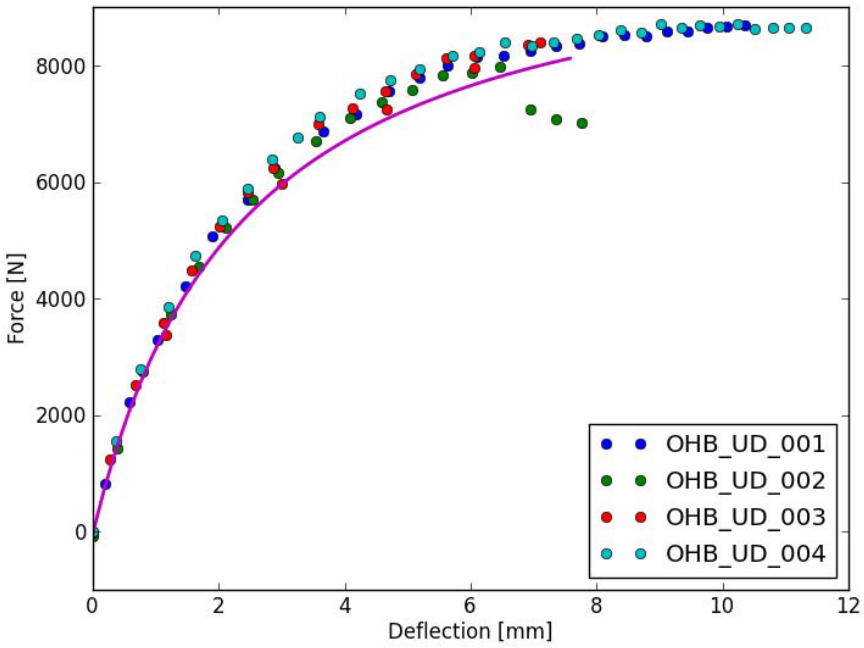

FIGURE 3.16: Load deflection curve of a compressive-bending holed plate.

Damage pattern It is experimentally observed that the damage of a open hole specimen made of 0 deg plies, in compressive-bending occurs in two steps. First, longitudinal splitting cracks are initiated on both ends of the central hole. Those splitting cracks are more preponderant on the face of the specimen which is in tension. Then, the global failure occurs when the fibers break in the transverse direction due to the loading. The first stage of splitting cracks is depicted on the photography in Figure 3.17 (A) where the cracks are highlighted by white dashed line. Those splitting cracks are reproduced by numerical simulations as represented in Figure 3.17 (B) and (C).

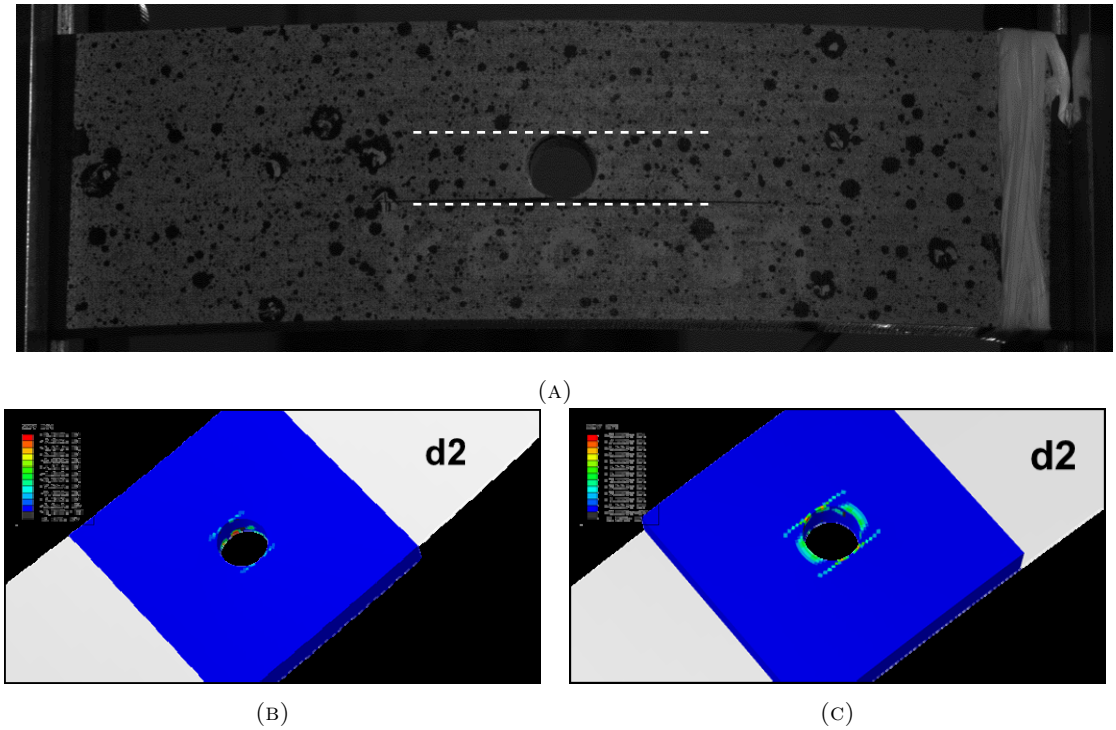

(A)

(B) (C)

FIGURE 3.17: Damage pattern of a compressive-bending holed plate: (A) Photography of a specimen on the face in tension; (B) Numerical result of the side in compression; (C) Numerical result of the side in tension (the experimental and numerical results are not taken at the same time).

3.4.3.3 Discussion

Regarding the global response, the numerical solution fits closely the experimental curves at low deflection. At large deflection, the simulation result slightly underestimates the load at constant deflection. Nevertheless this difference is small compared to the experimental discrepancy.

The assessment of the damage pattern is performed only qualitatively as it is complicated to determine accurately the local values of damage. The numerical simulations predict the splitting cracks observed experimentally which are more important on the side in tension compared to the side in compression. This asymmetry is captured by the material law through a coupling in the failure criterion between transverse compressive and in-plane shear stress.

3.4.4 Conclusion

The Abaqus "shell-to-solid" coupling used in conjunction with a shell kinematic constraint, is accurate enough to join multilayered shell elements to solid element inserts. The capabilities of this coupling were illustrated in three cases. First the capability of representing buckling instabilities was assessed for the elastic case. Then, the impact of the coupling on out-of-plane stress state was investigated for the elastic case. At last, the coupling was evaluated on an academic case of a bending holed plate with damage propagation. Those application cases allow us to validate this coupling in the following work.

Conclusion

In this chapter, the reference multi-model problem including an elastic and an anelastic domain was presented. The associated discretization was then detailed with the use of multilayered shell elements on the elastic domain and solid elements on the anelastic domain. The particular aspect of multidimensional coupling was treated in details.

First, an overview of relevant possible multidimensional coupling strategies were proposed as multipoint constraints, the Lagrange multiplier method, the penalty method, the Nitsche method and transition elements.

The selected coupling was the shell-to-solid coupling from Abaqus which enforces a load equality in a mean sense between the shell and the solid domains. This condition was used jointly with a shell kinematic constraint on the solid interface. This choice of coupling condition requires some care especially when the coupling surface is not sufficiently smooth. For this reason, a smoothing remeshing strategy was developed in the frame of this doctoral study using the Z-set software. The smoothing remeshing strategy allows to reduce artificial stress singularities arisen by edgy corners.

Finally, this coupling was applied to three different relevant use-cases to assess its ability to fulfill the targeted applications.

When treating large problems, it may be too restrictive to maintain a definitive partitioning of the global problem into two different domains to model respectively elastic and anelastic phenomena. Firstly, the initial domain where anelastic phenomena could occur has to be guessed a-priori. Secondly, through the computation this partitioning may become inadequate. Hence, the following part of this work is to provide a numerical strategy to progressively adapt the partitioning of the multi-model problem using a remeshing approach.

4 Progressive model adaptation through remeshing

This chapter presents the problematic of progressive adaptation of the multi-model problem through remeshing. First, the general adaptive strategy is presented. Then, the specificities of the strategy are detailed. In the second part, the model adaptation triggering strategy is detailed. The remeshing strategy is developed in a third part. In a fourth part, the state update is addressed. Finally, the strategy is applied to an academic test case of a compressive-bending holed plate.

Contents

3.1 Introduction 42

3.1.1 Reference multi-model problem 42

3.1.2 From continuous to discrete formulation 43

3.2 Multidimensional coupling 44

3.2.1 Bridge between 2D and 3D formulations - 3D stress recovery 44

3.2.2 Review of multidimensional coupling strategies 46

3.2.3 Conclusion 53

3.3 Discrete multi-model problem 54

3.3.1 Multidimensional coupling condition 54

3.3.2 “Smart” local remeshing strategy 56

3.3.3 Conclusion 59

3.4 Application cases 60

3.4.1 Influence of the coupling on the buckling behaviour 60

3.4.2 Influence of the coupling on the out-of-plane stress state 64

3.4.3 Influence of the coupling in presence of an anelastic behaviour 66

3.4.4 Conclusion 69

4.1 Progressive model adaptation strategy

The previous chapter focused on the resolution of a multi-model problem with a fixed decomposition and discretization. In this chapter, the evolution of this partitioning through the simulation is explored as illustrated in Figure 4.1 where two remesh adaptation steps are led. The objective is to provide an automatic tool which detects whenever the current partition is no longer adequate, launches the creation of the new partition and resumes the computation. This is achieved by using adaptive remeshing techniques.

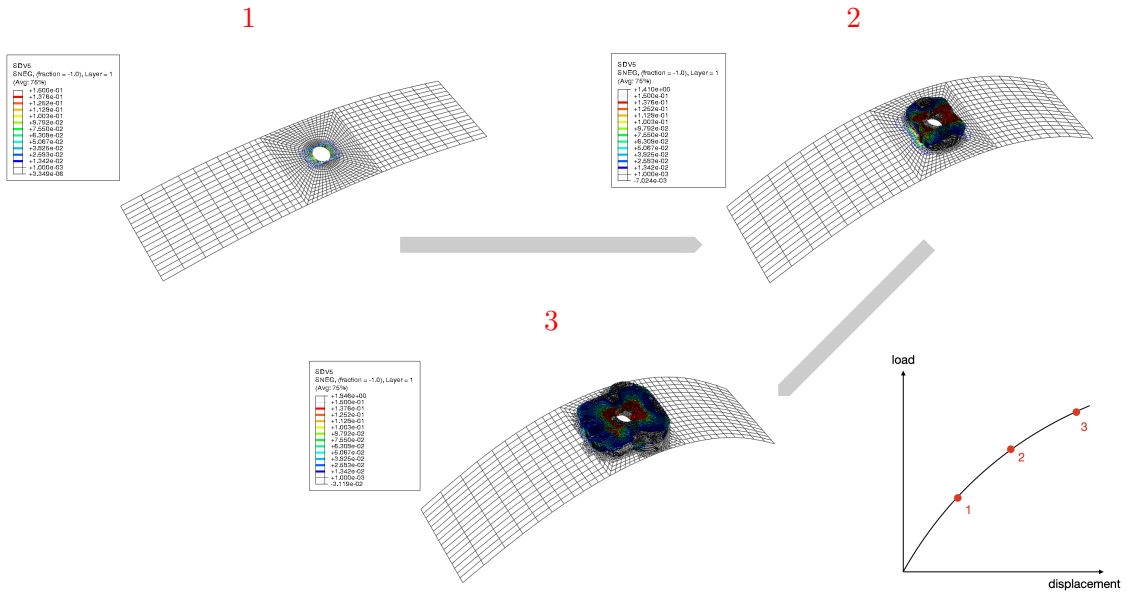

FIGURE 4.1: Illustration of an adaptive remeshing procedure on a composite laminate bending holed plate through a progressive loading.

First, a brief overview of adaptive remeshing techniques and their specific endeavours will be presented in section 4.1.1. Then, the general principle of the strategy developed in this chapter is presented. The following sections, 4.2 to 4.4, detail the different elements of the adaptive strategy. Finally a numerical example based on an academic test case of a compressive bending holed plate is detailed in section 4.5.

4.1.1 Brief overview of adaptive remeshing techniques

A large amount of works in the scientific literature tackle adaptive strategies based on mesh refinement as presented in section 2.3.3.2. The remeshing strategies are mostly driven by error indicators. When the error evolves beyond a threshold, the mesh of the finite element model is refined. Error indicators can be computed either *a posteriori* or *a priori* meaning respectively after or before the finite element solution is obtained. Then, the discretization, the mesh size for h-adaptive methods or the order of approximation for p-adaptive methods are selected depending on this computed error. The adaptive refinement strategies applied to linear elliptic problems have now reached a high level of maturity. Surveys on those numerical strategies are available for

instance in [Oden et al., 1989] and [Johnson and Hansbo, 1992]. Nevertheless, many situations do not lie in the frame of linear elasticity. When considering non-linear problems, adaptive refinement is still an on-going research topic.

In this manuscript, the main purpose is to be able to model local non-linear behaviour such as damage where needed. The material constitutive behaviour, OPFM, used in this work and detailed in section 2.2.2.6 is an history-dependent law. For the particular case of adaptive remeshing for history dependent non-linear problems, specific error indicators have been developed in the literature. Moreover, after a remeshing in presence of history-dependant material laws, the computation cannot be resumed directly from the initial state but from the previous time increment state. Hence specific update strategies are required.

The error indicator and state update strategies for history dependent behaviours and non-linear problems are developed hereunder.

Error indicators for history dependent and non-linear problems Error indicators for plastic behaviors are the object of several published works. In [Zienkiewicz et al., 2000], the authors introduce an error indicator that is a modification of that developed in [Zienkiewicz and Zhu, 1987] with an energy norm for an application to elastoplastic behaviours. To improve this aspect, the authors in [Perić et al., 1994] propose an error indicator based on the rate of plastic work for elastoplastic behaviour. In [Gallimard et al., 1996], the authors extended the domain of application of the indicator by including in it spatial and time components. Those indicators present suitable results when considering elastoplastic behaviour in large deformation problems. Nonetheless, in presence of high gradients of stress, for instance due to failure phenomena, the developed indicators are not directly sufficient.

When considering problems involving failure, the error indicator is usually based on a fracture indicator and more specially on the rate of this fracture indicator. Several fracture indicators have been explored in the literature such as those based on plastic work [Gillemot, 1976] or on damage work [Cescotto and Zhu, 1995]. For the special case of continuum damage models, such as that used in this manuscript, OPFM, an indicator based on the damage law seems to be more relevant.

Consequently, the strategy adopted in this manuscript is to estimate when the elastic behaviour in the $T^{(E)}$ domain is no longer adequate by using a failure indicator to trigger the multi-model adaptation. The chosen indicator is a physical indicator of damage from the model OPFM. This aspect is detailed in section 4.2.

State update for history dependent and non-linear problems For linear elastic problems, the state of the new model can be retrieved directly from the initial state. The update is less straightforward when considering history-dependant materials and in particular material behaviours including a threshold. Moreover, the data is available in a discrete space distribution at the integration point which implies the use of an interpolator to transfer the data. Those particularities of the state update strategy are detailed in section 4.4.

4.1.2 Multi-model adaptation scheme

The algorigram 1 depicts the basic principle of the discrete incremental resolution strategy. The notations are the same as those used in section 3.3. More details on the numerical implementation of the adaptive numerical multi-model strategy can be found in Appendix A.

The global mechanical multi-model problem is solved at each increment Δt_n of the current model including the non-overlapping coupling at the G interface. This coupling condition is the "shell-to-solid" coupling from Abaqus which enforces load compatibility in a mean sense using Lagrange multipliers. In addition to this coupling, a shell Reissner-Mindlin kinematic is applied to the solid interface. This choice is detailed in section 3.3 of the previous chapter.

There is no model update as long as the model (E) is valid over the discrete domain $T^{(E)}$ and at the vicinity of G in the $T^{(AE)}$ domain. It can be noted that the distribution of T into $T^{(E)}$ and $T^{(AE)}$ is not unique, a choice is proposed regarding the discretization strategy in the application section 4.5. A model validity indicator ϕ and a criterion α are selected to interrupt the incremental computation and trigger the adaptation scheme. The endeavours of those indicator and criterion are detailed in section 4.2.

Then, an identification step allows to target the critical elements $T^{(E)}_{crit} \subset T^{(E)}$ requiring the (AE) model. An extended zone at the vicinity of $T^{(E)}_{crit}$, defined by a distance D, is remeshed into solid ply-per-ply elements with a constant pre-defined mesh size h set-up to accurately calculate the damage model. This mesh-size is determined using a classic mesh convergence approach. The quantity D can be optimized with respect to the computational time. A fair value of D would allow finding a compromise between the execution time of the adaptation operation and the extension of the anelastic domain $T^{(AE)}$. This remeshing strategy is developed in more details in section 4.3.

After the remeshing process, the state update aims at producing a good representation of the mechanical state following the change in models and discretization, with the delicate transition from a shell to a solid kinematic. Additional equilibrium steps are added before the computation is resumed for the increment Δt_n. The state update stage is addressed in section 4.4.

Algorithm 1: Adaptive multi-model algorithm.

$t = t_0$;
$\Delta t = \Delta t_0$;
$T_0 = T_0^{(E)} \cap T_0^{(AE)}$;
while $t < t_{tot}$ **do**
    Resolution of the global multi-model problem at increment Δt_n;
    if $\phi_{T_n^{(E)}} < \alpha$ **then**
        $t = t_{n+1}$;
    else
        $t = t_n$;
        Definition of the zone to be remeshed $T_n^{(E)}{}_{crit}$;
        Remeshing into $T_n = T_n^{(E)} \cap T_n^{(AE)}$;
        State update;
    end
end

4.2 Model adaptation indicator and criterion

In the continuous problem, the model (AE) differs from (E) only when a stress based criterion α is achieved. If the evolution remains elastic, a material point characterized by the behaviour (AE) can naturally be described by an anelastic behaviour (E). Thus, a scalar function in space ϕ is introduced as an indicator of the validity of the model (E). The non-overlapping domain distribution is thus described by the following conditions:

$$\begin{cases} T^{(E)} \cup T^{(AE)} & = & T, \\ T^{(E)} \cap T^{(AE)} & = & \{\}, \\ M \in T^{(E)} & if & \phi(M) < \alpha. \end{cases} \tag{4.1}$$

ϕ is the used indicator and α the adaptation criterion. The model adaptation has to be triggered before the damage occurred. Thus, the criterion is not based on damage variables but on the failure indexes $f_i, \quad i \in \{1,2,3\}$ which are described in the previous chapter. In this respect, ϕ is set to $\phi = \max(f_i),\ i \in \{1,2,3\}$ as any damage in any direction should trigger the adaptation. This value is compared to the fixed threshold α, with $0 < \alpha < 1$. In the damage model, the condition $\alpha < 1$ (Figure 4.2) allows maintaining a margin and ensuring the validity of the model in a richer representation space after adaptation (ply-per-ply solid in $T^{(AE)}$ rather than homogenized shells in $T^{(E)}$). Thus, the adaptation is triggered before damage has occurred which simplifies substantially the state update step after the remeshing as explained in a further section.

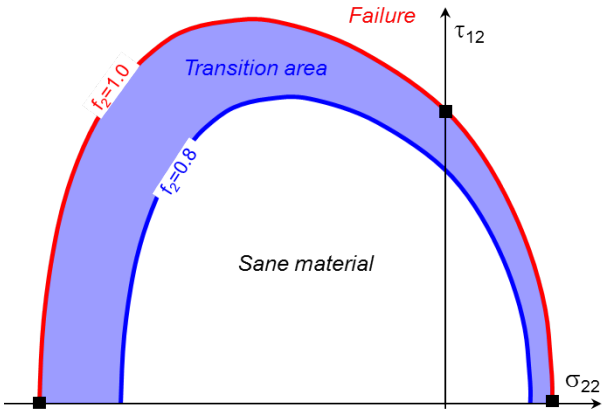

FIGURE 4.2: Shape of failure envelopes, with $\alpha = 0.8$.

Moreover as explained in section 3.3.1, the coupling scheme prescribes a shell kinematic on the first layer of solid elements close to the interface. It is not recommended to have a damage law right next to the coupling. To ensure that, the criterion α is also imposed at the vicinity of the discrete interface G in the $T^{(AE)}$ domain. Let's call that layer of element $T^{(AE)}_{bound}$. The domain

partition thus satisfies the following condition.

$$\begin{cases} T^{(E)} \cup T^{(AE)} & = & T, \\ T^{(E)} \cap T^{(AE)} & = & \{\}, \\ M \in T^{(E)} \cup T^{(AE)}_{bound} & if & \phi(M) < \alpha. \end{cases} \tag{4.2}$$

This condition prevents some stress concentrations at the boundary leading to an artificial damage initiation. An example of the presence of this boundary layer is illustrated in Figure 4.3.

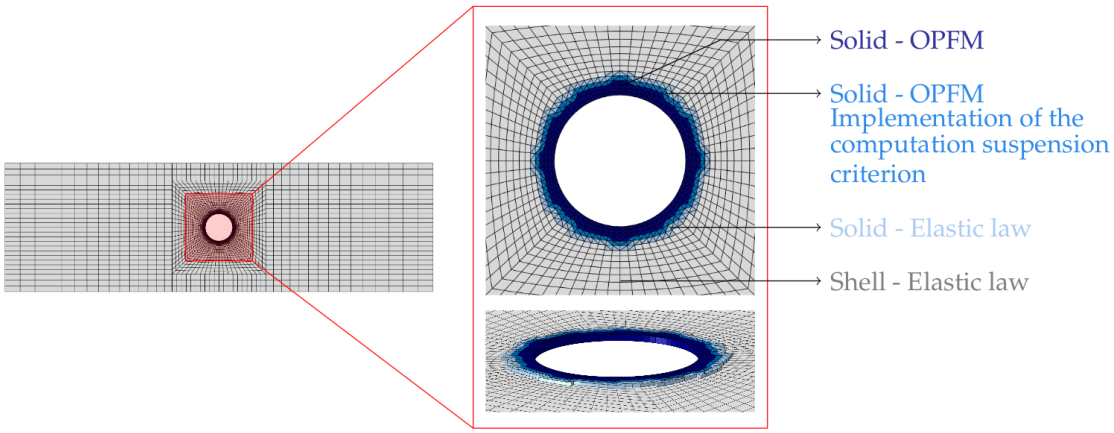

FIGURE 4.3: Localisation criterion implementation.

The failure indexes $f_i, \quad i \in \{1, 2, 3\}$ are reliant on the material behaviour. Consequently, in the non-linear model, the condition from Equation 4.2 is implemented locally at an integration point level.

4.3 Smart remeshing strategy

In this work, the remeshing is the main lever of action when developing the numerical adaptive multi-model method. The software Z-set provided a great flexibility to implement the proposed method thanks to its advanced remeshing capabilities. On one hand, a remeshing strategy was presented in chapter 3 to generate a multi-model mesh with stacked solid elements where needed and shell elements elsewhere. On the other hand, this section aims at providing some remeshing tricks that were used in the spirit of easing the multi-model adaptation strategy.

First, the process of identification of areas which must be remeshed is explained in section 4.3.1.

Generally, in mesh refinement, the use of triangular elements facilitates the generation of a non-distorted mesh with a better handling of the constraints on mesh size and conformity as described in section 4.3.2. The outcomes are different when using quadrilateral elements. In this manuscript, the elements used are triangular. The case of quadrangles therefore is only briefly discussed in section 4.3.3.

Finally, to ease the state update step, a specific remeshing process including mesh preservation tricks was developed and is presented in section 4.3.4.

4.3.1 Identification of areas to be remeshed

Once the computation is suspended, a first post-processing step is performed to assess all the critical points where the localisation criterion α, detailed in section 4.2, is exceeded. This post-processing is performed using Abaqus python and generates a file containing all the coordinates of the so-called critical points.

Then, the remeshing is based on all those coordinates. The principle of the identification of the local region to be remeshed is represented in Figure 4.4. It is performed in several steps. First, the zone to be remeshed is identified by the critical points and a desired extent surrounding them which corresponds to the remeshing radius D (Figure 4.4(A)). Then, the elements including the blue area in Figure 4.4(B) are selected to construct a set of elements represented in red in Figure 4.4(C). Those elements only are remeshed allowing to avoid non-necessary remeshing operations on the whole model.

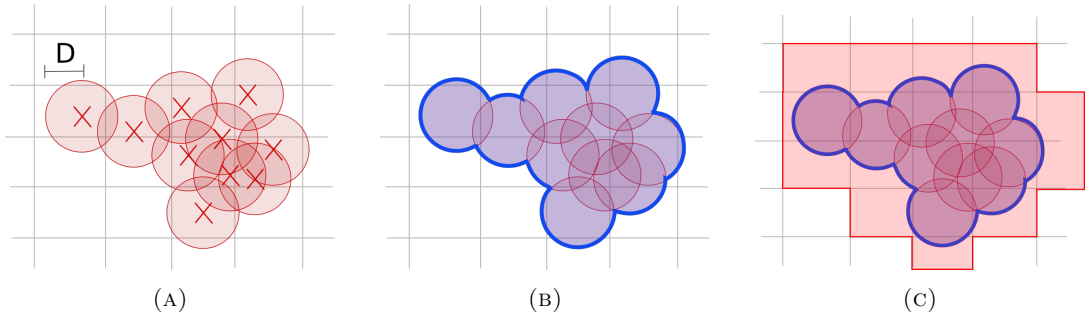

FIGURE 4.4: Identification steps of the local area to be remeshed: (A) Identification of the critical integration points; (B) Determination of an external envelope; (C) Determination of the elements to be remeshed.

The remeshing radius D is a user defined parameter. The remehing radius D results from a compromise between the number of adaptation processes and the extent of the volume part with respect to the whole model.

4.3.2 Remeshing steps

Once the elements to be remeshed are identified, the remeshing operation is performed. The mesher used in Z-set is developed by Distene. The user selects the minimal, maximal and evolution of the element sizes. Those sizes are used to produce a size map. The size map is a cartography of the wanted element sizes through the zone to be remeshed. Then, in a second step, a 2D remeshing of the structure with triangular elements is performed respecting the size map. Finally, a 3D extrusion of the remeshed zone is executed respecting the number and thickness's of the plies. Those three steps are illustrated in Figure 4.5.

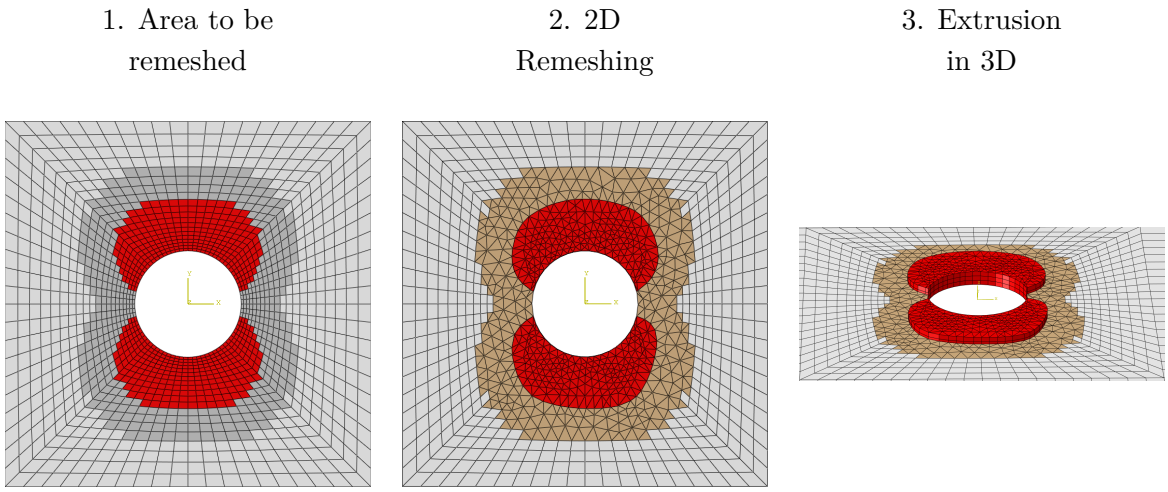

FIGURE 4.5: Remeshing strategy to create a 3D stacked volume mesh from a 2D initial geometry.

The 3D extrusion is performed along the shell normal, the shell mid-plane corresponding to the middle plane of the volume part. This remeshing tool is also available in the frame of non-plane geometries as illustrated in Figure 4.6. The element sizes in this case are, in an obvious manner, limited by the curvature of the extruded surface.

The advantage of using such a strategy is to allow maintaining an underlying 2D mesh that is used to produce a mesh with a through thickness conformity. Moreover, the nodal conformity is preserved at the smoothed interface allowing to avoid accuracy loss due to incompatible meshes.

4.3.3 Mesh refinement with quadrangular elements

When using advanced material behaviour laws, it can be numerically better to use quadrangular elements. Adaptive remeshing with quadrangular elements can be nonetheless intricate as it is more difficult to produce nodal conformity. For instance, let's consider the initial 2D mesh (Figure 4.7 (A)). The elements that are to be refined are highlighted in grey. Several options are possible. If nodal conformity is imposed as in Figure 4.7 (B), there is a need of transition elements

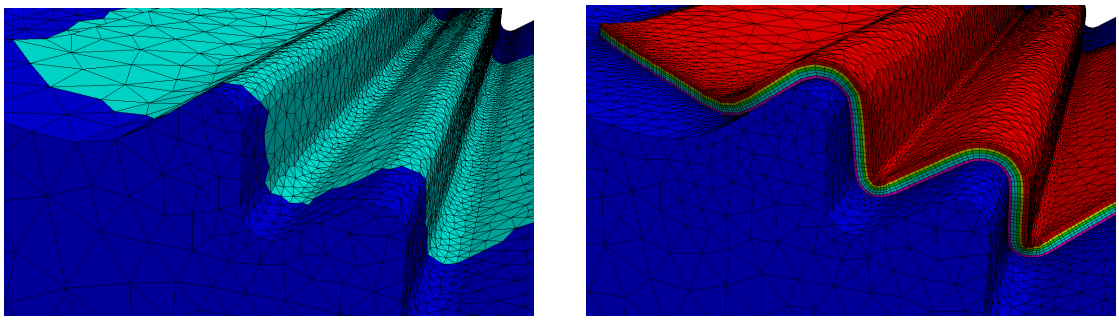

(A) (B)

FIGURE 4.6: Remeshing of a non-plane geometry: (A) underlying 2D mesh; (B) 3D extrusion.

to connect the refined area to the rest of the mesh. Among those transition elements, some quadrangular elements are distorted. Another option is to release the nodal conformity constraint as in Figure 4.7 (C). Then the nodes in red are "hanging" and supplementary conditions have to be applied on them.

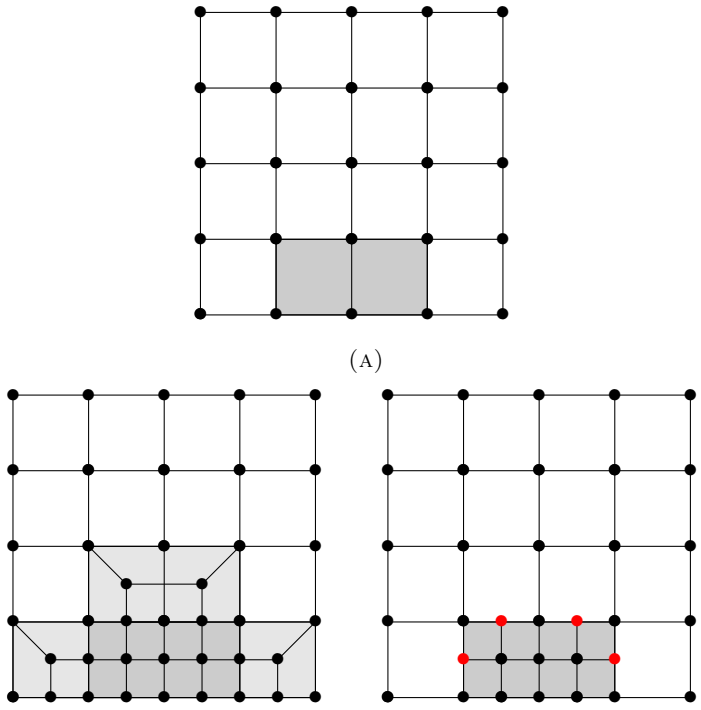

(A)

(B) (C)

FIGURE 4.7: Mesh refinement using quadrangles: (A) initial mesh with the grey area to be refined; (B) Refinement with nodal conformity; (C) refinement without nodal conformity.

For the same illustrative test case as in Figure 4.5, the remeshing steps when using quadrangles both in the area of interest and in the transition area is represented in Figure 4.8. The nodal conformity is not guaranteed between the refined area and the remaining un-touched mesh.

The main drawback when using quadrangle meshes is either the generation of highly distorted elements in the transition area or the lost of nodal conformity which induces the implementation

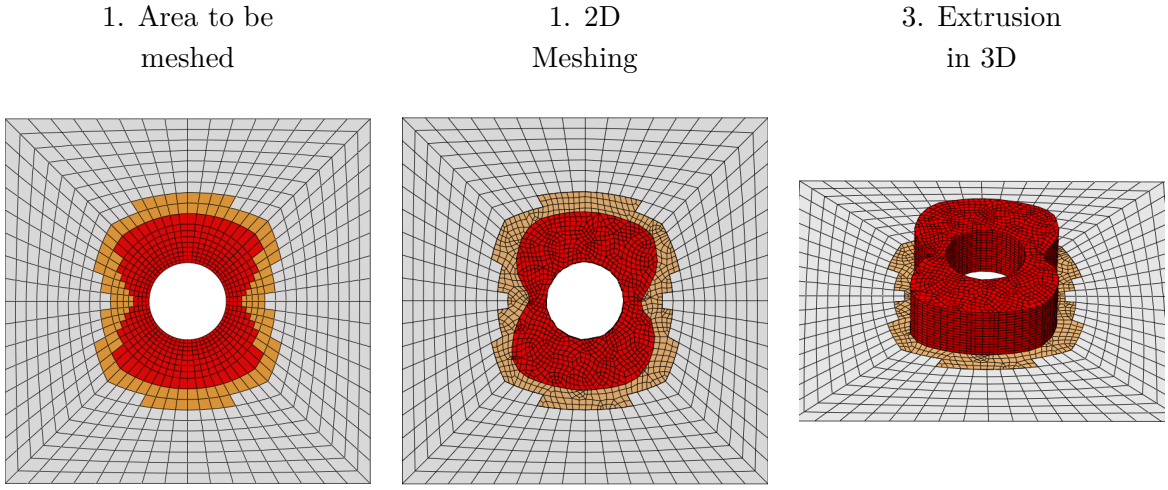

FIGURE 4.8: Remeshing strategy to create a 3D stacked volume mesh from a 2D initial geometry with quadrangles.

of a second coupling condition between the refined and the coarse shell elements in addition to the coupling condition between the shell and solid elements.

The use of quadrangle elements have not been explored in depth in this work and could be an interesting opening for the improvement of this numerical adaptive strategy. For instance, the transition volume part, coloured in red, contains quadrangle elements whilst the transition area, coloured in orange, may contain a few triangular elements. Thus, nodal conformity should be ensured between the transition area, coloured in orange, and the un-touched shell elements, coloured in grey.

4.3.4 Preservation of mesh in degraded areas

In the developed strategy, the underlying 2D mesh is preserved in order to facilitate the remeshing operations and to preserve the mesh in the areas where degradation phenomena occur to simplify the transfer field step.

The principle of mesh preservation is illustrated in Figure 4.9 where only the 2D underlying meshes in the area of interest are represented for the model respectively before (Figure 4.9 (A)) and after (Figure 4.9 (B)) adaptation. The color code is the following:

- Area 1: area preserved from the previous mesh generation,
- Area 2: area to be preserved for the next mesh generation,
- Area 1 + Area 2 + Area 3: $T^{(AE)}$ domain with volume elements,
- Area 4: $T^{(E)}$ domain with shell elements.

This mesh preservation technique allows to transfer exactly the data in the regions where there are non-zero history dependent material variables. The advantage of adopting such a strategy is to save time on the use of costly field transfer operations. Another advantage is to limit the errors induced by the transfer operations, described in the next section.

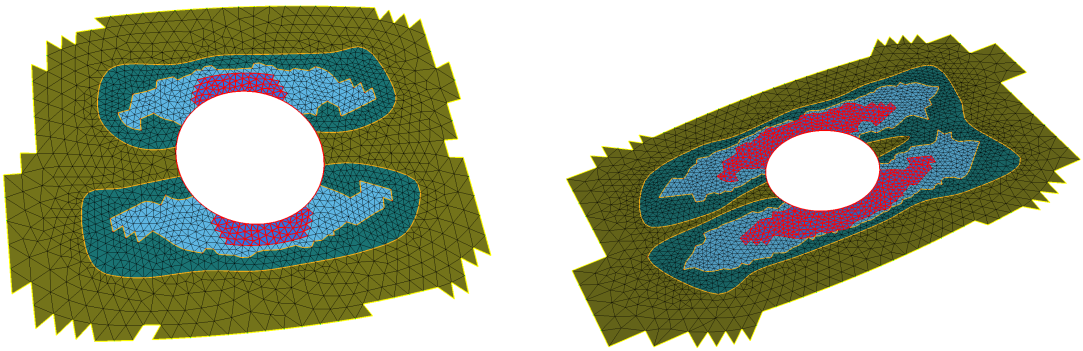

(A) Before adaptation (B) After adaptation

FIGURE 4.9: Underlying 2D mesh driving the remeshing process.

4.3.5 Conclusion

This section focused on some remeshing techniques, proposed to fit the composite laminate modelling problematics and to ease the different steps of the multi-model adaptive techniques. In that aim, the construction of the multi-model mesh which relies on an underlying 2D mesh was presented. The mesh can have a smooth frontier between the shell and the volume areas to reduce stress concentrations on the interface. The building of a smooth frontier was addressed in a previous chapter. Finally, a mesh preservation technique to facilitate the state update operations was detailed.

4.4 State update

After the model adaptation, the state of the new multi-model problem is updated. The transfer of information is needed when dealing with incremental problems when using for instance history- or rate-dependent materials. It is one of the most delicate stage within the overall process that consists in transferring all the needed information between two different meshes by the mean of transfer operators which should satisfy, as best as possible, the following conditions:

- consistency of the state variables associated with the constitutive equations,
- compatibility between the nodal and the integration point fields,
- equilibrium especially when using implicit resolution solvers,
- reduction of the numerical diffusion.

This operation is performed by the mean of transfer operators. Those are detailed in section 4.4.1. Then, the chosen field transfer strategy is presented in section 4.4.2. To finalize the state update, after the field transfer operations, additional computations steps are led to retrieve equilibrium. Those are presented in section 4.4.3.

4.4.1 Field transfer operators

Several transfer operators have been developed in the literature. The transfer strategy is generally differentiated into two types of fields, respectively nodal and integration point based fields such as represented in Figure 4.10. The transfer of nodal-based data, such as displacement is more simple as the field is defined continuously over the domain thanks to the element shape functions. The transfer of integration-point based data, which includes stress, strain and eventual material internal components for history-dependent material laws, is much more complex. Some common

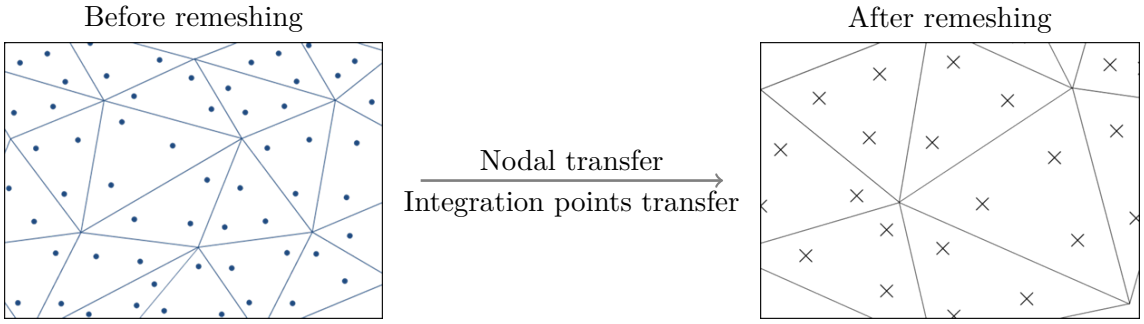

FIGURE 4.10: Field transfer principle: nodal based fields and integration based fields.

field transfer operators are detailed in the following paragraphs.

Direct transfer or collocation This method is usually used for transferring nodal data between meshes. The field at each point of the new mesh is determined by locating within which element of the initial mesh it stands and then use the form function of this initial element to retrieve the field.

This method takes advantage of the continuity of the displacement field to transfer its exact value. The collocation operator is consistent, meaning that if the meshes were identical, so will be the transferred fields. In the case of mesh refinement, this method is the most common as it provides accurate results. In the case of mesh coarsening, this technique may result in loss of information that is undesirable. To counter that effect, an averaging step is usually added. Nonetheless, in this work, only the refinement is tackled. Consequently, the collocation operator is chosen for transferring nodal-based data.

For the case of integration point fields, no spatial interpolation is obvious. Several methods have been explored [Perić et al., 1996], [Ortiz and Quigley, 1991], [Lee and Bathe, 1994]. Some common operators are detailed in the following paragraphs.

Nearest point transfer The field at each integration point of the new mesh is determined by locating which point of the initial mesh is closest and then copy directly this value of the field. This comes down to assume that the value of the field at an integration point is constant over an area surrounding this point.

Mobile least square transfer The field at each point of the new mesh is determined by an optimized interpolation based on a ponderation of the field at the nearest points from the initial mesh. Several interpolation strategies can be adopted and some of them are listed in [Zienkiewicz et al., 2000]. As an example, a possible strategy is presented hereunder:

1. The integration point fields in the initial mesh are interpolated to the nodal points of the initial mesh using its shape functions,
2. The corresponding nodal fields are transferred to the nodes of the new mesh,
3. The values at the integration points of the new mesh are calculated using the transferred nodal values and the shape functions of the new mesh elements.

Such a strategy may induce numerical diffusion. Numerical diffusion is undesirable especially when using a material behaviour having a stress threshold which is the case here. It may lead to an underestimation of the non-linear effects. For this reason, the mobile least square transfer is not retained is our numerical strategy.

Transfer by L2 projection In this transfer method, a new integration rule compatible with the initial and the final meshes is constructed. Thus, a sparse mass matrix based linear system is solved in order to obtain each projected nodal data on the new mesh. This is a highly accurate transfer operator which nonetheless requires a high computational effort. Such a complex transfer method is not necessary for our numerical strategy. As presented previously, the adaptation is performed before damage appears. Consequently, there is no prior damage in the parts where there is a mesh change and the mesh is preserved in the damaged parts.

Some transfer operators were presented in the previous paragraphs. Depending on the use case, a trade-off between the computational effort and field transfer accuracy drives the choice of the

transfer operators. In the following paragraph, the field transfer operators available in the Z-set software are presented.

Field transfer capabilities of the Z-set software The Z-set suite includes a module called Zcracks which includes advanced field transfer methods. Among the methods presented before, Zcracks contains four methods: the direct transfer, the mobile least square transfer and the transfer by L2 projection. The advantages and drawbacks of those methods are presented in Table 4.1.

Method	**Advantages**	**Drawbacks**
Nearest point	- No diffusion - Low time consumption - Material consistency	- No interpolation
Direct	- Low time consumption	- Diffuseness - Not optimal compared to L2 projection
Mobile least square	- Interpolation - No problem near boundaries	- Diffuseness - High time consumption
L2 projection	- Optimal nodal transfer	- Very high time consumption

TABLE 4.1: Field transfer methods available in Z-set.

The chosen method for nodal transfer is the direct transfer as time consumption is a critical aspect of the numerical method that is to be developed. For the integration point fields, the nearest point method is used to ensure material consistency in the transferred field. The specifics of the transfer strategy are detailed in the following section.

4.4.2 Field transfer strategy

The developed numerical adaptive multi-model approach implies some adjustments of the transfer strategy regarding the different material behaviours and element kinematics involved as illustrated in Figure 4.11. The transfer is performed in the un-deformed configuration.

The transfer between linear elastics parts is more trivial as the solution does not depend on the material previous states. The integration points fields are not transferred, since the nodal displacement values are sufficient to describe the state. Consequently, from shell to shell elements or from shell to newly solid elements, only the nodal displacement fields are transferred. As the material is linear elastic, the strains can be recomputed easily while considering the kinematic of

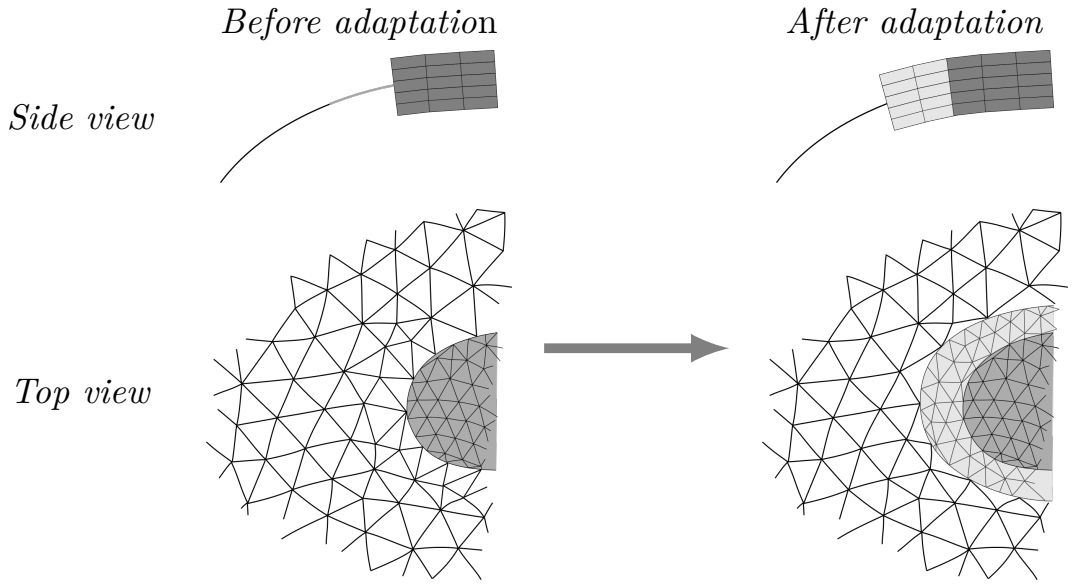

FIGURE 4.11: Models involved in the field transfer.

the different elements (shell or solid). The displacement fields are transferred by the collocation method through the whole domain T. For the particular case of shell to newly solid elements the values of the nodal fields are retrieved at solid nodes in two steps:

1. The solid nodes are projected to the shell predefined plane where the fields can be computed by the mean of the collocation technique.
2. The corresponding in-plane fields are used to retrieve the value of the displacements at the final solid node using the rotation fields. Thus the displacements fields of the newly solid zones initially respect the shell kinematics.

For the particular case of the nodal interface data, only one side of the interface data is transferred. The chosen side is the solid interface as the former interface is included into the newly solid domain.

Contrary to the elastic linear domains, from the initial anelastic region to the new anelastic region, the nodal values of displacements and the integration point values are transferred. The nodal fields are also transferred using the collocation method. For the values at integration points, the chosen transfer operator is the nearest point method. This guarantees a coherence at the material points of the transferred fields. The preservation of the discrete space of the damaged area as explained in section 4.3.4 allows to perform an exact transfer in this region. This last point is important to avoid errors in the transfer of material state variables. Moreover, due to the heterogeneity of material properties in thickness of a laminate (different plies with different orientations), the transfer is performed separately between the corresponding layers to avoid transferring integration point data from one layer to another one.

4.4.3 Equilibrium

As the resulting state after the transfer is not at equilibrium, due to an inadequacy between the nodal values and the integration point values, additional numerically affordable steps must be performed. This loss of mechanical equilibrium of the structure occurs at both the local and global scales of the structure. The selected strategy to retrieve the mechanical equilibrium is presented in the following paragraphs.

To retrieve local equilibrium in each element, an extra integration step of the material law is added by applying a delta of strain easily computable. For each integration point of the adapted mesh, let $\boldsymbol{\varepsilon}(\boldsymbol{u}_{\text{new_elem}})$ be the strain computed from the gradient of the nodal displacement fields and $\boldsymbol{\varepsilon}_{\text{nearest_IP}}$ the strain from the nearest integration point of the initial model. An integration operation is then performed at the targeted integration point with the application of a strain increment $\Delta\boldsymbol{\varepsilon} = \boldsymbol{\varepsilon}(\boldsymbol{u}_{\text{new_elem}}) - \boldsymbol{\varepsilon}_{\text{nearest_IP}}$ as illustrated in Figure 4.12. This local equilibrium step is performed by the Z-set software.

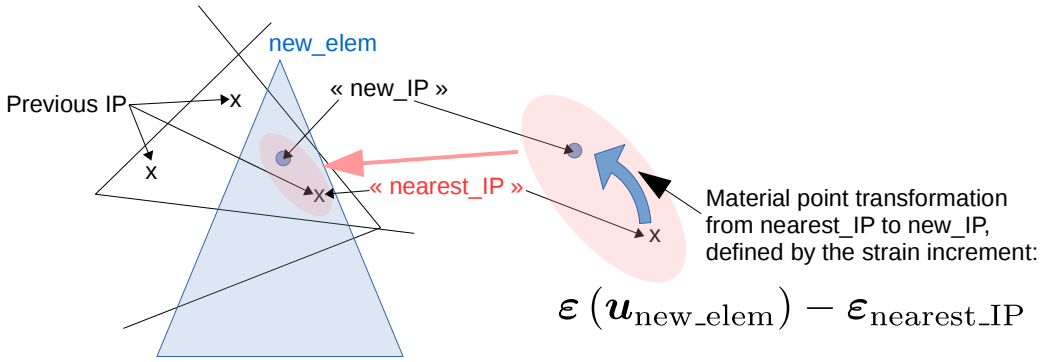

FIGURE 4.12: Local equilibrium step.

Nevertheless, after the state update, out-of-plane stresses may be enhanced artificially at the previous shell-solid interface. The local equilibrium step does not allow to suppress this phenomenon. Consequently, once this local equilibrium step is achieved, a global equilibrium step on a brief time increment is performed before the simulation is resumed. The global equilibrium step is performed by Abaqus. This global equilibrium also allows adjusting the coupling data that can produce stress concentrations if not well initiated. This is illustrated in Figure 4.13 for the case of a longitudinal holed plate in tension where the Figure 4.13 (A) represents the out-of plane normal stress field at the time increment t_n; the Figure 4.13 (B) represents the out-of plane normal stress field at the time increment t_{n+1} without a global equilibrium step and the Figure 4.13 (C) represents the out-of plane normal stress field at the time increment t_{n+1} with a global equilibrium step.

It can be observed that in absence of a global equilibrium step, the stresses are not well initiated due to the incoherence between the shell and the solid elements formulation for out-of-plane strain and stress. This causes over-constraints at the interface that drag through the following computation steps. This is partly due to the use of an history-dependent material law in the volume area which can crystallize the areas of stress concentrations.

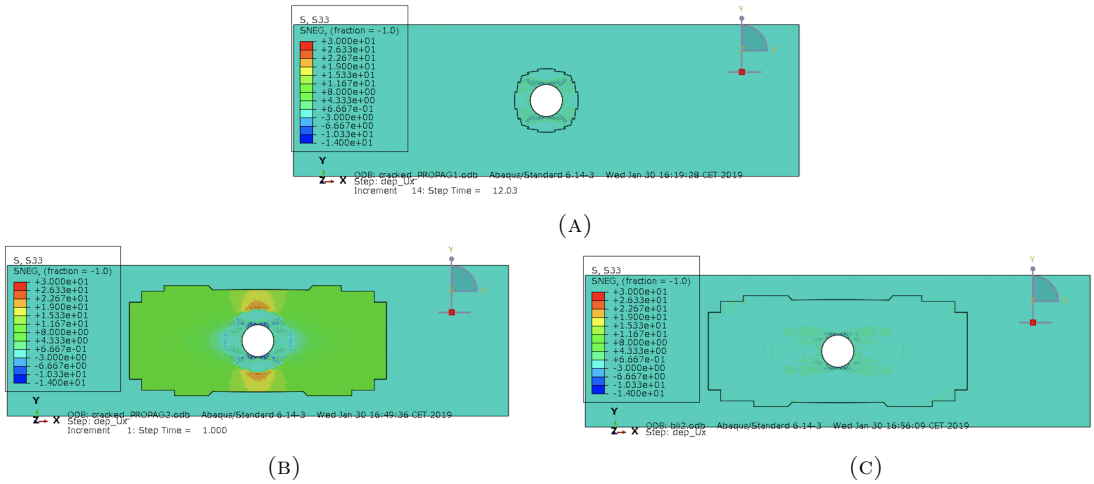

FIGURE 4.13: Mapping of the out-of-plane normal stress: (A) Initial model at t_n; (B) New model at t_{n+1} without a previous global equilibrium step; (C) New model at t_{n+1} with a previous global equilibrium step.

Both a local and a global equilibrium steps are thus led after each remesh adaptation process. If the model adaptation criterion is reached during equilibrium, which happens for instance when the volume area is not large enough, another remeshing operation is automatically launched followed by the whole state update scheme.

4.4.4 Conclusion

In conclusion, a state update for the multi-model adaptive method is presented with the nodal values being transferred with the collocation method and the integration point values being transferred with the nearest point transfer. The transfer operations are followed by a local and a global equilibrium steps before the computation is resumed.

The main problematics of the numerical multi-model adaptive method have now been presented in the previous sections. The following section treats the application of this approach to an academic test case of a holed plate subjected to a compressive bending test case.

4.5 Numerical application case

4.5.1 Description of the academic test case

The developed numerical strategy is applied to the same test case as presented in section 3.4.3. It is a holed plate made of 16 unidirectional plies oriented at 0 deg made of T700/M21 subjected to a compressive-bending loading. The solver used is Abaqus/Standard and the material damage law, OPFM, is implemented through a UMAT. The adaptation part is handled through Z-set which performs in particular the remeshing and state update operations. The initial model represented in Figure 4.14 (A) is fully shell elastic subjected to a bending loading at the left and right edges. Prior to the computations an optimum mesh size for each domain has been defined. The results are compared to the reference model Figure 4.14 (B) which includes an initial solid zone around the hole.

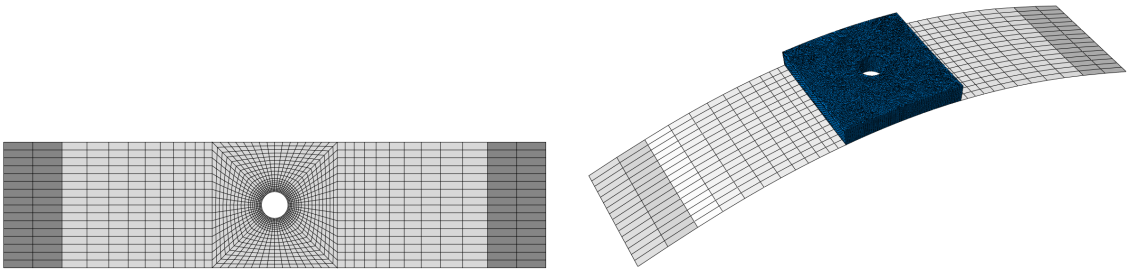

FIGURE 4.14: Initial (A) and reference (B) FE model of a bending holed plate made of 16-plies unidirectional laminate.

4.5.2 Numerical results

Even if bending occurs, the main damage mechanisms are in-plane in this particular case. Thus the remeshing is driven by the failure indexes f_1 and f_2. This is illustrated in Figure 4.15 with the mapping of the failure indexes at three different times on the timeline. The illustration is performed in the undeformed configuration to clearly see the progressive extension of the volume area. The illustration is zoomed on the damage which initiates around the center hole.

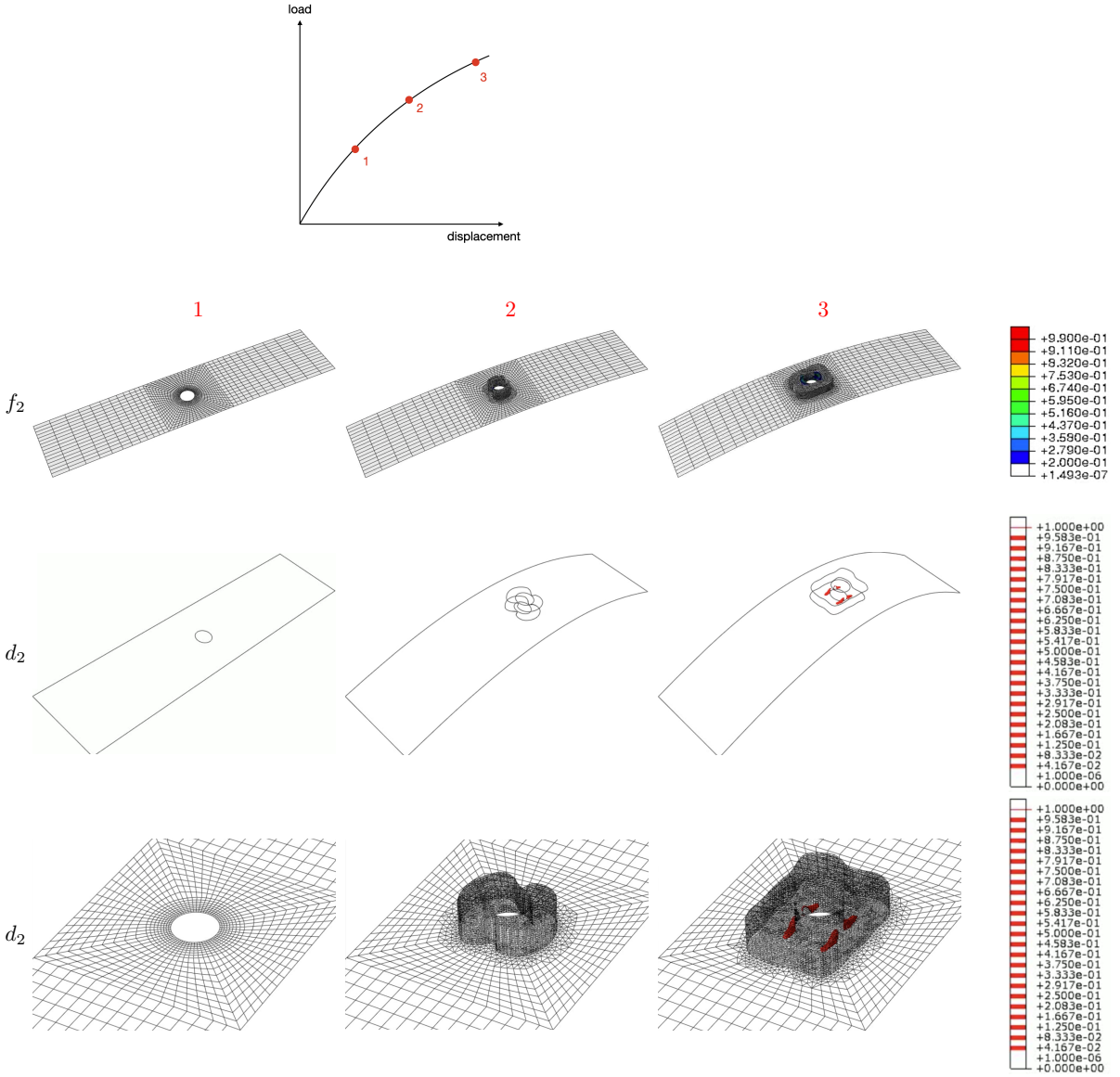

FIGURE 4.15: Failure indexes f_2 for the case of a bending holed plate laminate plot over the undeformed shape at the center of the probe.

The proposed method presents the strong advantage of being fully automatized. It is thus interesting to compare what computational time is allocated per adaptation stage and what gain is observed compared to the previously defined reference model.

4.5.3 Sensitivity to user parameters

The robustness of the adaptation strategy was tested through the variation of two main user parameters, the value of the localization criterion α and the remeshing distance D defined in section 4.3.2. Several reasonable sets of parameters, in the sense that the localization criterion α is close to 1 and the remeshing distance D has an order of magnitude related to the size of the problem, are presented in Table 4.2.

The results of the total computational time over the computational time of the reference model

Case	Localisation criteron α	Remeshing distance D [mm]
1	0.8	3.
2	0.8	5.
3	0.8	7.
4	0.6	3.
5	0.6	5.

TABLE 4.2: Sets of parameters of the adaptive multi-model approach for the compressive-bending holed plate.

represented in Figure 4.14 (B) for the different sets of parameters is illustrated in Figure 4.16, where the time allocated per operation is represented by a different color.

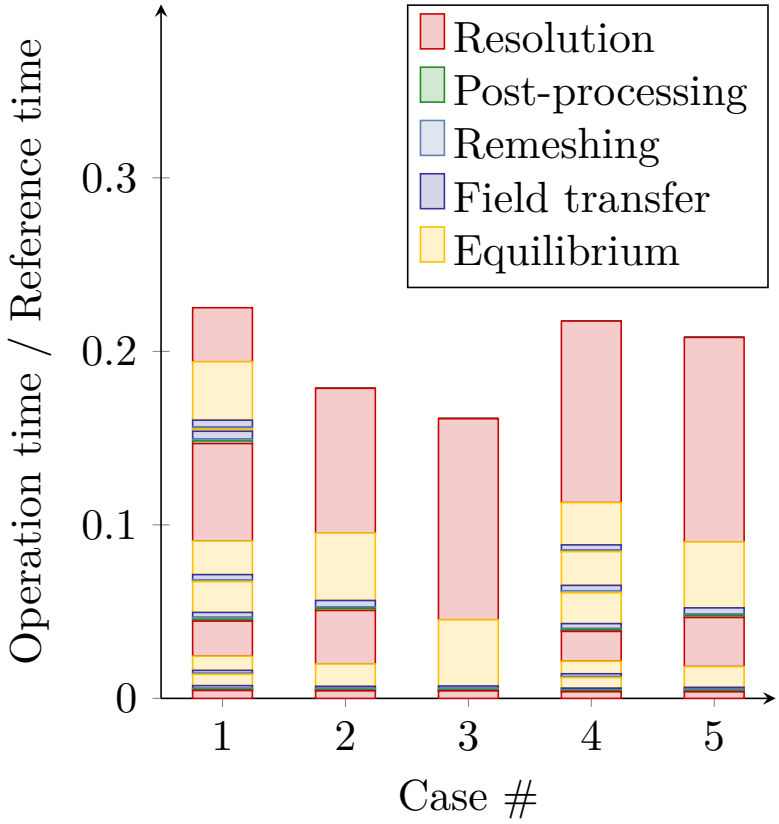

FIGURE 4.16: Computational time evaluation respective to the reference case for different sets of localisation criterion α and remeshing distance D.

The results of the study show a reduced computational time by a factor of 4 to 6 due to the reduction of the number of volume elements allowed by the developed strategy. The main contribution of the method is thus its flexibility on the area to be modelled more precisely. Also it can be noted that the method is not very sensitive to the change in user parameters. Although there are small tendencies observed such as: the bigger the remeshing radius, the smaller is the total computational time and the smaller the localisation criterion, the smaller is the total computational time. Even so, the total computation time of the developed strategy does not vary a lot compared to the reference computation given that the user parameters are chosen reasonably

with respect to the size of the studied problem. Therefore the robustness of the proposed method is demonstrated in this use case.

It can be noted that the equilibrium process generally lasts longer than the other operations. This is due to the fact that the equilibrium step includes both the equilibrium computation and the recovery of the computation from Z-set to Abaqus. Some software improvement can be made to reduce this computational time mainly due to the change of software frame.

4.5.4 Accuracy assessment

To assess in a precise manner the influence of the adaptive multi-model strategy on the solution of the developed numerical method, the results from the adaptive approach are compared to the last adapted model computed from the start. The error on the global response is evaluated for different mesh configurations respective to the last model decomposition run from the beginning.

Here, the global response is evaluated as the resulting load for a plate subjected to an imposed displacement. The analysis was led for three different mesh types, linear wedges, quadratic wedges and linear parallelepipeds. The relative error for each case with respect to the reference case is presented in Figure 4.17.

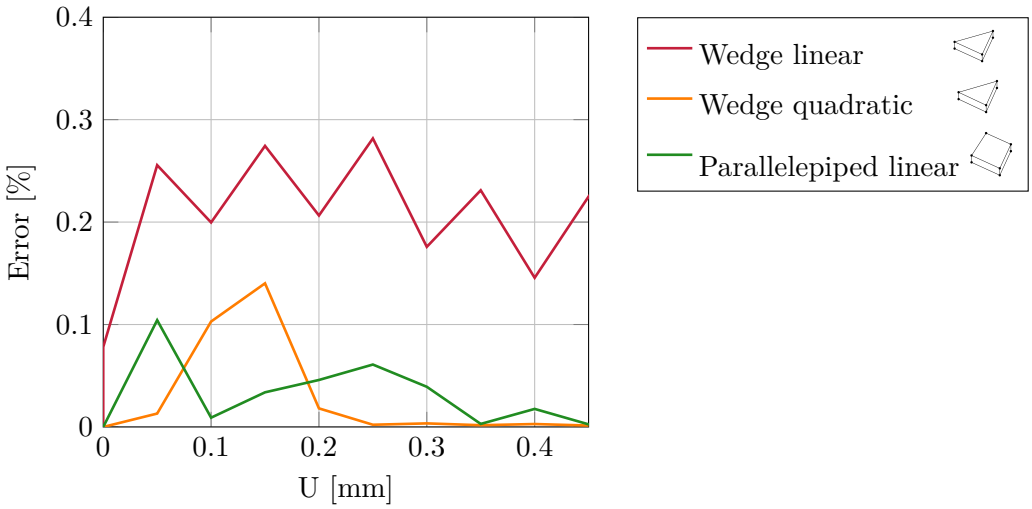

FIGURE 4.17: Relative error between the global displacement response between the adaptive result and its reference result for different meshes.

The errors are low, less than 0.4%, on the global response even if there might be larger local errors. On one hand, the error decreases when using parallelepiped elements instead of wedge ones by up to 0.28%. On the other hand, the error decreases when using quadratic elements instead of linear ones by up to 0.24%.

Conclusion

In this chapter, the adaptive multi-model approach is developed. Its principle is to launch a finite element analysis, that can be discretized using only shell elements at start, and automatically adapt its partition between shell and volume areas when the linear elastic model is no longer valid through the shell area.

First, a model adaptation indicator based on failure criteria was presented. This choice allows the model adaptation to suit the regions where damage can occur. Secondly, a remeshing strategy to create the new model partition with a volume area and a shell area was described. An underlying 2D mesh is preserved through the computation to be able to preserve the mesh in relevant areas where failure occurred. This smart remeshing strategy allows to justify the use of simple field transfer operators to reduce time consumption during the state update step. After the state update, a local and a global equilibrium computation steps are conducted before resuming the computation. Finally, the strategy was applied to an academic test case of a compressive-bending holed plate which shows promising results in terms of flexibility and robustness.

Now that the approach is validated on an academic test case, it is interesting to test it on more complex problems. Hence, the following and last part of this work is to construct a complex industrial test case and to assess the performances of the strategy in modelling the failure of a large composite component.

5 Experimental and virtual testing of a large composite structure

This chapter presents the design and analysis of a complex industrial test case which consists in the estimation of the residual strength of an impacted stiffened panel. First, the preliminary design of the test case is presented. Then, the damage introduced by impact is addressed considering both experimental and numerical results. At last, the simulation to estimate the residual strength in compression of the impacted stiffened panel is detailed considering also the experimental test results, and the applicability of such a method on a real composite structure is discussed.

Contents

4.1 Progressive model adaptation strategy 72
4.1.1 Brief overview of adaptive remeshing techniques 72
4.1.2 Multi-model adaptation scheme 74
4.2 Model adaptation indicator and criterion 76
4.3 Smart remeshing strategy 78
4.3.1 Identification of areas to be remeshed 78
4.3.2 Remeshing steps 79
4.3.3 Mesh refinement with quadrangular elements 79
4.3.4 Preservation of mesh in degraded areas 81
4.3.5 Conclusion 82
4.4 State update 83
4.4.1 Field transfer operators 83
4.4.2 Field transfer strategy 85
4.4.3 Equilibrium 87
4.4.4 Conclusion 88
4.5 Numerical application case 89
4.5.1 Description of the academic test case 89
4.5.2 Numerical results 89
4.5.3 Sensitivity to user parameters 90
4.5.4 Accuracy assessment 93

5.1 Introduction

The objective of this chapter is to challenge the numerical strategy on a more complex structural case that is representative of the industrial problematic with an experimental comparison. Composite structures are mostly used for slender laminated structures such as stiffened panels in the aeronautical industry. The composite laminates present the particularity of being able to present internal damages that are barely visible externally. This threshold is called the Barely Visible Impact Damage or BVID. The structure has to withstand the load even in presence of those small damages that are not perceptible. Even though some studies show promising advances on the monitoring of impacts through the lifecycle of an airplane [Goutaudier et al., 2020], the current approach is to make sure that a BVID defect induced by impact will not influence the residual strength of a component. In this chapter, the numerical adaptive method is challenged on this type of problem of residual strength estimation of pre-impacted stiffened panels.

The chosen application case is to simulate the ruin scenario of a pre-impacted panel in compression. For compressive loadings several ruin scenarios may occur such as stringer debonding, failure by global buckling and material failure propagation. For instance, Figure 5.1 represents a stiffened panel failure where both stringer debonding and global buckling are observed. The case of the final ruin piloted by the global buckling of the structure often happens with thin panels. For instance, if there is a damage on the skin, a part of the stress is redistributed on the stringers and it prevents the damage from propagating on a too large area. On the contrary, with thick panels, the rupture of the fibres in compression can propagate through the panel and lead to final failure. This experimental study corroborated by numerical results, on such an industrial

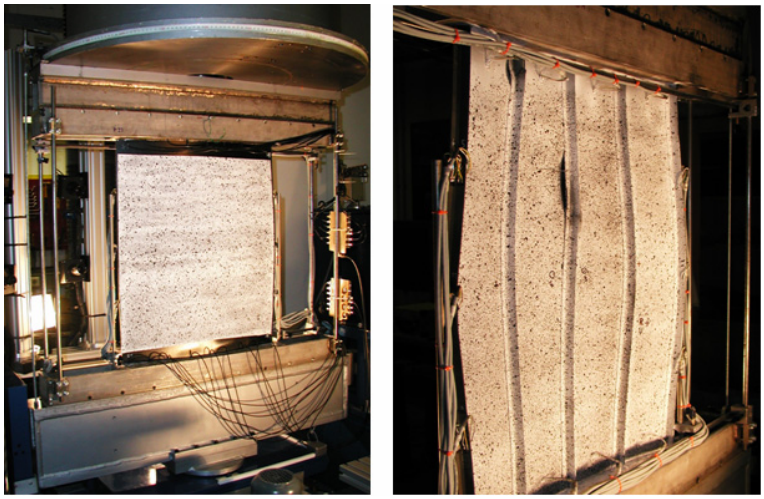

FIGURE 5.1: Image of a compression test of a stiffened panel [Winzen, 2006].

test case, is presented in this chapter through three sections. The first section of this chapter addresses the design of the use case with, in particular, the choice of the panel geometry and the impact strategy to produce the desired ruin scenarios. Then, the second section focuses on the introduction of damage mechanisms in the panel due to an impact with both experimental and numerical aspects. The last section details the test and simulation of the residual strength by

compression of the pre-impacted structure using the adaptive meshing strategy, associated to an advanced damage and failure model.

5.2 Designing for failure of a complex structural test case

5.2.1 A typical aeronautical component: the laminated stiffened panel

As stated beforehand, the retained use case for demonstrating the capability of the numerical adaptive method developed in this manuscript, is the damage tolerance study of a stiffened panel made of composite laminates. The residual strength of a pre-damaged structure is generally estimated in two steps firstly with the local introduction of damages, and secondly with the application of a global loading. Those steps are detailed hereunder.

1. For the case of stiffened panels, the damage may be for instance introduced by impact or by an initial debonding area. The impact induced damage is chosen here because numerous data are available in Airbus from experimental cases on laminated plates that are useful for numerical model calibration.
2. To assess the effect of damages, generally two types of loading are considered, the compression or the shearing of panels. Here, the compressive loading is chosen considering of available experimental devices at Onera.

One large stiffened panel, that was divided in two parts, has been provided by Airbus for the experimental study as reported in Figure 5.2. The idea was to have, at least, two panels in order to be able to reproduce two different ruin scenarios, a failure by global buckling and a failure by material rupture.

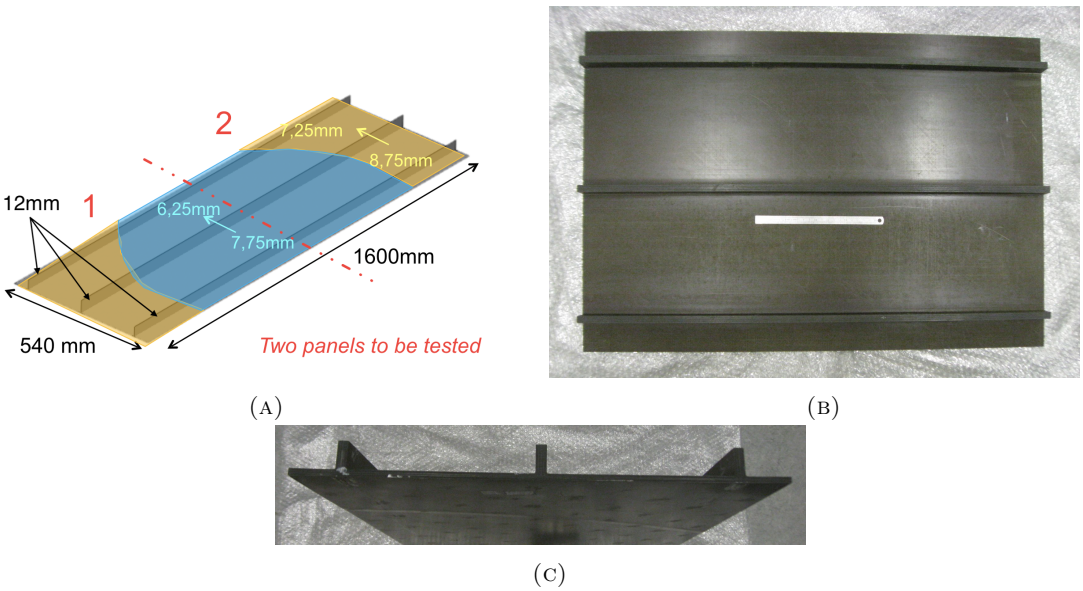

FIGURE 5.2: Stiffened panels geometry: (A) Image of the initial large panel; (B) Top view; (C) Rear view.

When designing the panels and the impact strategies in order to obtain the wanted failure scenarios, there were two main difficulties. On one hand, the provided panels are thick which is an experimental challenge due to the high load levels reached at failure, possibly higher than 1500kN. On the other hand, the provided panels present a complex variable stacking sequences through the width and the length of panel as illustrated in Figure 5.2 (A). Hence, the panels are not symmetrical and so should be the failure as well. In a nutshell, the provided panels present a very complex geometry representative of an industrial case which is interesting while challenging.

The length and the width of the panels being fixed, and equal respectively to 790mm and 540mm, the design study detailed in the next section focuses on the estimation of the adequate height of the stringer, and of the impact location and energy. It can be noted that the thickness of the provided panels is such that the compression machine load capacity available at Onera and equal to 1500kN becomes a limiting factor of the study. An additional constraint in the design is thus that the maximum compression load must not exceed a limit below this capacity for safety reasons.

5.2.2 Preliminary computations

5.2.2.1 Finite Element Model

In order to determine a relevant panel geometry, in particular the height of the stringers, to ensure the previous recommendations (i.e. to obtain a failure load lower than the maximal capacity of the Onera experimental device of value equal to 1500kN), and to obtain relevant failure modes respectively by global buckling and by material failure, some preliminary finite element simulations have been performed. Quasi-static compression simulations with Abaqus Standard were led using a linear elastic material model and shell elements. A fixed displacement rate of 0.5mm/min was imposed at the top of the panel. The number of elements is approximately 10 000. The geometry and boundary conditions of the panel are reported in Figure 5.3. An end side of the panel is clamped (all the displacement and rotation dofs are equal to zero), while a displacement in the panel longitudinal direction is imposed on the opposite side of the panel (the other dofs being fixed).

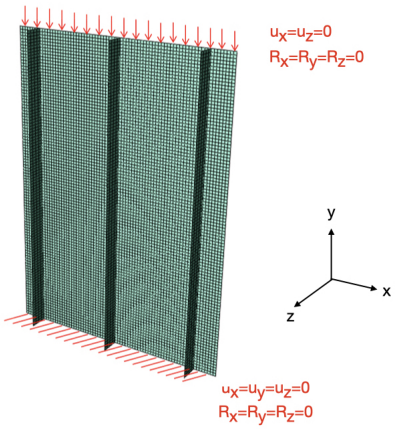

FIGURE 5.3: Finite element model of a stiffened panel.

5.2.2.2 Indicators

As stated before, two different types of ruin scenario are targeted, (i) the failure by global buckling of the panel and (ii) the material failure (fibre failure in compression). To be able to distinguish which one occurs, three indicators were considered: the first buckling load, the maximal collapse load and the material failure load. If the material failure load occurs before the maximal collapse load, the rupture is assumed to be driven by material failure otherwise the ruin of the panel is assumed to be induced by global buckling. It is important to notice here that the post-buckling range, *i.e.* the range between the first buckling load and the maximal collapse load, of the panel is very shallow due to the high stiffness of the structure.

[1] First buckling load This value was taken at the first change of strain slope of the shell elements. This method gives a rough estimation of the buckling load as the result precision depends on the time discretization.

[2] Maximal collapse load The maximal collapse load is the peak of the global load response, and corresponds to the global collapse of the panel.

[3] Material failure criterion As the constitutive behaviour used for the panel dimensioning is linear elastic, damage is not included in the present model. To assess if the material is broken, a failure criterion developed by Airbus is used. For an initially sane material, a maximal longitudinal strain criterion is considered to predict the ply failure in fibre compression mode. For an impacted material, the failure criterion remains similar but the strain at failure decreases as a function of damage due to impact. In other words, a set of allowable strains in compression were provided by Airbus for the material failure assessment. The allowable strains were determined experimentally for similar laminate stacking sequences. Moreover, for an impact on the skin, the strain at failure is defined as a function of impact energy based on test data. For an impact on the top of a stringer, the strain at failure is defined as a function of the delaminated area measured on test data.

5.2.2.3 Results of preliminary computations

During the preliminary computations, depending on the considered finite element model, the panels either buckled in one direction or in the opposite direction. The most critical situation in terms of load level would be if the panel buckled such that stringers are in traction. Consequently, the load vs displacement curves, obtained for different height of stringers, when the buckling occurred such that stringers are in traction, are presented in Figure 5.4. In such a configuration, a panel with a stringer height superior to 30mm would exceed the maximal machine capacity.

In the next paragraph, the idea consists in designing the impact (location and energy level) using the Airbus methodology described previously. The late methodology is based on the assumption that the strain at failure depends on the impact energy level in the skin. Whereas, in the stiffener, the strain at failure depends on the delaminated area due to impact. If the structure is sane, the strain allowable in the fibre direction is at approximately -10 000 microstrain in compression.

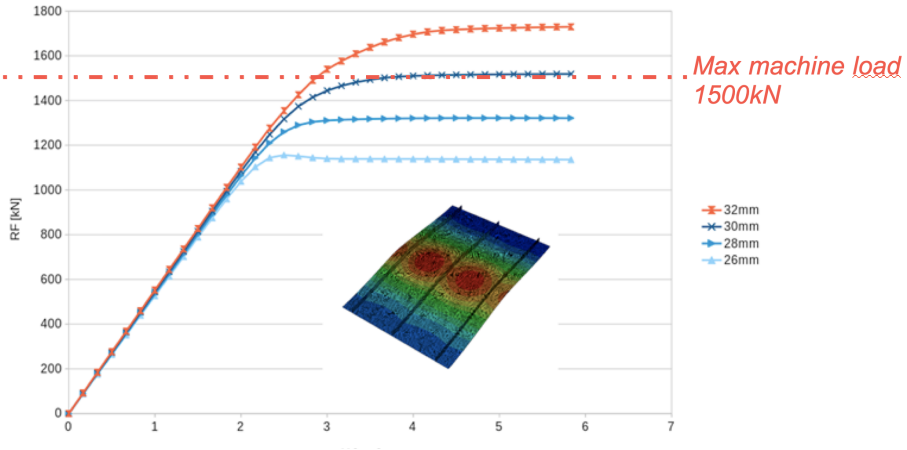

FIGURE 5.4: Load vs Displacement for different panel stringer heights.

For impacted panels, the strain at failure lowers. Figure 5.5 shows the evolution of the maximal strain from three different areas, composed of a set of elements (represented in red), in the structure. The first area (Figure 5.5 (a)) is located in the skin where the strains are the highest. The second area (Figure 5.5 (b)) is a part of the skin-stringer junction where the zones close to the panel edges were removed. The third and last area (Figure 5.5 (C)) is a part of the top of the stringer where the zones close to the panel edges were also removed.

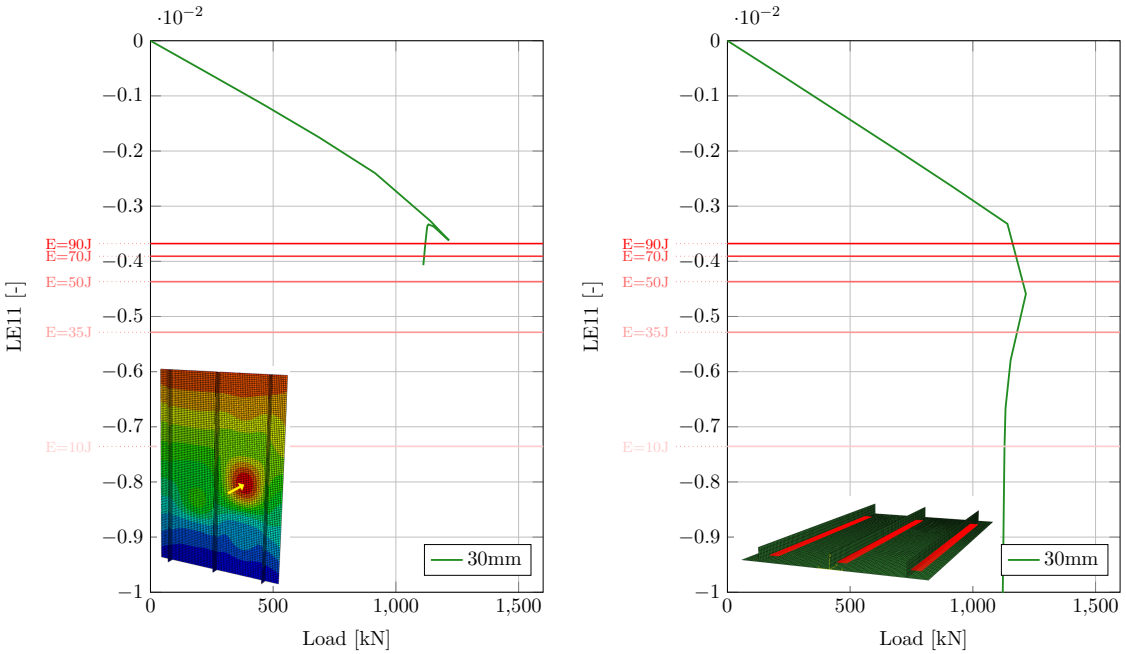

(A) Skin (B) Skin-stringer

FIGURE 5.5: Strain [-] vs Load [kN] with a stringer height equal to 30mm.

Those figures show that material rupture (fibre kinking in plies) can be reached before the global collapse of the panel for the following cases:

- The configuration with a 30mm stringer height with an impact on the skin of an energy superior to 90J.

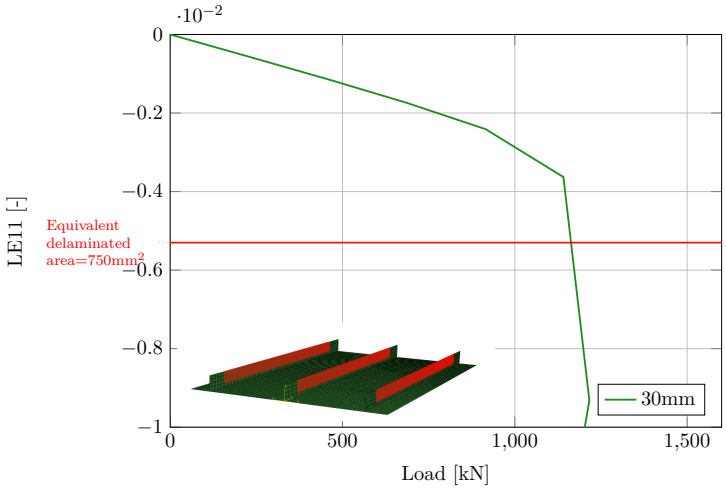

(C) Top-stringer

FIGURE 5.5: Strain [-] vs Load [kN] with a stringer height equal to 30mm (cont.).

- The configurations with a 30mm stringer height with an impact on the skin under a stringer of an energy superior to respectively 50J.
- The configurations with a 30mm stringer height with an impact on the top of the stringer with an energy to be calibrated which induces a delaminated area of 750mm^2.

5.2.3 Conclusion: Design of the stiffened panels

The final geometries of the two panels are reported in Figure 5.6. The height of the stringer has been chosen equal to 28mm for the impact on the skin, and to 30mm for the impact on the stringer. For the two stiffened panels, two ruin configurations are expected.

- **Case 1**: Final failure driven by material rupture after an impact on the top of the stringer at 20J located at mid-length of the panel.
- **Case 2**: Final failure due to global buckling after an impact on the skin at 50J located at approximately one third of the panel height.

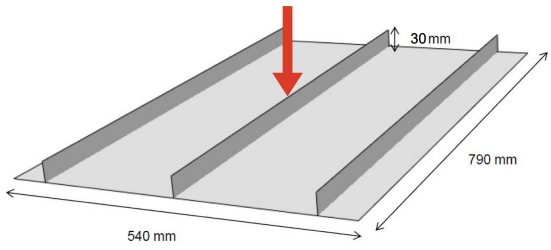

(A) Panel 1, Impact I_1

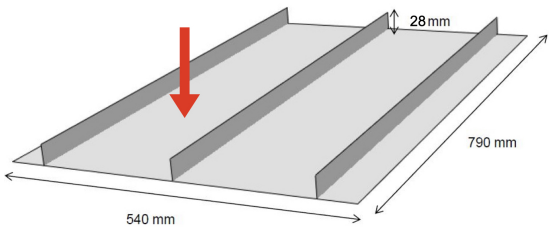

(B) Panel 2, Impact I_2

FIGURE 5.6: Final geometry of the designed panel: (A) Panel 1 and (B) Panel 2.

5.3 Initial damage introduced by low velocity/low energy impact

This section focuses on the damage introduced in the two panels by impact. Before impacting the two large panels, preliminary impact tests have been performed on smaller panels, presenting similar stacking sequences as the two stiffened panels. The objective was to determine the relation between the impact energy and the delaminated area, especially for the impact on the top of the stringer. Those experiments aimed at calibrating the impact energies for both use cases on large panels. This section first presents the experimental setting up, then the experimental results are presented and finally a numerical comparison is proposed.

5.3.1 Experiments

5.3.1.1 Impact machine and instrumentation

The impact machine, available at Onera, is a DYNATUP 8520 (Figure 5.7 (A)) with the following characteristics:

- load cell: 20kN,
- impactor: stroke:1200mm; mass:2.93-45.5kg; velocity:0.7-13.4m/s; energy:0.76-1170J,
- dimensions capability:100x150mm^2 to 1x1mm^2,
- laser optical sensor (to measure displacement on the opposite side of the impacted face during the test).

A non-destructive ultrasound pool (Figure 5.7 (B)) of 1x1x1m^3 equipped with ultrasonic transducers (central frequency from 0.5 to 10 MHz) is used to retrieve the delaminated area around the impact. The maximum scanned image dimensions is 300x300mm^2.

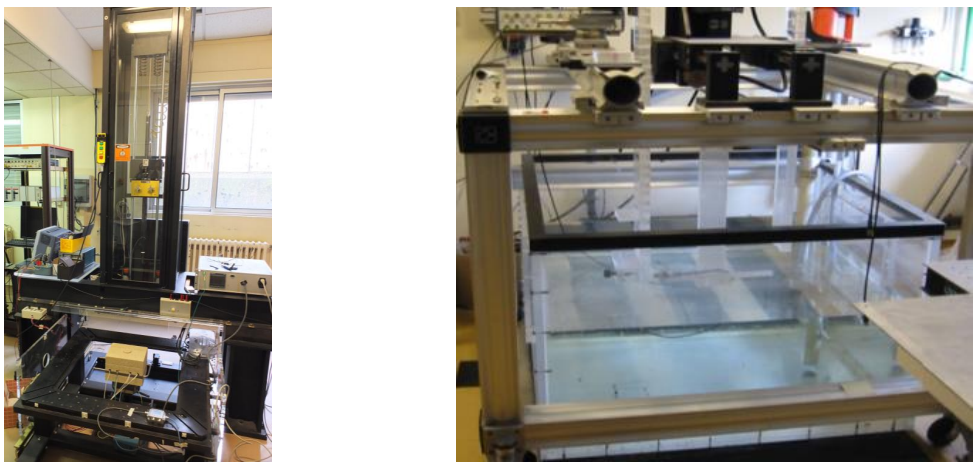

(A) (B)

FIGURE 5.7: Low velocity impact machine (a) - C-scan pool (b) [ONERA/DMAS, 2017].

5.3.1.2 Experimental protocol

The present experimental protocol is followed for the impact testing. The panels were fixed by clamps on a plate support with an impact window of 125x75mm^2. The impactor diameter has been chosen equal to 16mm and the impactor weight to 13.01kg.

1. Setting of the load cell, the anti-rebound mechanical stops, the impactor position and the laser displacement sensor under the impactor;
2. Positioning of the panel on its support;
3. Positioning of the system panel+support under the impactor;
4. Impact test at the targeted energy (20J for the Panel 1 and 50J on the Panel 2);
5. C-scan of the impacted area.

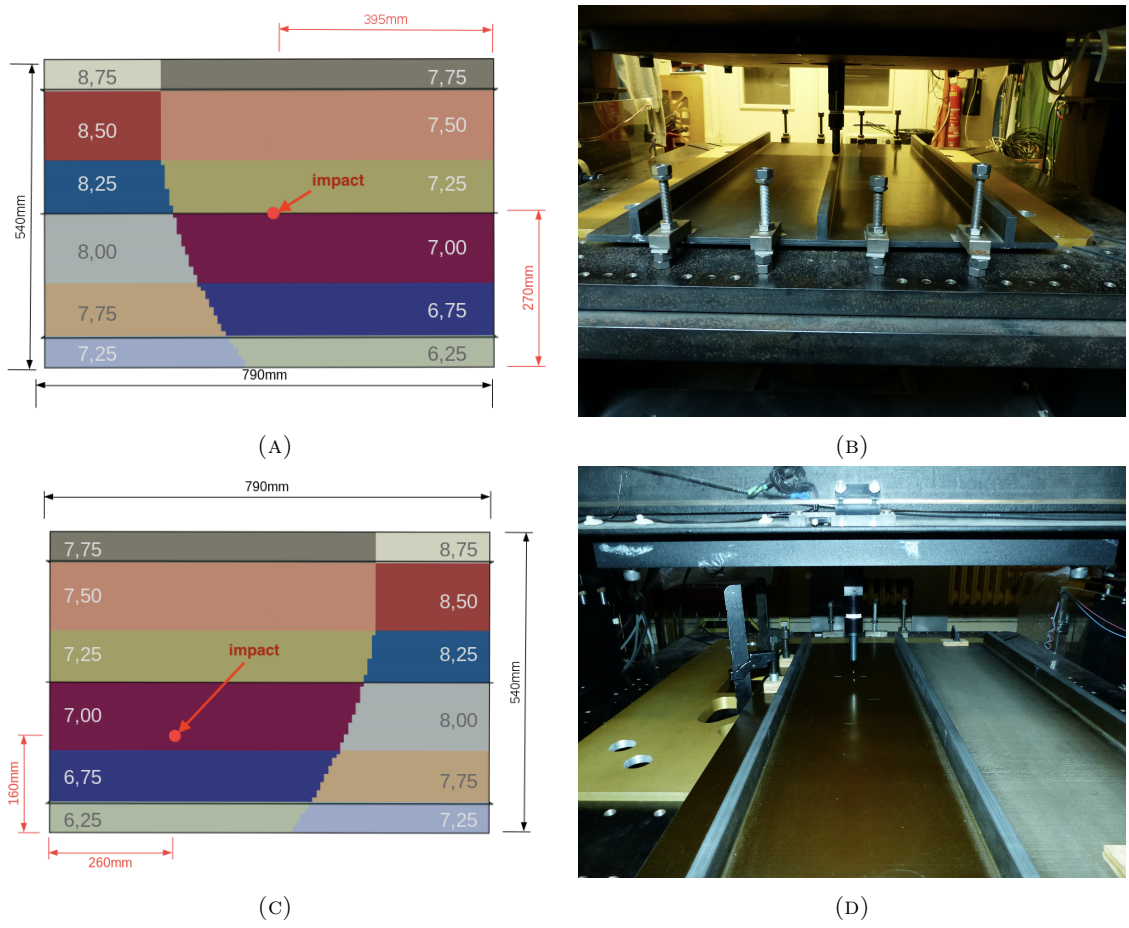

FIGURE 5.8: Position and mounting of impact testings: (A) Position of impact I_1 on Panel 1; (B) Mounting of impact I_1 on Panel 1; (C) Position of impact I_2 on Panel 2; (B) Mounting of impact I_2 on Panel 2.

Several trial impacts have been performed on a dummy panel prior to impacting the large panels in order to gain in experience, especially for the impact on the stringer. The impacts on skin showed more repeatability than the impacts on stringer edge. For the impact on stringer edge, the setting-up is mostly done by human eye causing the impact not to be perfectly centred. This induces a non-symmetrical repartition of the damage through the stringer thickness. The damage

is hence more visible on one side of the stringer than on the other as it has been observed with two C-scans, one on each side of the stringer. Furthermore, the panels being thick, two scans were performed (one per face) for both impacts.

5.3.1.3 Experimental results

In this section, several experimental results of both impacts respectively on Panel 1 and 2 are exposed. First, the load and energy evolutions of the impacts recorded by the impact machine are presented. Then, the C-scan images of the areas surrounding both impacts are shown. The C-scan images were used to determine the extent of the delaminated area for both impacts. Finally, X-ray tomographies were performed on both panels by CETIM to analyse the real geometry and the damage extent in a precise and volume manner for both panels.

Impact load and energy

The impact machine provided the evolution of the measured load and the computed energy as represented in Figures 5.9 and 5.10. Regarding the load evolution, it can be noted that, as expected, the maximum load level of the impact I_1 on the top stringer is lower than the maximal load of the impact I_2 on the skin. It can also be noted that the maximal load does not increase within the same proportions as the energy level. In this case, the energy level is more than twice superior for I_2 than I_1, but the load just increased by approximately 30%. Moreover, one can observe that the load response of the impact of the skin is much smoother than the load response of the impact on the stringer. This highlights that the damage mechanisms occurring during an impact on the skin are quite different from the damage mechanisms occurring during an impact on the stringer. Regarding the energy level, it can be noted that the actual impact energy is slightly higher than the targeted energy due to experimental uncertainties.

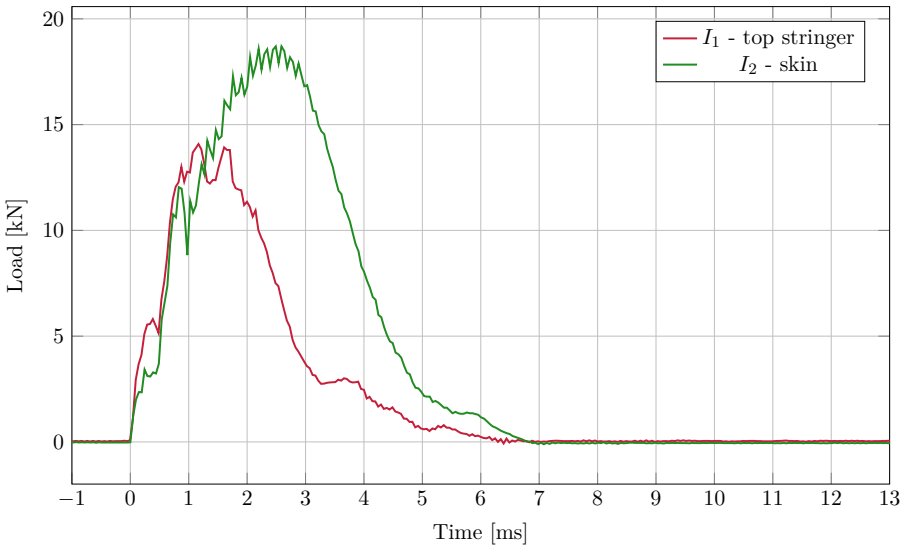

FIGURE 5.9: Experimental impact load vs time results for the two panels.

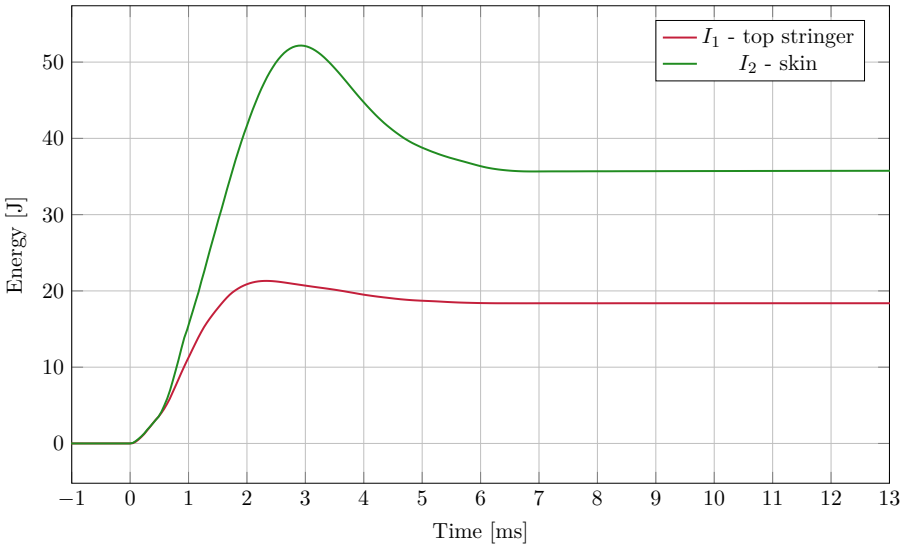

FIGURE 5.10: Experimental energy vs time results for the two panels.

C-scan images

The panels were scanned region per region in the C-scan pool. The scans are presented in Figures 5.11 and Figures 5.12 for respectively the impact I_1 on the top of the stringer and the impact I_2 on the skin. The scans were each performed on both sides of each one of the impact areas because of the consequent thickness of the panel which induces loss of information. Moreover, the C-scan images were used for projected delaminated area estimation which was computed as the area inside the envelope of the delaminated areas.

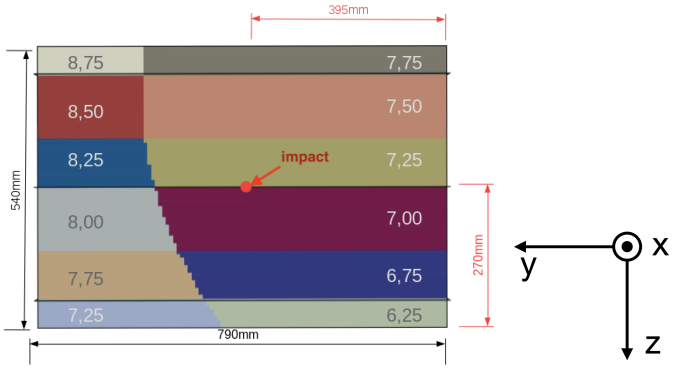

(A) Impact location

FIGURE 5.11: C-scan images of the top stringer impacted area (Impact I_1).

Regarding Figures 5.11 (B) and (C), performing the C-scan of the stringer was not an easy task and has necessitated a special attention. For instance, the whole height of the stringer could not be scanned due to the fact that the sensor was positioned above the panel skin with an offset. The extent of the observed damage is consequently limited to a given height from the top of the stringer. Moreover, Figures 5.11 (B) and (C) do not present the same color bar, the color bar of Figure 5.11 (B) being less wide than the color bar of Figure 5.11 (C). Even so, the Figure 5.11 (C) shows more damage than the Figure 5.11 (B), highlighting the unsymmetrical nature of the

damage through the stringer width. This is explained by the calibration of the impact position which was done by the human eye.

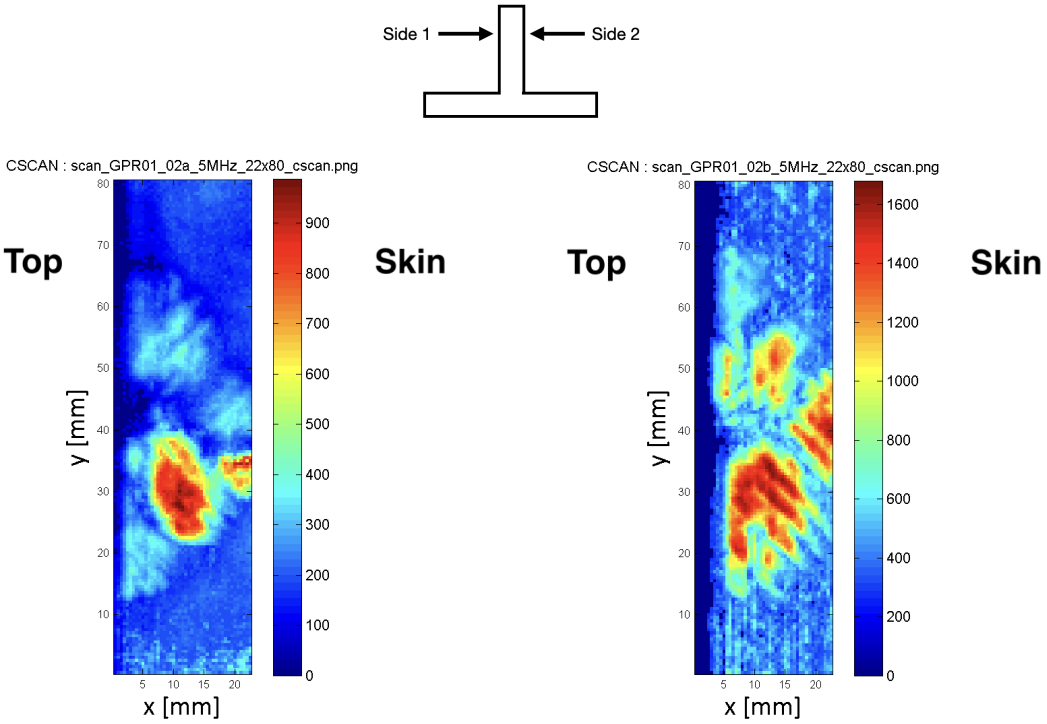

(B) I_1 Side 1 (C) I_1 Side 2

FIGURE 5.11: C-scan images of the top stringer impacted area (Impact I_1) (cont.).

Figures 5.12 (B) and (C) are the C-scan images for the impact I_2 on the skin respectively from above and from below the impact presented in Figure 5.12 (A). The length in the x direction of the observed damage is similar between the two figures. Nevertheless, the length in the y direction is slightly larger in the Figure 5.12 (C) than in the Figure 5.12 (B). This can be interpreted as the damage extends through the thickness of the skin, which is an usual experimental observation for an impact on a composite plate.

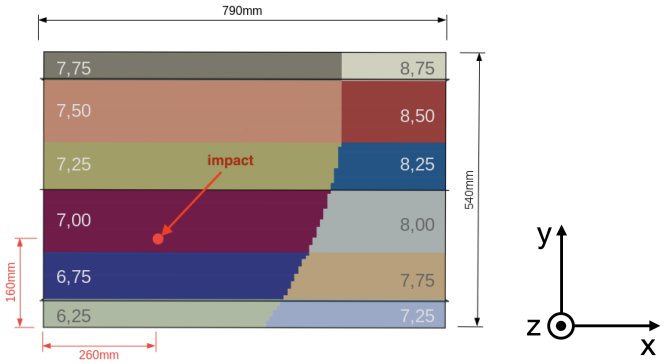

(A) Impact location

FIGURE 5.12: C-scan images of the skin impacted area (Impact I_2).

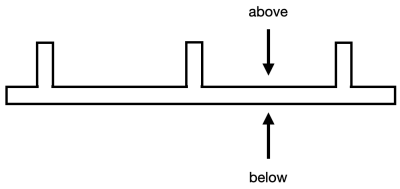

(B) Impact location

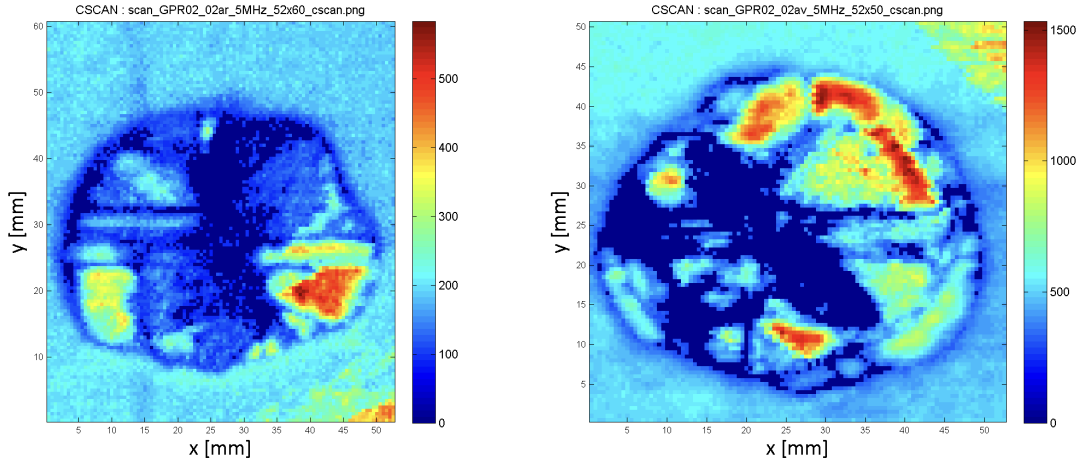

(C) I_2 above (D) I_2 below

FIGURE 5.12: C-scan images of the skin impacted area (Impact I_2) (cont.).

X-ray tomography

Within the frame of another collaboration between Airbus and Onera, whose objective was to quantify the geometrical and structural uncertainties within a complex industrial test case, X-ray tomographies were led on both panels. The results of the tomographies on large panels are detailed hereunder. Due to the dimensions of the panels, they have been scanned by CETIM in two times with an overlapping zone, the resolution being about 0.3mm. Then, the results were assembled by determining the 3 translations and 2 rotations to obtain a good match between the two overlapping zones including the central stringer. This process of assembly is illustrated in Figure 5.13.

Figures 5.14 and 5.15 represent the assembled geometries of respectively the Panel 1 and of the Panel 2 for both front and back views. The thickness variation of the skin is visible and so are the impact indentations. It can be observed that the stringer side of the skin is plane, whilst the opposite side presents the thickness variations.

The thickness evolution throughout the panels has been measured by tomography and is represented in Figures 5.16 (Panel 1) and 5.17 (Panel 2). The thickness varies from approximately 6mm to 11mm, the stringers being thicker than the skin. All stringers present the same thickness (coloured in red in Figures 5.16 (Panel 1) and 5.17 (Panel 2)), whereas the skin presents a variable thickness. The tomography results highlight the complex thickness changes along both the longitudinal and the transversal directions.

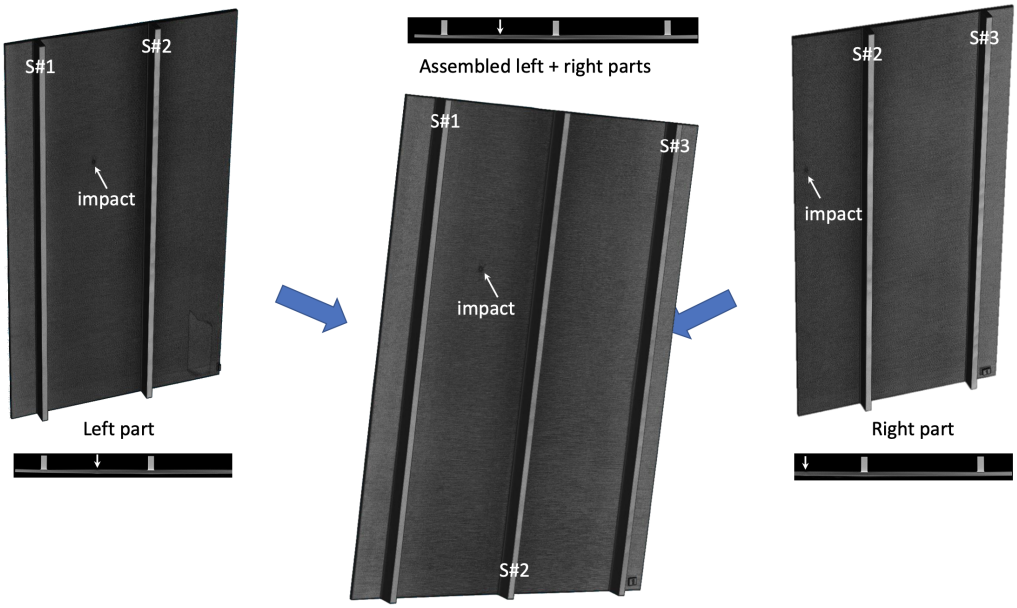

FIGURE 5.13: Assembly of two half panels' tomographies.

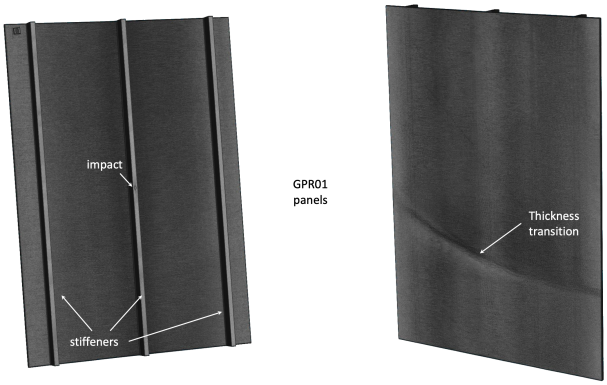

FIGURE 5.14: Tomography of Panel 1.

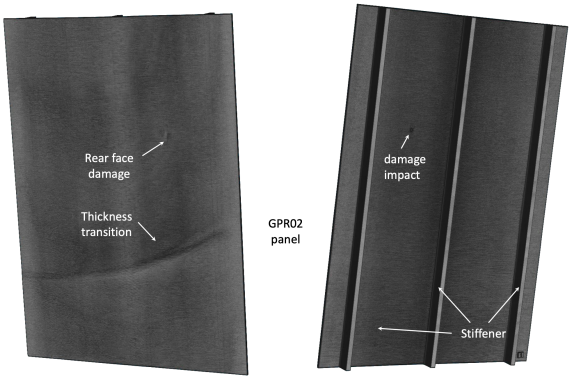

FIGURE 5.15: Tomography of Panel 2.

In addition, a more refined analysis of the delaminated area using the tomography was led for the impact on the top of the stringer of Panel 1. Those results are shown in Figure 5.18. Here, the results in terms of delaminated area are complementary of the C-scan and present in-depth information. The three dimensional aspect of the damage was retrieved. One can observe, for

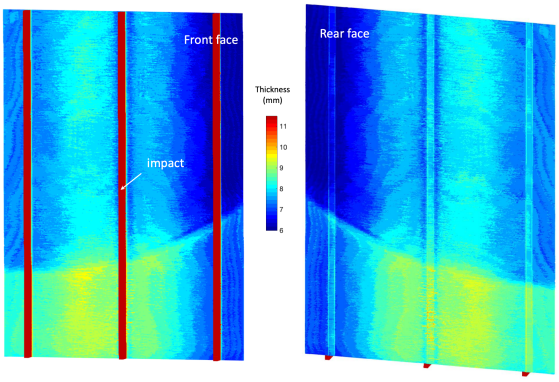

FIGURE 5.16: Thickness evolution measured by tomography of Panel 1.

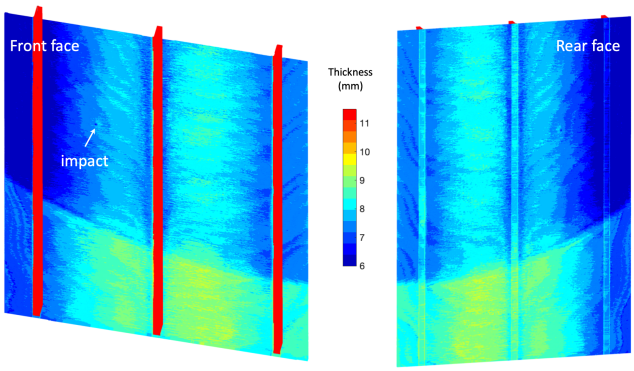

FIGURE 5.17: Thickness evolution measured by tomography of Panel 2.

instance, the particular shape of the impact damage, from a transverse cut view of the stringer, presenting two lobes. The two lobes are clearly unsymmetrical, one being more pronounced than the other, as deduced previously from the C-scan images.

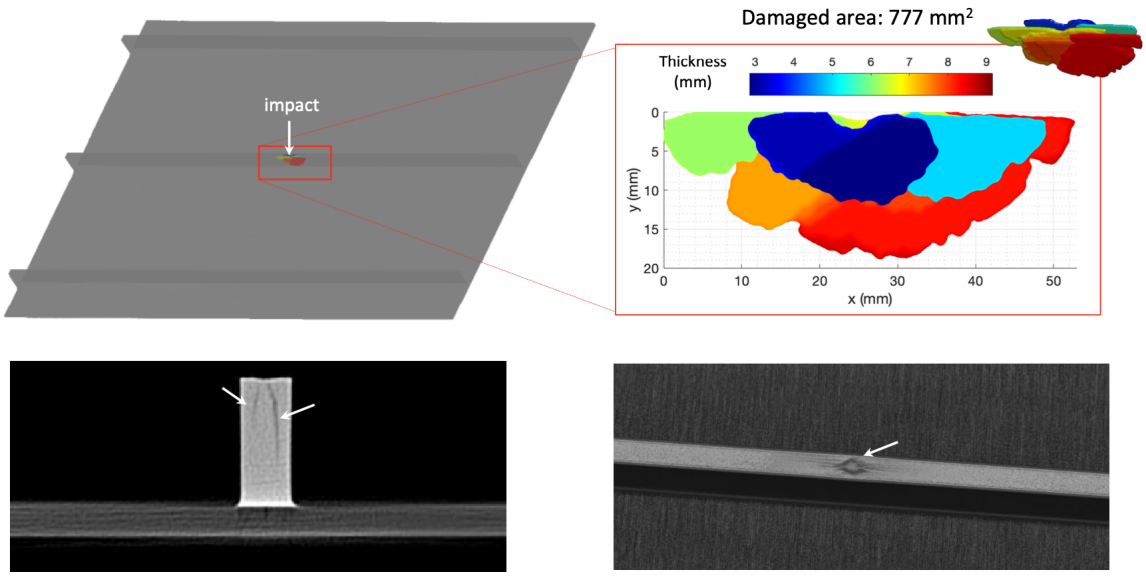

FIGURE 5.18: Tomography of the delaminated area of Panel 1.

Due to the resolution of the tomography (0.3mm), limited because of the size of the panel, the impact damage in the skin of Panel 2 could not be detected contrary to C-scan control.

Delaminated areas and BVID

Finally, the results of the delaminated area (from both the C-scan and tomography), the dissipated energy, the maximal load, and the BVID are reported in Table 5.1.

Id.	E_{target} **[J]**	E_{real} **[J]**	F_{max} **[kN]**	**Delam. area C-scan [mm²]**	**Delam. area tomo. [mm²]**	**BVID diam. [mm]**	**BVID depth [mm]**
I_1	20	21.01	14.32	880	777	5.5	0.04
I_2	50	51.52	18.93	1680	-	6.0	0.20

TABLE 5.1: Impact results on stiffened panels.

The projected delaminated area, computed using the C-scan images, is determined by the computation of the area delimited by the external boundary of the delamination. This technique is routinely used by Airbus's teams. The delaminated area computed from the tomography is close but slightly inferior to the one computed on the basis of the C-scan. This can be explained by the resolution of the tomography limited to 0.3mm due to the large dimensions of the impacted panels.

Furthermore, regarding the energy results, the targeted energies are close to the real ones. It can be noted that the ratio between the delaminated areas from the impact I_1 over the impact I_2 is smaller thant the ratio between the corresponding energy levels. Consequently, an impact on the top of the stringer is more critical than an impact on the skin. It comforts the wanted scenarios which are a failure by material rupture for the panel impacted on the top of a stringer and a failure by global buckling for the panel impacted on the skin.

5.3.1.4 Conclusion

The previous section focused on presenting the experimental data for the impact on both the top of the middle stringer for Panel 1 and on the skin for Panel 2. The load and energy evolutions through time and the ultimate damage extent were quantified. The objective of the following section is to confront those observations with numerical results from impact simulations.

5.3.2 Numerical comparisons

The numerical simulations of impacts on the two stiffened panels required a large amount of model preparation and are computationally costly. Both impacts were simulated using Abaqus/Standard with a dynamic implicit solver. The two models are first exposed and the obtained results are further detailed and compared with the experimental observations presented previously.

5.3.2.1 Finite element models

Geometry and mesh Both simulations involve two geometrical entities, the panel itself and the impactor, but are modelled in three parts. The panels are modelled with two different parts distinguishing the zone of interest where the impact occurs and the remaining part to gain in numerical efficiency. The finite element models of Panel 1 and Panel 2 are presented respectively in Figure 5.19 and Figure 5.20.

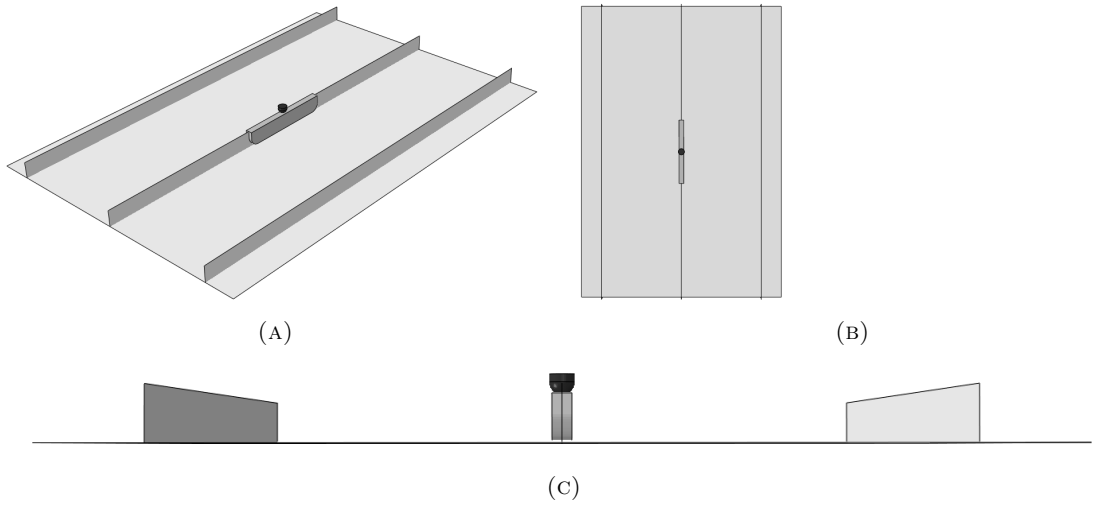

FIGURE 5.19: Finite element model of the impact on the top stringer I_1 of the Panel 1: (A) 3D view; (B) (xz) plane; (C) (xy) plane.

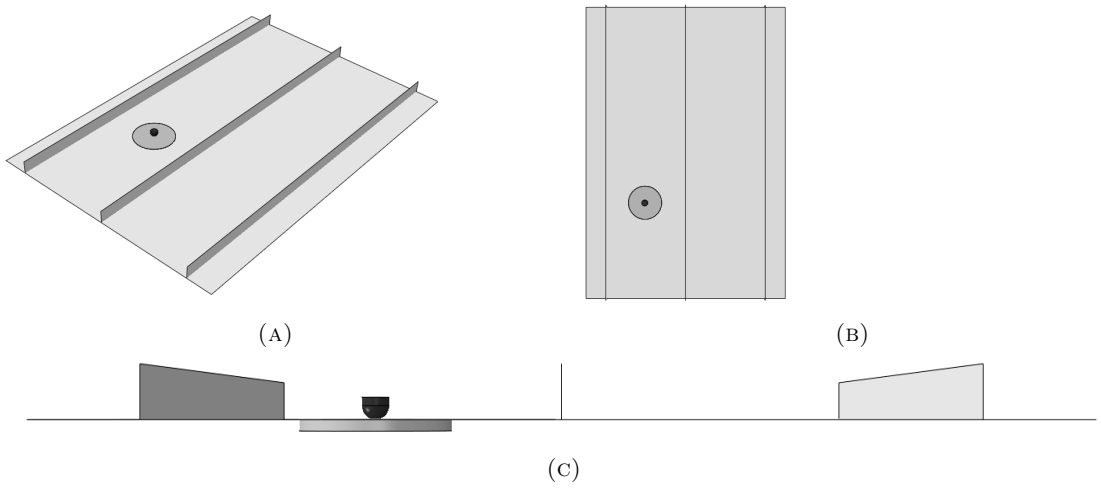

FIGURE 5.20: Finite element model of the impact on the skin I_2 of the Panel 2: (A) 3D view; (B) (xz) plane; (C) (xy) plane.

The zone surrounding the impact is modelled with ply-per-ply solid elements and the damage law OPFM. On the complementary zone, the panel is modelled using homogenized structural shell elements. It can be noted that the lay-up varies through the panel so lots of composite sections are implemented as represented in Figures 5.11 and 5.12. The hemispherical impactor is modelled with rigid elements with a mass inertia of $0.01301t$ corresponding to the actual mass of the impactor. Images of the meshes are presented in Figure 5.21. It can be noted that the number of elements in the volume areas is much larger than the number of shell elements used in the rest of each panel structure. This is mostly due to the need of limiting the volume elements' distortion considering the ply thickness. Furthermore, the model of the impact on the stringer is much larger than the model of the impact on the skin because the stacking sequence of the stringer presents more plies than the stacking sequence of the skin.

Panel 1

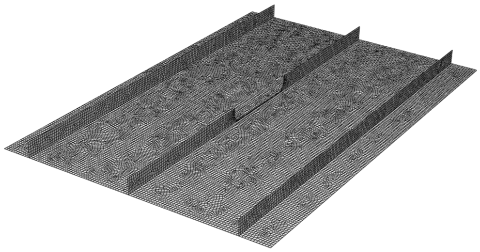

S4R and S3 elements:23325
Element size: 2.0-5.0mm

Panel 2

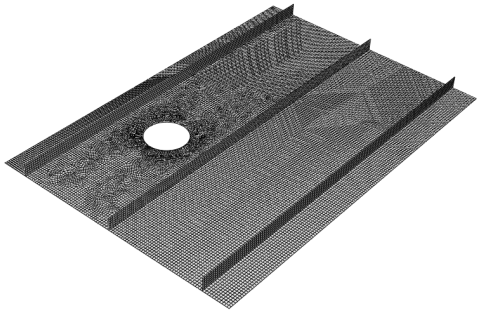

S4R and S3 elements: 23483
Element size: 2.0-5.0mm

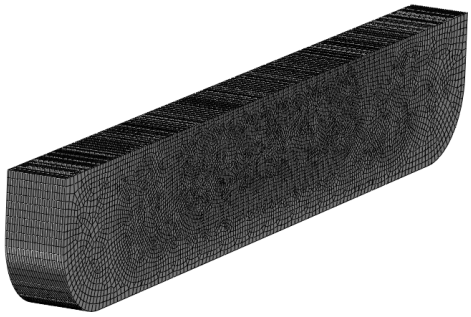

C3D8R and C3D6 elements: 370368
Element size: 0.8-1.5mm

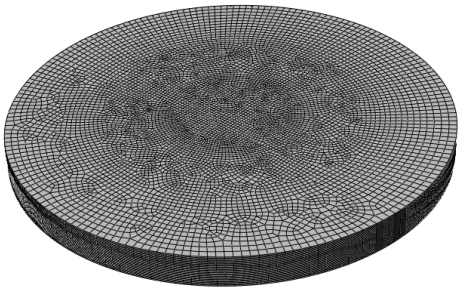

C3D8R and C3D6 elements: 197938
Element size: 0.65-1.3mm

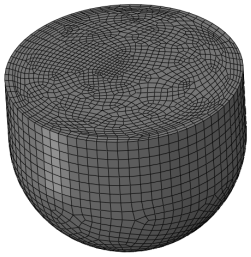

C3D8R elements: 10423
Element size: 0.7mm

FIGURE 5.21: Finite element mesh of the different entities for the simulation of impacts on stiffened panels: I_1 for Panel 1 and I_2 for Panel 2.

The multidimensional coupling between the two zones of the panel (respectively shell and solid zones) is detailed in chapter 3. As a reminder, the two zones are coupled by a surface-to-surface condition, the shell-to-solid coupling condition available in Abaqus. It ensures a certain displacement continuity. However, this condition does not guarantee the kinematic compatibility between the shell and the solid zone. Consequently an additional constraint is applied on the solid interface for it to respect the Reissner-Mindlin shell behaviour. It is implemented in Abaqus with the MPC SLIDER.

Material Only the zone of interest is modelled with a damage law. Here, the used law is the Onera Progressive Failure Model (presented in chapter 2) which has been identified for the used material and which accounts for several damage mechanisms. These constitutive equations have been implemented as a UMAT in Abaqus/Standard. On the rest of the structure, the OPFM model is also used but the damage has been deactivated. It can be noted that non linear elasticity and viscosity are modelled through the entire structure.

Boundary conditions and loading The boundary conditions for the panel are presented in Figure 5.22, where the rectangle in red represents the window of impact. The edges of the panel are clamped and the out-of-plane displacement is constrained outside the window of impact which size is $125 \times 75mm^2$. This condition is stiffer than in reality because, on the experimental mounting, the panel is on a bearing plane and is only constrained in the negative out-of-plane direction.

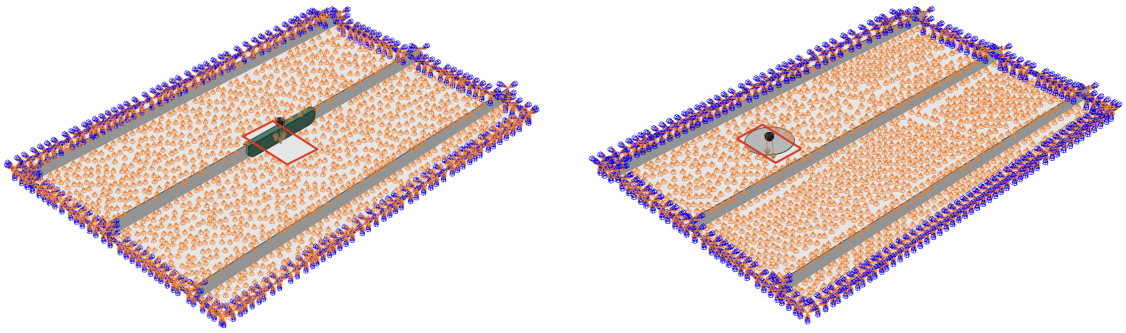

(A) (B)

FIGURE 5.22: Boundary conditions for the impact simulation: (A) Panel 1; (B) Panel 2.

The impactor movement is limited to the normal direction and is subjected to an initial velocity field (calculated with Equation 5.1) to transmit the same amount of energy E as measured in the experiment.

$$\begin{cases} v_{init}(\text{Panel 1}) = \sqrt{\frac{2E}{m}} = \sqrt{\frac{2\times 21010\text{mJ}}{0.01301\text{t}}} = 1787\text{mm s}^{-1} \\ v_{init}(\text{Panel 2}) = \sqrt{\frac{2E}{m}} = \sqrt{\frac{2\times 51520\text{mJ}}{0.01301\text{t}}} = 2814\text{mm s}^{-1} \end{cases} \tag{5.1}$$

Interaction The contact between the impactor and the panel is enforced through a hard contact normal behaviour and a frictionless tangential behaviour.

5.3.3 Numerical results

In order to compare the results of simulations to the experimental ones, two types of results are retained. On one hand, the load response of the impactor is plotted to assess if the global response of the structure to the impact is correctly modelled. On the other hand, the damage variables from the OPFM constitutive behaviour are represented in order to estimate if the damage extent is well captured by the numerical simulations.

Load response

Figure 5.23 represents the experimental and numerical load response for the impact I_1 on the top of the stringer of the Panel 1. The simulation was not led until completion due to convergence issues. One can observe that in the simulation, the response is much stiffer than the experimental response. Indeed, the main damage mechanism for such an impact is delamination. Usually, such a mechanism is described using cohesive zone elements, but it induces an additional numerical complexity, in particular when using remeshing techniques. Therefore, the delamination is accounted for in the diffused damage variable d_3 smeared through the ply. The predicted behaviour using diffuse damage does not dissipate enough energy compared to cohesive zone models. This explains, at least partially, why the prediction of the model is too stiff. This choice, arguable from a physical point of view, simplifies considerably the numerical procedure developed in this manuscript.

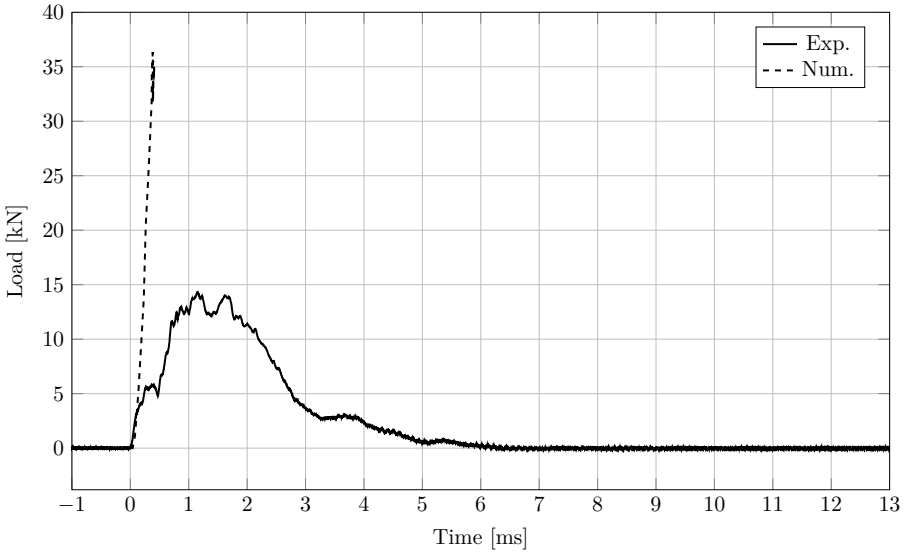

FIGURE 5.23: Impact load of the impact I_1 on Panel 1.

For the impact I_2 on the skin, the numerical load response is stiffer than the experimental load curve. As for the impact I_1, this may be also explained by the boundary conditions which are stiffer in the simulation (all out-of-plane dofs are constrained outside the impact window) than in the experiments. Furthermore, the numerical load response is much smoother than the experimental one even if the curve contains a high number of points. Thus, it seems that the numerical model does not capture in a refined manner the impact behaviour.

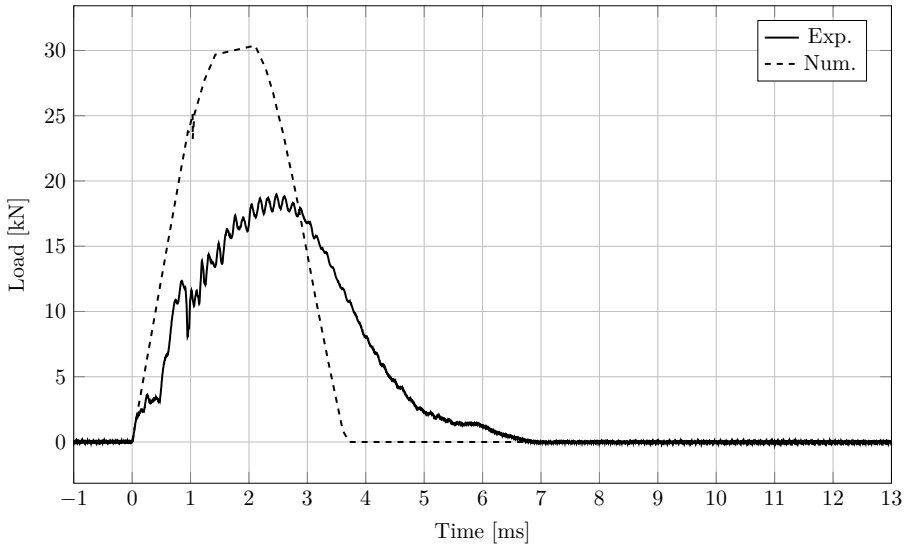

FIGURE 5.24: Impact load of the impact I_2 on Panel 2.

Damage variables

Figures 5.25 and 5.26 present the damage variables predicted with the OPFM constitutive behaviour in all three directions (d_1, d_2, and d_3 referring presently to the damage in respectively the longitudinal, the transversal, and the out-of-plane directions of the corresponding ply). As a reminder from chapter 2, the damage variable scales from 0 to 1, 0 being a healthy state, and 1 being a fully damaged state. In the following figures, as soon as a damage initiates (damage variable higher than 0), it is represented in red. Hence, in this choice of representation, the level of deterioration of each element is discarded.

The damage results for the impact I_1 are reported in Figure 5.25. As written previously, this computation was not led until completion due to the duration and the convergence difficulties of the simulation. This can be explained partly by the contact computation between the impactor and the stringer plies which present multiple orientations. Consequently, the observed damages are not the final ones.

Contrary to the experimental results, the damage shapes are here symmetrical because the impactor is positioned precisely at the middle of the stringer. The shape of d_3 in Figure 5.25 is interesting because it is consistent with the observed experimental shapes with the two lobes reported in Figure 5.18. Nonetheless, the two lobes from the numerical results does not exactly correspond to the same lobes observed experimentally. In fact, in the numerical model, the plies are modelled in a continuous manner. Whereas, in the real panels, the stacking of the plies was not performed all at once. This could have had an effect on the inter-ply interfaces and may explain partly the discrepancy between the experimental and the numerical lobes. Moreover, the numerical simulation underestimates the extent of the delaminated area. This can be partly explained by the fact that the out-of-plane properties of the used composite laminate material, which should here contribute more to the damage mechanisms, were not identified for the Onera Progressive Failure Model. Moreover, here the dissipated energy is underestimated. The use of cohesive zone elements to predict delamination can be considered as a perspective of this work.

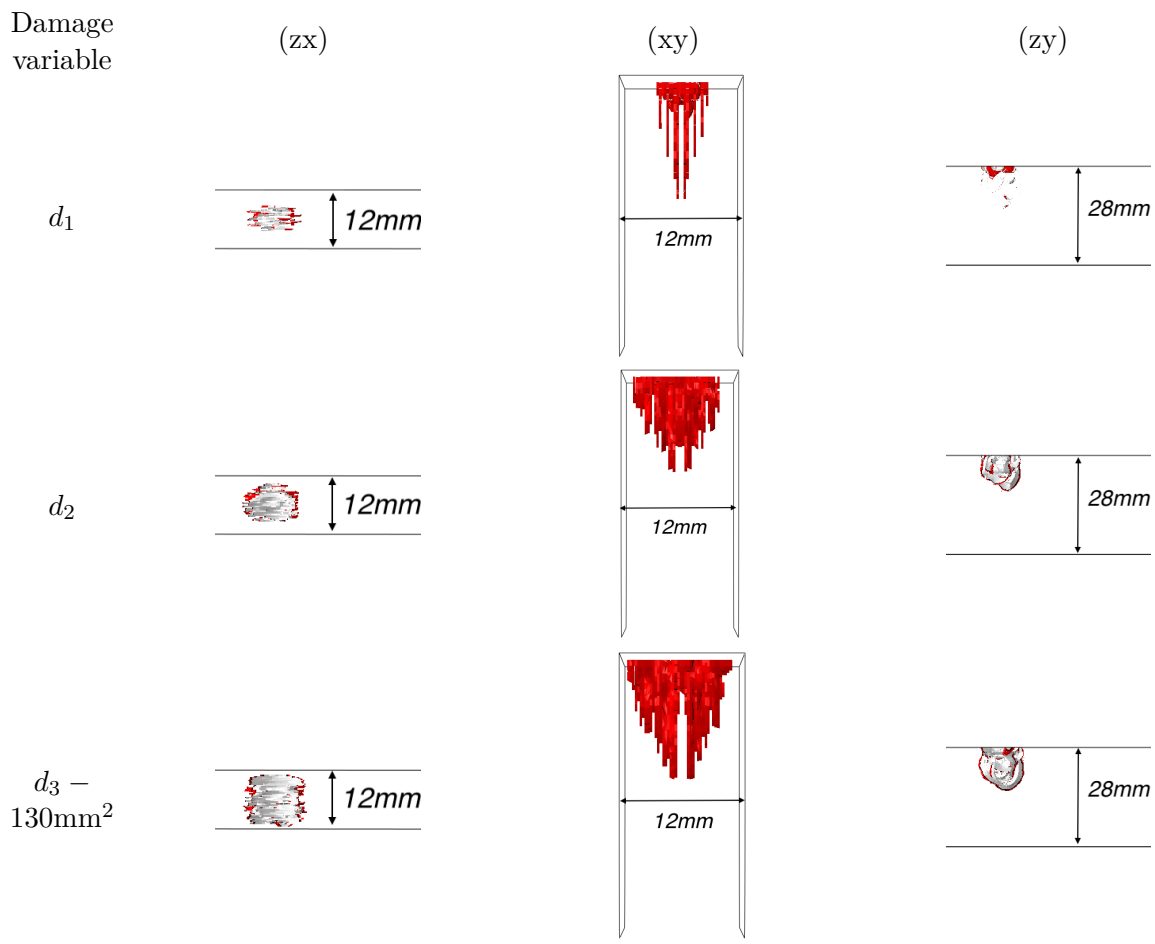

FIGURE 5.25: Damage fields for impact on Panel 1.

For the Panel 2 impacted on the skin, illustrated in Figure 5.26, the damage variable presenting the largest extent is the out-of-plane damage variable d_3 (representing the delamination). The damage in the fibre direction essentially occurs under the impactor tip (Figure 5.26) and correspond to fibre kinking. Matrix damage in the in-plane transverse direction forms a cone shape where the most damaged part is located on the opposite side of the impact (Figure 5.26). It is interesting to notice that the through thickness shape of the damage varies with the involved ply orientation.

Whilst in the experimental results the damage presents a quasi-circular border, in the numerical results, the damage presents an oval shape with a bigger length in the longitudinal direction. The damage seemed to have been more sensitive to some ply orientations. Regarding the total delaminated area, the results from the simulation is lower than the experimental ones. It is interesting to note that, even though the load response is overestimated in the numerical simulations, the damage still remains too low. The use of a continuous model for rendering the out-of-plane damage, especially the inter-ply de-cohesion, may become insufficient.

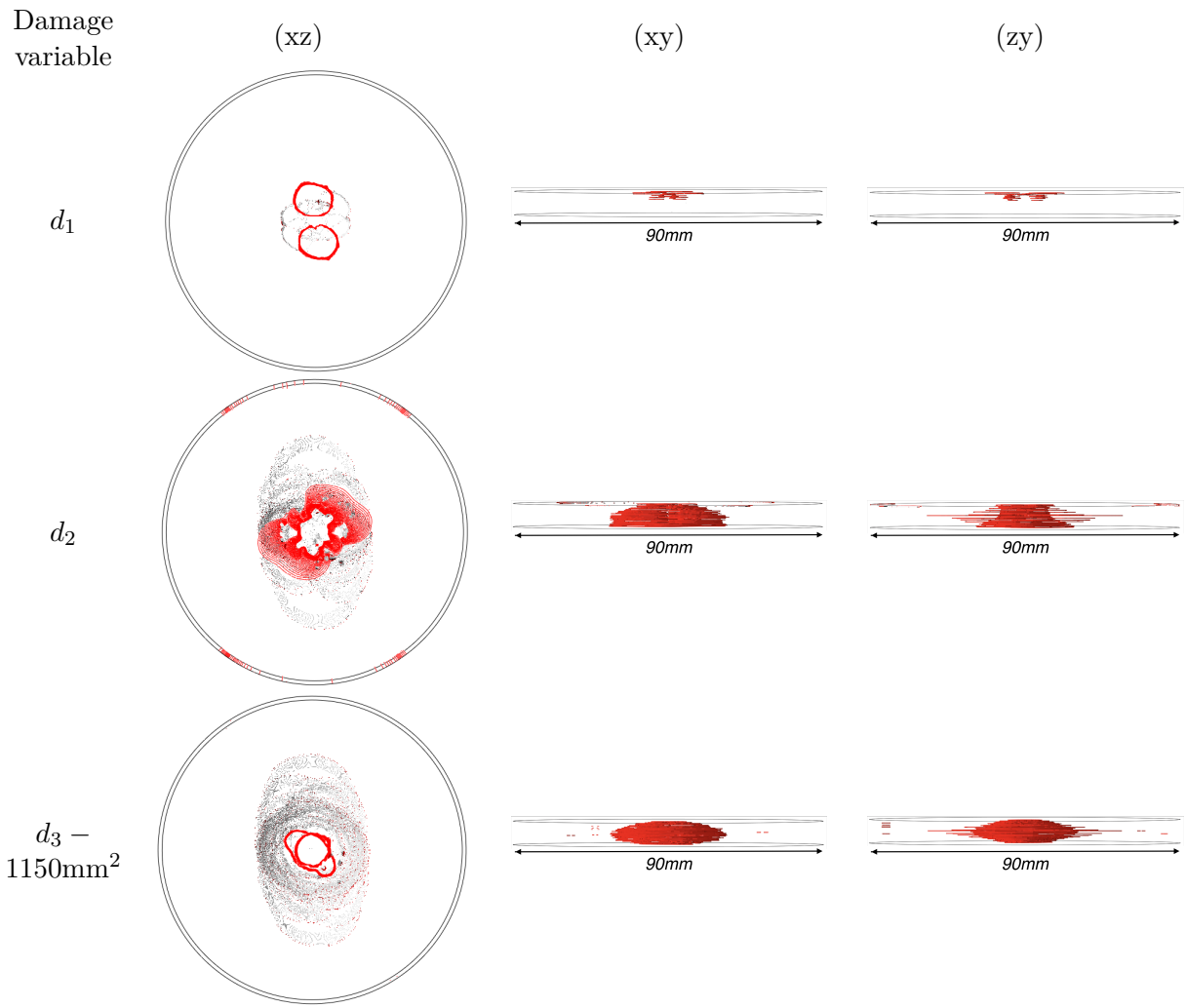

FIGURE 5.26: Damage fields for impact on Panel 2.

5.3.3.1 Conclusion

For both impacts, the load responses are not well reproduced. It can be explained by the complexity of the simulated structure (variable stacking sequences through the panel). Moreover, there are several sources of experimental uncertainty. For instance, the size of the panels is such that the experimental boundary conditions are not enforced near the impact, and are thus less well mastered than impacts on plates for instance. Furthermore, the numerical model was as much simplified as possible. For instance, the chosen contact condition was the most basic one (hard contact for the normal behaviour and frictionless for the tangential behaviour).

Nonetheless, the objective of the numerical simulations was rather to provide a reasonable initial state for the compression of the impacted stiffened panel, to model precisely the effect of an impact on a complex structure. For this reason, the overload of the numerical loading curves compared to the experimental ones is not so problematic in this study. The objective was to obtain damages with a similar distribution as the experimental ones.

In the following section, the residual strength estimations of the impacted stiffened panels are addressed experimentally and numerically only for Panel 2.

5.4 Residual strength of impacted stiffened panels using the adaptive meshing strategy

As a recall, the chosen loading to estimate the residual strength of the previously impacted panels is compression. In this section, both experimental and numerical results are presented only for the Panel 2 (impacted on the skin) for the sake of simplicity. This choice has been made since the case of the impact on the stringer is much more complex for several reasons. Firstly, the impact computation is more complicated and presents a higher computational time since the impact is performed on elements which present variable orientations and hence a variable stiffness. Secondly, the extent of the damaged area in the stringer is such that the damage would certainly have propagated to the skin. And consequently, when using the adaptive multi-model approach, the skin-stringer junction should be modelled which is complex. This section is thus limited to the case of Panel 2 illustrated in Figure 5.20, where the impact is performed in a simpler zone from a stacking sequence point of view.

5.4.1 Experiments

5.4.1.1 Hydraulic machine and instrumentation

The following devices were used to perform and monitor the compression tests:

- an hydraulic machine with a maximal capacity load of 1500kN;
- 2 Keyence sensors located respectively on the right and on the left sides of the panel to measure the longitudinal displacement;
- 4 optical cameras with a resolution of 2048x2048 pixels to perform stereo digital image correlation on both faces of the panel with the commercial software Vic3D©;
- 1 infrared camera to monitor the damage evolution with a resolution of 512x464 pixels and an acquisition frequency of 100Hz focused on the rear face of the panel where delamination cracks are the largest;
- 2 acoustic sensors to monitor the damage acoustically using the commercial software provided by MISTRAS.

Due to the particular shape of the panels to be tested (unsymmetrical and thick stiffened panels), specific mounting devices (bearing supports) were designed to maintain the panels on both ends. The whole design of the compression testing is reported in Figure 5.27 (A). The bearing supports (represented in purple in Figure 5.27 (A)) are adapted to maintain the panels which present on one side a flat surface, and on the other side a face with an alternation of stiffeners and skin portions. The bearing supports are then mounted on the compression machine, one of the bearing supports being fixed on the base (represented in yellow in Figure 5.27 (A)) and the other one being fixed on the piston shaft (represented in green and blue-green in Figure 5.27 (A)). The Figure 5.27 (B) are photographies of the mounting of the stiffened panel in the compression machine.

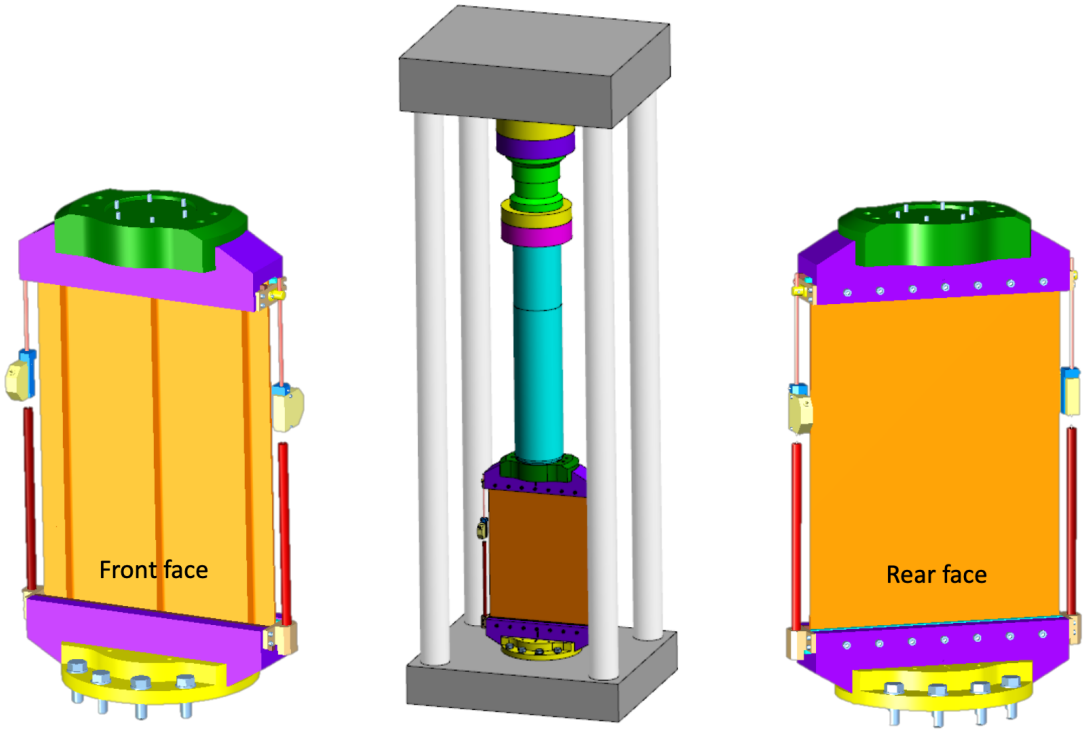

(A)

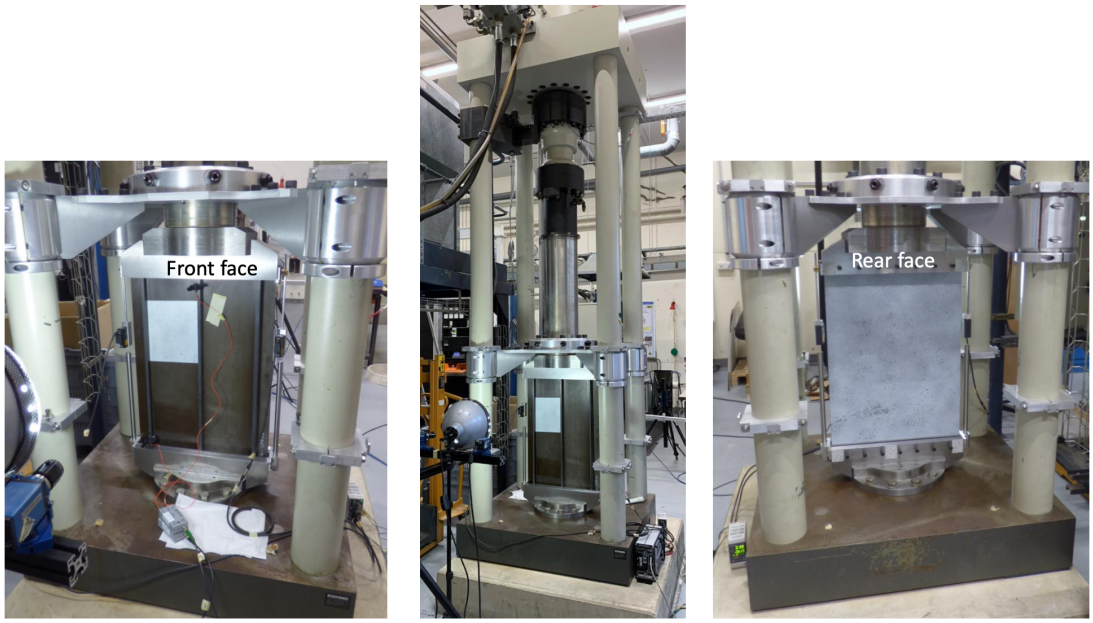

(B)

FIGURE 5.27: Stiffened panel mounting on a compression machine.

5.4.1.2 Experimental protocol

The compression testing was performed in three phases, a first loading phase where the response of the panel is quasi-linear, a second loading phase where both a buckling phenomenon and acoustic events appear, and finally a third and ultimate loading phase until the final failure of the panel. The three phases were not performed with a same displacement rate. Hence, the following experimental protocol is enforced for the compression testing.

1. Setting of the panel inside the bearing supports;
2. Positioning of the panel in the hydraulic machine;
3. First loading phase with a displacement rate of 0.1mm.s^{-1};
4. Second loading phase with a displacement rate of 0.2mm.s^{-1};
5. Third and ultimate loading phase with a displacement rate of 0.2mm.s^{-1}.

5.4.1.3 Experimental results of the panel compression

The experimental results are presented in four parts in the current section: the first loading phase; the second loading phase; the third loading phase; and a focus on the failure mode of the panel. Regarding the digital image correlation results, four different fields were computed in general: the three displacement fields (U_x, U_y, and U_z), and a strain field (ϵ_{yy}), where x and y are respectively the transversal and the longitudinal directions of the panel. The strain field ϵ_{yy} is a relevant indicator of the buckling for a compression loading in the y direction.

First loading phase

Figure 5.28 represents the loading vs time curve during the first loading phase. The maximal load (represented by the red dot) achieved is approximately half the failure load. The discontinuity observed around 480kN is due to an issue in the piloting of the hydraulic actuator. The Figure 5.29 are digital image correlation results at the maximal load of the first loading phase for both the back of the panel (Figure 5.29 (A)), and a portion of the front of the panel centred around the impact (Figure 5.29 (B)).

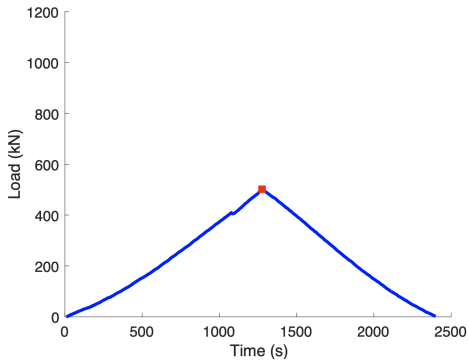

FIGURE 5.28: First loading phase of the compression of Panel 2.

During the first loading phase, the displacement fields U_y are graduated both for the whole back of the panel and for the region centred around the impact on the front of the panel. The displacement fields U_x present a lower magnitude than the magnitude of the two other directions. The U_z displacement field present a same order of magnitude as the U_y field. This may be explained by the fact that the panel is not symmetrical and was not perfectly plane before beginning the experiments. Moreover, in Figure 5.29 (B), the impact indentation is visible on the z field. Nevertheless, none of the other presented fields seems to be influenced by the initial impact damage during the first loading phase. The impact was designed here to have a limited

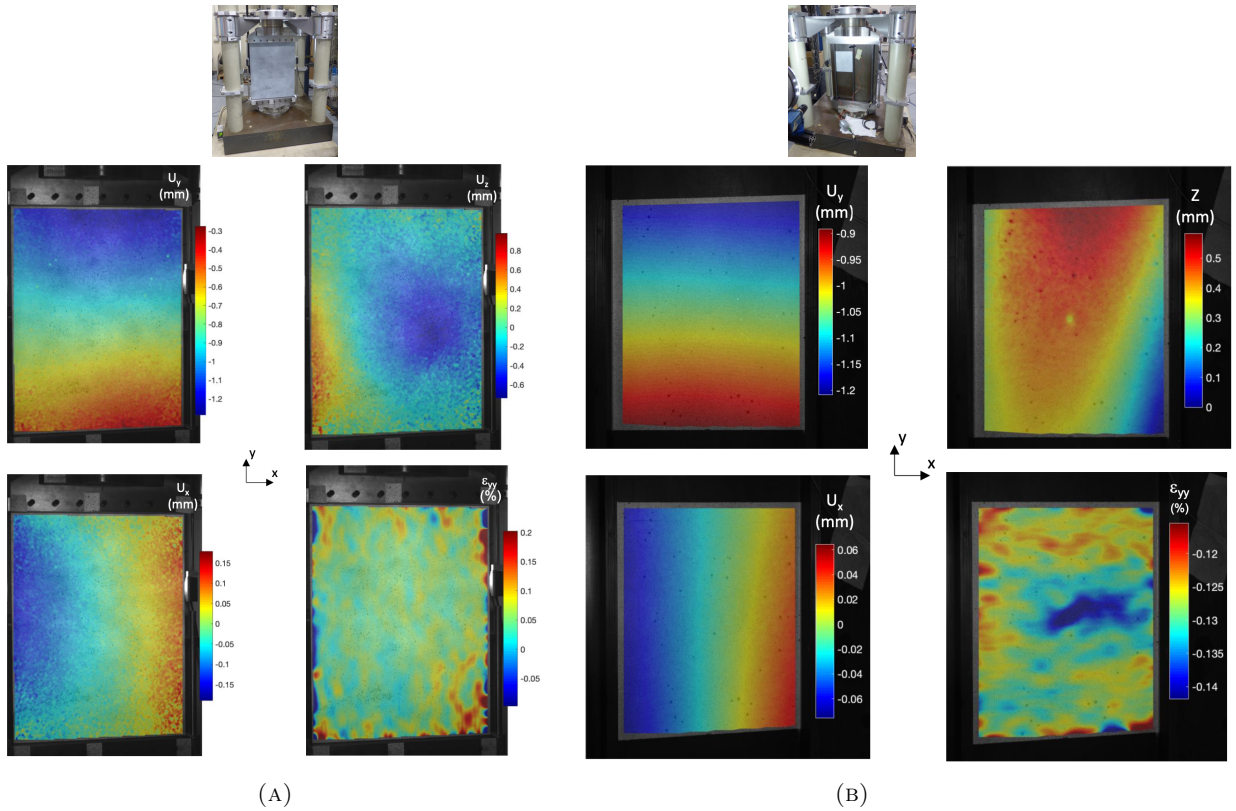

FIGURE 5.29: Digital image correlation of the Panel 2 at the maximal load of the first loading phase: (A) back of the panel; (B) centred around the impact.

influence on the global behaviour of the panel and especially on its final failure. Consequently, the previous observations comfort that design.

Second loading phase

The second loading phase is interesting because buckling and damage initiate within this stage. Figure 5.30 illustrates the loading vs time and the acoustic energy vs time curves during the second loading phase. The second loading phase was stopped at approximately 1000kN before reaching the final failure.

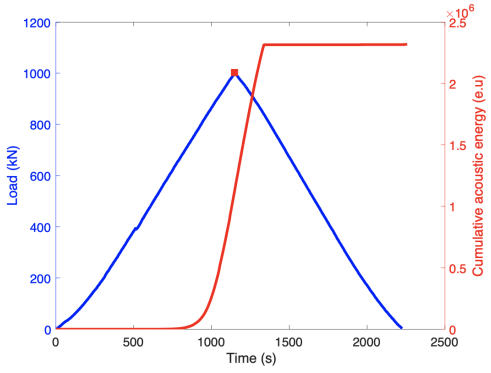

FIGURE 5.30: Second loading phase of the compression of Panel 2.

First, the onset of acoustic events and the related strain fields evolution are analysed. Figure 5.31 represents the strain field ϵ_{yy} on an area surrounding the impact at three different frames.

The frame 1 is taken before any acoustic event was recorded. It can be seen that the strain fields is mostly noisy. Then, the frame 2 corresponds to the beginning of the acoustic event (when the acoustic energy becomes to increase). It is interesting to note that the ϵ_{yy} strain field begins to present a specific pattern especially at the vicinity of the impact. Finally, in frame 3, the ϵ_{yy} strain field shows that there is a local buckling surrounding the impact location. The impact location seems to present a neutral position between an upper and a lower buckling lobes.

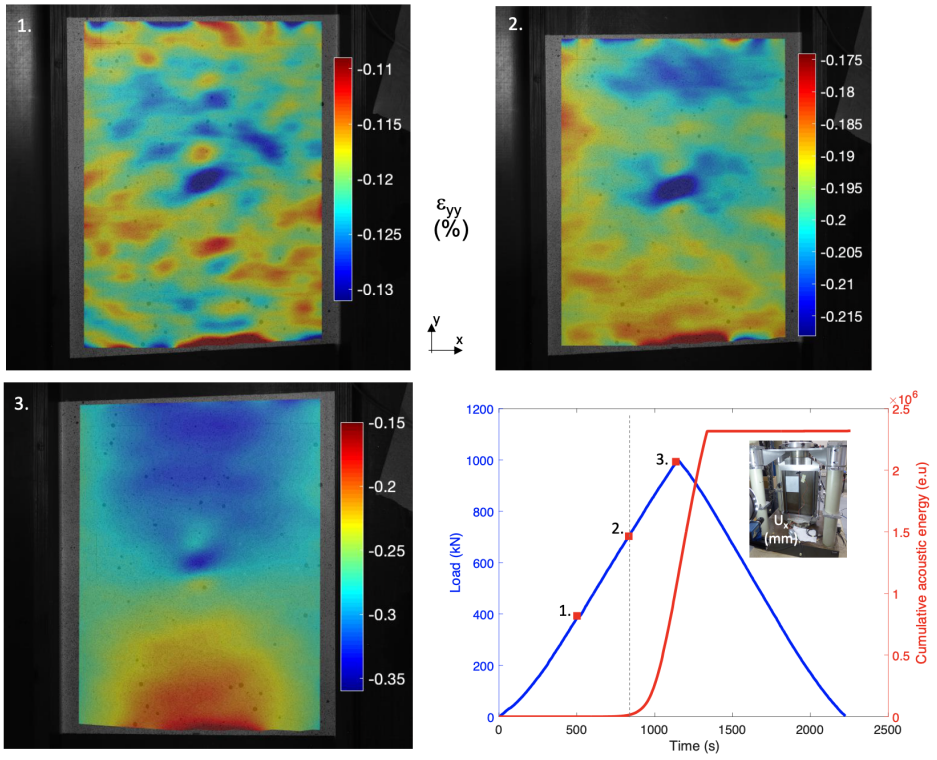

FIGURE 5.31: Digital image correlation of the Panel 2 at the acoustic threshold load during the second loading phase.

The global buckling of the panel is now considered, with notably the study of the load-displacement curve and the displacement fields. Figure 5.32 illustrates the out-of-plane displacement U_z field on the back of the panel at different frames during the loading, the different frames being reported on the load-displacement curve on the same figure. The inflection of the global load-displacement curve begins at the frame 2. The buckling is not very recognizable on the frames 1 and 2. The buckling mode is more shaped in the frame 3 and this shape sticks for the rest of the second loading phase as observed in the frame 4. The buckling mode is not symmetrical according to both in-plane directions, which was foreseeable due to the unsymmetrical nature of the panel ans strongly linked to the evolution of the thickness pattern.

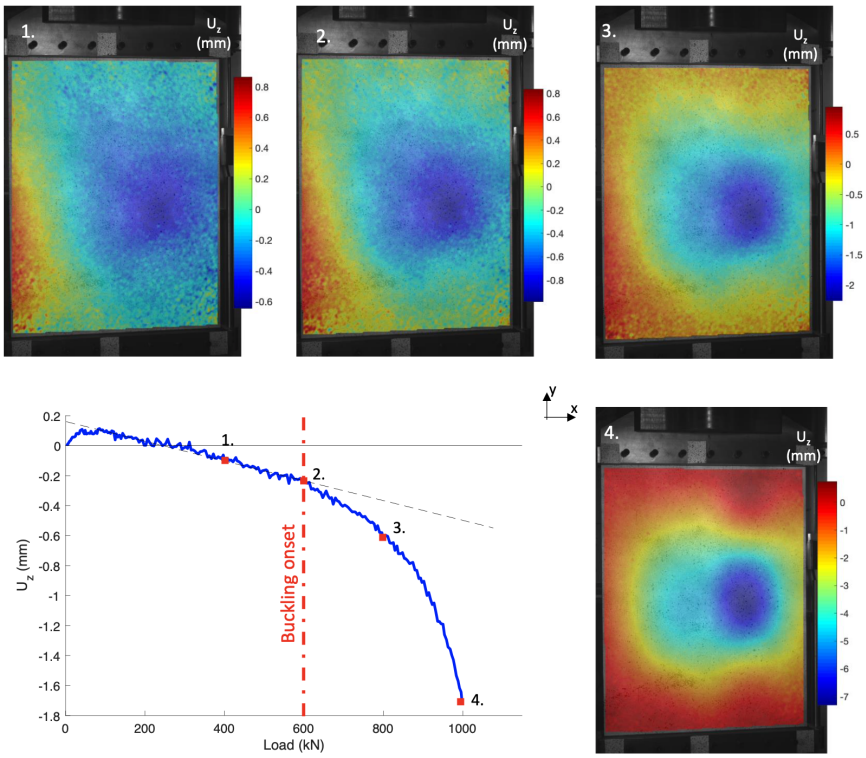

FIGURE 5.32: Digital image correlation of the Panel 2 at the buckling threshold load during the second loading phase.

Figure 5.33 presents the displacements fields U_x, U_y, and U_z and the strain field ϵ_{yy} at the maximal load (illustrated by the red dot in Figure 5.30) for the whole back of the panel (Figure 5.33 (A)) and the area centred around the impact on the front of the panel (Figure 5.33 (B)). The global buckling mode is particularly visible in the ϵ_{yy} strain field. As observed before, the impact locally influences the buckling mode. However, there is no evidence of a propagation of the damage originating from the impact. The analysis of the results of the infrared camera confirm the non-propagation of the initial impact damage, at least close to the surface. At this stage, the global response of the panel is, as expected, driven by the global buckling and not by material rupture.

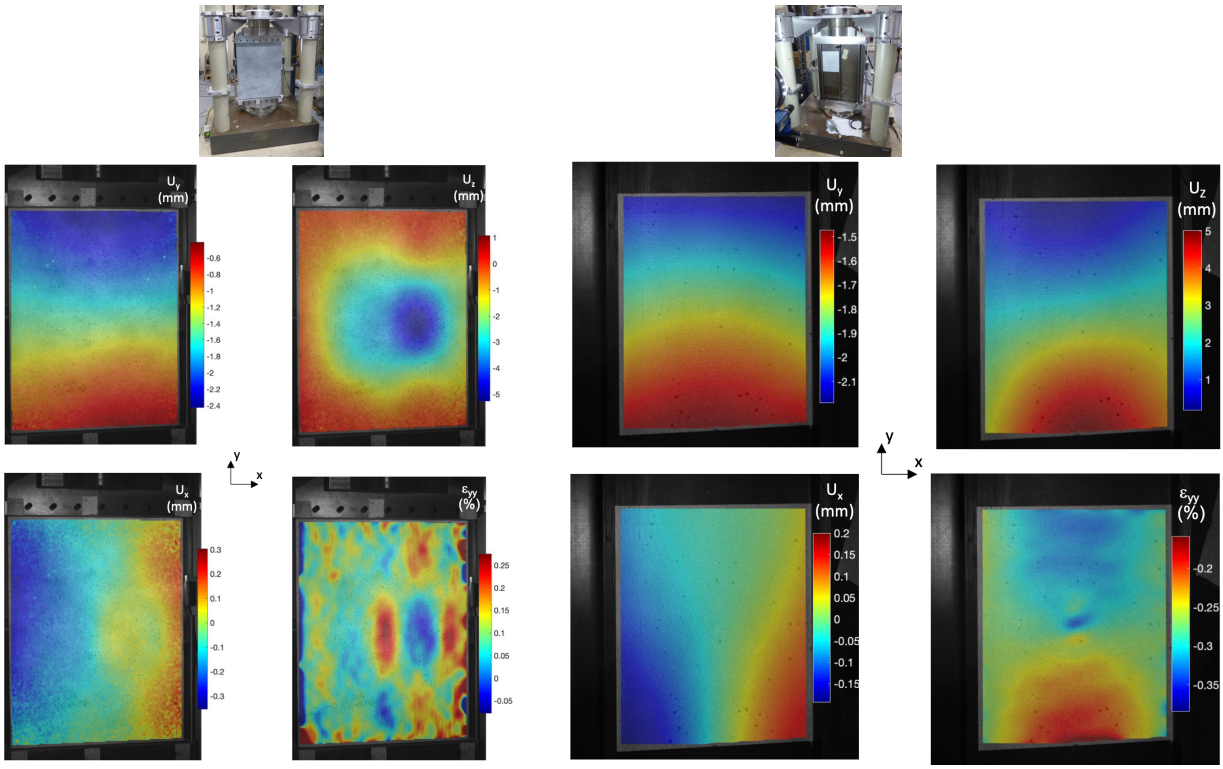

(A) (B)

FIGURE 5.33: Digital image correlation of the Panel 2 at the maximal load of the second loading phase: (A) back of the panel; (B) centred around the impact.

Third and ultimate loading phase

The third loading phase ends with the final rupture of the panel. Figure 5.34 illustrates the load vs time and the acoustic energy curves. The failure occurs at approximately 1100kN. Regarding the buckling mode, the rear face is loaded in compression, and the front face with the stringers in tension. Moreover, the acoustic events begin just before the final failure at an approximate load of 1000kN, which corresponds to the highest value obtained previously. Hence, a Koiser effect seems to occur, meaning that the damage restarts propagating at the highest value previously attained.

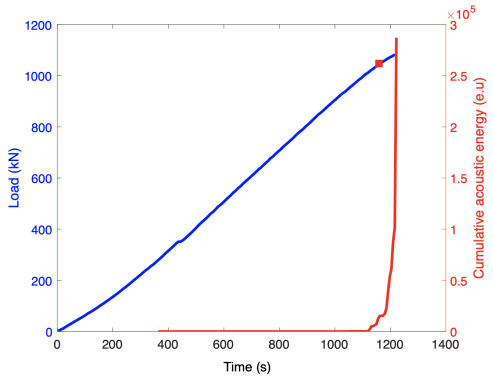

FIGURE 5.34: Third and ultimate loading phase of the compression of Panel 2.

Digital image correlation fields are reported in Figure 5.35 at the moment represented by a red

dot in Figure 5.34. The fields are very similar to the obtained fields at the maximal load of the second loading phase. It shows that the failure occurred abruptly. Prior to failure, the maximal out-of-plane displacement is equal to 7mm which is a high value for such a thick panel. The failure mechanisms are detailed in the following part.

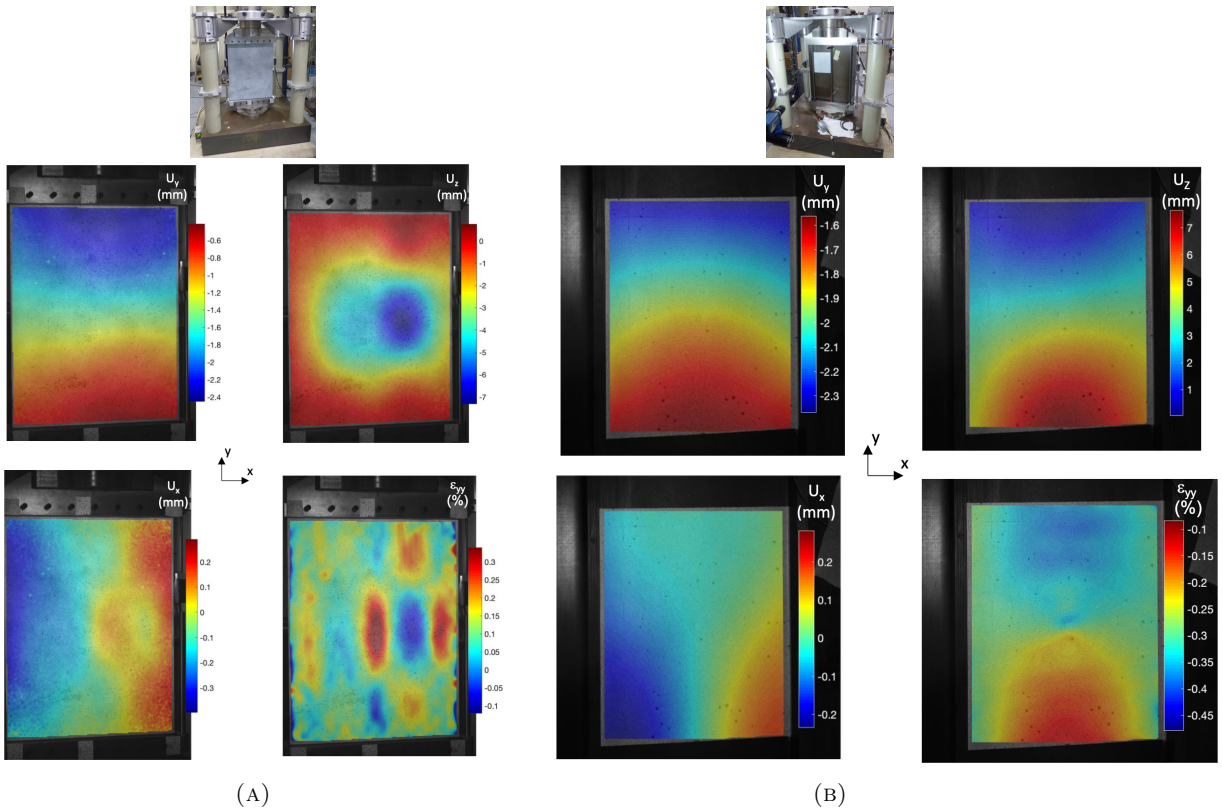

FIGURE 5.35: Digital image correlation of the Panel 2 just before the failure load during the third loading phase: (A) back of the panel; (B) centred around the impact.

Failure mode

The final failure of the panel occurred at the interface between the bearing supports and the panel. The infrared camera allowed to monitor the damage initiation and propagation. In Figure 5.36 several infrared images at different time frames are shown (the acquisition frequency is equal to 100Hz). Referring to the middle image of the Figure 5.36, the infrared camera captured a slight extension of the damage around the impact. Nevertheless, the damage around the impact was not at the origin of the final failure of the panel. In the most right infrared image of the Figure 5.36, one can observe that the failure initiates at the level of the upper bearing support. A large delamination area extends from the upper bearing support to one fourth of the panel length. Hence, it can be deduced that the mounting of the panel on the bearing supports was very stiff, which provoked a failure by shear of the panel at this level. Consequently, the panel did not collapse by global buckling as expected.

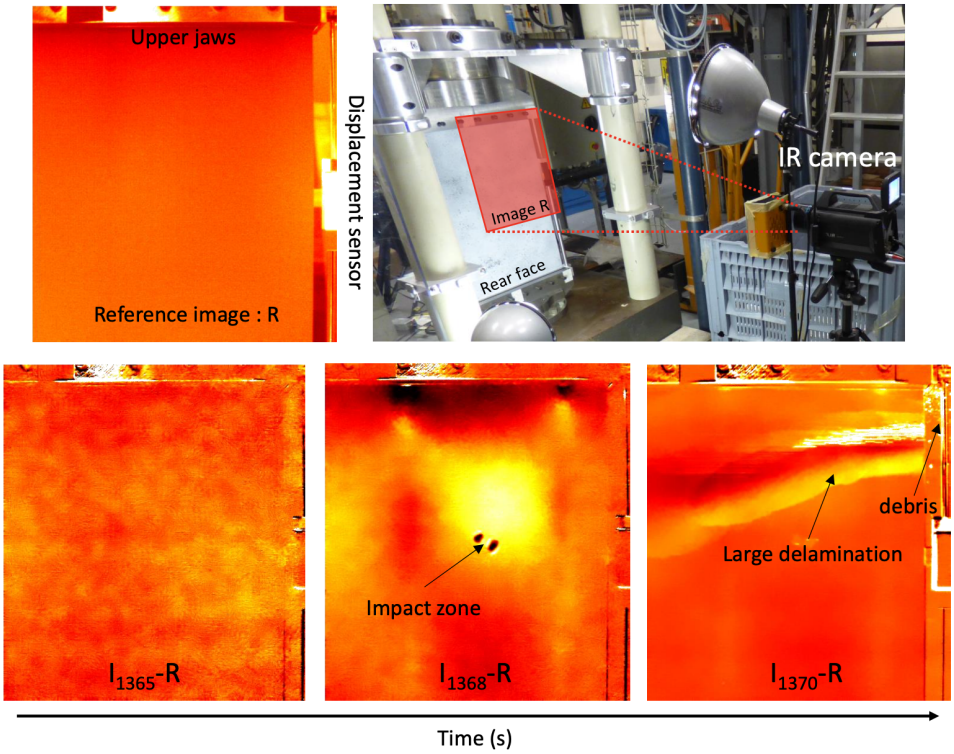

FIGURE 5.36: Infrared images of the failure scenario of the Panel 2 in compression.

A post-mortem analysis of the failed area was performed using digital image correlation results as illustrated in Figure 5.37. The out-of plane displacement field U_z, represented in Figure 5.37 (B), corresponds to the instant marked by the red dot in Figure 5.37 (A). The failed area, where is located the large delamination, is also highlighted by the U_z results.

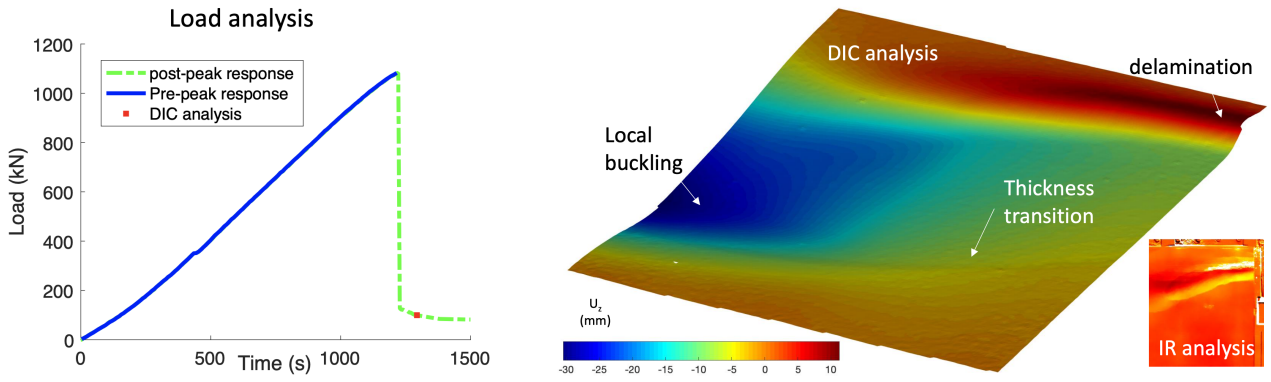

(A) (B)

FIGURE 5.37: DIC of the Panel 2 after the global failure in compression.

5.4.1.4 Conclusion

The experimental set-up and results have been detailed for the compression until failure of Panel 2, pre-impacted on the skin. The compression was led in three loading phases. In the first load phase, the global response of the panel is quasi-linear and no damage occurs. In the second loading phase, the panel is subjected to global buckling. Finally, the third and ultimate loading phase led to the final failure of the panel. The final failure was an abrupt material failure at the level of the bearing supports. Hence, the final failure of the panel was not due to global buckling as expected. This can be explained by the fact that the bearing supports were highly stiff, thus not allowing the panel to buckle as pleased. Nevertheless, as designed, the failure did not originate at the vicinity of the impact damage.

The following section aims at computing the compression of the stiffened panel using the numerical multi-model approach developed in the chapters 3 and 4 of this manuscript.

5.4.2 Numerical comparisons for the compression of an impacted stiffened panel

The objective of this section is to assess the performance of the adaptive multi-model numerical approach on the complex use case of compression of a pre-impacted stiffened panel (Panel 2). However, the numerical approach, detailed in chapters 3 and 4, could not be applied here in a direct manner due to the complexity of the finite element model (variable stacking sequences through the length and the width of the panel) associated with a low flexibility of the used solver software (Abaqus Standard).

As a reminder, the principle of the adaptive multi-model approach is to assess whether a damage may occur at a location within a shell region, to remesh there locally into volume elements, to perform a field transfer operation in order to initialize the state, and finally to perform a reequilibrium step to achieve equilibrium before resuming the computation. Unfortunately, when applying this numerical approach to the studied test case, the reequilibrium step could not reach convergence. This may be explained partially by the fact that only an unique stacking sequence could be used during the adaptation processes. The handling of different stacking sequences in a same volume part considering the continuity of the external plies is not trivial and was not taken into account in this complex test case. Hence, the volume insertions were not necessarily consistent with the surrounding shell areas inducing the convergence difficulties.

A variant of the approach was then used to subvert this issue. The main differences between the original numerical approach and that used for this application case is that during the field transfer operation, only the material variables (damage indicators, ...) are transferred, there is no nodal transfer. Then, an imposed displacement problem is solved with all the displacements equal to zero. The computation is thereafter started from the beginning. It is important to stress that the use of the variant approach is not due to a specific limitation of the original numerical approach but rather to adapt the approach to the complexity of the run model and the lack of flexibility of the finite element commercial software. For instance, it would have been interesting to retrieve nodal reactions from the previous mesh and apply them on the new mesh progressively during the continuation of the computation. From a mechanical point of view, the variant approach can be considered as an artificial unloading, to perform the reequilibrium and then reloading the structure from zero to a higher value than the previous one. For the present quasi-static loading case, these additional unloadings do not modify in a significant manner the obtained predictions.

The initial finite element problem is the result of the simulation of impact on Panel 2 presented in a previous section. The corresponding initial problem is illustrated in Figure 5.38.

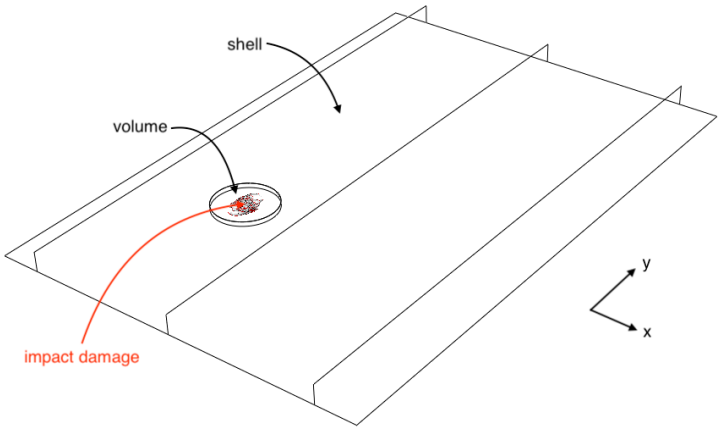

FIGURE 5.38: Initial finite element model for the compression of the Panel 2.

A first remeshing and field transfer was led prior to the quasi-static computation to reduce the initial volume insertion which is unnecessary large. The first mesh is presented in Figure 5.39, where Figure 5.39 (A) is a view of the Panel 2, Figure 5.39 (B) is a view of the remeshed area with volume elements, and a shell transition, and Figure 5.39 (C) is a view of the inserted volume elements. At the beginning of the computation, the boundary conditions are changed to model the compression of the panel. One side of the panel is clamped, while the other side is subjected to an imposed displacement.

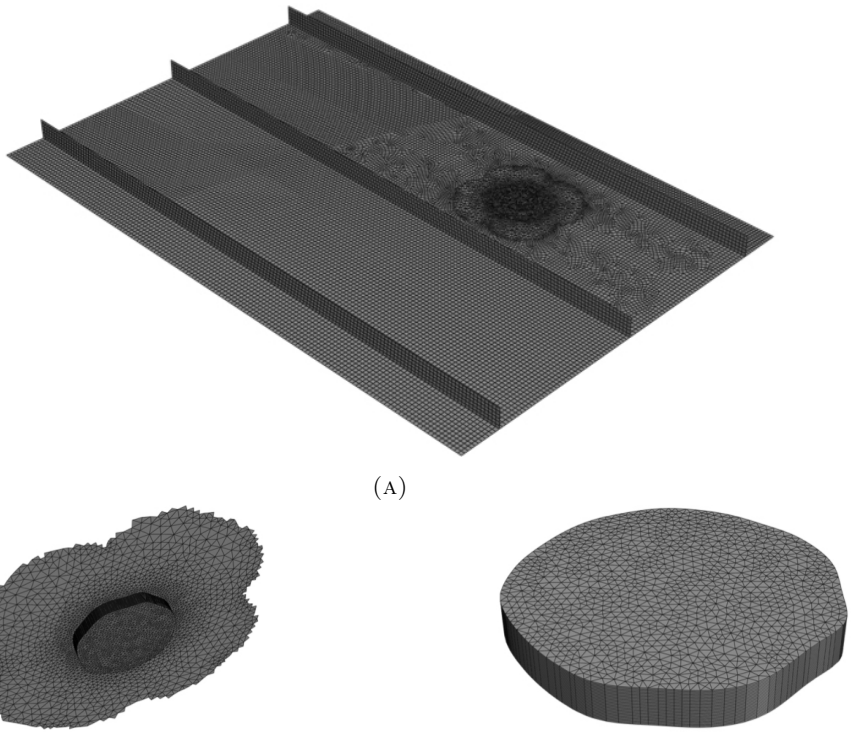

(A)

(B) (C)

FIGURE 5.39: Initial mesh of for the compression of the Panel 2.

The numerical results from the variant of the numerical adaptive approach are compared to the experimental results in the following section.

5.4.2.1 Comparison of numerical and experimental results on a pre-impacted stiffened panel in compression

As detailed in section 5.2.2, the test case of Panel 2 was designed to fail by global buckling even in presence of an initial impact damage. The impact damage was originally designed not to expand. Consequently, the remeshing process should not originate from the initial impacted area, but from areas presenting high stress concentration. This observation is corroborated by the numerical results detailed in this section. In fact, in this test case, the use of the numerical adaptive multi-model approach would not have been necessary. Material damage does not occur before the collapse by global buckling of the Panel 2. Nevertheless, in order to induce mesh adaptation, a low value of the criterion α, which is the threshold of the remeshing method indicator, was chosen. α was set to a value equal to 0.35 in order to be able to conduct two model adaptation operations during the simulation. For comparison, a simulation with a high value of the failure criterion α was run, and during which no adaptation process was triggered, which is consistent with the experimental results.

The numerical results are presented in two parts. First, the global response with the load vs time curve is shown. Then, the out-of-plane displacement fields were examined to assess the performance of the simulations for the three experimental loading phases.

Load response

Figure 5.40 represents the numerical load response vs time of the Panel 2. Regarding the numerical result, two model adaptation operations were led as illustrated in Figure 5.40. Solution jumps are observed after each adaptation process, and the structural response softens. Two possible reasons may explain this phenomenon: firstly, the use of an unique "thin" stacking sequence (which corresponds to that of the thinner stacking sequences of the whole structure) for each volume area addition; secondly, the addition of volume elements which are less stiff than shell elements, partially due to the non-handling of the ply drop off in the remeshing procedure.

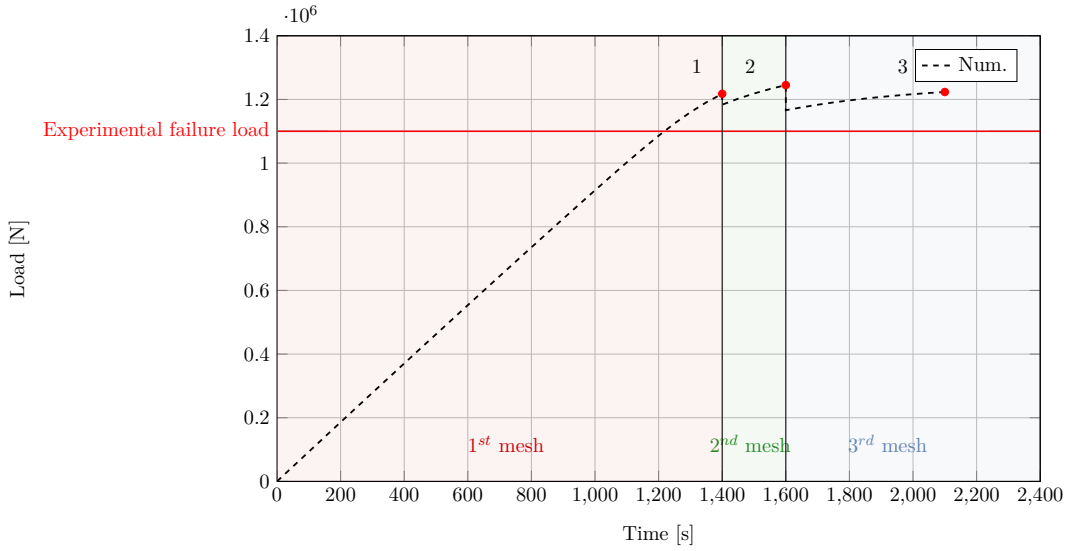

FIGURE 5.40: Load vs time numerical result of Panel 2 with two remeshing steps.

It is worth mentioning that the failure of the panel, which is due to the failure of stringers by shear at the end of the bearing supports and to a large delamination originating at top rigth corner of the panel, is not represented in the simulation. Therefore, it does not come as a surprise that a numerical final failure by global collapse presents a higher load than the experimental one by 6%.

The displacement field U_z (magnified by a factor of 5) at the time moments 1, 2, and 3 represented in Figure 5.40 and corresponding respectively to the first, the second, and the third meshes, are depicted in Figure 5.41. The volume insertions are visible on the three meshes. The first mesh (Figure 5.41 (A)) only includes the volume insertion containing the impact damage. Then, in Figure 5.41 (B), it can be noted that the regions presenting higher stress concentrations are at the skin-stringer junction where the remeshing was led. In order to manage the remeshing at the vicinity of such a T-junction, only the remeshing of the skin was allowed. Moreover, the nodal compatibility between the skin and the stringer was preserved to avoid implementing a supplementary surface condition between the skin and the stringer. It is also interesting to note, regarding the third mesh (Figure 5.41 (C)), that the remeshing was performed at the location of the buckling lobes which present high stress levels.

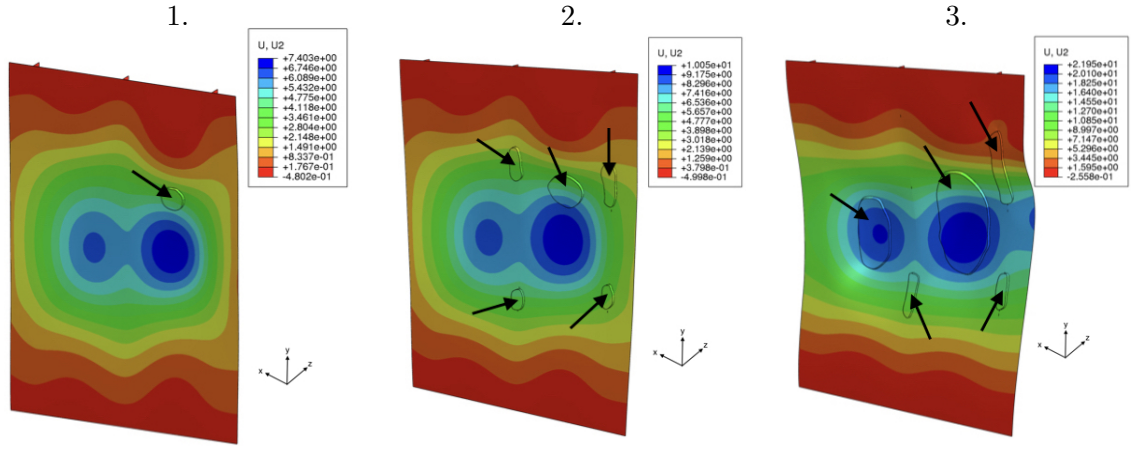

(A) t=1400s (B) t=1600s (C) t=2100s

FIGURE 5.41: U_z displacement for three different meshes: volume insertions are pointed out with black arrows.

First loading phase

Figure 5.42 represents the first loading vs time curve (A), and the out-of-plane displacements fields at the back of the panel for the maximal load (red dot), obtained experimentally (B) and numerically (C). As illustrated in Figure 5.42 (B), the displacement field U_z does not show a distinguishable buckling mode yet, the absolute maximal and minimal values of U_z are rather similar. However, an intermediate buckling mode appears on the numerical result with a dominant lobe at the center left of the panel. This buckling mode will evolve during the simulation. Hence, at the beginning of the simulation, during the first loading phase, the out-of-plane displacement fields are not similar between the experiment and the simulation. This discrepancy could be due to the use of ideal boundary conditions in the simulations. A short term perspective could be to

introduce measured displacement fields by DIC as the boundary conditions (displacements and rotations).

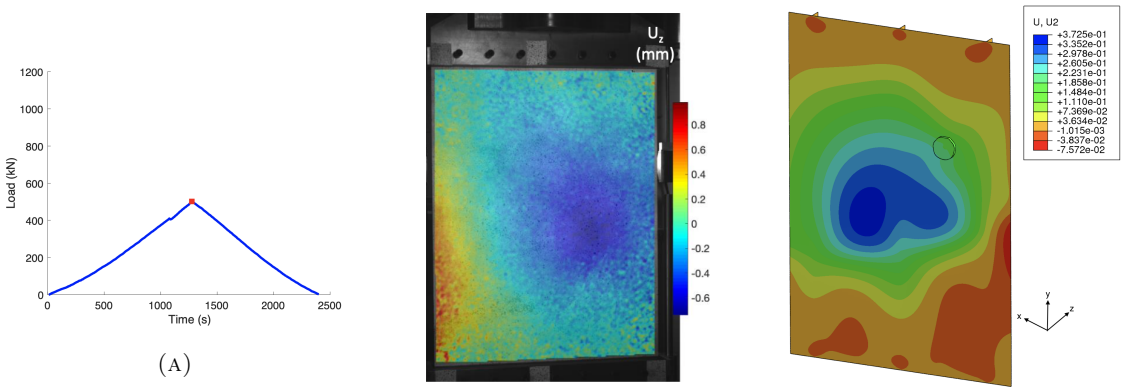

(A) (B) (C)

FIGURE 5.42: U_z displacement during the first loading phase.

Second loading phase

The evolution of the displacement field U_z through the second loading phase is presented in Figure 5.43, experimentally ((B), (C), (D)) and numerically ((E), (F), (G)), for respectively the imposed displacement marked 2, 3, and 4 in (A). Along with the increase of the imposed displacement, the buckling mode settles in for the experimental results. For the numerical results, the buckling mode progressively evolves. The right lobe tends to widen. Nevertheless, the simulation underestimates the out-of-plane displacement magnitude. Hence, the simulated model is stiffer than the experiment, again probably due to the use of perfect boundary conditions.

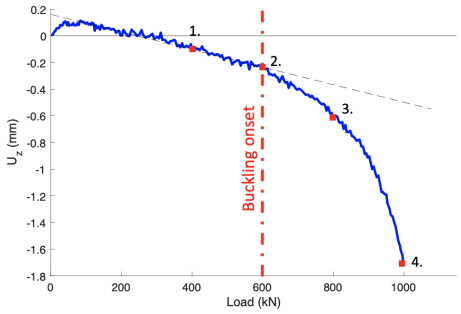

(A)

FIGURE 5.43: U_z displacement during the second loading phase.

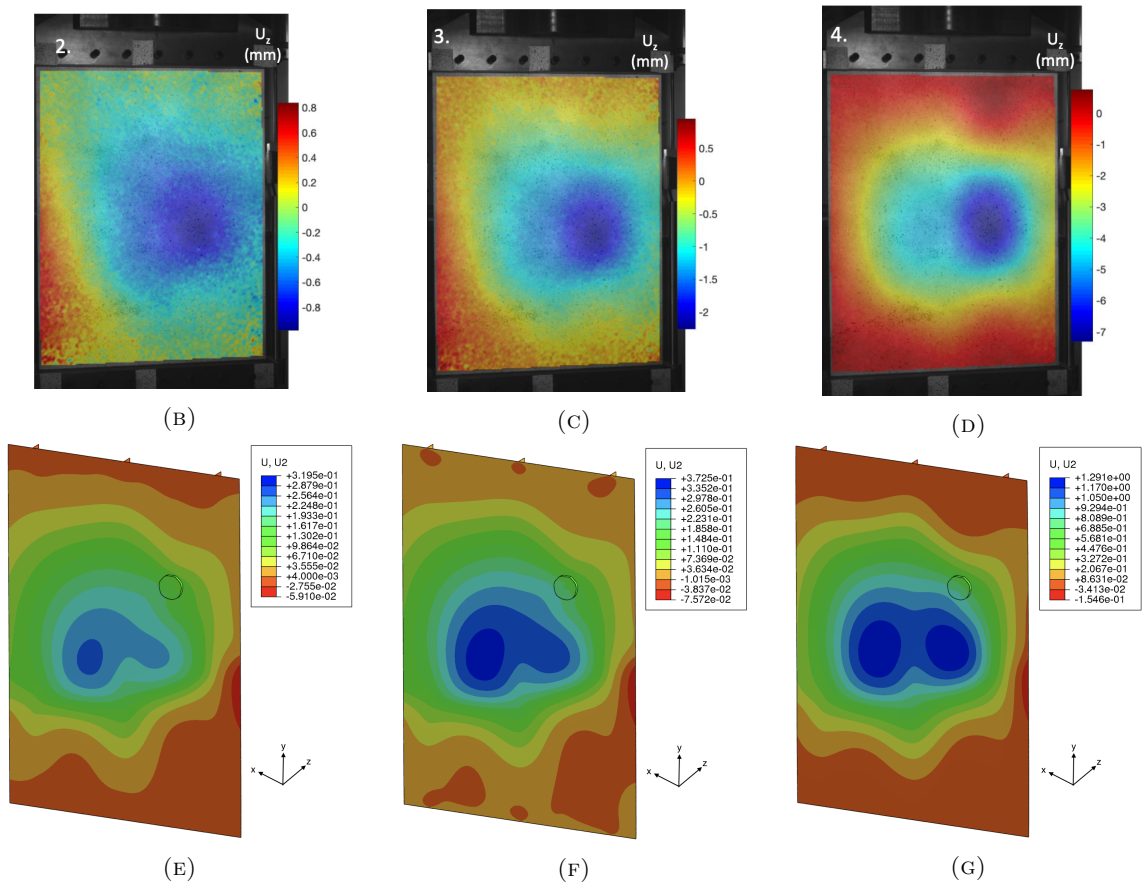

FIGURE 5.43: U_z displacement during the second loading phase (cont.).

Third and ultimate loading phase

The out-of-plane displacement fields at the red point illustrated in Figure 5.44 (A), are shown in Figure 5.44 (B) (experimental result), and Figure 5.44 (C) (numerical result). While for the previous loading phase, the buckling mode was different experimentally than numerically, here, the numerical result evolved and the buckling mode fits the experimental one.

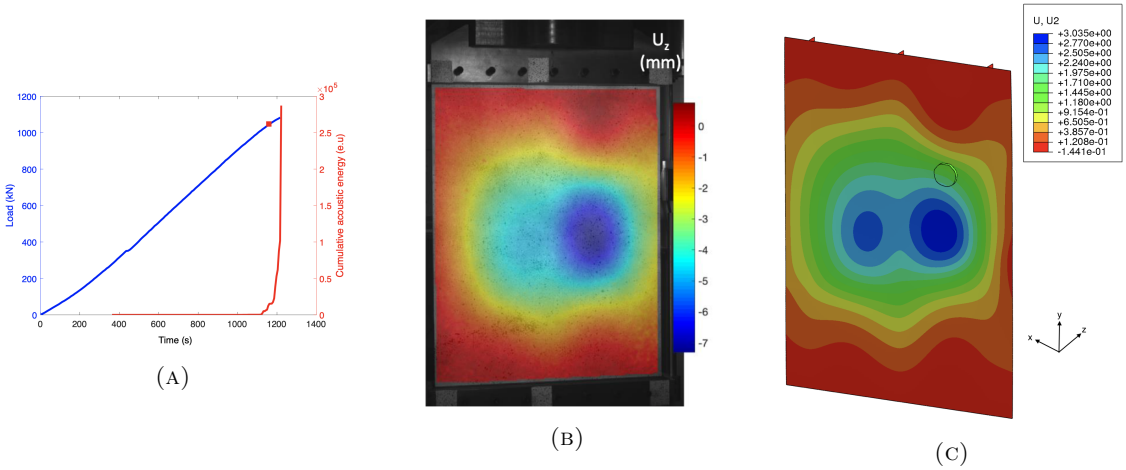

FIGURE 5.44: U_z displacement during the third and ultimate loading phase.

As for the previous loading phase, the simulation presents a stiffer behaviour than the experiment.

Hence, the simulation fits at least qualitatively the experimental behaviour before the predicted collapse of the panel, which is 6% higher than the experimental one, which may be explained by the observed failure mode (shear failure of stringers at the bearing supports).

To illustrate the low level of material damage state within the panel prior to global buckling, the failure indicator f_2, which represents transverse matrix failure, is shown in Figure 5.45. As a reminder, a failure index inferior to 1 is representative of a sane material, and if it exceeds 1, damage initiates. Globally, the value of f_2 remains below 0.35, which shows that the structure is mostly sane during the compression loading.

f_2 exceeds 1 only on a tip of a volume insertion on the skin-stringer junction, pointed by a red arrow on the Figure 5.45. This corresponds to a high stress region. It is relevant to note that, in the present numerical approach, the out-of-plane failure index f_3 is set to zero all over the shell area. Hence, cases in which out-of-plane damage would have initiated under a normal out-of-plane stress state would not have been captured. Especially, this can occur at corners and junctions such as the skin-stringer junctions. Consequently, the poor representation of the failure scenario could be partly explained by the inability of the proposed approach to detect normal out-of-plane stress states. This can be a perspective of the current approach.

Nevertheless, the previously described obervation could also be explained by the fact that the threshold is reached at the vicinity of the shell-volume coupling where there is a discrepancy in stacking sequence. Consequently, it may also result from a numerical artefact.

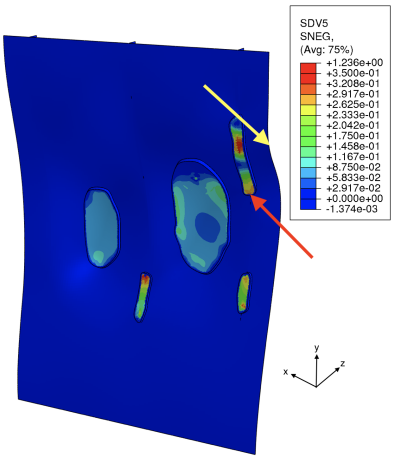

FIGURE 5.45: Failure indicator f_2 during the third and ultimate loading phase.

As for the experimental data, the numerical results represent the non-symmetrical response of the panel which is due to the un-symmetrical variable distribution of thickness through the panel. Moreover, it is important to observe a distortion pointed out by the yellow arrow in Figure 5.45. This distortion recalls the global failure scenario of the panel presented in section 5.4.1.3. The distortion is slightly below the region where the damage initiated experimentally but is in the same area.

5.4.2.2 On the numerical cost of the method

The present section aims at giving an overview of the repartition of the computational time between the different steps of the adaptive multi-model strategy for the studied complex industrial case. The simulations were led on 12 CPUs (12 cores of 2019's Xeon cluster node with 128GB RAM) and the computational characteristics of each of the three meshes are presented in Table 5.2, where the times correspond to the wall-clock time (spent human time during execution).

In Table 5.2, the approximate pre-computational time comprises the post-processing when necessary (about 10-30s), the remeshing (about 10-30s), the reading of the result file from Abaqus by Zset (depends on the mesh size, 400s for the initial mesh, 2 130s for the mesh 2), the field transfer (30s to 350s), and the reequilibrium at the initial time t=0s (about 7-8 iterations, 180s for mesh 1 and 2 100s for mesh 2). It can be noted that the reading of the result file by Zset is quite slow, while it is an interfacing operation and not a core step of the adaptive multi-model numerical method. Moreover, the initialisation computational time refers to the time required by the simulation to get back from t=0s to the given remeshing time (t=1400s from mesh 1 to mesh 2, and t=1600s from mesh 2 to mesh 3). The initialisation computational time is linked to the fact that convergence could not be reached during reequilibrium for the present complex test case, thus not allowing the simulation to restart directly from the final time increment before adaptation. The effective computational time corresponds the continuation of the simulation, which relates respectively to t$\in$ $[0, 1400s]$ for mesh 1, t$\in$ $[1400, 1600s]$ for mesh 2, and t$\in$ $[1600, 2100s]$ for mesh 3.

Mesh	**Mesh 1**	**Mesh 2**	**Mesh 3**
Dofs	227 350	631 215	2 046 848
Memory usage	15GB	31GB	82GB
Time per iteration	25s	65s	267s
Approximate pre-computational time	1 000s	1 700s	4 600s
Initialisation computational time	0s	4 750s	36 579s
Effective computational time	1 831s	3 120s	13 350s

TABLE 5.2: Computational time for three meshes during the progressive adaptive simulation.

A major observation from Table 5.2 is that there is a large discrepancy between the effective computational times between the meshes 1, 2, and 3, even though the volume insertions are limited through the panel. Consequently, the present method is interesting to optimize the computational efforts.

However, the pre-computational times are still important. They represent roughly 50% of the effective computational time. As stated beforehand, a major part of the pre-computational time is affected to interfacing between Abaqus and Z-set. Hence, a more efficient interfacing between the two softwares would significantly reduce the time share of the pre-computational time.

Moreover, the initialisation computational time represents also a very important part of the computation. Ultimately, with improvements of the numerical method for the handling of more complex models (management of variable stacking sequences), the initialisation computational time would be suppressed.

To sum up, provided that the interfacing between Z-set and Abaqus is made faster, and the initialisation of the computation is suppressed, the developed numerical approach should provide a reasonable and possibly reduced total computational time compared to a full volume model. Another interesting feature of the proposed method is the reduction of memory storage requirements as volume elements are inserted where needed. In the mean time, the developed numerical approach may also be used as a flexible tool for engineers to remesh automatically an initial given shell model by inserting volume elements with potentially a more complex material constitutive behaviour where required (remeshing operations remain always very low).

5.4.3 Conclusion

In a nutshell, the developed numerical model is able to render qualitatively, the physical phenomena encountered in the Panel 2 throughout the compression loading. In particular, the final global buckling mode is well captured by the simulation. Also, the possible distortion at the origin of the final failure of the panel is captured by the simulation.

In the studied test case, the use of the numerical adaptive multi-model strategy was not necessary, since there was no significant damage propagation. Nevertheless, it allowed to assess the possible benefits of using such an approach. For instance, the stress state of highly loaded areas could be monitored more precisely with volume elements.

The approach being at an early development stage, the numerical performances in terms of computational times are not optimal yet. The main advantage of the numerical approach being for now, the flexibility it provides thanks to the automatic enrichment of areas presenting high stress levels. It has been demonstrated that the strategy could be applied on a complex industrial test case. The introduction of ply drop-off management into the procedure would be a necessity to go further. Moreover, a special attention to the boundary conditions, extracted from displacement fields measured by DIC, must be paid to capture more precisely the whole buckling scenario.

Conclusion

This chapter addressed the design and analysis of a complex structure, representative of industrial applications, and with a complex loading scenario, which is the residual strength estimation of a pre-impacted stiffened panel in compression. Two test cases were designed, with two similar panels. The first test case is a panel pre-impacted on the center of the middle stringer (Panel 1) and configured to fail by material failure with a propagation of the damage from the impact location. The second test case is a panel pre-impacted on the skin (Panel 2), configured to fail by global buckling, and where the impact damage should remain confined (no damage propagation prior to failure).

Firstly, the experimental and numerical impact results were presented. The induced experimental damages were slightly smaller than expected. This is explained by the complexity of mastering the boundary conditions of the mounting for such large panels for an impact. Then, both impacts were simulated. The simulated response were stiffer than the experiment but with a lower damage result, especially for the impact on the center of the middle stringer. Delamination is simulated with a diffuse continuous damage model to reduce the numerical complexity, but at the same time which does not dissipate enough energy, explaining thus the underestimation of the damaged area. The unusual configuration of this impact, for which the material law was not designed, can explain partly those results. In the frame of this PhD, the impact was more a mean to introduce damage than the real target of the study. While the initial damaged area is underestimated, the shape of the damage pattern is relevant even for the impact on the stringer. The main objective was to assess the performance of the adaptive multi-model approach on the compression phase of the panel after the introduction of damage by impact. Consequently, the impact simulation results were stated sufficient to become the initial models for the compression loading phase.

Secondly, only the experimental and numerical results of the Panel 2 were presented for the compression phase, the Panel 1 being too complex to be simulated using the adaptive numerical multi-model approach. The Panel 2 was designed to fail by global buckling with a confined extension of the initial impact damage. The experimental results corroborate that the initial impact damage does not extend in this configuration. However, even though a global buckling phenomenon was observed, the final failure of the panel was a brutal propagation of damage from the junction of the panel to its bearing supports.

Regarding the adaptive multi-model approach, the numerical strategy developed in chapters 3 and 4 could not be applied directly on the test case addressed in the present chapter. After each adaptation process, the equilibrium could not be achieved due to convergence issues. The main reasons are the complexity of the test case, with in particular, the presence of variable stacking sequences through the panel and the lack of flexibility induced by the use of a commercial finite element software (Abaqus). Indeed, it is not trivial to introduce in the strategy the management of the ply drop-off considering the industrial stacking sequence design rule (continuity of the external plies for instance). A variant of the numerical approach was therefore proposed.

It can be noted that the Panel 2 test case was not the best one to demonstrate that the numerical adaptation process follows damage propagation, as no damage propagation is planned. On the

other way round, what can be observed numerically, is the absence of volume insertions at the vicinity of the impact damage location and the presence of volume insertions at high stress concentration locations (corresponding to the buckling lobes). Consequently, the adaptive multi-model approach allowed to follow precisely the stress state at high stress locations which is interesting and promising for other application cases.

Even though the studied test case has a high level of complexity, a variant of the numerical multi-model approach has been used and allowed to follow the ruin of the panel in compression, which is yet a notable achievement of this study.

A perspective of the experimental validation of the approach would be to apply the numerical approach to test cases presenting an intermediary complexity level. In fact, the industrial test case was too complex with both the impact test, followed by the compression test of the panel with buckling instabilities. A potential intermediary test case would be, for instance, a test case comprising a pre-defined singularity where damage would necessarily initiate. For example, a bolted joint would be an interesting intermediary test case.

6 Conclusion

In this work, a complex numerical strategy has been elaborated to model damage propagation in composite laminated structures, targeting in particular large structural components. Our strategy consisted in the adaptation of the Finite Element mesh and the constitutive equations modelling to the need through the structure and the simulation time. An adaptive multi-model strategy based on an innovative remeshing technique has been designed.

The main difficulty was to consider simultaneously all the aspects involved in such a strategy among others, the damage modelling, the multi-dimensional coupling, the remeshing, and the state update. Moreover, the numerical strategy was developed with various constraints such as the compatibility with the Abaqus commercial software and with the models used in Airbus. Yet, the developed numerical approach is flexible and simple enough to be used in the frame of a commercial Finite Element solver.

The final numerical application demonstrated the ability of the proposed approach to be used on a large industrial structure and showed successful comparison with experimental results on an academic test case (open hole plate subjected to a compressive-bending loading).

Achievements

The main requirement for the numerical approach was to be able to simulate complex mechanical behaviours by making use of simple tools for each step of the adaptive multi-model approach. Hence, the Abaqus software was used for the resolution of the multi-model problem at each fixed decomposition, and the adaptation scheme was performed with the Z-set software. A main contribution of the present work was to implement the global adaptive scheme of the numerical approach within the Z-set software, to ensure a smooth dialogue between Abaqus and Z-set, and to handle the different steps of the model adaptation process.

For instance, regarding the multi-dimensional coupling condition, we first studied the couplings available in Abaqus in order to avoid further non-necessary developments. We decided to select the “shell-to-solid” coupling condition after an extensive study of other existing multi-dimensional couplings techniques. Indeed the “shell-to-solid” coupling condition of Abaqus provided the most satisfying results on diverse test cases of interest for Airbus (buckling, out-of-plane behaviour, damage). This technique enforces a load equality in an average sense between the shell and the solid domains. However we noted that this sole condition was not sufficient when considering cases with a substantial out-of-plane behaviour. For this reason, we proposed to use it jointly

with a shell kinematic constraint on the solid interface. This way the multi-dimensional coupling can be solved in a monolithic manner within the Abaqus framework.

Nevertheless, we observed that the "shell-to-solid" coupling condition requires some cautions when the coupling surface exhibits edgy corners. For this reason, a smoothing meshing strategy was developed using the Z-set software. This procedure significantly reduces the undesired stress-concentrations at the interface.

For the sake of simplicity in the development of the adaptive scheme, we focused on a single criterion with a physical meaning to monitor the model adaptation. More precisely, we proposed using a failure based criterion with a security margin, which allows performing the remeshing before any damage occurrence. In addition, this technique simplifies considerably the field transfer operations, yielding to a lower computational time. The criterion was coded into the material behavior implemented as a UMAT.

Many efforts were invested in the development of the remeshing strategy which has a central role in the proposed numerical procedure. Indeed, the remeshing drives both the accuracy and the computational time of the simulation. We evidenced the importance of introducing a so-called remeshing radius to extend the robustness of this type of strategy. In a way this remeshing radius acts as a regularization parameter which provides an additional security margin to prevent from flawed meshes, possibly not compliant with the damage to be captured (recall that the remeshing is performed before damage has occurred). Furthermore, we designed a technique making use of an underlying 2D mesh through the computation in order to preserve the mesh in relevant areas where failure occurred. Interestingly, the numerical results showed that using simple field transfer operators does not necessarily imply a reduction of the accuracy. Furthermore, all of these steps in the proposed remeshing strategy result in a significant reduction of the computational time during the state update step.

Finally, an important contribution of this work was to implement the proposed multi-model strategy for complex situations of interest for Airbus. The test cases consist in two impacted stiffened panels subjected to compression, which are representative of industrial configurations. Preliminary numerical models have been designed to select the panel geometries, the impact load levels and locations in order to provide two different ruin scenarios: one by global buckling and another one driven by material failure. The proposed multi-model strategy could not have been applied directly to the pre-impacted panel test case due to the complexity of the finite element model and the low flexibility provided by the commercial finite element software. However, a variant of the adaptive multi-model technique provided numerical predictions for the test case planned to fail by global buckling. These predictions were compared to the experimental testings and showed qualitative resemblance between simulations and experiments. Hence, the developed method is promising for the simulations of damage propagation applied to large composite structures.

Perspectives

Several challenges still need to be addressed to increase the domain of application and the performances of this numerical adaptive approach. Some possible perspectives of this work are listed hereunder.

- Having a better dialogue between the commercial software Abaqus and the Z-set software would simplify the handling of the field transfer and the reequilibrium operations, thus saving computational time.
- Regarding the remeshing, the extension of the numerical approach to quadrangular elements with a conform mesh would be beneficial for the convergence of the used damage model.
- Implementing cohesive zone models would improve the accuracy of damage prediction, but would require consequent numerical developments, especially for handling field transfer and reequilibrium operations in a context of discontinuity.
- Enabling the handling of ply drop-off would also be of interest. This aspect lacked for the industrial test case developed in this manuscript.

A Numerical implementation

The general numerical scheme of the numerical multi-model adaptation process is piloted by the Z-set software as illustrated in Figure A.1. Only the FE resolutions are performed by the Abaqus implicit FE solver.

First, the Z-set software launches the FE resolution of the problem using the Abaqus implicit solver. Each increment Δt of the current multi-model is solved, including the non-overlapping coupling. The non-overlapping coupling condition is the "shell-to-solid" coupling from Abaqus, coupled with a shell Reissner-Mindlin kinematic, the "MPC SLIDER" applied to the solid interface.

There is no model update as long as the model (E) is valid over the discrete domain $T^{(E)}$ and at the vicinity of G in the $T^{(AE)}$ domain. The model validity indicator ϕ is introduced within a UMAT. When the model validity criterion exceeds the criterion α, the incremental computation within Abaqus is interrupted and the adaptation scheme is triggered by the Z-set software.

First, an identification step allows to target the critical elements $T^{(E)}_{crit} \subset T^{(E)}$ requiring the (AE) model by a post-processing using an Abaqus Python script.

Then, the Z-set software performs the whole model adaptation and state update processes. With the list of the identified critical elements, an extended zone at the vicinity of $T^{(E)}_{crit}$, defined by a distance D, is remeshed into solid ply-per-ply elements. After the remeshing process, the state update aims at producing a good representation of the mechanical state following the change in models and discretization, with the delicate transition from a shell to a solid kinematic. Additional equilibrium steps are added before the computation is resumed for the current increment.

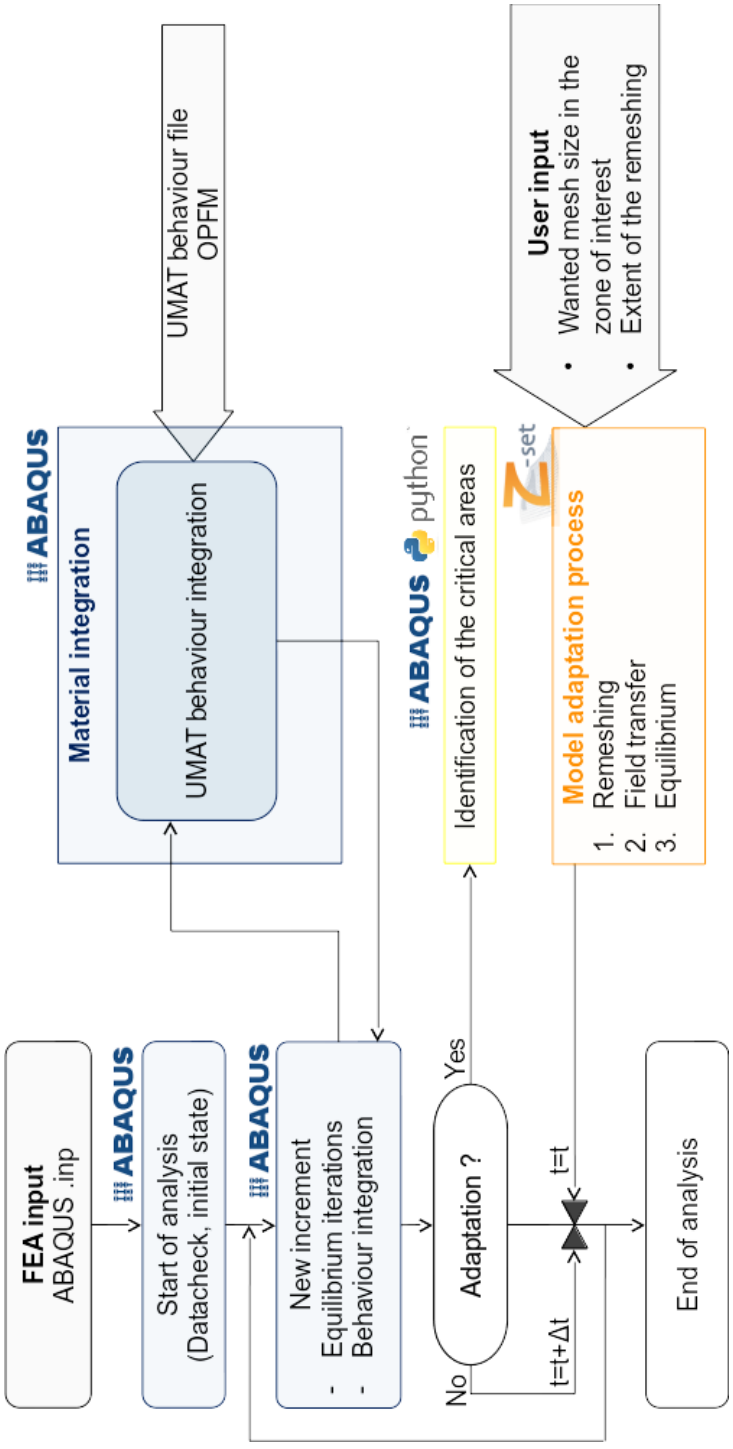

FIGURE A.1: Numerical implementation.

B Résumé de synthèse

Les industriels du domaine aéronautique s'intéressent à la réalisation de simulations prédictives à l'échelle de la structure complète. La complexité des problèmes mécaniques concernés est telle qu'il faut recourir à des modèles matériaux et à une discrétisation par éléments finis simplifiés. Ainsi, la structure primaire d'un avion étant majoritairement composée d'éléments élancés, et les problématiques principales des simulations menées étant liées aux instabilités de flambage dans un contexte de grandes transformations géométriques, ce sont souvent des éléments finis structuraux comme les coques qui sont employés dans les modèles.

Récemment, la généralisation des stratifiés composites dans les fuselages ou les ailes des avions modernes (ils représentent, par exemple, plus de 50% de la masse structurale d'un avion A350), a complexifié les modélisations numériques utilisées par les ingénieurs. En effet, ces matériaux, choisis pour leur légèreté et leur flexibilité en matière de propriétés mécaniques, peuvent, en service, contenir des dommages internes qui sont à peine visibles. Pour des raisons de sûreté, la manière actuelle d'estimer la tolérance aux dommages de pièces structurales est fortement conservative, alors même que ces petits endommagements ne peuvent avoir, le plus souvent, qu'un impact très faible sur l'intégrité des structures. Il est par conséquent intéressant de pouvoir simuler précisément l'impact d'un endommagement initialement localisé et de son évolution sur la tenue en service d'un composant.

Ainsi le Chapitre 2 de ce manuscrit s'intéresse à la problématique suivante : comment simuler des comportements complexes tels que des endommagements dans des structures de grande dimension ? Pour simuler fidèlement l'endommagement d'un stratifié, une modélisation précise est nécessaire avec une discrétisation spatiale fine, où chaque pli est représenté et caractérisé par une loi matériau complexe. De telles lois sont généralement écrites avec des formalismes tridimensionnels anisotropes, afin notamment de prendre en compte des phénomènes hors-plan. La généralisation de ce type de modélisation n'est pas acceptable en termes de coût de calcul à l'échelle de grandes structures, de sorte que le développement de stratégies de calcul ad-hoc est aujourd'hui essentiel pour les concepteurs aéronautiques. L'idée est d'ajuster la finesse de la modélisation au besoin, dans l'espace et dans le temps, au cours de la simulation.

Ainsi, de nombreux travaux s'intéressent au développement d'approches multi-échelles qui exploitent plusieurs niveaux de modélisation. Les approches dites descendantes sont les plus répandues actuellement. Le principe est de réaliser une première analyse globale simplifiée et d'en extraire les conditions aux limites souhaitées pour lancer une analyse locale non-linéaire sur la partie critique de la pièce. Ce type d'approche n'est exacte que pour des problèmes où les non-linéarités locales ont peu d'influence sur le modèle global. Pour y palier des méthodes itératives

peuvent être employées en exploitant une décomposition de domaines. Elles permettent de diviser le problème en espace et/ou en temps et de le résoudre sur chacun des domaines en parallèle en itérant sur un problème allégé posé uniquement aux interfaces. La sensibilité de convergence de ces méthodes itératives au conditionnement des opérateurs traités limite souvent leur robustesse, et le peu de flexibilité des solveurs commerciaux rendent particulièrement délicate leur mise en œuvre dans un contexte industriel. De plus si la localisation des phénomènes non-linéaires qu'on souhaite modéliser évolue significativement, des techniques d'adaptation peuvent devenir plus efficaces. Cela revient à optimiser l'effort numérique investi tout au long de la simulation, en ajustant par exemple le schéma de résolution, la modélisation éléments finis ou encore la loi de comportement.

La méthode proposée dans ce manuscrit de thèse entre dans ce cadre, en exploitant des algorithmes de remaillage adaptatif, implémentés dans le logiciel Z-set, mais en s'imposant le cadre d'une résolution numérique utilisant un code de calcul éléments finis industriel (ABAQUS). Ainsi, ce manuscrit introduit une nouvelle approche numérique d'adaptation multi-modèles pour la simulation de phénomènes complexes locaux dans de grandes structures composites. L'objectif est de disposer d'une approche adaptée à la problématique des structures composites stratifiées (stratifié de plis unidirectionnels en fibres de carbone et matrice thermodurcissable), avec un schéma de résolution générique et robuste, offrant un temps de calcul réduit par rapport à une modélisation exploitant uniquement le modèle non-linéaire.

Dans le Chapitre 3, on pose un problème de référence multi-modèles à décomposition fixée. Il consiste en un domaine généralement élastique comprenant quelques inclusions anélastiques dans les zones de fortes concentration de contraintes, où le modèle raffiné permet de capturer des phénomènes complexes se produisant dans les stratifiés composites, comme par exemple des endommagements.

En particulier, dans la zone d'intérêt, le comportement du matériau est régi par le modèle Onera Progressive Failure Model (OPFM), formulé à l'échelle du pli et détaillé dans [Laurin et al., 2007]. Ce modèle permet de prendre en compte plusieurs sources de non-linéarités, élasticité non-linéaire sens fibre, visco-élasticité et endommagement. Les différents mécanismes d'endommagement d'un stratifié (rupture fibre, rupture matrice, décollement fibre/matrice, délaminage) peuvent être représentés de manière continue permettant l'économie de l'usage de zones cohésives par exemple. Des indicateurs d'état par élément procurés par la loi permettent d'estimer l'endommagement et constituent une base pertinente pour le critère d'adaptation de modèles.

De plus, le domaine élastique est modélisé avec des éléments de coque multicouches, tandis que le domaine anélastique est modélisé avec des éléments solides comprenant au moins un élément par pli dans l'épaisseur. Cette technique nécessite par conséquent la mise en œuvre d'un couplage multidimensionnel. Une étude sur plusieurs cas tests représentatifs, présentant des sollicitations de complexité croissante sur le couplage, a permis de valider un raccord de type "shell-to-solid coupling" réalisé dans ABAQUS, et assorti d'une contrainte cinématique supplémentaire sur l'interface volumique afin de garantir une compatibilité cinématique à l'interface.

Ensuite, dans le Chapitre 4, on s'intéresse à l'approche d'adaptation du problème multi-modèles. Le principe général de lancer une résolution éléments finis d'un problème, pouvant être modélisé avec uniquement le modèle simplifié au départ, et automatiquement mettre à jour le problème lorsque le modèle simplifié n'est plus pertinent et doit être enrichi.

Les problématiques étudiées sont notamment : la mise en place d'un critère de déclenchement de l'adaptation de modèle, le développement d'une stratégie de remaillage, et une approche de mise à jour de l'état, comprenant notamment des opérations de transfert de champs et d'équilibrage. En particulier, la stratégie de remaillage est l'une des principales contributions de ce travail. Son développement a été pensé pour permettre de simplifier le plus possible les autres aspects de l'approche numérique.

Pour déclencher l'adaptation de modèle, un indicateur fondé sur des indices d'endommagement formulés en contraintes a été retenu et est comparé à un critère. Le critère intègre en particulier une marge afin de remailler avant l'apparition de non-linéarités dus à un potentiel endommagement. Ainsi, on s'assure de remailler le modèle dans les zones où un endommagement est susceptible d'apparaitre. Ce critère est intégré au calcul ABAQUS par une UMAT dans le contexte d'un schéma d'intégration implicite.

Une part importante du présent travail se rapporte au développement de la stratégie de remaillage. Par exemple, une technique de régularisation du maillage au niveau de l'interface entre les domaines raffiné et simplifié a notamment permis d'utiliser des conditions de couplage déjà disponibles dans le logiciel de résolution éléments finis. Selon un autre exemple, la mise en place d'une stratégie de préservation du maillage dans les zones endommagées a permis de simplifier fortement les opérations de mise à jour l'état. Ainsi, les opérations de transfert de champs ne sont plus réalisées que dans des zones élastiques, ce qui permet de réduire les potentiels erreurs induites et de réduire également la durée d'exécution de ces opérations.

Le Chapitre 4 se conclue sur l'application de l'approche numérique à une plaque trouée en flexion rotulée, le trou représentant un dommage initial, dont l'influence risque de se propager dans la structure sous sollicitations mécaniques. Ainsi, l'approche numérique a permis de remailler progressivement le problème conformément aux motifs d'endommagement observés expérimentalement sur ce cas, permettant une première validation qualitative de la méthode. Ce cas test a permis de mettre en valeur la robustesse et la flexibilité de la stratégie numérique proposée dans ce manuscrit.

Enfin, le Chapitre 5 s'intéresse à l'application de la stratégie numérique à des cas tests représentatifs des applications industrielles, à savoir l'estimation de la performance résiduelle de panneaux raidis pré-impactés. L'objectif était de mettre en place deux cas tests expérimentaux afin de produire deux modes de ruine distincts. A cette fin, un prédimensionnement des cas tests, notamment en adaptant la géométrie des panneaux, et la stratégie d'impact (localisation, énergie), a été réalisé. Des essais d'impact, expérimentaux et numériques, ont permis d'introduire des endommagements dans la structure et de fournir un point de départ initial pour l'application de l'approche numérique qui cherche à simuler la compression des panneaux après l'impact.

La stratégie numérique a pu être appliquée au cas d'un panneau raidi pré-impacté, étant pourtant un cas test d'un niveau de complexité élevé. La stratégie numérique n'a pas pu permettre de rendre compte de l'endommagement final du panneau, lequel s'étant produit au niveau des conditions aux limites, notamment à cause de la complexité de la géométrie du panneau (épaisseur variable ayant provoqué un couplage torsion-flexion-compression). Néanmoins, la stratégie numérique a permis de mettre en avant les zones fortement sollicitées, similaires aux zones observées expérimentalement, lorsqu'on s'éloigne des zones d'application des conditions aux limites. Ainsi, la méthode numérique présente des résultats prometteurs pour la simulation de cas tests industriels.

Bibliography

[Allix, 2001] Allix, O. (2001). A composite damage meso-model for impact problems. *Composite Science and Technology*, 61:2193–2205.

[Anagnostou et al., 1990] Anagnostou, G., Maday, Y., Mavriplis, C., and Patera, A. (1990). On the mortar element method: Generalizations and implementation. Philadelphia. Third International Conference on Domain Decomposition Methods for Partial Differential Equations.

[Areias and Belytschko, 2006] Areias, P. M. A. and Belytschko, T. (2006). A comment on the article "a finite element method for simulation of strong and weak discontinuities in solid mechanics" by a. hansbo and p. hansbo [comput. methods appl. mech. engrg. 193 (2004) 3523–3540]. *Computer Methods in Applied Mechanics and Engineering*, 195(9-12):1275–1276.

[Babuška and Rheinboldt, 1978] Babuška, I. and Rheinboldt, W. C. (1978). A-posteriori error estimates for the finite element method. *International Journal for Numerical Methods in Engineering*, 12(10):1597–1615.

[Belgacem, 1999] Belgacem, F. B. (1999). The mortar finite element method with lagrange multipliers. *Numerische Mathematik*, 84:173–197.

[Belytschko and Black, 1999] Belytschko, T. and Black, T. (1999). Elastic crack growth in finite elements with minimal remeshing. *International Journal for Numerical Methods in Engineering*, 45(5):601–620.

[BenDhia, 1999] BenDhia, H. (1999). Numerical modelling of multiscale mechanical problems : the arlequin method. pages 757–766. European Conference on Computational Mechanics.

[Bernardi et al., 1993] Bernardi, C., Maday, Y., and Patera, A. T. (1993). Domain decomposition by the mortar element method. In eds., H. K. . M. G., editor, *Asymptotic and Numerical Methods for Partial Differential Equations with Critical Parameters*, volume C 384, pages 269–286. N.A.T.O. ASI Series.

[Berthelot, 2010] Berthelot, J. (2010). *Mécanique des Matériaux et Structures Composites.*

[B.F.Oliveira and G.J.Creus, 2000] B.F.Oliveira and G.J.Creus (2000). Viscoelastic failure analysis of composite plates and shells. *Composite Structures*, 49(4):369–384.

[Blumenfeld and Piquet, 2011] Blumenfeld, L. and Piquet, B. (2011). Fast 48. Technical report, Airbus SAS.

[Bouvet et al., 2009] Bouvet, C., Castanié, B., Bizeul, M., and Barrau, J. (2009). Low velocity impact modelling in laminate composite panels with discrete interface elements. *International Journal of Solids and Structures*, 46:2809–2821.

[Bouvet et al., 2012] Bouvet, C., Rivallant, S., and Barrau, J. (2012). Low velocity impact modeling in composite laminates capturing permanent indentation. *Composites Science and Technology*, 72:1977–1988.

[Carrera, 2000] Carrera, E. (2000). A priori vs. a posteriori evaluation of transverse stresses in multilayered orthotropic plates. *Composite Structures*, 48(4):245–260.

[Carrera, 2002] Carrera, E. (2002). Theories and finite elements for multilayered, anisotropic, composite plates and shells. *Archives of Computational Methods in Engineering*, 9(2):87–140.

[Cescotto and Zhu, 1995] Cescotto, S. and Zhu, Y. (1995). Modelling of ductile fracture initiation during bulk forming. *Computational plasticity: fundamentals and applications*.

[Chantrait, 2014] Chantrait, T. (2014). *Approche multiéchelle en espace et en temps pour la prévision des endommagements dans les structures composites soumises à un impact de faible énergie*. PhD thesis, Université Paris-Saclay.

[Chantrait et al., 2013] Chantrait, T., Rannou, J., and Gravouil, A. (2013). Low intrusive coupling of implicit and explicit integration schemes for structural dynamics: Application to low energy impacts on composite structures. V International Conference on Computational Methods for Coupled Problems in Science and Engineering.

[Chapelle and Bathe, 2011] Chapelle, D. and Bathe, K.-J. (2011). *The Finite Element Analysis of Shells - Fundamentals*. Springer.

[Chen et al., 2014] Chen, B., Pinho, S., Carvalho, N. D., Baiz, P., and Tay, T. (2014). A floating node method for the modelling of discontinuities in composites. *Engineering Fracture Mechanics*, 127:104–134.

[Combescure and Gravouil, 2001] Combescure, A. and Gravouil, A. (2001). A time–space multiscale algorithm for transient structural nonlinear problems. *Mécanique & Industries*, 2:43–55.

[Dávila, 1994] Dávila, C. G. (1994). Solid-to-shell transition elements for the computation of interlaminar stresses. *Computing Systems in Engineering*, 5:193–202.

[Demkowicz et al., 1985] Demkowicz, L., Devloo, P., and Oden, J. (1985). An h-type mesh refinement strategy based on a minimum interpolation error. *Computational Methods in Applied Mechanics and Engineering*, 53:67–89.

[Dureisseix and Bavestrello, 2006] Dureisseix, D. and Bavestrello, H. (2006). Information transfer between incompatible finite element meshes: application to coupled thermo-viscoelasticity. *Computational Methods in Applied Mechanics and Engineering*, 195:44–47.

[Farhat and Roux, 1994] Farhat, C. and Roux, F.-X. (1994). The dual schur complement method with well-posed local neumann problems. *Contemporary Mathematics*, 157:193–201.

[Felippa, 2004] Felippa, C. A. (2004). *Introduction to Finite Element Method*, volume 885. University of Colorado.

[Främby et al., 2016] Främby, J., Brouzoulis, J., and Fagerström, M. (2016). Assessment of two methods for the accurate prediction of transverse stress distributions in laminates. *Composite Structures*, 140:602–611.

[Fries and Belytschko, 2010] Fries, T. and Belytschko, T. (2010). The extended/generalized finite element method: An overview of the method and its applications. *Computer Methods in Applied Mechanics and Engineering*, 84(3):253–304.

[Gallimard et al., 1996] Gallimard, L., Ladeveze, P., and Pelle, J. (1996). Error estimation and adaptivity in elastoplasticity. *International Journal for Numerical Methods in Engineering*, 39(2):189–217.

[Gendre, 2009] Gendre, L. (2009). *Approche globale / locale non-intrusive : application aux structures avec plasticitée localisée*. PhD thesis, École Normale Supérieure de Cachan.

[Gendre et al., 2009] Gendre, L., Allix, O., Gosselet, P., and Comte, F. (2009). Non-intrusive and exact global/local techniques for structural problems with local plasticity. *Computational Mechanics*, 44:233–245.

[Gillemot, 1976] Gillemot, L. F. (1976). Criterion of crack initiation and spreading. *Engineering Fracture Mechanics*, 8(1):239–253.

[Gosselet and Rey, 2006] Gosselet, P. and Rey, C. (2006). Non-overlapping domain decomposition methods in structural mechanics. *Archives of Computational Methods in Engineering*, 13:515–572.

[Goutaudier et al., 2020] Goutaudier, D., Osmond, G., and Gendre, D. (2020). Impact localization on a composite fuselage with a sparse network of accelerometers. *Comptes Rendus. Mécanique*, 348(3):191–209.

[Gravouil and A.Combescure, 2001] Gravouil, A. and A.Combescure (2001). Multi-time-step explicit–implicit method for non-linear structural dynamics. *International Journal for Numerical Methods in Engineering*, 50:199–225.

[Guguin, 2015] Guguin, G. (2015). *Stratégie non-intrusive de couplage plaque/3D pour la simulation des assemblages de plaques composites stratifiées*. PhD thesis, École Normale Supérieure de Cachan.

[Guguin et al., 2014] Guguin, G., Allix, O., Gosselet, P., , and Guinard, S. (2014). Nonintrusive coupling of 3d and 2d laminated composite models based on finite element 3d recovery. *International Journal for Numerical Methods in Engineering*, 98:324–343.

[Hahn and Tsai, 1973] Hahn, H. T. and Tsai, S. W. (1973). Nonlinear elastic behavior of unidirectional composite laminae. *Journal of Composite Materials*, 7(1):102–118.

[Hallett et al., 2009] Hallett, S., Green, B., Jiang, W.-G., and Wisnom, M. (2009). An experimental and numerical investigation into the damage mechanisms in notched composites. *Composites Part A: Applied Science and Manufacturing*, 40:613–624.

[Hallett et al., 2008] Hallett, S., Jiang, W.-G., Khan, B., and Wisnom, M. (2008). Modelling the interaction between matrix cracks and delamination damage in scaled quasi-isotropic specimens. *Composites Science and Technology*, 68:80–89.

[Hansbo and Hansbo, 2004] Hansbo, A. and Hansbo, P. (2004). A finite element method for the simulation of strong and weak discontinuities in solid mechanics. *Computational Methods in Applied Mechanics and Engineering*, 193:3523–3540.

[Hansbo, 2005] Hansbo, P. (2005). Nitsche's method for interface problems in computa- tional mechanics. *GAMM Mitteillungen, Surveys for Applied Mathematics and Mechanics*, 28(2):183 – 206.

[Hirai et al., 1984] Hirai, I., Wang, B. P., and Pilkey, W. D. (1984). An efficient zooming method for finite element analysis. *International Journal for Numerical Methods in Engineering*, 20:1671–1683.

[Hongkarnjanakul, 2013] Hongkarnjanakul, N. (2013). *Modélisation numérique pour la tolérance aux dommages d'impact sur stratifié composite : de l'impact à la résistance résiduelle en compression*. PhD thesis, Université de Toulouse.

[Huchette, 2005] Huchette, C. (2005). *Sur la complémentarité des approches expérimentales et numériques pour la modélisation des mécanismes d'endommagement des composites stratifiés*. PhD thesis, Université Paris 6.

[Jara-Almonte and Knight, 1988] Jara-Almonte, C. and Knight, C. (1988). The specified boundary stiffness/force sbsf method for finite element subregion analysis. *International Journal for Numerical Methods in Engineering*, 26:1567–1578.

[Johnson and Hansbo, 1992] Johnson, C. and Hansbo, P. (1992). Adaptive finite element methods in computational mechanics. *Computational Methods in Applied Mechanics and Engineering*, 101:143–181.

[Kant and Manjunatha, 1994] Kant, T. and Manjunatha, B. (1994). On accurate estimation of transverse stresses in multilayer laminates. *Computers & Structures*, 50(3):351–365.

[Kassim and Topping, 1987] Kassim, A. M. A. and Topping, B. H. V. (1987). Static reanalysis: a review. *Journal of Structural Engineering*, 113(5):1029–1045.

[Kelley, 1982] Kelley, F. (1982). Mesh requirements for the analysis of a stress concentration by the specified boundary displacement method. In *Proceedings of the second international computers in engineering conference, ASME*, pages 39–42.

[Kirsch, 2008] Kirsch, U. (2008). *Reanalysis of structures: A unified approach for linear, nonlinear, static and dynamic systems*. Springer, Solid Mechanics and its Applications.

[Kocaman et al., 2019] Kocaman, E., Chen, B., and Pinho, S. (2019). A polymorphic element formulation towards multiscale modelling of composite structures. *Computer Methods in Applied Mechanics and Engineering*, 346:359–387.

[Koiter, 1970] Koiter, W. T. (1970). On the mathematical foundation of shell theory. volume 3, pages 123–130. Congrès intternational de Mathématiques.

[Ladevèze, 2012] Ladevèze, P. (2012). *Nonlinear Computational Structural Mechanics: New Approaches and Non-Incremental Methods of Calculation.* Springer Science, Business Media.

[Ladevèze et al., 2000] Ladevèze, P., Allix, O., Deü, J.-F., and Lévêque, D. (2000). A mesomodel for localisation and damage computation in laminates. *Comput. Methods Appl. Mech. Engrg.*, 183:105–122.

[Ladevèze and Pécastaings, 1988] Ladevèze, P. and Pécastaings, F. (1988). The optimal version of reissner's theory. *Journal of Appied Mechanics*, 55(2):413–418.

[Laurin, 2009] Laurin, F. (2009). Rt8/11905 dmsc. Technical report, ONERA - The French Aerospace Lab.

[Laurin et al., 2007] Laurin, F., Carrère, N., and Maire, J.-F. (2007). A multiscale progressive failure approach for composite laminates based on thermodynamical viscoelastic and damage models. *Composites: Part A*, 38:198–209.

[Laurin et al., 2013] Laurin, F., Julien, C., and Huchette, C. (2013). Implementation in fe code abaqus of theonera 3d multiscale progressive failure approach. Technical report, ONERA - The French Aerospace Lab.

[Lee and Bathe, 1994] Lee, N.-S. and Bathe, K.-J. (1994). Error indicators and adaptive remeshing in large deformation finite element analysis. *Finite Elements in Analysis and Design*, 16:99–139.

[Liao et al., 1988] Liao, C., Reddy, J., and Engelstad, S. (1988). A solid-shell transition element for geometrically non-linear analysis of laminated composite structures. *International Journal for Numerical Methods in Engineering*, 26:1843–1854.

[Maimí et al., 2007a] Maimí, P., Camanho, P., Mayugo, J., and Dávila, C. (2007a). A continuum damage model for composite laminates: Part i – constitutive model. *Mechanics of Materials*, 39:897–908.

[Maimí et al., 2007b] Maimí, P., Camanho, P., Mayugo, J., and Dávila, C. (2007b). A continuum damage model for composite laminates: Part ii – computational implementation and validation. *Mechanics of Materials*, 39:909–919.

[Maire, 1992] Maire, J.-F. (1992). *Etudes théorique et expérimentale du comportement de matériaux composites en contraintes planes.* PhD thesis, Université de Franche Comté.

[Mandel, 1993] Mandel, J. (1993). Balancing domain decomposition. *Communications in Numerical Methods in Engineering*, 9:233–241.

[Mao and Sun, 1991] Mao, K. and Sun, C. (1991). A refined global-local finite element analysis method. *International Journal for Numerical Methods in Engineering*, 32:29–43.

[McCune et al., 2000] McCune, R. W., Armstrong, C. G., and Robinson, D. J. (2000). Mixed-dimensional coupling in finite element models. *International Journal for Numerical Methods in Engineering*, 49:725–750.

[Meer and Sluys, 2009] Meer, F. P. V. D. and Sluys, S. J. (2009). A phantom node formulation with mixed mode cohesive law for splitting in laminates. *International Journal of Fracture*, 158:107–124.

[Melenk and Babuška, 1996] Melenk, J. and Babuška, I. (1996). The partition of unity finite element method: Basic theory and applications. *Computer Methods in Applied Mechanics and Engineering*.

[Mindlin, 1951] Mindlin (1951). Influence of rotatory inertia and shear in flexural motions of isotropic elastic plates. *Journal of Applied Mechanics*, 18:1031–1036.

[Moës et al., 1999] Moës, N., Dolbow, J., and Belytschko, T. (1999). A finite element method for crack growth without remeshing. *International Journal for Numerical Methods in Engineering*, 46(1):131–150.

[Nguyen et al., 2013] Nguyen, V. P., Kerfriden, P., Claus, S., Bordas, S. P., and Noor, A. (2013). Nitsche's method method for mixed dimensional analysis: conforming and non-conforming continuum-beam and continuum-plate coupling.

[Nitsche, 1971] Nitsche, J. (1971). über ein variationsprinzip zur lösung von dirichlet-problemen bei verwendung von teilräumen, die keinen randbedingungen unterworfen sind. *Abhandlungen aus dem Mathematischen Seminar der Universität Hamburg*, 36:9–15.

[Oden et al., 1989] Oden, J., Demkowicz, L., Rachowicz, W., and Westermann, T. (1989). Toward a universal h-p adaptive finite element strategy. part 2: A posteriori error estimation. *Computational Methods in Applied Mechanics and Engineering*, 77:113–180.

[ONERA/DMAS, 2017] ONERA/DMAS (2017). *Catalogue de moyens techniques - Département Matériaux et Structures Composites*.

[Orifici et al., 2008] Orifici, A. C., Herszberg, I., and Thomson, R. S. (2008). Review of methodologies for composite material modelling incorporating failure. *Composite Structures*, 86(1-3):194–210.

[Ortiz and Quigley, 1991] Ortiz, M. and Quigley, J. (1991). Adaptive mesh refinement in strain localization problems. *Computater Methods in Applied Mechanics and Engineering*, 90:781–804.

[Pagano, 1970] Pagano, N. J. (1970). Exact solutions for rectangular bidirectional composites and sandwich plates. *Journal of Composite Materials*, 4(1):20–34.

[Pagano, 1978] Pagano, N. J. (1978). Stress fields in composite laminates. *International Journal of Solid and Structures*, 14:385–400.

[Perić et al., 1996] Perić, D., Hochard, C., Dutko, M., and Owen, D. (1996). Transfer operators for evolving meshes in small strain elasto-plasticity. *Computational Methods in Applied Mechanics and Engineering*, 137:331–344.

[Perić et al., 1994] Perić, D., Yu, J., and Owen, D. (1994). On error estimates and adaptivity in elastoplastic solids: Applications to the numerical simulation of strain localization in classical and cosserat continua. *International Journal for Numerical Methods in Engineering*, 37(8):1351–1379.

[Pinho et al., 2005] Pinho, S., Dávila, C., Camanho, P., Iannucci, L., and Robinson, P. (2005). Failure models and criteria for frp under in-plane or three-dimensional stress states including shear non-linearity. Technical report, NASA Langley Research Center.

[Reddy, 1997] Reddy, J. N. (1997). *Mechanics of Laminated Composite Plates, Theory and Analysis*. CRC Press.

[Reddy and D. H. Robbins, 1994] Reddy, J. N. and D. H. Robbins, J. (1994). Theories and computational models for composite laminates. *Applied Mechanics Reviews*, 47(6):147–169.

[Reissner, 1945] Reissner, E. (1945). The effect of transverse shear deformation on the bending of elastic plates. *Journal of Applied Mechanics*, 12:69–76.

[Remmers et al., 2003] Remmers, J. J. C., Wells, G. N., and de Borst, R. (2003). A solid-like shell element allowing for arbitrary delaminations. *International Journal for Numerical Methods in Engineering*, 58(13):2013–2040.

[Remy-Petipas, 2000] Remy-Petipas, C. (2000). *Analyse et prévision du comportement à long terme des composites fibres de carbone/matrice organique*. PhD thesis, Université de Franche Comté.

[Schwarz, 1870] Schwarz, H. A. (1870). *Ueber einen Grenzübergang durch alternirendes Verfahren*. Zürcher u. Furrer.

[Series et al., 2003] Series, L., Feyel, F., and Roux, F.-X. (2003). Une méthode de décomposition de domaine avec deux multiplicateurs de lagrange. 16ème Congrès Français de Mécanique.

[Simmonds, 1972] Simmonds, J. G. (1972). Pointwise displacement errors in linear shell theory resulting from errors in the stress-strain relations. *Journal of Applied Mathematics and Physics (ZAMP)*, 23:265–269.

[Song et al., 2006] Song, J., Areias, P. M. A., and Belytschko, T. (2006). A method for dynamic crack and shear band propagation with phantom nodes. *International Journal for Numerical Methods in Engineering*, 67(6):868–893.

[Strouboulis et al., 2000] Strouboulis, T., Babuška, I., and Copps, K. (2000). The design and analysis of the generalized finite element method. *Computer Methods in Applied Mechanics and Engineering*, 181(1-3):43–69.

[Surana, 1980] Surana, K. S. (1980). Transition finite elements for three-dimensional stress analysis. *International Journal for Numerical Methods in Engineering*, 15(7):991–1020.

[Surana, 1982] Surana, K. S. (1982). Geometrically non-linear formulation for the three dimensional solid-shell transition finite elements. *Computers & Structures*, 15(5):549–566.

[Tallec et al., 1991] Tallec, P. L., Roeck, Y.-H. D., and Vidrascu, M. (1991). Domain-decomposition methods for large linearly elliptic three dimensional problems. *Journal for Computational and Applied Mathematics*, 34:93–117.

[Todeschini, 2014] Todeschini, Y. (2014). Comparaison de deux approches numériques pour la simulation du délaminage dans les structures composites. Technical report, ONERA - The French Aerospace Lab.

[Touzeau, 2012] Touzeau, J. (2012). *Approche numérique multiéchelle / multimodèle de la dégradation des matériaux composites*. PhD thesis, École Centrale Paris.

[Turon et al., 2006] Turon, A., Camanho, P., Costa, J., and Dávila, C. (2006). A damage model for the simulation of delamination in advanced composites under variable-mode loading. *Mechanics of Materials*, 38:1072–1089.

[https://www.airbus.com/,] https://www.airbus.com/. Test programme and certification. https://www.airbus.com/aircraft/how-is-an-aircraft-built/test-programme-and-certification.html.

[https://www.digitalengineering247.com/, 2016] https://www.digitalengineering247.com/ (2016). Adams Simulation Saves Millions by Replacing Physical Testing in Aircraft Certification. https://www.digitalengineering247.com/article/adams-simulation-saves-millions-by-replacing-physical-testing-in-aircraft-certification/. [Online; accessed July-2020].

[Villon et al., 2002] Villon, P., Borouchaki, H., and Saanouni, K. (2002). Transfert de champs plastiquement admissibles. *Comptes Rendus Mécanique*, 330:313–318.

[Wang and Pilkey, 1980] Wang, B. P. and Pilkey, W. D. (1980). Efficient reanalysis of locally modified structures. Technical report, Department of Mechanical & Aerospace Engineering, University of Virginia, Charlottesville.

[Whitcomb, 1991] Whitcomb, J. (1991). Iterative global/local finite element analysis. *Computers and Structures*, 40:1027–1031.

[Whitcomb, 1993] Whitcomb, J. (1993). Application of iterative global/local finite-element analysis. part 2: Geometrically non-linear analysis. *Communications in Numerical Methods in Engineering*, 9(9):757–766.

[Whitcomb and WOO, 1993] Whitcomb, J. D. and WOO, K. (1993). Application of iterative global/local finite-element analysis. part 1: Linear analysis. *Communications in Numerical Methods in Engineering*, 9(9):745–756.

[Whitney and Pagano, 1970] Whitney, J. M. and Pagano, N. J. (1970). Shear deformation in heterogeneous anisotropic plates. *Journal of Applied Mechanics*, 37(4):1031–1036.

[Winzen, 2006] Winzen, A. (2006). Simulation of stringer stiffened cfrp panels in consideration of skin-stringer separation. Technical report, DLR.

[Yang et al., 2000] Yang, H. T. Y., Saigal, S., Masud, A., and Kapania, R. K. (2000). A survey of recent shell finite elements. *International Journal for Numerical Methods in Engineering*, 47:101–127.

[Yastrebov et al., 2017] Yastrebov, V., Akula, B., and Vignollet, J. (2017). Contact along virtual interfaces: coupling the x-fem with the mortar discretization. 7th GACM Colloquium on Computational Mechanics for Young Scientists from Academia and Industry.

[Zhang and Yang, 2009] Zhang, Y. and Yang, C. (2009). Recent developments in finite element analysis for laminated composite plates. *Composite Structures*, 88:147–157.

[Zhu and Zienkiewicz, 1988] Zhu, J. and Zienkiewicz, O. (1988). Adaptive techniques in the finite element method. *Communications in applied numerical methods*, 4:197–204.

[Zienkiewicz and Zhu, 1987] Zienkiewicz, O. and Zhu, J. (1987). A simple error estimator and adaptive procedure for practical engineering analysis. *International Journal for Numerical Methods in Engineering*, 24 (2):337–357.

[Zienkiewicz et al., 2000] Zienkiewicz, O. C., Taylor, R. L., Taylor, R. L., and Taylor, R. L. (2000). *The finite element method - Vol. 1: the Basis; Vol. 2: solid mechanics*, volume 1-2. Butterworth-heinemann.

[Zobeiry et al., 2015] Zobeiry, N., Vaziri, R., and Poursartip, A. (2015). Characterization of strain-softening behavior and failure mechanisms of composites under tension and compression. *Composites*, Part A 68:29–41.

université PARIS-SACLAY

ÉCOLE DOCTORALE
Sciences mécaniques et énergétiques, matériaux et géosciences (SMEMAG)

Titre: Approche multi-modèle adaptative pour la simulation de propagation d'endommagement dans une large structure composite stratifiée

Mots clés: Mécanique numérique, Remaillage adaptatif, Structure composite stratifiée

Résumé: Les industriels du domaine aéronautique s'intéressent à la réalisation de simulations prédictives à l'échelle structurale. Dans ces situations, la taille des problèmes mécaniques concernés est telle que l'utilisation de modèles matériaux et de discrétisations éléments finis simplifiés, telles que des coques, est indispensable. De plus, dans un contexte d'utilisation croissante de stratifiés composites, les industriels s'intéressent à simuler l'impact d'un endommagement initialement localisé et de son évolution, sur la tenue en service d'un composant. Or, pour simuler fidèlement l'endommagement d'un tel stratifié, une modélisation plus précise est nécessaire avec une discrétisation fine et une loi matériau complexe. La généralisation de ce type de modélisation n'est pas acceptable à l'échelle de grandes structures, de sorte que le développement de stratégies de calcul ad-hoc est aujourd'hui essentiel pour les concepteurs aéronautiques, l'idée sous-jacente étant de pouvoir ajuster la finesse de modélisation au besoin, dans l'espace et dans le temps.
La méthode proposée dans la thèse entre dans ce cadre, en exploitant des algorithmes de remaillage adaptatif, mais en s'imposant le cadre d'une résolution numérique utilisant un code de calcul aux éléments finis industriel. Ainsi, ce manuscrit introduit une nouvelle approche numérique d'adaptation multi-modèles. Dans un premier temps, on pose un problème de référence multi-modèles à décomposition fixée. Il consiste en un domaine généralement élastique comprenant quelques inclusions anélastiques où le modèle raffiné permet de capturer des phénomènes complexes se produisant dans les stratifiés composites. Dans le modèle discret, le domaine élastique est modélisé avec des éléments de coque multicouches, tandis que le domaine anélastique est modélisé avec des éléments solides comprenant au moins un élément par pli dans l'épaisseur. Cette technique nécessite la mise en oeuvre d'un couplage multidimensionnel. Dans un second temps, l'opération d'adaptation de modèle résulte notamment de l'étude du déclenchement de l'adaptation, de la stratégie remaillage, et de la problématique de mise à jour de l'état. La stratégie de remaillage est l'une des principales contributions de ce travail car elle permet de simplifier les autres opérations tel que la mise à jour de l'état. Les résultats de l'approche multi-modèle adaptative appliquée à des cas de test académiques, montrent la flexibilité fournie par notre méthode.

Title: An adaptive multi-model approach for damage propagation simulations in large composite structures

Keywords: Computational mechanics, Adaptive remeshing, Laminated composite structures

Abstract: Aeronautics manufacturers are interested in carrying out predictive simulations at the structural scale. In these situations, the size of the mechanical problems concerned is such that the use of material models and of simplified finite element discretizations, such as shell elements, is essential. Moreover, in a context of growing usage of composite laminates, industrials are interested in simulating the impact of an initially localized damage and its evolution, on the in-service behavior of a component. However, to faithfully simulate the damage of such a laminate, a fine discretization and a complex material law is required. The generalization of this type of modelling is not acceptable, in terms of calculation cost, at the scale of large structures, so that the development of ad-hoc calculation strategies is essential today for aeronautical designers, the underlying idea being to be able to adjust the fineness of the modelling as needed, in space and time.
The method proposed in the thesis falls within this framework, by exploiting adaptive remeshing algorithms, while imposing the framework of a numerical resolution using an industrial finite element calculation software. Thus, this manuscript introduces a new numerical approach relying on multi-model adaptation for the simulation of local complex phenomena in large composite structures. Firstly, a multi-model reference problem at a fixed decomposition is stated. It consists of an elastic domain with some anelastic inclusions where the model is more refined to capture complex phenomena occurring in composite laminates. In the discrete model, the elastic domain is modelled with multilayered shell elements while the anelastic domain is modelled with solid elements with, at least, one element per ply through the thickness. This technique requires to couple two domains with different kinematics with a multidimensional coupling condition. Secondly, the progressive adaptation of the multi-model problem through remeshing involve in particular the study of the model adaptation triggering strategy, the remeshing strategy, and the state update problematic. The remeshing strategy is one of the main contributions of this work as it allows simplifying the other operations such as the state update. The adaptive multi-model approach is applied to an academic test case of a compressive-bending holed plate showing the flexibility provided by our method.

Université Paris-Saclay
Espace Technologique / Immeuble Discovery
Route de l'Orme aux Merisiers RD 128 / 91190 Saint-Aubin, France